THREE DIMENSIONAL MHD SIMULATIONS OF THE DYNAMICS AND ENERGETICS OF CORONAL FLUX TUBES

Thomas Alexander Howson

A Thesis Submitted for the Degree of PhD
at the
University of St Andrews

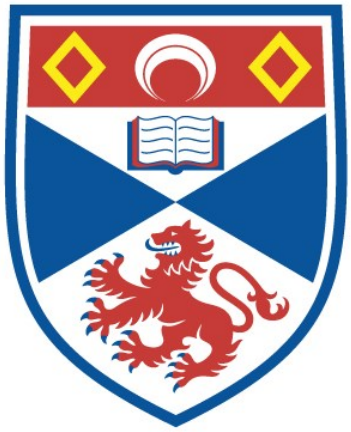

2019

Three Dimensional MHD Simulations of the Dynamics and Energetics of Coronal Flux Tubes

Thomas Alexander Howson

University of
St Andrews

This thesis is submitted in partial fulfilment for the degree of
Doctor of Philosophy (PhD)
at the University of St Andrews

September 2018

Abstract

In this thesis we present the results of three-dimensional MHD simulations of the evolution of magnetic flux tubes within the solar atmosphere. We consider the dynamics and energetics of coronal loops that are perturbed from an equilibrium state by wave motions or driven continuously by an imposed velocity field. In each case, we investigate the dissipation of magnetic and kinetic energy and evaluate the implications for the heating of coronal plasma.

We present models of transversely oscillating flux tubes which experience rapid damping as kink mode energy is transferred into azimuthal Alfvén modes. This mode conversion is typically associated with a density enhancement within the flux tube, however, we demonstrate that it can also proceed with an increased internal magnetic field strength. In either regime, the azimuthal wave modes are subject to dissipation through phase mixing and may promote the development of the magnetic Kelvin-Helmholtz instability. This is associated with the generation of further small scales in the magnetic and velocity fields and, in a non-ideal regime, will enhance the rate of wave dissipation. We show that the growth rate of the instability is sensitive to the implemented transport coefficients and the presence of helical magnetic field.

Additionally, we consider the effects of thermal conduction and optically thin radiation on the evolution of a flux tube tectonics model. We present the results of simulations in which two magnetic flux tubes are twisted around each other by the action of rotational drivers imposed at the loop foot points. Large currents develop at the interface of the flux tubes and magnetic reconnection is triggered as the braiding progresses. The inclusion of conduction and optically thin radiation reduces the high temperatures and gas pressures observed in the centre of the numerical domain. As a result, these processes modify the reconnection outflows, distribution of plasma and the evolution of the magnetic field.

Candidate's declaration

I, Thomas Alexander Howson, do hereby certify that this thesis, submitted for the degree of PhD, which is approximately 50,000 words in length, has been written by me, and that it is the record of work carried out by me, or principally by myself in collaboration with others as acknowledged, and that it has not been submitted in any previous application for any degree.

I was admitted as a research student at the University of St Andrews in August 2015.

I received funding from an organisation or institution and have acknowledged the funders in the full text of my thesis.

Date: ..... Signature of candidate: .....

Supervisor's declaration

I hereby certify that the candidate has fulfilled the conditions of the Resolution and Regulations appropriate for the degree of PhD in the University of St Andrews and that the candidate is qualified to submit this thesis in application for that degree.

Date: ..... Signature of supervisor: .....

Permission for publication

In submitting this thesis to the University of St Andrews we understand that we are giving permission for it to be made available for use in accordance with the regulations of the University Library for the time being in force, subject to any copyright vested in the work not being affected thereby. We also understand, unless exempt by an award of an embargo as requested below, that the title and the abstract will be published, and that a copy of the work may be made and supplied to any bona fide library or research worker, that this thesis will be electronically accessible for personal or research use and that the library has the right to migrate this thesis into new electronic forms as required to ensure continued access to the thesis.

I, Thomas Alexander Howson, confirm that my thesis does not contain any third-party material that requires copyright clearance.

The following is an agreed request by candidate and supervisor regarding the publication of this thesis:

Printed copy

No embargo on print copy.

Electric copy

No embargo on electronic copy.

Date: ..... Signature of candidate: .....

Date: ..... Signature of supervisor: .....

Underpinning Research Data or Digital Outputs

Candidate's declaration

I, Thomas Alexander Howson, hereby certify that no requirements to deposit original research data or digital outputs apply to this thesis and that, where appropriate, secondary data used have been referenced in the full text of my thesis.

Date: ..... Signature of candidate: .....

Financial Support

The research leading to the results presented within this thesis has received funding from the UK Science and Technology Facilities Council and the European Union Horizon 2020 research and innovation programme. This work used the DIRAC 1, UKMHD Consortium machine at the University of St Andrews and the Darwin Data Analytic system at the University of Cambridge.

Publications

This thesis contains work which has been adapted from the following publications:

1. T. A. Howson, I. De Moortel & P. Antolin. The effects of resistivity and viscosity on the Kelvin-Helmholtz instability in oscillating coronal loops. A&A, 602:A74, June 2017. doi: 10.1051/0004-6361/201630259.

2. T. A. Howson, I. De Moortel & P. Antolin. Energetics of the Kelvin-Helmholtz instability induced by transverse waves in twisted coronal loops. A&A, 607:A77, November 2017. doi: 10.1051/0004-6361/201731178.

Collaboration Statement

The numerical simulations presented in this thesis were carried out by myself under the supervision of Prof. Ineke De Moortel and Dr. Patrick Antolin. I am grateful to Prof. Alan Hood, Prof. Peter Cargill and Dr. Andrew Wright for their helpful discussions on numerical methods, the Kelvin-Helmholtz instability and MHD resonances, respectively.

Acknowledgements

So I'm sat here on a rainy September day in St Andrews (surely not) wondering how to say thank you to everyone who has helped me to reach this point. It's difficult to believe that I'm actually going to be submitting my thesis tomorrow!

Firstly, I have to say a massive thank you to Ineke. Despite her ability to only ever ask questions that I don't know the answer to, I've really enjoyed working on my PhD with her over the past three years. I've learnt so much about thinking critically, conducting reasearch and, most importantly, the best Munros. Thanks to her, I'll always remember to ask 'Who actually cares about this?'

Secondly, thank you to Patrick and his inexhaustible enthusiasm for solar physics. I have to say that his seemingly endless criticism of my draft papers has improved the work in this thesis immeasurably.

I'd also like to say thank you to Thomas and Tom for agreeing to spend substantial time and effort trying to figure out what I'm waffling on about over the next 200 pages. Without you there really would be little point in this thesis!

I'd like to thank all of the members of the Maths department and Steve's football players. They made sure that there was always something to make me smile - even when I still had 50,000 words left to write. I'd especially like to mention my Christmas officemates, Ben and Hendrik-Jan. They were never short of distractions and my thesis might have been substantially longer without their influence!

Thank you to my parents and to my sisters, Rachael and Eleanor, and to Angus (although I'm not sure how much he helped). I'm convinced that they can't wait to read every word of this thesis. And there better not be any skimming through chapters - there will be a test! I also have to say thank you to my grandparents for their limitless encouragement over the years. Thank you to Sarah too - who would have thought that 20 years later I'd still remember you trying to answer my questions about how electricity travels from one end of a wire to the other?

Finally, I'd like to thank Hope, especially for making my time in St Andrews so enjoyable. Her disdain for all things mathematical has been invaluable, particularly when my mind won't stop thinking about my latest idea for a new simulation. I'd just like to say, thanks for reminding me that it really doesn't matter if $\mathbf{B}$ isn't divergence free.

Contents

Chapter 1

Introduction

In this thesis, we consider the dynamics and the heating of plasma within the atmosphere of our local star; the Sun. The solar atmosphere consists of three distinct, but highly coupled layers; the photosphere, the chromosphere and the corona. The photosphere is the lowest of these layers and is typically observed as the solar surface. It is around 500 km thick and has a temperature of approximately 6000 K. Immediately above the photosphere lies the chromosphere, which is 2500 km thick and has a temperature that varies with height from 4400 K at low altitudes up to 30 000 K at higher altitudes. Finally, the corona is the outermost layer of the atmosphere and stretches from the top of the chromosphere into the solar system. It is the hottest of the three atmospheric layers with temperatures in excess of 10^6 K. The cause of these high temperatures is not well understood. The open question regarding how plasma is heated to, and maintained, at these temperatures is known as the coronal heating problem. The search for an explanation of this phenomenon motivates the work presented within this thesis.

Energy is continuously lost from the corona through the processes of thermal conduction, optically thin radiation (OTR) and the flow of mass - both into space via the solar wind and through the draining of plasma into the lower atmosphere (De Moortel and Browning, 2015). Conduction acts to transfer heat from the hot corona to the cooler atmospheric layers below. Meanwhile, due to the low coronal density, the effects of radiation tend to be relatively small. However, in regions of enhanced density, such as in prominences, radiation can cause significant heat loss (Parenti, 2014). Additionally, further energy is required to power the fast solar wind that originates in regions of open magnetic field. Since the solar corona is highly inhomogeneous in nature, different regions of the atmosphere have distinct energy requirements. In particular, Withbroe and Noyes (1977) estimate the energy budget to be around 800 W m^{-2} in coronal hole

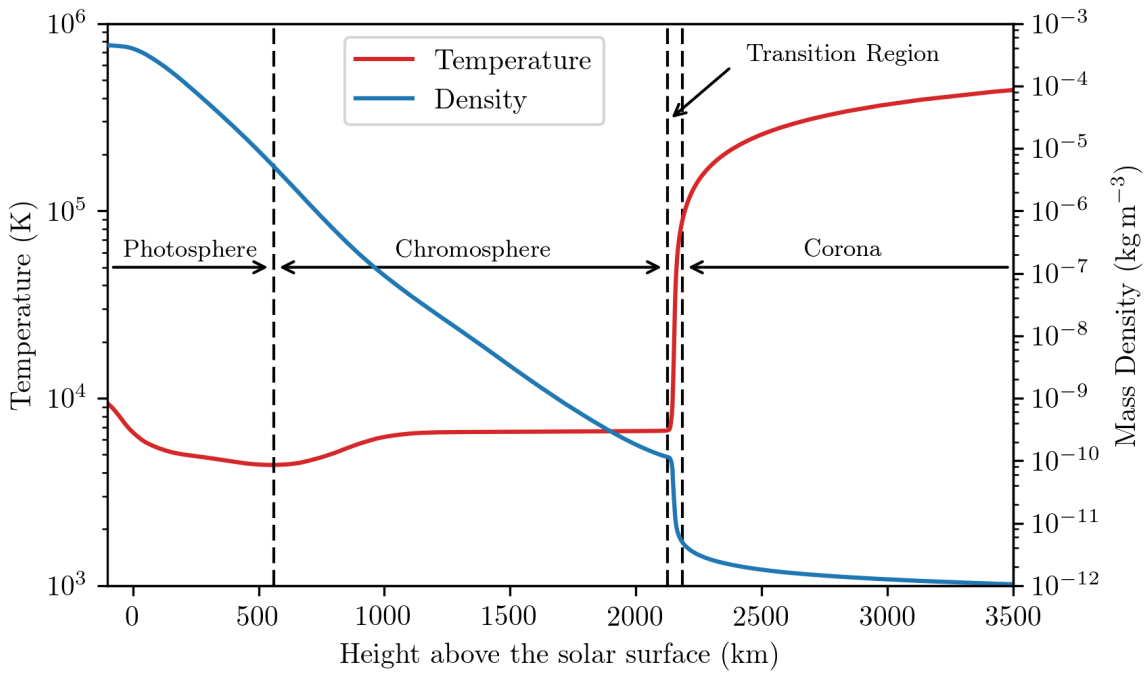

Figure 1.1: Mean temperature (red) and density (blue) as a function of altitude in the lower solar atmosphere. Plot generated using data from Avrett and Loeser (2008).

regions, 10000 W m^{-2} in active regions and 300 W m^{-2} for the Quiet Sun.

Although the temperature increases with distance from the solar surface, the density falls by around eight orders of magnitude between the photosphere and the tenuous corona. This density (blue) decrease is shown alongside the temperature (red) increase in Figure 1.1. The wide range of temperatures and densities present throughout the solar atmosphere results in various physical processes being relevant at different altitudes. This ensures that a complete consideration of the atmosphere is extremely difficult. Investigations are further confounded by the exchange of mass and energy across atmospheric boundaries which significantly complicates the nature of the coronal heating problem.

It is well established that the source of the energy that heats the corona is the Sun's magnetic field (e.g. Klimchuk, 2006). Convective flows within the interior of the Sun ensure that the solar surface is in turbulent motion. Consequently, plasma flows in the photosphere pull on any magnetic field that is protruding from the solar interior and inject a (Poynting) flux of magnetic energy into the atmosphere. However, given the low dissipation rates within the solar corona, the subsequent mechanisms for releasing the magnetic energy in the form of heat remain unclear (Erdélyi and Ballai, 2007; Parnell and De Moortel, 2012; De Moortel and Browning, 2015).

The majority of proposed mechanisms fall approximately into one of two broad

categories. Either energy is deposited by the damping and dispersion of coronal waves (wave heating, e.g. Heyvaerts and Priest, 1983; Antolin and Shibata, 2010; McIntosh et al., 2011; Pagano and De Moortel, 2017) or magnetic energy slowly accumulates in the corona before being released by the stressed magnetic field (braiding and reconnection heating, e.g. Hood et al., 2009; Wilmot-Smith et al., 2010; Pontin et al., 2011; Bareford et al., 2016; Reale et al., 2016). Alternatively, some heating models attempt to combine the ideas of wave and reconnection heating. In these systems, wave energy is typically used to drive the formation of a turbulent-like regime in the plasma (e.g. van Ballegooijen et al., 2011; Magyar et al., 2017). This process generates small scales within both the magnetic and velocity fields and may lead to heating through magnetic reconnection (see Yamada et al., 2010, for a comprehensive review of this process in laboratory and astrophyiscal plasmas).

1.1 MHD Equations

On account of the high temperatures on the Sun, much of the fluid exists in ionised form (plasma) in which some, or all, of the electrons have been stripped away from the atomic nuclei. The existence of free, charged particles ensures that the plasma experiences forces exerted by the magnetic field. On the other hand, plasma flows are able to advect the magnetic field through the solar atmosphere. This coupling of magnetic effects with hydrodynamic processes results in a complicated physical system that is very difficult to understand.

The modelling of astrophysical plasmas such as the solar corona can be tackled using a variety of methods. For example, we could attempt to determine the behaviour of all of the individual particles that constitute the plasma. Unfortunately, due to the large number of particles that must be tracked, the computational cost of adopting this approach is usually prohibitively high. As a result, we often rely on modelling the collective or average behaviour of the plasma particles.

As such, the numerical simulations presented within this thesis implement a fluid description of the plasma. In the literature, a multi-fluid approach is occasionally adopted, in which the negatively charged electrons, the positively charged ions and the neutral atoms are treated separately (see Khomenko, 2017, for a review). However, in fully ionised plasmas, electric charge considerations typically restrict any vastly different ion and electron behaviour and therefore a single fluid model (in which electrons and ions are treated together) often suffices. Indeed, we implement this description for the models presented hereafter. In this regime, the governing equations are the Mag-

netohydrodynamic (MHD) equations which are formed by coupling the Navier-Stokes equations of hydrodynamics to Maxwell's equations of electromagnetism.

This set of equations (displayed below) are highly coupled and, despite providing a great simplification from tracking every particle, they still represent a significant challenge to solve. Analytic techniques can provide a useful insight into simplified situations (e.g. with spatial invariance in one or more dimensions) such as MHD equilibria (e.g. Hundhausen and Low, 1994), waves (e.g. Heyvaerts and Priest, 1983) and instability analysis (e.g. Hood and Priest, 1979), however, in general, the equations can only be advanced through time using numerical techniques. These methods typically require high performance computing and capturing the multi-scale nature of many coronal processes remains difficult. Further simplifications such as reduced MHD (see, for example, Kadomtsev and Pogutse, 1974; Strauss, 1976) can, in certain situations (see Goldstraw et al., 2017, for an analysis), provide a valid description of the physical system at a reduced computational cost. However, for the remainder of this thesis we shall restrict our consideration to the full, three-dimensional, resistive form of the MHD equations.

1.1.1 Maxwell's Equations

In order to formulate the full set of MHD equations, we begin by listing Maxwell's four equations of electromagnetism (in mks units):

1. Ampère's Law
$$\nabla \times \mathbf{B} = \mu_0 \mathbf{j} + \frac{1}{c^2}\frac{\partial \mathbf{E}}{\partial t}, \tag{1.1}$$

2. Faraday's Law
$$\nabla \times \mathbf{E} = -\frac{\partial \mathbf{B}}{\partial t}, \tag{1.2}$$

3. Gauss' Law
$$\nabla \cdot \mathbf{E} = \frac{\rho_c}{\epsilon_0}, \tag{1.3}$$

4. Solenoidal Constraint
$$\nabla \cdot \mathbf{B} = 0. \tag{1.4}$$

In these equations, $\mathbf{B}$ denotes the magnetic field, $\mathbf{j}$ is the current density, $\mathbf{E}$ is the electric field and ρ_c is the charge density. Additionally, $\mu_0 = 4\pi \times 10^7$ H m^{-1} is the magnetic permeability $c \approx 3.0 \times 10^8$ m s^{-1} is the speed of light and $\epsilon_0 \approx 8.9 \times$

10^{-12} F m^{-1}. We note that the solenoidal constraint implies that there are no magnetic monopoles; alternatively, there are no sources or sinks within the magnetic field.

Non-relativistic MHD

Relativistic effects can become significant in some exotic astrophysical plasmas (e.g. in accretion discs around black holes, see for example McKinney et al., 2012), however, typically in the Sun, we assume that typical speeds (v_0) are much smaller than the speed of light; $v_0 \ll c$. We can use this assumption to simplify equation (1.1).

By introducing typical sizes for the electric field, E_0 and the magnetic field, B_0 and typical length and time scales, l_0 and t_0, respectively, we can use equation (1.2) and $v_0 = \dfrac{l_0}{t_0}$ to find

$$\frac{E_0}{l_0} \approx \frac{B_0}{t_0} \implies E_0 \approx v_0 B_0. \tag{1.5}$$

Using this relation we find

$$\left| \frac{1}{c^2} \frac{\partial \mathbf{E}}{\partial t} \right| \approx \frac{E_0}{c^2 t_0} = \frac{v_0 B_0}{c^2 t_0} = \frac{v_0^2 B_0}{c^2 l_0} \approx \frac{v^2}{c^2} \left| \nabla \times \mathbf{B} \right|. \tag{1.6}$$

Since we assume $v_0 \ll c$, we can neglect the second term on the right-hand side of equation (1.1). Hence for the remainder of this thesis, we use the following approximation of Ampère's law

$$\nabla \times \mathbf{B} = \mu_0 \mathbf{j}. \tag{1.7}$$

1.1.2 Fluid Equations

The following equations govern the behaviour of the plasma and are coupled to Maxwell's equations through the equation of motion (1.9) and Ohm's Law (1.12) which will be discussed later.

1. Continuity of Mass
$$\frac{\partial \rho}{\partial t} + \nabla \cdot (\rho \mathbf{v}) = 0, \tag{1.8}$$

2. Equation of Motion
$$\rho \frac{\mathrm{D}\mathbf{v}}{\mathrm{D}t} = \mathbf{j} \times \mathbf{B} - \nabla P + \rho \mathbf{g} + \mathbf{F}, \tag{1.9}$$

3. Energy Equation
$$\frac{\rho^\gamma}{\gamma - 1} \frac{\mathrm{D}}{\mathrm{D}t} \left(\frac{P}{\rho^\gamma} \right) = -\mathcal{L}, \tag{1.10}$$

4. Ideal Gas Law

$$P = \frac{1}{\mu}\rho RT. \tag{1.11}$$

Here, ρ is the plasma density, $\mathbf{v}$ is the plasma velocity, P is the gas pressure, T is the temperature, $\mathbf{g}$ is acceleration due to gravity and $\mathbf{F}$ denotes any additional forces that may be included in the system (e.g. frictional forces). In addition, γ is the ratio of specific heats, μ is the mean atomic weight and $R \approx 8.3 \times 10^3$ J K^{-1} kg^{-1}. Finally, $\mathcal{L}$ is some function that describes how internal energy is lost, perhaps through optically thin radiation or thermal conduction, for example. Alternatively, the right-hand side of (1.10) can represent a gain in internal energy through the dissipation of kinetic or magnetic energy. In the case $\mathcal{L} = 0$, the plasma is said to be adiabatic.

1.1.3 Ohm's Law

As mentioned above, Ohm's Law couples Maxwell's equations to the fluid equations and is given by

$$\mathbf{j} = \sigma\left(\mathbf{E} + \mathbf{v} \times \mathbf{B}\right), \tag{1.12}$$

where σ is the electrical conductivity. In some situations, e.g. in the solar chromosphere, a more generalised form of Ohm's law should be used. In such cases, we consider the separate behaviour of ions, electrons, and importantly, neutral atoms. Consequently, the form of equation 1.12 can become significantly more complicated. For further information we refer the reader to Chapter 2 of Priest (2014).

1.1.4 Induction Equation

By taking the curl of Ohm's Law (1.12), we can eliminate $\mathbf{j}$ and $\mathbf{E}$ using Ampère's Law (1.7), Faraday's Law (1.2) and the solenoidal constraint (1.4) to obtain

$$\frac{\partial \mathbf{B}}{\partial t} = \nabla \times (\mathbf{v} \times \mathbf{B}) + \eta \nabla^2 \mathbf{B}. \tag{1.13}$$

Here, we have used the vector identity $\nabla \times (\nabla \times \mathbf{A}) = \nabla\left(\nabla \cdot \mathbf{A}\right) - \nabla^2 \mathbf{A}$ and assumed that the magnetic diffusivity, $\eta = \frac{1}{\mu\sigma}$, is spatially uniform.

The induction equation describes the evolution of the magnetic field through time and the two terms on the right-hand side of equation 1.13 are called the advection and diffusion terms, respectively. The ratio of these terms is called the magnetic Reynolds

number and using typical values can be defined as

$$R_M = \frac{\frac{v_0 B_0}{l_0}}{\frac{\eta B_0}{l_0^2}} = \frac{l_0 v_0}{\eta}. \tag{1.14}$$

In the majority of the coronal volume, $R_M \gg 1$, meaning the advection term dominates, and magnetic field is *frozen* into the plasma. In this regime, magnetic field lines move with plasma flows. Alternatively, when $R_M \ll 1$, the diffusion term in the induction equation dominates. If this is the case, the magnetic field can slip through the plasma. This regime occurs in current sheets and when magnetic reconnection changes the connectivity of plasma elements.

1.1.5 Magnetic Energy

The magnetic energy within a given volume of plasma, V, is given by

$$E_B = \int_V \frac{B^2}{2\mu_0} \, \mathrm{d}V. \tag{1.15}$$

We consider how this changes in time and obtain

$$\frac{\partial E_B}{\partial t} = \frac{\partial}{\partial t}\left(\int_V \frac{B^2}{2\mu_0} \, \mathrm{d}V\right) = \frac{1}{\mu_0}\int_V \mathbf{B} \cdot \frac{\partial \mathbf{B}}{\partial t} \, \mathrm{d}V, \tag{1.16}$$

where we have assumed that the volume, V, is constant. Using the induction equation (1.13), Ampère's Law (1.7) and vector identies, we can then rewrite the change in magnetic energy as

$$\frac{\partial E_B}{\partial t} = \int_S \left(\frac{(\mathbf{v} \times \mathbf{B}) \times \mathbf{B}}{\mu_0} - \eta \mathbf{j} \times \mathbf{B}\right) \cdot \mathrm{d}\mathbf{S} - \int_V \left(\mu_0 \eta j^2 + \mathbf{v} \cdot (\mathbf{j} \times \mathbf{B})\right) \, \mathrm{d}V. \tag{1.17}$$

Here, the surface integral is taken over the boundary of the volume, V. We can use Ohm's Law (1.12) to rewrite the surface integral and we obtain

$$\frac{\partial E_B}{\partial t} = -\underbrace{\int_S \frac{\mathbf{E} \times \mathbf{B}}{\mu_0} \cdot \mathrm{d}\mathbf{S}}_{\text{Poynting flux}} - \underbrace{\mu_0 \int_V \eta j^2 \, \mathrm{d}V}_{\text{Ohmic heating}} - \underbrace{\int_V \mathbf{v} \cdot (\mathbf{j} \times \mathbf{B}) \, \mathrm{d}V}_{\text{Work done by Lorentz force}}. \tag{1.18}$$

The Poynting flux describes the flow of magnetic energy through the boundary of the volume. This is integral for injecting magnetic energy into the solar atmosphere from below the surface and will be briefly discussed later (Section 1.5). The Ohmic heating

term is associated with the dissipation of magnetic energy in the presence of currents. It does not contribute to the change in magnetic energy in fully ideal plasmas ($\eta = 0$), however, can cause plasma heating if a resistivity is present. In general, this is not a reversible process. Finally, the third integral in equation (1.18) represents the work done by the action of the $\mathbf{j} \times \mathbf{B}$ force e.g. in the generation of flows by non-straight field lines (tension force).

1.2 MHD Equilibria

The initial conditions of the simulations presented within this thesis invariably consist of some MHD equilibrium which is then modified by the introduction of some wave energy. The initial equilibria considered are (possibly numerical) solutions to equation 1.9 with the left-hand side set to $\mathbf{0}$ (no flows).

We typically neglect the effects of gravity ($\mathbf{g} = \mathbf{0}$) and any dissipative forces, $\mathbf{F}$, are not considered for the purposes of the initial equilibrium. Hence, we typically seek solutions to

$$\mathbf{j} \times \mathbf{B} = \nabla P. \tag{1.19}$$

Here the left-hand side is the Lorentz force and the right-hand side is the gas pressure force. Considering the Lorentz force, it is clear that it only acts perpendicular to the magnetic field. Further, we can rewrite the left-hand side of equation 1.19 as

$$\mathbf{j} \times \mathbf{B} = \frac{1}{\mu_0} (\mathbf{B} \cdot \nabla) \mathbf{B} - \nabla \left(\frac{B^2}{2\mu_0} \right). \tag{1.20}$$

Here, the first term on the right-hand side is the magnetic tension force and acts to straighten field lines. The second term is the magnetic pressure force and acts from regions of high field strength to regions of low field strength.

Returning to equation 1.19, we define the dimensionless plasma-β as the ratio between the plasma (gas) and magnetic pressures,

$$\beta = \frac{2\mu_0 P}{B^2}. \tag{1.21}$$

In the case, $\beta \gg 1$, the gas pressure gradient is the dominant force. This is typically the case in the lower solar atmosphere. However, in the corona, transition region and upper chromosphere, generally $\beta \ll 1$ and so the plasma dynamics are dominated by magnetic forces. Hence we can find approximate coronal equilibria by balancing the magnetic tension and pressure forces.

The exact form of the equilibrium used for different simulations will be explained in detail in subsequent chapters. However, at this stage we note that it is often convenient to solve $\mathbf{j} \times \mathbf{B} = \mathbf{0}$ analytically, before introducing a plasma pressure which is then allowed to relax numerically. In a magnetically dominated plasma ($\beta \ll 1$), we expect this relaxation to have little effect on the field profile.

1.3 MHD Waves

Within this thesis, we investigate the behaviour of various MHD waves within coronal magnetic flux tubes. We often consider complex magnetic geometries or non-linear effects such as the formation of dynamic instabilities which require a numerical approach. However, in simple geometries, linear MHD wave solutions are tractable with an analytic treatment.

1.3.1 Uniform Media

We begin by considering an equilibrium state in which a magnetic field $\mathbf{B}_0 = (0, 0, B_0)$ is embedded within a stationary plasma of uniform density, ρ_0 and pressure, P_0. We follow the analysis presented in Chapter 4 of Priest (2014) and consider a linear perturbation of the equilibrium state such that $\mathbf{B} = \mathbf{B}_0 + \mathbf{B}_1$, $\rho = \rho_0 + \rho_1$, $P = P_0 + P_1$ and $\mathbf{v} = \mathbf{v}_0 + \mathbf{v}_1$. Here, a subscript 0 denotes the equilibrium state and a subscript 1 denotes the perturbation. We note that $\mathbf{v}_0 = 0$ and hence $\mathbf{v} = \mathbf{v}_1$. We assume that we can neglect the products of any perturbed variables and for simplicity we do not consider non-ideal (resistive and viscous) effects. Furthermore, time derivatives of equilibrium quantities vanish and we set $\mathcal{L} = 0$ in equation 1.10. In other words, the system is adiabatic.

We can then linearise the MHD equations to obtain

$$\frac{\partial \mathbf{B}_1}{\partial t} = \nabla \times (\mathbf{v}_1 \times \mathbf{B}_0)\,, \tag{1.22}$$

$$\rho_0 \frac{\mathrm{D}\mathbf{v}_1}{\mathrm{D}t} = \frac{1}{\mu_0} (\nabla \times \mathbf{B}_1) \times \mathbf{B}_0 - \nabla P_1, \tag{1.23}$$

$$\frac{\partial \rho_1}{\partial t} = -\rho_0 \nabla \cdot \mathbf{v}_1, \tag{1.24}$$

$$\frac{\partial}{\partial t} \left(P_1 - \rho_1 \frac{\gamma P_0}{\rho_0} \right) = 0, \tag{1.25}$$

$$\nabla \cdot \mathbf{B}_1 = 0. \tag{1.26}$$

At this point, it is useful to define the sound speed, c_s as

$$c_s^2 = \frac{\gamma P_0}{\rho_0}. \tag{1.27}$$

We also note that in the case of no equlibrium flow, by neglecting the product of perturbed quantities, the Lagrangian derivative in the equation of motion can be reduced to

$$\rho_0 \frac{\partial \mathbf{v}_1}{\partial t} = \frac{1}{\mu_0} (\nabla \times \mathbf{B}_1) \times \mathbf{B}_0 - \nabla P_1. \tag{1.28}$$

To proceed further, we assume that all perturbations of the equilibrium are of the form $e^{i(\mathbf{k}\cdot\mathbf{r}-\omega t)}$, where $\mathbf{k}$ is the wave vector, $\mathbf{r}$ is the position vector and ω is the frequency. Substituting the assumed form into the linearised MHD equations yields

$$-\omega \mathbf{B}_1 = \mathbf{k} \times (\mathbf{v}_1 \times \mathbf{B}_0) = (\mathbf{k} \cdot \mathbf{B}_0)\, \mathbf{v}_1 - \mathbf{B}_0 (\mathbf{k} \cdot \mathbf{v}_1), \tag{1.29}$$

$$-\omega \rho_0 \mathbf{v}_1 = \frac{(\mathbf{k} \times \mathbf{B}_1) \times \mathbf{B}_0}{\mu_0} - P_1 \mathbf{k} = \frac{(\mathbf{k} \cdot \mathbf{B}_0)\, \mathbf{B}_1 - (\mathbf{B}_0 \cdot \mathbf{B}_1)\, \mathbf{k}}{\mu_0} - P_1 \mathbf{k}, \tag{1.30}$$

$$-\omega \rho_1 = -\rho_0 (\mathbf{k} \cdot \mathbf{v}_1), \tag{1.31}$$

$$-\omega \left(P_1 - \rho_1 c_s^2 \right) = 0, \tag{1.32}$$

$$\mathbf{k} \cdot \mathbf{B}_1 = 0, \tag{1.33}$$

where we have used an identity for the triple vector product to find equations 1.29 and 1.30. It is clear that equation 1.32 yields $P_1 = \rho_1 c_s^2$ and we use this together with equations 1.29 and 1.31 to rewrite equation 1.30 as

$$\begin{aligned} \mu_0 \rho_0 \omega^2 \mathbf{v}_1 = (\mathbf{k} \cdot \mathbf{B}_0)^2 \mathbf{v}_1 - (\mathbf{k} \cdot \mathbf{v}_1)(\mathbf{k} \cdot \mathbf{B}_0) \mathbf{B}_0 \\ + \left\{ \left(B_0^2 + \mu_0 c_s^2 \rho_0 \right) (\mathbf{k} \cdot \mathbf{v_1}) - (\mathbf{k} \cdot \mathbf{B}_0)(\mathbf{B}_0 \cdot \mathbf{v}_1) \right\} \mathbf{k}. \end{aligned} \tag{1.34}$$

We now consider the components of equation 1.34 parallel to the equilibrium field, $\mathbf{B}_0$, and parallel to the wave vector, $\mathbf{k}$. In the first case, on the right-hand side, most terms identically vanish and we obtain

$$\omega^2 (\mathbf{B}_0 \cdot \mathbf{v}_1) = c_s^2 (\mathbf{k} \cdot \mathbf{v}_1)(\mathbf{k} \cdot \mathbf{B}_0). \tag{1.35}$$

For the second case, the first two terms on the right-hand side of 1.34 cancel and we

find

$$\mu_0\rho_0\omega^2\left(\mathbf{k}\cdot\mathbf{v}_1\right) = k^2\left\{\left(B_0^2+\mu_0c_s^2\rho_0\right)\left(\mathbf{k}\cdot\mathbf{v_1}\right)-\left(\mathbf{k}\cdot\mathbf{B}_0\right)\left(\mathbf{B}_0\cdot\mathbf{v}_1\right)\right\}, \tag{1.36}$$

where $k^2 = (\mathbf{k}\cdot\mathbf{k})$. At this point, it is helpful to define the Alfvén speed, c_A as

$$c_A^2 = \frac{B_0^2}{\mu_0\rho_0}. \tag{1.37}$$

Further, we now denote the angle between the equilibrium field, $\mathbf{B}_0$, and the wave vector, $\mathbf{k}$, as θ. Finally, eliminating the $(\mathbf{B}_0\cdot\mathbf{v}_1)$ term from equations 1.35 and 1.36 and rearranging yields

$$\left(\omega^4-k^2\left(c_A^2+c_s^2\right)\omega^2+k^4c_A^2c_s^2\cos\theta\right)\left(\mathbf{k}\cdot\mathbf{v}_1\right)=0. \tag{1.38}$$

The solutions of this equation provide the dispersion relation for linear Alfvén and magnetoacoustic waves in a uniform medium. We begin with the Alfvén wave case given by $\mathbf{k}\cdot\mathbf{v}_1 = 0$. We see that equation 1.35 then implies $\mathbf{B}_0\cdot\mathbf{v}_1 = 0$ and equation 1.34 reduces to

$$\frac{\omega}{k} = c_A\cos\theta. \tag{1.39}$$

This is the phase speed for Alfvén waves. For the magnetoacoustic case, we require the first term on the left-hand side of equation 1.38 to be identically zero. By solving the quadratic in ω^2, we obtain

$$\frac{\omega^2}{k^2} = \frac{1}{2}\left\{\left(c_s^2+c_A^2\right)\pm\sqrt{\left(c_s^2+c_A^2\right)^2-4\left(c_sc_A\cos\theta\right)^2}\right\}. \tag{1.40}$$

The positive (negative) square root is associated with the fast (slow) magnetoacoustic wave. For brevity, we often refer to these two waves as simply the fast and slow waves.

We note the special cases $\theta = 0$ and $\theta = \dfrac{\pi}{2}$. In the first instance, the phase speed reduces to the faster (slower) of the Alfvén and sound speeds for the fast (slow) wave. Typically in the corona, $c_A^2 > c_s^2$, and hence fast waves travelling parallel to the equilibrium field will propagate at the Alfvén speed. In the second instance, perpendicular to the equilibrium field, the fast wave propagates at the sum of the Alfvén and sound speeds and the slow wave does not propagate at all.

1.3.2 Non-Uniform Media

Hitherto, we have limited our consideration to the case of a uniform plasma and magnetic field, however, high resolution observations of the solar corona have highlighted its spatial (and temporal) inhomogeneity. In this section, we extend our analysis to consider the behaviour of MHD waves in a cylinder (e.g. Edwin and Roberts, 1983; Nakariakov and Verwichte, 2005).

We begin with a long, slender (loop radius, a, much smaller than loop length, l) cylindrical flux tube with an internal density, ρ_i, and external density, ρ_e. The magnetic field is assumed to be parallel to the loop axis and has a magnitude, B_i, within the flux tube and B_e, externally. We show a schematic of the background configuration in Figure 1.2.

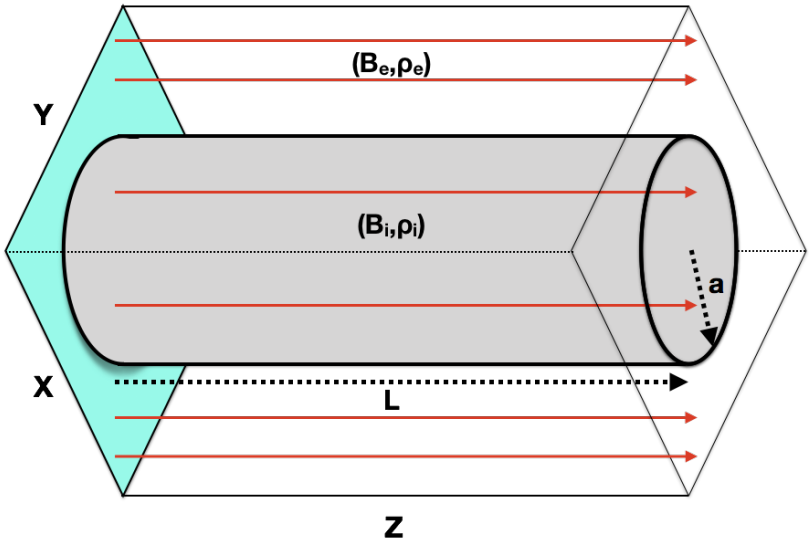

Figure 1.2: Schematic of the flux tube considered within this section.

For the following analysis, we work in cylindrical co-ordinates, (R, ϕ, z), with the z direction aligned with the loop axis. Additionally, for brevity, we will drop the subscript 1 for perturbed quantites but retain the subscript 0 for equilibrium values.

Since there is no magnetic tension force (straight field lines), the equation of motion (1.9), in the case of no net force (initial equilibrium), reduces to a requirement of pressure balance across the boundary of the flux tube. Hence we have

$$\frac{B_e^2}{2\mu_0} + P_e = \frac{B_i^2}{2\mu_0} + P_i = P_t, \tag{1.41}$$

where the combined gas and magnetic pressure, P_t, is a constant.

Written explicitly, the three components of the linearised induction equation (1.22)

are

$$\frac{\partial B_R}{\partial t} = B_0 \frac{\partial v_R}{\partial z}, \tag{1.42}$$

$$\frac{\partial B_\phi}{\partial t} = B_0 \frac{\partial v_\phi}{\partial z}, \tag{1.43}$$

$$\frac{\partial B_z}{\partial t} = \frac{-B_0}{R}\left(\frac{\partial \left(R v_R\right)}{\partial R} + \frac{\partial v_\phi}{\partial \phi}\right) = B_0 \left(\frac{\partial v_z}{\partial z} - \nabla \cdot \mathbf{v}\right), \tag{1.44}$$

where, B_0 is the magnitude of the equilibrium field. By differentiating the linearised equation of motion (1.28) with respect to time we find

$$\rho_0 \frac{\partial^2 \mathbf{v}}{\partial t^2} = \frac{1}{\mu_0}\frac{\partial}{\partial t}\left\{(\nabla \times \mathbf{B}) \times \mathbf{B}_0 - \nabla P_1\right\} \tag{1.45}$$

$$= \frac{1}{\mu_0}\left(\mathbf{B_0} \cdot \nabla\right)\frac{\partial \mathbf{B}}{\partial t} - \nabla\left(\frac{\partial P_t}{\partial t}\right). \tag{1.46}$$

Here we have decomposed the Lorentz force into the tension and pressure components and combined the gas and magnetic pressure into the total pressure term. Now we can introduce equations 1.42 - 1.44, to find that the three components of the equation of motion are

$$\rho_0\left(\frac{\partial^2 v_R}{\partial t^2} - c_A^2 \frac{\partial^2 v_R}{\partial z^2}\right) + \frac{\partial^2 P_t}{\partial R \partial t} = 0, \tag{1.47}$$

$$\rho_0\left(\frac{\partial^2 v_\phi}{\partial t^2} - c_A^2 \frac{\partial^2 v_\phi}{\partial z^2}\right) + \frac{1}{R}\frac{\partial^2 P_t}{\partial \phi \partial t} = 0, \tag{1.48}$$

$$\frac{\partial^2 v_z}{\partial t^2} + \frac{\partial^2 P_t}{\partial z \partial t} = c_A^2 \frac{\partial}{\partial z}\left\{\frac{\partial v_z}{\partial z} - \nabla \cdot \mathbf{v}\right\}. \tag{1.49}$$

Using the adiabatic energy equation and the definition of the sound speed, we can replace the perturbed density in the linearised mass continuity equation (1.24) with the perturbed gas pressure to find

$$\frac{\partial P}{\partial t} = \frac{\partial P_t}{\partial t} - \frac{1}{\mu_0}\mathbf{B}_0 \cdot \frac{\partial \mathbf{B}}{\partial t} = -c_s^2\left(\rho_0 \nabla \cdot \mathbf{v}\right) \tag{1.50}$$

$$\implies \frac{1}{\rho_0}\frac{\partial P_t}{\partial t} = c_A^2 \frac{\partial v_z}{\partial z} - c_f^2\left(\nabla \cdot \mathbf{v}\right) \tag{1.51}$$

$$\implies \nabla \cdot \mathbf{v} = \frac{c_A^2}{c_f^2}\frac{\partial v_z}{\partial z} - \frac{1}{\rho_0 c_f^2}\frac{\partial P_t}{\partial t}. \tag{1.52}$$

Here we have defined the fast speed as $c_f^2 = c_s^2 + c_A^2$. Substituting this expression into

equation 1.49, we find that the z component of the equation of motion becomes

$$\frac{\partial^2 v_z}{\partial t^2} - c_t^2 \frac{\partial^2 v_z}{\partial z^2} + \frac{c_s^2}{c_f^2} \frac{1}{\rho_0} \frac{\partial^2 P_t}{\partial z \partial t} = 0, \tag{1.53}$$

where we have defined the tube speed, c_t as

$$c_t = \frac{c_A^2 c_s^2}{c_A^2 + c_s^2}. \tag{1.54}$$

We now assume perturbations of the form $f(R)e^{i(\omega t - m\phi + kz)}$, where m and k are the azimuthal and vertical wave numbers, respectively. Here we note that the azimuthal wavenumber, m, must be an integer. For such perturbations, the three components of the equation of motion (1.47, 1.48 and 1.53) satisfy

$$\rho_0 \left(c_A^2 k^2 - \omega^2\right) v_R(R) + i\omega \frac{\mathrm{d}P_t}{\mathrm{d}R} = 0, \tag{1.55}$$

$$\rho_0 \left(c_A^2 k^2 - \omega^2\right) v_\phi(R) + \frac{m\omega P_t(R)}{R} = 0, \tag{1.56}$$

$$\rho_0 \left(c_t^2 k^2 - \omega^2\right) v_z(R) + \frac{k\omega c_s^2 P_t(R)}{c_f^2} = 0. \tag{1.57}$$

Further, we can use equation 1.51 to obtain

$$\frac{i\omega P_t(R)}{\rho_0} = i\left(c_f^2 - c_A^2\right) k v_z(R) - \frac{c_f^2}{R}\left(\frac{\mathrm{d}(Rv_R)}{\mathrm{d}R} + imv_\phi\right) \tag{1.58}$$

$$\implies \frac{1}{R}\frac{\mathrm{d}(Rv_R)}{\mathrm{d}R} + \frac{i\omega P_t(R)}{\rho_0 c_f^2} = i\left(\frac{mv_\phi(R)}{R} + \frac{c_s^2 k v_z(R)}{c_f^2}\right). \tag{1.59}$$

We can then use the ϕ and z components of the equation of motion (1.56 and 1.57) to eliminate v_ϕ and v_z from equation 1.59. We obtain

$$\frac{1}{R}\frac{\mathrm{d}(Rv_R)}{\mathrm{d}R} + \frac{i\omega P_t(R)}{\rho_0 c_f^2} = i\left(\frac{m^2 \omega P_t(R)}{R^2 \rho_0 \left(\omega^2 - c_A^2 k^2\right)} + \frac{c_s^4 k^2 \omega}{c_f^4 \rho_0 \left(\omega^2 - c_t^2 k^2\right)}\right). \tag{1.60}$$

Then, following algebraic manipulation, we can rewrite this as

$$\rho_0 \left(k^2 c_A^2 - \omega^2\right) \frac{1}{R}\frac{\mathrm{d}(Rv_R)}{\mathrm{d}R} = -i\omega P_t(R)\left(n^2 + \frac{m^2}{R^2}\right), \tag{1.61}$$

where

$$n^2 = \frac{\left(k^2 c_A^2 - \omega^2\right)\left(k^2 c_A^2 - \omega^2\right)}{\left(c_s^2 + c_A^2\right)\left(k^2 c_t^2 - \omega^2\right)}. \tag{1.62}$$

Equations 1.55 and 1.61 are a coupled pair of differential equations and eliminating $v_R(R)$ in favour of the total pressure perturbation, $P_t(R)$, yields

$$\rho_0 \left(k^2 c_A^2 - \omega^2\right) \frac{1}{R} \frac{\mathrm{d}}{\mathrm{d}R} \left(\frac{R}{\rho_0 \left(k^2 c_A^2 - \omega^2\right)} \frac{\mathrm{d}P_t(R)}{\mathrm{d}R} \right) = \left(n^2 + \frac{m^2}{R^2} \right) P_t(R). \tag{1.63}$$

Within the flux tube, all plasma parameters in the equilibrium state are constant. Consequently, wave speeds are also constant and hence we can define $n = n_i$ in the interior plasma. Thus equation 1.63 reduces to

$$R^2 \frac{\mathrm{d}^2 P_t(R)}{\mathrm{d}R^2} + R \frac{\mathrm{d}P_t(R)}{\mathrm{d}R} - \left(n_i^2 r^2 + m^2\right) P_t(R) = 0. \tag{1.64}$$

This differential equation is the modified Bessel equation and has solutions $I_m(n_i R)$ and $K_m(n_i R)$, where I and K are modified Bessel functions of the first and second kind, respectively. Bessel functions of the second kind have a singularity at the origin and so the integration constant associated with $K_m(n_i R)$ is set to 0 inside the flux tube.

Hence, for $R < a$ we have

$$P_t(R) = A_m I_m \left(n_i R\right), \tag{1.65}$$

where A_m is an arbitrary constant. In the external plasma, the equilibrium parameters are also constant and we shall set $n = n_e$. By taking $n_e > 0$, again we obtain the modified Bessel's equation, however, in this case we reject the Bessel function of the first kind because they are unbounded at infinity. Retaining the Bessel function of the second kind yields

$$P_t(R) = B_m K_m \left(n_e R\right), \tag{1.66}$$

where B_m is a constant.

The solutions for P_t and v_R must be continuous at the boundary of the flux tube, which allows us to eliminate the integration constants. Continuity of P_t at $R = a$ implies

$$\frac{A_m}{B_m} = \frac{K_m \left(n_e a\right)}{I_m \left(n_i a\right)}, \tag{1.67}$$

and from equation 1.55 we find

$$\frac{A_m}{B_m} = \frac{\rho_0 \left(k^2 c_{A,i}^2 - \omega^2\right) n_e K'_m \left(n_e a\right)}{\rho_0 \left(k^2 c_{A,e}^2 - \omega^2\right) n_i I'_m \left(n_i a\right)}, \tag{1.68}$$

where the dashes indicate derivatives of the modified Bessel functions. Finally, we obtain the dispersion relation by combining equations 1.67 and 1.68,

$$\frac{n_i}{\rho_0 \left(k^2 c_{A,i}^2 - \omega^2\right)} \frac{I'_m \left(n_i a\right)}{I_m \left(n_i a\right)} = \frac{n_e}{\rho_e \left(k^2 c_{A,e}^2 - \omega^2\right)} \frac{K'_m (n_e a)}{K_m \left(n_e a\right)}. \tag{1.69}$$

Numerical solutions

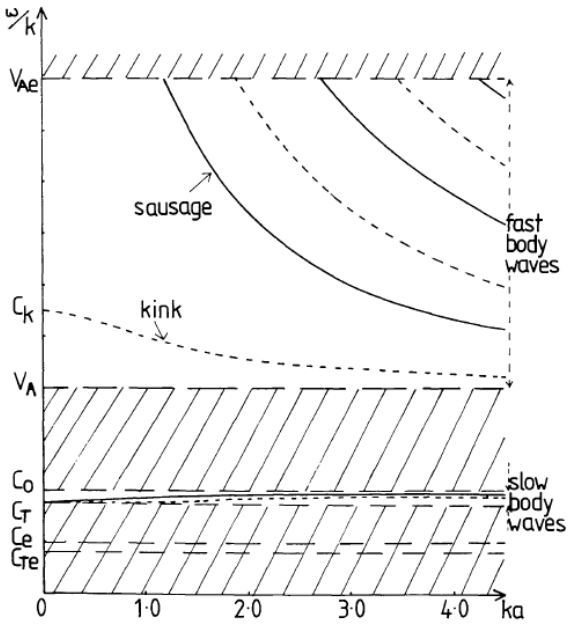

Figure 1.3: Phase-speeds of MHD wave modes in coronal-like flux tubes. This figure has been reproduced from Edwin and Roberts (1983).

This dispersion relation is impossible to solve analytically and typically numerical methods are employed to extract ω as a function of the wave numbers (e.g. Edwin and Roberts, 1983). For typical coronal conditions the Alfvén speed is larger than the sound speed ($\beta \ll 1$) and the solutions found under this regime are shown in Figure 1.3.

In general, MHD waves on a cylindrical flux tube can be *body* or *surface* waves. In the case of body waves, the interior of the flux tube oscillates and the exterior is evanescent. In the case of surface waves, on the other hand, both the internal and external environments are evanescent. Under coronal conditions, only the former are

permitted and hence the solutions in Figure 1.3 are all body modes.

The case with azimuthal wave number, $m = 0$, is named the sausage mode (see Figure 1.3). This corresponds to a periodic contraction and expansion of the cylindrical cross-section. The case with $m = 1$ is the kink mode and will be discussed extensively within subsequent chapters of this thesis. The kink mode induces a transverse displacement of the central axis of the cylinder and is frequently observed within the solar corona (e.g. Aschwanden et al., 1999, 2002; Okamoto et al., 2007; Tomczyk et al., 2007). In the literature, higher azimuthal wave number modes are known as fluting modes.

1.4 Kelvin-Helmholtz Instability

The Kelvin-Helmholtz instability (KHI) is a phenomenon associated with a fluid velocity shear in hydrodynamic (no magnetic field) regimes. In the presence of a velocity gradient, the fluid(s) can become unstable and generate vortices that can grow in time. The instability can still develop within magnetised plasmas, however, the magnetic field has a stabilising effect that can reduce the growth rate or suppress the formation of the vortices completely.

The instability has been observed in a wide variety of hydrodynamic settings as well as in a range of astrophysical plasmas. These include the classic case of wind generating water waves (e.g. Miles, 1957) and the formation of Kelvin-Helmholtz vortices in the solar atmosphere (e.g. Foullon et al., 2011) and in the Earth's magnetosphere (e.g. Miura, 1984; Otto and Fairfield, 2000; Hasegawa et al., 2004). It is also expected to have an effect on plasma evolution in more exotic astrophysical regimes such as in accretion discs (e.g. Ghosh and Lamb, 1979; Stella and Rosner, 1984; Papaloizou and Pringle, 1985; McKinney et al., 2012).

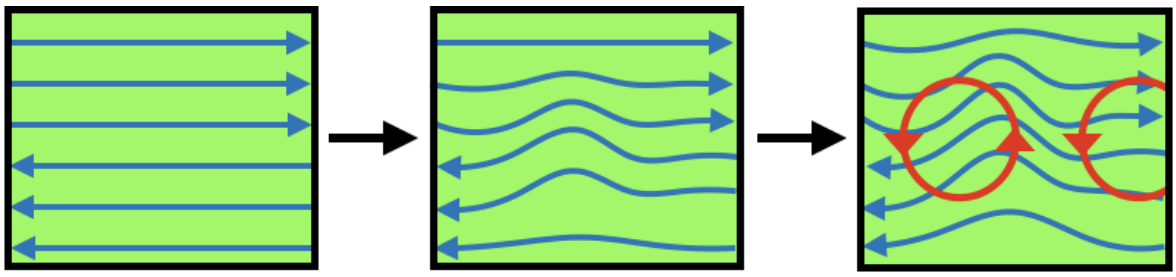

Figure 1.4: Schematic of the evolution of the Kelvin-Helmholtz instability. Here the blue arrows represent fluid streamlines being distorted during the development of the instability.

The classic hydrodynamic instability forms at locations of significant velocity shear. In the left-hand panel of Figure 1.4, we show oppositely directed streamlines in the upper and lower half of the box. As a result, there is a velocity shear across the midplane. In the second panel, we consider a small perturbation of the background flow. This has the effect of compressing some of the streamlines, generating a faster flow. In other regions the streamlines expand and we obtain reduced velocities. In the regions with increased flow there is an associated decrease in pressure and the opposite effect is observed in regions with lower speed. This generates a pressure force which enhances the size of the perturbation. Ultimately, the velocity shear generates rotational flows and the characteristic Kelvin-Helmholtz vortices form (right-hand panel of 1.4). We present a more rigorous analysis of the instability in a magnetised plasma in the following section.

1.4.1 Magnetohydrodynamic KHI

The inclusion of a magnetic field can stabilise a flow that would be unstable in a purely hydrodynamic setting and an analysis is presented in Chandrasekhar (1961). For the following we begin with an equilibrium containing a steady flow and a uniform magnetic field that is aligned with a velocity discontinuity in the $z = 0$ plane. For our initial conditions we take,

$$\rho_0(z) = \begin{cases} \rho_1, & z > 0, \\ \rho_2, & z < 0, \end{cases} \tag{1.70}$$

$$\mathbf{v}_0(z) = \begin{cases} \mathbf{u}_0 = (u_x, u_y, 0) & z > 0, \\ \mathbf{w}_0 = (w_x, w_y, 0) & z < 0, \end{cases} \tag{1.71}$$

$$\mathbf{B}_0 = (B_0, 0, 0). \tag{1.72}$$

Further, the equilibrium pressure, P_0, is constant everywhere. Gravitational, viscous and resistive effects are neglected for simplicity.

Since there is a steady flow, $\mathbf{v}_0$ in the equilibrium state, the linearised MHD equations include a few additional terms that are not included in the set presented in

equations 1.22 - 1.26. Instead, they can now be expressed as

$$\left(\frac{\partial}{\partial t} + \mathbf{v}_0 \cdot \nabla\right) \mathbf{B}_1 = \nabla \times (\mathbf{v}_1 \times \mathbf{B}_0) + (\mathbf{B}_1 \cdot \nabla)\, \mathbf{v}_0, \tag{1.73}$$

$$\rho_0 \left\{ \left(\frac{\partial}{\partial t} + \mathbf{v}_0 \cdot \nabla\right) \mathbf{v}_1 + (\mathbf{v}_1 \cdot \nabla)\, \mathbf{v}_0 \right\} = \mathbf{j}_1 \times \mathbf{B}_0 + \mathbf{j}_0 \times \mathbf{B}_1 - \nabla P_1, \tag{1.74}$$

$$\left(\frac{\partial}{\partial t} + \mathbf{v}_0 \cdot \nabla\right) \rho_1 = \nabla \cdot (\rho_0 \mathbf{v}_1), \tag{1.75}$$

$$\left(\frac{\partial}{\partial t} + \mathbf{v}_0 \cdot \nabla\right) P_1 = -\,(\mathbf{v}_1 \cdot \nabla)\, P_0 - \gamma P_0 \nabla \cdot \mathbf{v}_1, \tag{1.76}$$

$$\nabla \cdot \mathbf{B}_1 = 0. \tag{1.77}$$

where we have introduced the current densities, $\mathbf{j}_0$ and $\mathbf{j}_1$, in the equation of motion (1.74) using Ampère's Law (1.7).

In order to analyse the stability of this system, we consider perturbations of the form

$$f(z)\, e^{i(k_x x + k_y y - \omega t)}, \tag{1.78}$$

where we note that z is the non-uniform direction in the equilibrium state. Here, k_x and k_y are the wave numbers in the x and y directions respectively. We assume that any perturbations are incompressible, or in other words satisfy, $\nabla \cdot \mathbf{v}_1 = 0$. Therefore

$$-\frac{\mathrm{d}}{\mathrm{d}z} v_{1,z} = i k_x v_{1,x} + i k_y v_{1,y}. \tag{1.79}$$

We obtain a similar relation for the magnetic field using the solenoidal constraint;

$$-\frac{\mathrm{d}}{\mathrm{d}z} B_{1,z} = i k_x B_{1,x} + i k_y B_{1,y}. \tag{1.80}$$

For brevity, we also introduce $\Omega = k_x v_{0,x} + k_y v_{0,y} - \omega$. Using the incompressibility and solenoidal constraints (1.79 and 1.80), equations 1.73 - 1.76 then yield

$$i\Omega B_{1,x} = i k_x B_0 v_{1,x} + B_{1,z} \frac{\mathrm{d}}{\mathrm{d}z} v_{0,x}, \tag{1.81}$$

$$i\Omega B_{1,y} = i k_x B_0 v_{1,y} + B_{1,z} \frac{\mathrm{d}}{\mathrm{d}z} v_{0,y}, \tag{1.82}$$

$$i\Omega B_{1,z} = i k_x B_0 v_{1,z}, \tag{1.83}$$

$$i\rho_0 \Omega v_{1,x} + \rho_0 v_{1,z} \frac{\mathrm{d}}{\mathrm{d}z} v_{0,x} = -i k_x P_1, \tag{1.84}$$

$$i\rho_0\Omega v_{1,y} + \rho_0 v_{1,z}\frac{\mathrm{d}}{\mathrm{d}z}v_{0,y} = -ik_y P_1 + \frac{B_0}{\mu_0}\left(ik_x B_{1,y} - ik_y B_{1,x}\right), \tag{1.85}$$

$$i\rho_0\Omega v_{1,z} = -\frac{\mathrm{d}}{\mathrm{d}z}P_1 - \frac{B_0}{\mu_0}\left(\frac{\mathrm{d}}{\mathrm{d}z}B_{x,1} - ik_x B_{1,z}\right), \tag{1.86}$$

$$i\Omega\rho_1 = v_{1,z}\frac{\mathrm{d}}{\mathrm{d}z}\rho_0. \tag{1.87}$$

Now, by multiplying equation (1.84) by ik_x and equation (1.85) by ik_y and then summing the results, we find

$$\begin{aligned} i\rho_0\Omega\left(ik_x v_{1,x} + ik_y v_{1,y}\right) + i\rho_0 v_{1,z}\frac{\mathrm{d}}{\mathrm{d}z}\left(k_x v_{0,x} + k_y v_{0,y}\right) & \\ = -i\rho_0\Omega\frac{\mathrm{d}}{\mathrm{d}z}v_{1,z} + \rho_0 v_{1,z}\frac{\mathrm{d}\Omega}{\mathrm{d}z} & \\ = -i\rho_0\Omega^2\frac{\mathrm{d}}{\mathrm{d}z}\left(\frac{v_{1,z}}{\Omega}\right) & \\ = \left(k_x^2 + k_y^2\right)P_1 + \frac{ik_y B_0}{\mu_0}\left(ik_x B_{1,y} - ik_y B_{1,x}\right). & \end{aligned} \tag{1.88}$$

Lagrangian displacements and perturbations

At this point, it is convenient to introduce the Lagrangian displacement, $\boldsymbol{\xi}$. We can consider the displacement of a plasma element by the background flow, $\mathbf{v}_0$, and also by the perturbed flow, $\mathbf{v}_1$. We define $\boldsymbol{\xi}$ as the difference in these displacements. In other words, the Lagrangian displacement is defined as the relative displacement of a plasma element between the two flows. We have

$$\boldsymbol{\xi} = \mathbf{x}_1 - \mathbf{x}_0, \tag{1.89}$$

where $\mathbf{x}_1$ and $\mathbf{x}_0$ are the displacements associated with the perturbed and background flows, respectively. From here we can then see that the perturbed velocity can be written as

$$\mathbf{v}_1 = \frac{\mathrm{D}\mathbf{x}_1}{\mathrm{D}t} = \frac{\mathrm{D}}{\mathrm{D}t}\left(\mathbf{x}_0 + \boldsymbol{\xi}\right) = \mathbf{v}_0 + \frac{\partial\boldsymbol{\xi}}{\partial t} + \left(\mathbf{v}_0\cdot\nabla\right)\boldsymbol{\xi}. \tag{1.90}$$

For a plasma quantity X (e.g. density, temperature, velocity), we define the Lagrangian perturbation, ΔX as the difference in X observed for the same plasma element in each of the two flows. We have

$$\Delta X = \hat{X}^L(\mathbf{a}, t) - X^L(\mathbf{a}, t), \tag{1.91}$$

where $\mathbf{a}$ is the position vector of the fluid element at $t = 0$. Alternatively, we can define the Eulerian perturbation, δX as the difference in X observed for the same position,

$\mathbf{x}$ in each of the two flows. In this case we have

$$\delta X = \hat{X}^E(\mathbf{x}, t) - X^E(\mathbf{x}, t). \tag{1.92}$$

Using a Taylor expansion and assuming a linear perturbation, we can now rewrite equation 1.91 as

$$\begin{aligned}\Delta X =& \hat{X}^E(\mathbf{x} + \boldsymbol{\xi}, t) - X^E(\mathbf{x}, t) \\ =& \hat{X}^E(\mathbf{x}, t) - X^E(\mathbf{x}, t) + \boldsymbol{\xi} \cdot \nabla X\left(\mathbf{x}, t\right) + O\left(\xi^2\right) \\ =& \delta X + \boldsymbol{\xi} \cdot \nabla X\left(\mathbf{x}, t\right).\end{aligned} \tag{1.93}$$

By replacing the parameter X with the velocity and by rearranging equation 1.93, we obtain

$$\mathbf{v}_1 = \frac{\mathrm{D}\boldsymbol{\xi}}{\mathrm{D}t} - \boldsymbol{\xi} \cdot \nabla \mathbf{v}_0. \tag{1.94}$$

With a perturbation of the form shown in equation 1.78, the Lagrangian displacements reduce to

$$v_{1,x} = i\Omega\xi_x - \xi_z \frac{\mathrm{d}}{\mathrm{d}z} v_{0,x}, \tag{1.95}$$

$$v_{1,y} = i\Omega\xi_y - \xi_z \frac{\mathrm{d}}{\mathrm{d}z} v_{0,y}, \tag{1.96}$$

$$v_{1,z} = i\Omega\xi_z. \tag{1.97}$$

We can then substitute these into equations 1.86 and 1.88 to obtain

$$\rho_0 \Omega^2 \xi_z = \frac{\mathrm{d}}{\mathrm{d}z} P_1 + \frac{B_0}{\mu_0} \left(\frac{\mathrm{d}}{\mathrm{d}z} B_{1,x} - ik_x B_{1,z} \right), \tag{1.98}$$

$$\Omega^2 \frac{\mathrm{d}}{\mathrm{d}z} \xi_z = \left(k_x^2 + k_y^2\right) P_1 + \frac{ik_y B_0}{\mu_0} \left(ik_x B_{1,y} - ik_y B_{1,x}\right). \tag{1.99}$$

Differentiating the first of these two equations with respect to z means we can eliminate pressure and find

$$\begin{aligned}\rho_0 \Omega^2 \xi_z = \frac{1}{k_x^2 + k_y^2} \frac{\mathrm{d}}{\mathrm{d}z} \left(\rho_0 \Omega^2 \frac{\mathrm{d}}{\mathrm{d}z} \xi_z - ik_y \frac{B_0}{\mu_0} \left(ik_x B_{1,y} - ik_y B_{1,x}\right) \right) \\ + \frac{B_0}{\mu_0} \left(\frac{\mathrm{d}}{\mathrm{d}z} B_{1,x} - ik_x B_{1,z} \right).\end{aligned} \tag{1.100}$$

We can now use the solenoidal constraint (1.80) to eliminate $B_{1,y}$ and in addition we notice that terms containing $B_{1,x}$ in equation 1.100 vanish. The resulting equation is

$$\rho_0\Omega^2\xi_z = \frac{1}{k_x^2+k_y^2}\frac{\mathrm{d}}{\mathrm{d}z}\left(\rho_0\Omega^2\frac{\mathrm{d}}{\mathrm{d}z}\xi_z + ik_x\frac{B_0}{\mu_0}\frac{\mathrm{d}}{\mathrm{d}z}B_{1,z}\right) - \frac{ik_xB_0B_{1,z}}{\mu_0}. \tag{1.101}$$

The final component of the perturbed magnetic field, $B_{1,z}$, can be removed using equations 1.83 and 1.97. In particular we have

$$B_{1,z} = ik_xB_0\xi_z. \tag{1.102}$$

Hence we find

$$\rho_0\Omega^2\xi_z = \frac{1}{k_x^2+k_y^2}\frac{\mathrm{d}}{\mathrm{d}z}\left(\left(\rho_0\Omega^2 - \frac{\left(k_xB_0\right)^2}{\mu_0}\right)\frac{\mathrm{d}}{\mathrm{d}z}\xi_z\right) + \frac{\left(k_xB_0\right)^2\xi_z}{\mu_0}. \tag{1.103}$$

In the case $z \neq 0$ (away from the flow interface), derivatives of ρ_0 are zero and hence this equation can be factorised to show

$$\left(\rho_0\Omega^2 - \frac{\left(k_xB_0\right)^2}{\mu_0}\right)\left(\frac{\mathrm{d}^2}{\mathrm{d}z^2} - \left(k_x^2+k_y^2\right)\right)\xi_z = 0. \tag{1.104}$$

Although the first term is not necessarily non-zero, the dispersion relation for the magnetic Kelvin-Helmholtz instability is obtained by considering solutions to

$$\left(\frac{\mathrm{d}^2}{\mathrm{d}z^2} - \left(k_x^2+k_y^2\right)\right)\xi_z = 0. \tag{1.105}$$

The general solutions are

$$\xi_z(z) = C_0e^{-kz} + C_1e^{kz}, \tag{1.106}$$

where we have defined $k^2 = k_y^2 + k_z^2$. Since we require the perturbation to become zero at large distances from the flow interface ($z \to \pm\infty$) we obtain the solution

$$\xi_z(z) = C_0\begin{cases} e^{kz} & \text{if } z < 0, \\ e^{-kz} & \text{if } z > 0. \end{cases} \tag{1.107}$$

Here, we have noted that ξ_z must be continuous at the flow interface to deduce $C_0 = C_1$. Finally, in order to find the dispersion relation, we integrate equation 1.103 with respect to z, from $-\epsilon$ to ϵ as $\epsilon \to 0$. On performing this integration, we see that there are zero contributions from terms that are continuous or form step functions at $z = 0$. The

only remaining terms arise from derivatives of step functions (δ-functions) and we find

$$\rho_+\Omega_+^2(-k) - \rho_-\Omega_-^2 k + \frac{2k\left(\mathbf{k}\cdot\mathbf{B}_0\right)^2}{\mu_0} = 0. \tag{1.108}$$

We can now reintroduce ω to find the following quadratic

$$\left\{\rho_+ + \rho_-\right\}\omega^2 + \left\{-2\rho_+\left(\mathbf{k}\cdot\mathbf{u}\right) - 2\rho_-\left(\mathbf{k}\cdot\mathbf{w}\right)\right\}\omega - \frac{2\left(\mathbf{k}\cdot\mathbf{B}_0\right)^2}{\mu_0} + \rho_+\left(\mathbf{k}\cdot\mathbf{u}\right)^2 + \rho_-\left(\mathbf{k}\cdot\mathbf{w}\right)^2 = 0. \tag{1.109}$$

By solving for ω, we obtain

$$\omega = \frac{\rho_+\left(\mathbf{k}\cdot\mathbf{u}\right) + \rho_-\left(\mathbf{k}\cdot\mathbf{w}\right)}{\rho_+ + \rho_-} \pm \sqrt{\frac{2\left(\mathbf{k}\cdot\mathbf{B}_0\right)^2}{\mu_0\left(\rho_+ + \rho_-\right)} - \frac{\rho_+\rho_-\left(\mathbf{k}\cdot\Delta\mathbf{V}\right)^2}{\rho_+ + \rho_-}}. \tag{1.110}$$

Here we have defined $\Delta\mathbf{V}$ as the velocity difference, $\mathbf{u} - \mathbf{w}$, across the flow interface. This equation represents the dispersion relation and we shall now briefly discuss the constituent terms.

The first term on the right-hand side (outside the square root) merely corresponds to the advection of a spatially oscillating flow through the observer's rest frame. It vanishes if the problem is considered in the zero-momentum observing frame.

The sign of the term within the root determines whether or not the system is stable; namely, if it is positive, we will observe oscillatory behaviour and if it is negative, an instability will develop. Hence for instability we require

$$\frac{2\left(\mathbf{k}\cdot\mathbf{B}_0\right)^2}{\mu_0} < \rho_+\rho_-\left(\mathbf{k}\cdot\Delta\mathbf{V}\right)^2 \tag{1.111}$$

$$\implies \frac{2B_0^2\cos^2\phi}{\mu_0\rho_+\rho_-} < \left(\Delta V\right)^2\cos^2\theta, \tag{1.112}$$

where ϕ and θ are the angles between the wave vector and the magnetic field and velocity shear, respectively. We note that if $\phi = \dfrac{\pi}{2}$, then the restoring force of magnetic tension disappears. This is known as an interchange mode and, provided the right-hand side is not also identically zero, will always be unstable in an ideal regime.

In subsequent chapters, we will consider the manner in which an oscillating flow can become unstable and may lead to the deformation of coronal structures. Whilst this complex regime is not directly comparable to the typical mathematical definition of the instability, for simplicity, and for consistency with the existing literature, we

will identify this as a manifestation of the magnetic Kelvin-Helmholtz instability. We will discuss the formation of the instability during the decay of MHD waves in cylindrical flux tubes and we will investigate paradigms in which its development may be suppressed.

1.5 Energetics of the Corona

As mentioned previously, the temperature of the corona is maintained at temperatures in excess of 1 MK despite the significant loss of thermal energy through the conduction of heat to the cooler chromosphere and by optically thin radiation. Magnetic energy injected into the solar atmosphere from the surface is expected to be the source of the required energy (Klimchuk, 2006). Convective flows within the interior of the sun ensure that the photosphere is in turbulent motion. Consequently, plasma flows at the surface pull on any magnetic field that is protruding into the higher levels of the atmosphere. This in turn leads to a Poynting flux, S, into the atmosphere which can be defined (see Parnell and De Moortel, 2012) as

$$S = \frac{1}{\mu_0}\int_{\mathbf{S}} \mathbf{E}\times\mathbf{B}\cdot\mathbf{dS} = \frac{1}{\mu_0}\int_{\mathbf{S}} \left\{(\mathbf{B}_p\cdot\mathbf{B}_p)\,v_n - (\mathbf{B}_p\cdot\mathbf{v}_p)\,B_n\right\}\,\mathrm{d}S. \tag{1.113}$$

Here, $\mathbf{S}$ is some area of the solar surface, a subscript p denotes a projection onto $\mathbf{S}$ and a subscript n is the component of a vector perpendicular to the surface. The first term on the right-hand side corresponds to the emergence of new flux through the solar surface and the second terms represents the pull exerted on magnetic field by plasma flows. Typically in coronal heating models, we assume that the magnetic field has already emerged into the coronal volume and so we neglect the effects of the first term. Whilst the second term can conceivably represent a loss of magnetic energy, the random nature of photospheric motions ensures that when integrated over time, this term typically injects energy into the solar atmosphere.

The time scales associated with photospheric motions are anticipated to be important for determining the nature of the magnetic energy that is transferred into the corona. Long time scales (with respect to the Alfvén travel time along a coronal structure) are expected to be associated with a slow stressing of magnetic field and short time scales are more likely to generate MHD waves that may be able to transfer energy to high altitudes. In Chapters 2 - 4, we discuss the energetics and dynamics that arise from wave phenomena. In Chapter 5, on the other hand, we consider the energy release associated with the slow braiding of the magnetic field.

The propagation of waves through the lower layers of the solar atmosphere into the corona is not well understood and a significant proportion of wave power may be reflected at steep wave speed gradients in, for example, the transition region between the chromosphere and corona (e.g. De Pontieu et al., 2005; McIntosh and Jefferies, 2006; Santamaria et al., 2015). Therefore, it remains unclear how much wave power is transmitted into the upper atmosphere. Despite this, many observational studies (e.g. McIntosh et al., 2011) have highlighted the presence of significant wave energy within the corona that may be sufficient to maintain the high temperatures, particularly in the quiescent Sun.

1.5.1 Wave Heating

In this section, we discuss some common themes of coronal wave heating models, including the processes of resonant absorption and phase mixing. A more thorough discussion of reconnection heating is presented in Chapter 5.

According to equation 1.18, in the presence of resistivity, magnetic fields will dissipate energy through Ohmic heating at a rate that is propotional to ηj^2. Further, in the presence of viscosity, velocity fields will also dissipate their energy through viscous heating. Therefore, Alfvén wave energy, which, over the course of a wave period, is equipartioned into kinetic and magnetic energy is able to heat the background plasma in the presence of non-zero diffusivity. However, since the transport coefficients are small in the corona, any significant heating requires the formation of small scales in the magnetic and velocity fields. We detail two plasma processes that can cause the generation of the required small scales.

Resonant Absorption

We consider a coronal loop oscillating with a standing, transverse, kink wave such as those observed by Aschwanden et al. (1999). Such oscillations often appear to be induced by impulsive events (e.g. a solar flare) that excite nearby loop structures and cause a deviation from an equilibrium state (Zimovets and Nakariakov, 2015). These standing waves frequently experience rapid damping, and in particular their amplitudes decay at a rate much faster than expected given coronal dissipation levels. However, the decay of these wave modes is not expected to be directly associated with plasma heating. Instead, energy is transferred from the global kink mode to localised, azimuthal Alfvén waves that exist on resonant field lines within the boundary of the coronal loop (Ionson, 1978).

Resonant field lines are predicted to exist on some radial shell on which the natural Alfvén frequency matches the frequency of the kink mode, which is given by a density weighted average of the Alfvén frequencies of the interior and exterior plasma (Priest, 2014). If we assume that the loop is dense (lower Alfvén speed) compared to the surrounding plasma and that the Alfvén speed varies smoothly across the radius of the loop, then there will exist a narrow layer of resonant field lines somewhere within the boundary of the flux tube. This promotes an efficient transfer of energy from the kink mode to an azimuthally polarised Alfvén mode (Ionson, 1978; Sakurai et al., 1991). An analagous process exists for propagating MHD waves, however, in the literature this is usually referred to as mode coupling.

Since azimuthal Alfvén waves are only weakly incompressible and exist over small length scales that are difficult to resolve given current observational constraints, they are often impossible to detect in the corona. It is important to note that, during this process, although the easily detectable kink wave has been damped, no plasma heating has occured. Indeed, this process will still occur in an ideal, inviscid plasma, where no dissipation of energy is possible. We note that identification of the Alfvén wave may be possible with high resolution Doppler velocity observations (e.g. Antolin et al., 2017), however, line-of-sight effects can significantly complicate matters. Therefore, there may be significant wave power hidden in these unobservable modes which enhances uncertainties in estimating coronal wave energy.

As the Alfvén wave only exists in a narrow layer, magnetic and velocity field gradients associated with the wave are typically much larger than those associated with the kink mode. This promotes the dissipation of wave energy as heat. Furthermore, the large velocity shear that is associated with the torsional wave may be unstable to the Kelvin-Helmholtz instability which can lead to turbulent-like plasma and induce enhanced energy dissipation. This phenomenon will be explored in subsequent chapters.

Phase Mixing

Alfvén waves, such as those induced by resonant absorption/mode coupling, can exist on neighbouring field lines that do not have identical Alfvén speeds. In this case, the wave on one field line will become out of phase with the wave on the neighbouring field line. This process is known as phase mixing and will occur for both standing and propagating waves.

In Figure 1.5, we consider the propagation of a shear Alfvén wave along the z-axis

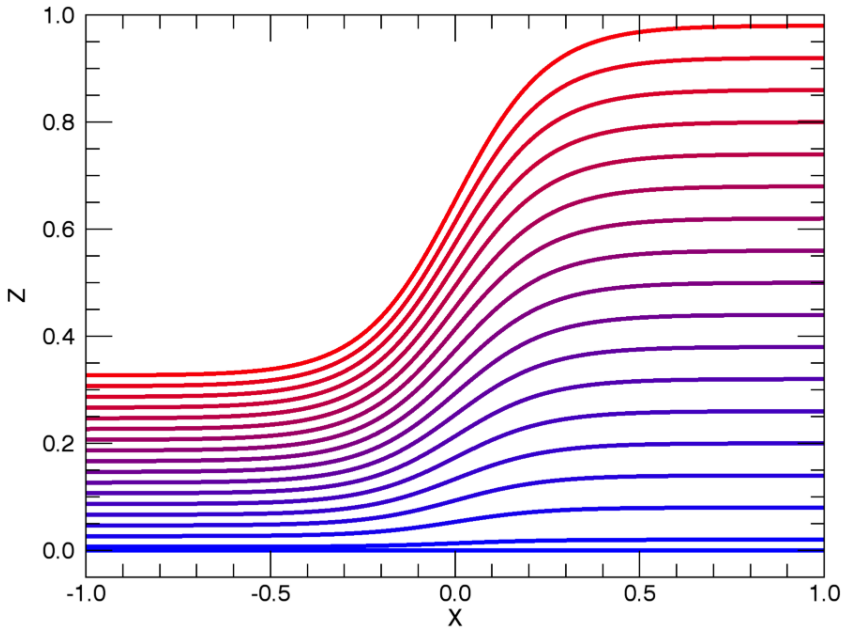

Figure 1.5: Schematic of the phase mixing process. The Alfvén speed increases along the x-axis. Shear Alfvén waves polarised in the y-direction are generated at $z = 0$ and propagate in the positive z direction. The wave front for $x > 0$ travels faster than for $x < 0$, causing large gradients to form in regions of non-constant Alfvén speed.

in the presence of a non-uniform Alfvén speed along the x axis. Each line identifies the nature of the wave front at a particular time. As phase mixing progresses, we observe a steepening of the Alfvén wave front in the regions of large gradients in the Alfvén speed. This will lead to the generation of small length scales in the velocity and magnetic fields and can significantly enhance the rate of wave heating.

It is important to note that, although frequently treated separately, resonant absorption (or mode coupling) and phase mixing often occur in conjunction in wave heating models (e.g. Ruderman et al., 1997a,b; Pascoe et al., 2011; Pagano and De Moortel, 2017).

Limitations of Wave Heating

Due to the inability of 3-D numerical models (see section 1.6.3) to attain the high Reynold's number environment of the solar corona, wave heating simulations typically assume transport coefficients that are many orders of magnitude larger than the expected values. Despite this, only moderate plasma heating can be achieved with very strong foot point driving (Pagano and De Moortel, 2017).

In order to progress, both resonant absorption/mode coupling and phase mixing require a gradient in the Alfvén speed. In coronal wave models, this non-uniformity is typically assumed to be associated with a density profile that varies along the radius of an atmospheric flux tube. However it remains unclear whether wave heating alone is able to generate the assumed, fixed, density profile. Indeed, Cargill et al. (2016) argue that the location and rate of wave heating is unable to sustain the density for the observed lifetime of a coronal loop.

1.6 Numerical Methods

Within this thesis, we will present the results of large scale, 3-D, resistive, MHD simulations of waves within coronal-like magnetic flux tubes. Throughout, we have implemented the widely-used and well-studied numerical code, Lare3d, (Arber et al., 2001). Whilst the intricate details of this code are beyond the scope of this PhD, we now present an outline of the code.

Lare3d implements a **La**grangian **Re**map scheme in which each timestep is split into two; a Lagrangian step and a remap step. During the first stage, the numerical grid is advected by plasma flows and the MHD equations are advanced through time in normalised, Lagrangian form. This is achieved using a finite difference approach in which plasma quantities are defined at specific locations on a discrete grid. Subsequently, in order to maintain the initial form of the domain, the plasma quantities are remapped to their respective locations on the original grid. The code has been optimised for parallel processing which enables researchers to run large scale simulations over multiple processing units on High Performance Computing (HPC) machines.

The code allows the user to include (or exclude) additional physics such as gravity, optically thin radiation, thermal conduction and the effects of partially ionised plasmas as required. The inclusion of these effects typically increases computational run time and so they are not usually considered unless they are integral to the model being studied. In particular, they are not included in the simulations presented in Chapters 2 and 4. We discuss the implications of thermal conduction and optically thin radiation in greater detail in Chapter 5.

1.6.1 Numerical Grid

In order to enhance numerical stability, Lare3d implements a staggered grid in which different plasma parameters are defined in different locations within a grid cell. In

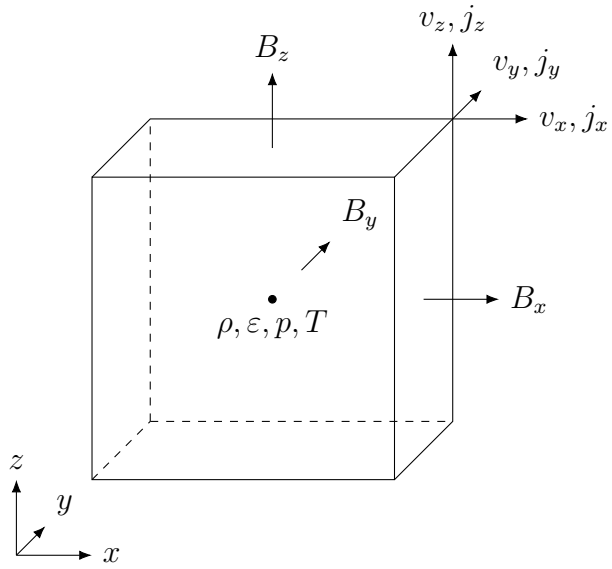

Figure 1.6: Location of plasma parameters within a grid cell.

three dimensions, each grid cell is a cuboid with dimensions of $\Delta_x \times \Delta_y \times \Delta_z$, where Δ_j for $j = x, y, z$, denotes the spatial resolution along the j-axis. Scalar quantities such as density, temperature and pressure are defined at the centre of the cuboid, velocities and current densities are defined on the vertices and the magnetic field components are defined on the faces of the grid cells. In particular, the B_j component of the field is defined at the centre of the face located at the minimum and maximum values of j. A schematic of the grid cell is depicted in Figure 1.6.

In order to compute the derivatives required by the MHD equations, in this discrete regime, a finite difference approach is implemented. In this manner, plasma parameters in neighbouring cells are used to compute spatial derivatives. For example, in a one-dimensional scheme, the derivative of B_x with respect to x in the centre of the j^{th} grid cell is given by

$$\left(\frac{\partial B_x}{\partial x}\right)_j = \frac{B_x\left(j+1\right) - B_x\left(j\right)}{\Delta x}, \tag{1.114}$$

where $B_x(j)$ is the value of B_x on the lower edge of the j^{th} cell. This provides an estimate for the value of the continuous derivative at the centre of the j^{th} cell.

Returning to three dimensions, we note that all of the finite difference approximations required to calculate $\nabla \cdot \mathbf{B}$ find estimates at the cell centre. Therefore, the arrangement of the magnetic field components allows the code to ensure the solenoidal constraint (1.4) remains (numerically) satisfied.

1.6.2 Normalisation

When measured in SI units, some coronal parameters are very small, such as the coronal density, $\rho_c \approx 10^{-12}$ kg m^{-3} whilst some are altogether much larger, such as the coronal temperature $T_C \approx 10^6$ K. This wide range of scales can lead to significant computational rounding errors when multiplying variables. Instead, the Lare3d code advances the MHD equations in normalised form, using the natural scales of the system, and thus, constraining plasma parameters to values of order unity.

Instead of using a typical coronal field strength of 10^{-3} T, we can implement a field strength of 1 (in dimensionless units) within the code, where we have chosen a normalising field strength, $B_0 = 10^{-3}$ T. Choosing three values, in this case, a normalising field strength, B_0, length scale, L_0, and typical density, ρ_0, constrains normalising values for the remaining plasma parameters. In terms of the chosen normalising values, we have

$$v_0 = \frac{B_0}{\sqrt{\mu_0 \rho_0}}, \tag{1.115}$$

$$P_0 = \frac{B_0^2}{\mu_0}, \tag{1.116}$$

$$t_0 = \frac{L_0 \sqrt{\mu_0 \rho_0}}{B_0}, \tag{1.117}$$

$$j_0 = \frac{B_0}{\mu_0 L_0}, \tag{1.118}$$

$$E_0 = \frac{B_0^2}{\sqrt{\mu_0 \rho_0}}, \tag{1.119}$$

$$T_0 = \frac{B_0^2 \bar{m}}{\mu_0 \rho_0 k_B}. \tag{1.120}$$

1.6.3 Non-Ideal MHD in Lare3d

Whilst an ideal application of the Lare3d code is often useful, within this thesis we do not restrict ourselves to the non-diffusive case. In particular we often consider non-zero resistivities (η) and viscosities (ν). However, even in the case where these transport coefficients are set to 0, a resolution-dependent, numerical, diffusivity is typically present (e.g. Bowness et al., 2013). This phenomenon is associated with

attempting to solve the continuous MHD equations on a discrete grid. In particular, within any finite difference scheme, spatial resolution constraints limit the accuracy to which derivatives can be calculated. Decreasing the values of Δ_x, Δ_y and Δ_z reduces this numerical effect, however, it cannot be eliminated on a finite grid. Large gradients (small scales) can enhance the effects of numerical diffusivity and can lead to the volume integrated energy not being conserved throughout the simulation.

For a given numerical experiment and grid configuration, the effective numerical diffusivity limits the η and ν parameter space that can be explored. Imposing transport coefficients below this value will produce almost identical results to running the same simulation with $\eta = \nu = 0$. This numerical diffusivity imposes an upper bound on the magnetic Reynolds number, R_M, (eq. 1.14) that can be obtained in a given numerical simulation. Estimates of the R_M within the solar corona suggest that it is many orders of magnitude larger than the value that can be obtained in large scale, 3-D, numerical simulations. This implies that numerical models of coronal structures are far too diffusive to accurately replicate solar conditions.

Resistivity

Resistivity acts to reduce gradients within the magnetic field and transfers magnetic energy to internal energy by Ohmic heating (see equation 1.18). Non-zero resistivity will allow field lines to diffuse through the plasma, a phenomenon which is not possible in ideal MHD.

Within the Lare3d code, resistivity, η is normalised as

$$\eta_0 = \mu_0 v_0 L_0, \tag{1.121}$$

and may be spatially and temporally uniform or can be set to attain larger values in regions of high current. The latter technique is used to replicate the effects of a narrow diffusion region that cannot be spatially resolved within the simulation.

Viscosity

Viscosity acts to reduce gradients within the velocity field and transfers kinetic energy to internal energy by viscous heating. The frictional effect of viscous forces contributes to the additional force term, $\mathbf{F}$, in the equation of motion 1.9 and the associated plasma temperature increase is contained within the $\mathcal{L}$ term in energy equation 1.10. More specifically, in the Lare3d code, viscosity is calculated using a strain rate tensor, ϵ, and

a stress tensor, σ, where the components of these are defined (using tensor notation) as

$$\epsilon_{i,j} = \frac{1}{2}\left(\frac{\partial v_i}{\partial x_j} + \frac{\partial v_j}{\partial x_i}\right), \tag{1.122}$$

$$\sigma_{i,j} = 2\nu\left(\epsilon_{i,j} - \frac{1}{3}\delta_{i,j}\nabla\cdot\mathbf{v}\right). \tag{1.123}$$

Here $\delta_{i,j}$ is the Kronecker delta. It takes the value of 1 for $i = j$ and 0 otherwise. The i^{th} component of the viscous force is then given by

$$(F_\nu)_i = \frac{\partial\sigma_{i,1}}{\partial x} + \frac{\partial\sigma_{i,2}}{\partial y} + \frac{\partial\sigma_{i,3}}{\partial z}, \tag{1.124}$$

and the heating associated with all components of the viscous force is calculated as

$$H_\nu = \sum_{i,j}\epsilon_{i,j}\sigma_{i,j}. \tag{1.125}$$

Further, within the Lare3d code, a normalised viscosity is implemented using the normalising value $\nu_0 = \rho_0 L_0 v_0$.

Shock Viscosities

The formation of shocks is associated with a steeping in the gradient of various plasma quantities that typically coincides with a super-Alfvénic/sonic flow. As a shock forms, the gradients inevitably become unresolved on a discrete grid and this precludes a simple finite difference scheme from correctly advancing the differential equations. In order to alleviate this problem, the Lare3d code implements jump conditions across shock fronts in which plasma quantities before and after the discontinuity are updated using spatially integrated MHD equations.

A consequence of attempting to track discontinuities in a second (or higher) order accurate scheme is the formation of non-physical oscillations in the vicinity of a shock front. These artefacts can be removed by including an artificial viscosity that acts close to an MHD shock. The code uses a tensor shock viscosity, σ^{shock} that has a similar form to the normal viscosity tensor described above,

$$\sigma^{\text{shock}}_{i,j} = \left(\nu_1\rho c_f L + \nu_2\rho L^2|s|\right)\left(\epsilon_{i,j} - \frac{1}{3}\delta_{i,j}\nabla\cdot\mathbf{v}\right). \tag{1.126}$$

Here, $\nu_{1,2}$ are shock viscosity parameters set by the user, c_f is the fast speed, L is the distance across a cell perpendicular to the shock front and s is the component of the

strain rate tensor, ϵ, in the same direction.

Ideally, this shock viscosity will have no effect in smooth regions of the domain, however, this is only the case as the grid size $\Delta_{x,y,z}$ goes to 0. Across the shock, however, $\nabla \cdot \mathbf{v}$ can become arbitrarily large and so this term will remain significant near the discontinuity even with high spatial resolution.

1.6.4 Non-Uniform Grids

The Lare3d code affords the possibility of introducing a numerical grid that does not have a constant spatial resolution along each co-ordinate axis. In particular, it is possible to stretch regions of the domain such that fewer grid points are required in locations with no small scales or of little physical interest. Indeed, this technique is implemented in the models presented within this thesis.

In particular, a non-uniform grid allows the boundaries to be far removed from the interesting wave dynamics in the centre of the domain without requiring a prohibitively large number of grid points or compromising the spatial resolution in regions of interest. This technique minimises the impact of wave reflections from the boundaries of the domain on the plasma phenomena being investigated. Despite this, care must be taken that grid stretching is not too extreme as this can generate spurious reflections as MHD waves are transmitted across a non-uniform region of the numerical domain. The exact form of the grid stretching used in our simulations is described in detail in subsequent chapters.

1.7 Outline

Within this thesis, we investigate the dynamics and energetics of magnetic flux tubes, particularly in the context of the coronal heating problem. We present the results of 3-D numerical simulations of MHD waves in coronal structures (Chapters 2-4) and of the effects of heat transfer mechanisms on a magnetic reconnection heating model (Chapter 5). We are particularly interested in the spatial and temporal evolution of currents and vorticities within the flux tubes and we identify the characteristics of the associated energy dissipation.

In Chapter 2, following the work of Antolin et al. (2014), we present a model for the formation of the magnetic Kelvin-Helmholtz instability in a transversely oscillating flux tube. We confirm the existence of resonant field lines within the boundary of the magnetic structure and examine the decay of an imposed, fundamental, standing kink

mode. We see that resonant absorption transfers energy to localised, azimuthal Alfvén waves (Ionson, 1978). As with previous work, Terradas et al. (2008b); Antolin et al. (2014), we confirm that the radial velocity shear associated with the Alfvén mode can become unstable to the KHI and will ultimately result in the development of a turbulent-like regime. We present the results of a parameter study conducted on the dissipation coefficients implemented within the simulation. In particular, we show that the growth rate of the instability is sensitive to both the viscosity and resistivity included in the domain. We include analysis of the energetics of the system and discuss the implications for wave energy dissipation. Additionally, we show that the instability can also form if the transverse oscillation is generated by an impulsive event in the external plasma.

In Chapter 3, we consider the effects of including twisted magnetic field within the oscillating flux tube. We highlight the suppressive effects of weakly twisted field on the development of the instability. In particular, we show that the characteristic vortices and density deformation develop later and at a slower rate when azimuthal field is present. Despite this, we argue that the KHI remains relevant in the context of wave energy dissipation as large currents are still able to form in this case.

In Chapter 4 we demonstrate that resonant absorption may be able to proceed even in the absence of the typically assumed non-uniform density profile. We show that a standing kink mode in an expanding magnetic flux tube will still transfer energy to azimuthal Alfvén waves, albeit possibly at a slower rate than in the classical case. In this regime, the necessary transverse gradient in the natural Alfvén frequency of field lines, is associated with a contrast between the internal and external magnetic field strength. We present results demonstrating the effects of the mode conversion and compare the observed wave dynamics to the straight field case presented in Chapter 2.

In Chapter 5, we consider a flux tube tectonics model (see e.g. Priest et al., 2002) in which two expanding magnetic flux tubes are braided around each other by rotational foot point drivers (De Moortel and Galsgaard, 2006a,b; O'Hara and De Moortel, 2016). We include the effects of thermal conduction and optically thin radiation and compare the plasma dynamics and energetics to the case in which these processes are not included. We evaluate the modification of the plasma temperatures and also highlight the effects that conduction and radiation have on the evolution of the magnetic field.

Finally in Chapter 6, we present a summary of our findings and suggest possible future work.

Chapter 2

The Effects of Dissipation on the Growth of the KHI in Oscillating Coronal Loops

2.1 Introduction

In this chapter we discuss the development of the Kelvin-Helmholtz Instability (KHI) in transversely oscillating coronal loops. As was discussed in the previous chapter, the KHI is a fluid phenomenon that forms in regions of strong velocity shear and a classic example is given by the formation of waves by wind passing over water. The instability is often associated with the production of vortices and can transfer a fluid from a laminar flow into a turbulent regime. Whilst the formation of water waves occurs in a purely hydrodynamic setting, the instability can also occur in magnetised plasmas. For example, the instability has been observed in the fast solar wind and within the Earth's magnetosphere (see Section 4.1 of Southwood and Hughes, 1983, for an introduction). In these cases, the dynamics of the instability are modified by the presence of the magnetic field. In particular, a strong field aligned parallel to the velocity shear may stabilise the fluid via the action of the magnetic tension force (Soler et al., 2010).

Direct observations of the instability on the Sun are limited in number, however, Foullon et al. (2011) and Ofman and Thompson (2011) observed the development of vortices around the boundary of a Coronal Mass Ejection (CME) using data from the Solar Dynamics Observatory. In these studies, the authors claimed that the vortex formation was evidence of the KHI developing due to the interaction of the erupting

plasma and the quiescent atmosphere. Furthermore, Okamoto et al. (2015) and Antolin et al. (2015a) detected observations of prominence oscillations that exhibited thread-like substructure and out-of-phase behaviour between the transverse oscillation and their Doppler velocities. The authors claimed that these features were evidence of resonant absorption and the turbulent aftermath of the KHI. The CME was thought to trigger the instability via field-aligned flows, whereas in the case of the prominences, the KHI was generated by velocity shear caused by resonant absorption. It is the latter mechanism that we investigate in this chapter.

The possible existence of the KHI in the Sun's atmosphere suggests it may be important in the context of heating the solar corona. As we shall see, the development of the instability causes the transfer of energy to small length scales through the formation of vortices and then, in turn, smaller and smaller substructures. Ultimately, the plasma begins to behave in a turbulent-like manner and, in any non-ideal medium, this process will terminate when length scales reach the dissipation scale. At this point, kinetic and magnetic energy is readily deposited as heat. Even in the weakly non-ideal regime in the solar corona, if such an energy cascade exists, then the dissipation of kinetic and magnetic energy may proceed at a sufficient rate to maintain the observed plasma temperatures.

Since magnetic field is approximately *frozen* into the coronal plasma, small length scales in the velocity field are typically associated with corresponding small length scales in the magnetic field. The formation of these small spatial scales is important in the context of plasma heating as they enhance the typically weak levels of dissipation present within the coronal volume. Viscous forces act on gradients in the velocity field whilst resistive terms act in a similar manner on the magnetic field. Hence, the magnitude of viscous and resistive effects in a plasma has consequences for the development, and the potential heating rate, of the KHI. On the other hand, Antolin et al. (2014) found that these forces suppress the growth of the instability and in some cases prevent its formation completely.

Transverse oscillations of coronal structures have been widely reported in many studies (e.g. Aschwanden et al., 1999, 2002; Okamoto et al., 2007; Tomczyk et al., 2007) since the Transition Region and Coronal Explorer mission (TRACE; NASA solar observatory launched 1998) allowed high spatial and temporal resolution imaging of the solar atmosphere. These oscillations are often interpreted as standing kink modes and despite the vacuous conditions of the corona, many of these waves are observed to damp rapidly - often within a couple of wave periods. It is widely expected that this enhanced damping is associated with the process of resonant absorption (mode coupling

in the case of propagating coronal waves) through which wave energy is transferred to local Alfvén waves (Ionson, 1978, or see Chapter 1). In this way, energy is removed from the transverse mode and deposited in weakly compressible, azimuthal modes that exist on a resonant layer within the boundary of the coronal structure.

Whilst the process of resonant absorption is ideal (it is not directly associated with any energy dissipation), it is of interest with regards to the coronal heating problem. The resultant Alfvén waves have much smaller length scales than the original kink mode and thus are more susceptible to dissipation. Further, the presence of a density gradient (and hence non-uniform Alfvén speed) across the resonant layer allows phase mixing to generate even smaller length scales. As we shall show, the azimuthal waves are also associated with a velocity shear perpendicular to the direction of oscillation that may become unstable to the Kelvin-Helmholtz instability.

In the remainder of this chapter we present a model of a coronal loop that oscillates with a standing kink mode. We demonstrate how this is damped through the process of resonant absorption and show that the formation of Alfvén waves can induce the development of the KHI. The inclusion of viscosity and resistivity in the model inhibits the growth of the azimuthal waves and so reduces the velocity shear and slows the growth of the instability. We attempt to quantify the effects that both of these dissipative mechanisms have on the formation of the KHI in transversely oscillating coronal loops. Finally, we consider the manner in which these transfer coefficients affect the rate of wave energy dissipation.

2.2 Numerical Model

Analytic studies have considered the KHI in ideal magnetised plasmas (e.g. Browning and Priest, 1984), however, the inclusion of dissipative terms in such models can only be achieved numerically. To proceed, we use the code Lare3D (outlined in chapter 1) and follow the set-up of Antolin et al. (2014) to model a straight, density-enhanced coronal loop (see Figure 2.1). We note that it is common practice to model coronal loops as straight flux tubes, since it is much simpler to define suitable initial conditions. This technique is widely accepted because the curvature of a coronal loop is typically small in comparison to its length.

The flux tube has a length of 200 Mm and a radius of approximately 1 Mm. The plasma density within the loop (ρ_i) is three times the density outside the loop ($\rho_e = 8.4 \times 10^{-13}$ kg m^{-3}) and varies smoothly with a tanh profile (see Figure 2.2a) across

the boundary region of the loop. At all heights, the density is defined by

$$\rho(R) = \rho_e + \frac{(\rho_i - \rho_e)}{2}\left(1 - \tanh\left\{\frac{R - r_a}{r_b}\right\}\right), \tag{2.1}$$

where $r_a = 1$ Mm is the loop radius measured to the centre of the boundary layer and $r_b = \frac{1}{16}$ Mm. This ensures the width of the boundary layer is approximately 0.4 Mm. We label the central region, with approximately constant density, as the core, the region with a large density gradient as the shell and the low, approximately constant, density region as the exterior.

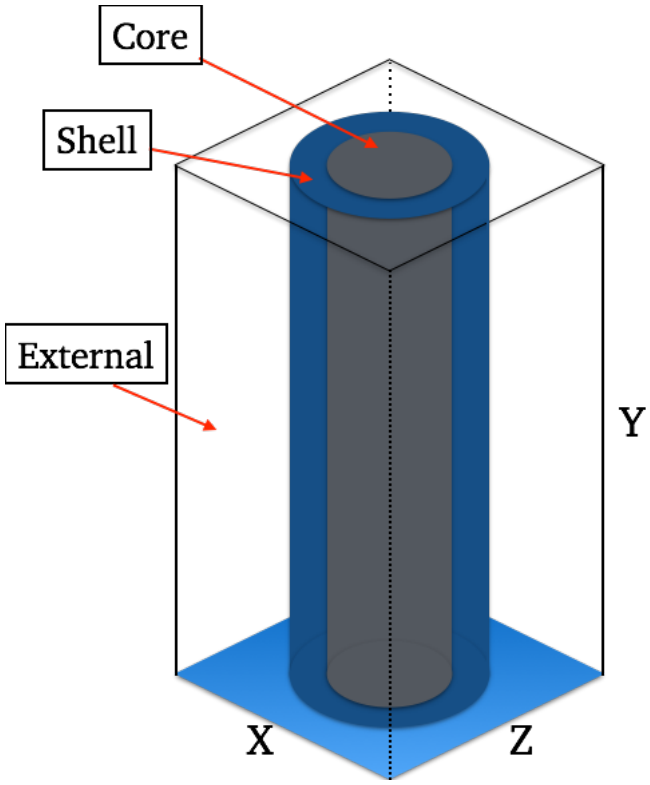

Figure 2.1: Initial configuration.

The numerical grid contains a uniform magnetic field of strength 21 G that is aligned with the loop axis (y direction). As a result, the Lorentz force is zero everywhere and so, in order to construct an initial equilibrium, we require $\nabla P = \mathbf{0}$ throughout the domain. This is achieved by setting the temperature to be

$$T = \frac{P_0}{\rho}, \tag{2.2}$$

where ρ is the density and P_0 is a constant that ensures the plasma-$\beta = 0.05$ everywhere. The resulting temperature profile is displayed in Figure 2.2b. Initially, the

exterior temperature is 2.5 MK and the interior temperature is cooler at approximately 0.8 MK. For the remainder of this chapter, we neglect the effects of gravity, loop curvature, thermal conduction and radiation.

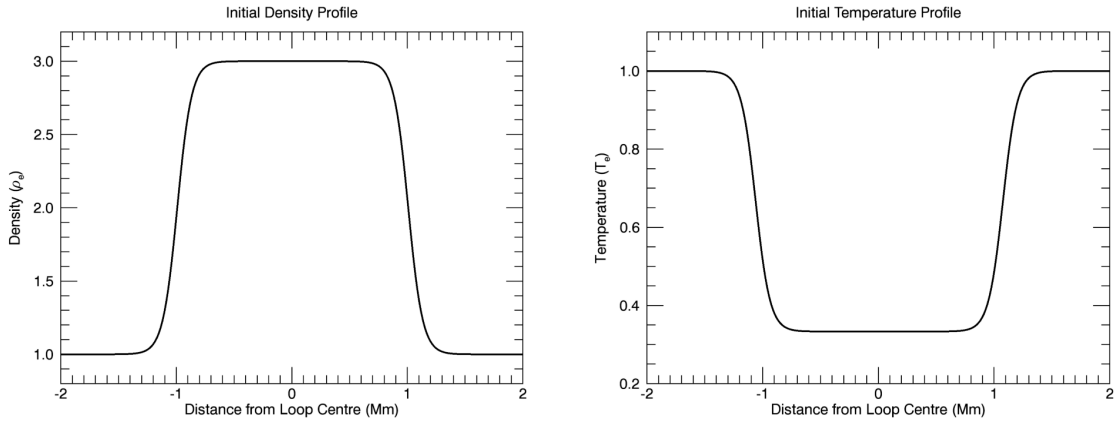

(a) Density. (b) Temperature.

Figure 2.2: Initial density and temperature profiles through the loop cross-section. Here, the density is normalised to the initial exterior density, $\rho_e = 8.4 \times 10^{-13}$ kg m^{-3} and the temperature is normalised to the initial exterior temperature $T_e = 2.5$ MK.

For the majority of the following experiments, we use $512 \times 100 \times 512$ grid cells over a domain of size 64 Mm $\times$ 200 Mm $\times$ 64 Mm. In addition, we also run several lower resolution simulations with half the number of grid points in the x and z directions. In these cases, there is no change to the y axis. Higher resolution is used in the x and z axes since, in previous studies (e.g. Antolin et al., 2014), the fine scale dynamics evolved in these directions.

Non-Uniform Grid

In order to minimise the effects of the domain boundaries, a non-uniform grid is used in the x-z-plane, with the finest spatial resolution located in the centre of the plane. The grid resolution along the x-axis, Δ_x is shown in Figure 2.3. The z-axis grid has an identical form. The non-uniformity of the numerical grid has little effect on the simulation as the oscillating loop remains within a uniform central region for the entirety of the experiment. This can be seen by comparing the location of the dashed and dot-dashed lines in Figure 2.3. Beyond the uniform region, the width of each grid cell increases by a factor such that the full length of the domain (in both the x and z directions) is fixed at 32 Mm.

Tests implementing a uniform domain produced qualitatively similar results as the

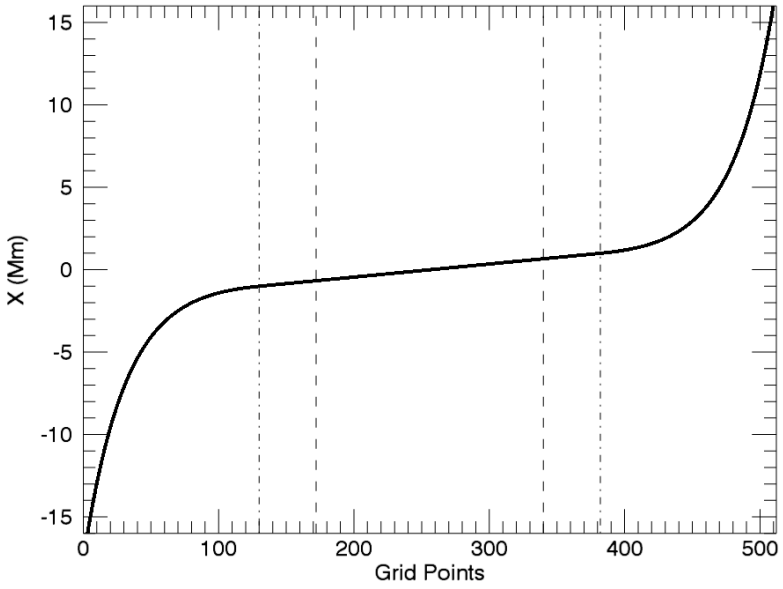

Figure 2.3: Form of the non-uniform grid along the x-axis. The dashed lines represent the maximum horizontal extent of the loop during the oscillation. The dot-dashed lines represent the boundaries of the uniform region.

simulations presented below, however, in these cases, the proximity of the boundary to the oscillating loop produced unphysical effects (e.g. reflections of plasma flows at the domain boundaries). In contrast, the y-axis is uniform along the entire length of the flux tube. The most refined resolution obtained within the central region of the domain corresponds to 15.9 km $\times$ 2000 km $\times$ 15.9 km.

2.2.1 Initial perturbation

Since there are no forces acting anywhere within the initial setup, in the absence of any velocity profile, the flux tube would be maintained in an equilibrium. In order to induce a fundamental standing kink mode, at time $t = 0$, we initialise a velocity profile in the domain. This is given by

$$\begin{aligned} v_x &= A(\rho - \rho_e)\cos\left(\frac{2\pi y}{L}\right), \\ v_y &= 0, \\ v_z &= 0, \end{aligned} \tag{2.3}$$

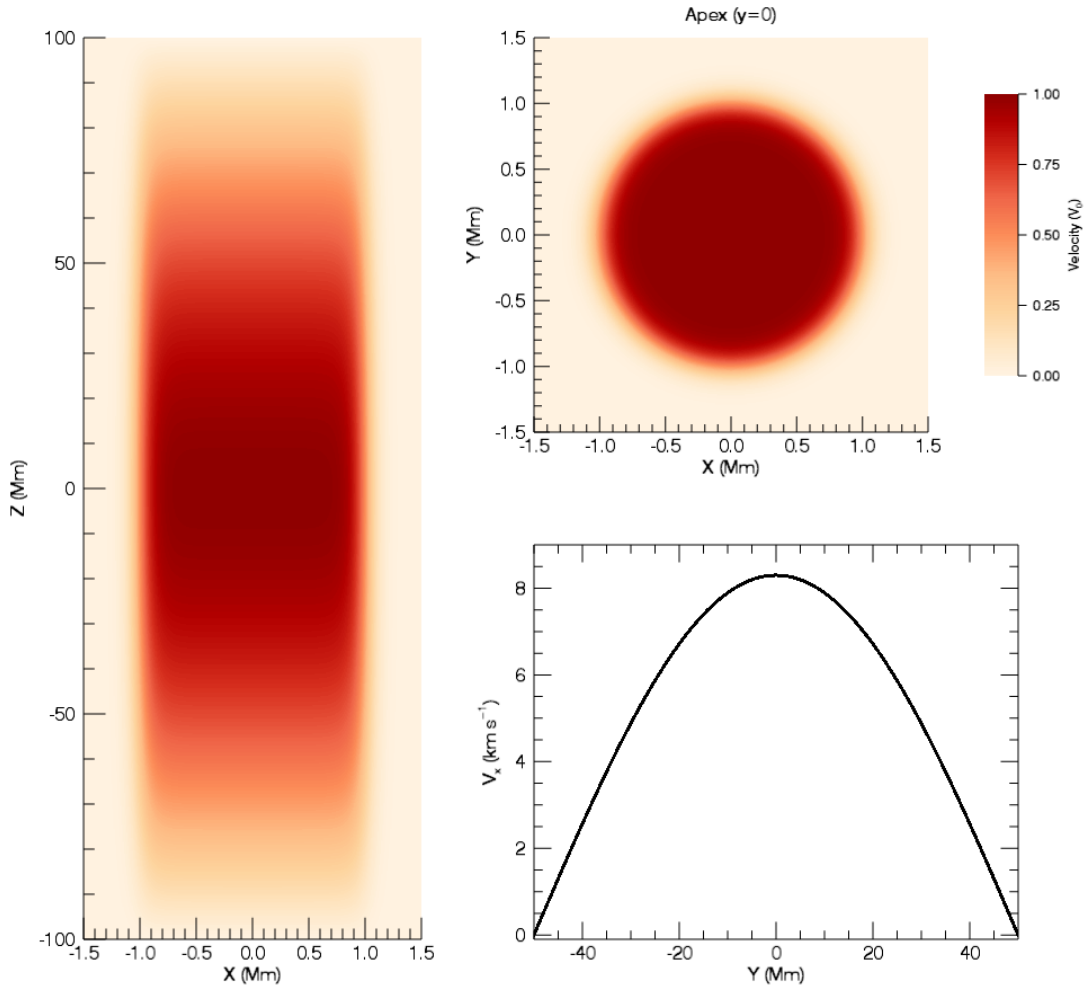

Figure 2.4: Initial velocity perturbation. *Left*: vertical cut through loop axis. *Upper right*: horizontal cut at loop apex. *Lower right*: velocity (v_x) along loop axis.

where $L = 200$ Mm is the length of the loop and A is a constant that produces a maximum velocity of 8.3 km s^{-1}, approximately 1% of the local Alfvén speed. The form of this velocity is shown in Figure 2.4. We show a vertical cut through the loop axis (left-hand panel), a horizontal cut through the loop apex (upper right panel) and the initial velocity profile along the loop axis (lower right panel).

Returning to equation 2.3, at any point in the loop exterior, we have $\rho = \rho_e$ and so we only perturb the loop itself. Indeed, it is the core region that experiences the greatest initial velocity. Furthermore, the loop apex is situated at $y = 0$ and so this loop cross-section is displaced the most by the initial perturbation and will become the location of the wave's anti-node. Meanwhile, in order to ensure that the perturbation

generates a standing wave, at all times, velocities on the y boundary ($y = \pm 50$ Mm) are forced to be zero. As a result, we ensure that the wave's nodes are located at the loop foot points. Throughout the duration of all the simulations, other variables are all constant across the y boundaries (zero gradients). The x and z boundaries are all periodic and, on account of the grid's non-uniformity, are well removed from the interesting wave dynamics.

2.2.2 Parameter Space

As we indicated in Chapter 1, the Lare3D code allows the user to control both the resistivity, (η) and viscosity, (ν) that are present in the numerical domain. We investigate the parameter space covered by the following (dimensionless) values of η and ν:

$$\eta = [10^{-3}, 10^{-4}, 10^{-5}, 10^{-6}, 10^{-20}],$$
$$\nu = [10^{-3}, 10^{-4}, 10^{-5}, 10^{-6}, 10^{-20}].$$

With the exception of $\eta = \nu = 10^{-20}$, these values are associated with Reynolds numbers that are several orders of magnitude larger than expected coronal values. As the numerical resistivity present in our domain (discussed later) is of the order 10^{-5}-10^{-6}, decreasing η below this level has little effect on the simulation. In other words, a simulation with $\eta = \nu = 10^{-20}$, is our best approximation to an ideal experiment albeit with numerical dissipation having some effect.

Even if the dissipation coefficients are set to 0, there will be some loss of kinetic and magnetic energy due to these numerical effects. This loss is grid dependent and is reduced as the spatial resolution improves. In locations where energy is dissipated on account of the user-controlled viscosity and resistivity, the internal energy increases by an equivalent amount (heating), however, numerical dissipation is not tracked and there is no associated heating observed. This is in contrast to similar studies (e.g. Karampelas et al., 2017) which implement energy-conserving numerical schemes and convert all lost kinetic and magnetic energy into heat.

It is of some interest that the levels of viscous and resistive dissipation present in our simulations are similar to those found in prominences and the chromosphere (Forteza et al., 2007; Soler et al., 2009, 2015; Khomenko and Collados, 2012). In these locations, the plasma temperature is much lower and many ion species are only partially

ionised. In the cooler regions of the solar atmosphere, the interaction of neutral atoms with ionised elements acts to enhance both the resistivity and the viscosity within the plasma. Consequently, even though we are modelling a coronal loop, the following results may have relevance to oscillations within prominences and chromospheric structures. Indeed, similar work investigating the KHI within solar prominences is presented in Okamoto et al. (2015) and Antolin et al. (2015a).

2.3 Oscillation and Resonant Absorption

The initial perturbation (described above) displaces the magnetic flux tube and the greatest effect is observed at the loop apex. For the chosen perturbation, the centre of the loop is displaced by approximately 0.27 Mm (see Figure 2.5), which we note is less than the radius of the loop (approximately 1 Mm). This confirms that we are modelling a relatively low amplitude oscillation and we note that significantly larger amplitude oscillations have been observed within the corona (many such events are included in a statistical analysis by Goddard et al., 2016).

Since the magnetic field is approximately *frozen* into the plasma ($R_m \gg 1$), this displacement bends field lines that are held in place at the $y = \pm 100$ Mm boundaries. Magnetic tension then acts as a restoring force to generate a transverse, standing kink wave that oscillates about the initial equilibrium. The time period of this oscillation is approximately 280 s.

The frequency of a kink mode in a magnetic cylinder is independent of the initial velocity perturbation and is given by Priest (2014) as

$$\omega_K = \sqrt{\frac{2B^2k_y^2}{\mu_0\left(\rho_i + \rho_e\right)}}, \tag{2.4}$$

where ρ_i and ρ_e are the internal and external plasma densities, respectively and k_y is the wave number. We note that here we have assumed that, as is the case in our model, the exterior magnetic field strength is equal to the interior field strength. Meanwhile, the frequency of a torsional Alfvén wave on a cylinder, with constant magnetic field strength, B, and density ρ, is given by

$$\omega_A = \sqrt{\frac{B^2k_y^2}{\mu_0\rho}}. \tag{2.5}$$

In any location for which $\omega_K = \omega_A$, a resonance will occur that will efficiently transfer energy from the kink oscillation to localised, azimuthal, Alfvén waves on the

magnetic cylinder with the required natural frequency, ω_A. In particular, we see that on a cylinder with density, $\rho = \frac{\rho_e + \rho_i}{2}$, we have $\omega_A = \omega_K$. In our case, this is initially satisfied on a hollow cylinder ($R = 1$ Mm) that is located within the boundary region of the loop.

The existence of this resonance allows for azimuthal wave modes to be excited within the loop's boundary layer. The length scales of these localised Alfvén waves are typically much smaller than those associated with the global kink mode and therefore the dissipation of wave energy occurs much more readily. Furthermore, as there is a gradient in the Alfvén speed across the loop's boundary region, wave energy dissipation is enhanced through the process of phase mixing.

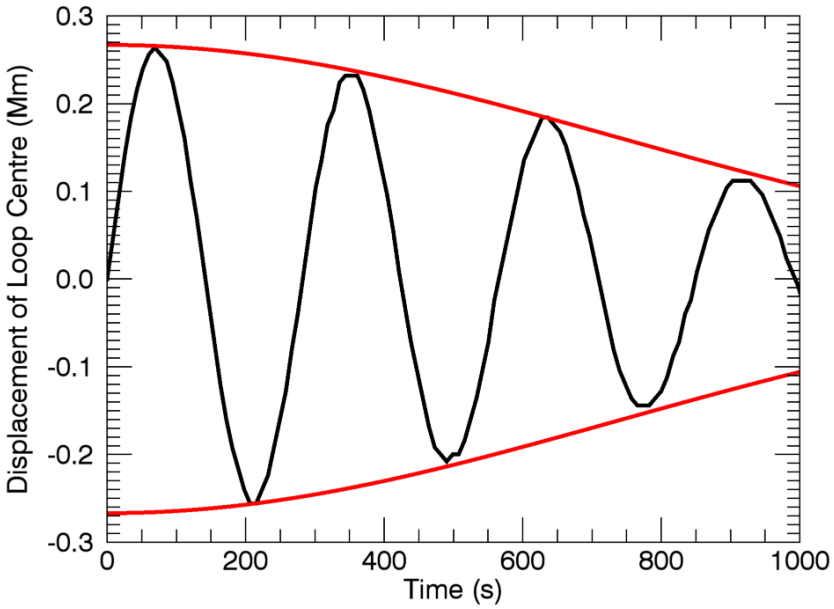

Figure 2.5: Damping of the standing kink mode. The displacement of the loop centre is plotted against time (black line). In order to demonstrate the damping behaviour, a Gaussian envelope (red lines) is also shown. These lines are given by $y = \pm 0.267 e^{-\left(\frac{t}{1040}\right)^2}$.

This transfer of energy between the wave modes causes the kink mode to damp at a much faster rate than would be expected in the low dissipation regime that exists in the solar corona. This rapid damping of the transverse oscillation is known to follow a Gaussian profile (e.g. Hood et al., 2013; Pascoe et al., 2013) rather than the exponential curve that is more often associated with wave decay. In Figure 2.5 we plot the position of the loop centre against time in one of our simulations ($\eta = 10^{-20}, \nu = 10^{-20}$) and overplot a Gaussian envelope to demonstrate this behaviour. The process of resonant

absorption is ideal and, as such, is independent of the coefficients of resistivity and viscosity used in the simulation. In particular, the choice of simulation displayed in Figure 2.5 was arbitrary, and curves produced using other simulations coincide with the (black) one shown.

This phenomenon has significance for attempts to detect the dissipation of wave energy in the Sun's atmosphere. Since the kink wave is associated with the displacement of the loop axis, it is observable with high temporal and spatial resolution imaging e.g. using the instruments aboard the Solar Dynamics Observatory. However, the Alfvén waves that can be excited during the decay of standing kink modes are not as easy to detect. Certainly, they are not associated with any displacement of the loop axis. Furthermore, they are only mildly compressible and, consequently, are only accompanied by small perturbations in the emitted radiation. Some inferences can be made by studying Doppler velocities in oscillating loop observations (Antolin et al., 2017), however, these are severely inhibited by spatial resolution limitations. In the coming years, enhanced observational capabilities, such as those provided by the DKIST instrument may allow easier detection of the velocity (or even the magnetic) field perturbations. However, presently this remains beyond the capacity of contemporary telescopes. For this reason, we note that it is not sufficient to observe the damping of waves and claim the corona is being heated. Instead, wave energy may simply be transferred from one mode to another (undetectable) mode.

The Alfvén waves that are excited during the simulations are readily observed in the velocity field. In Figure 2.6, we highlight the transfer of wave energy from the core region to the boundary of the loop as resonant absorption progresses. At each time, we find the square of the azimuthal component of the velocity along the line $x = x_c, y = 0$, where $x_c = x_c(t)$ is the x co-ordinate of the loop centre (along this line the azimuthal velocity is simply given by the v_x component). Combining these lines through time produces the contour plot displayed.

At the beginning of the simulation, the kinetic energy is predominantly located within the core of the loop, however, over several wave periods, it is transferred to the shell region. We can see from Figure 2.6, that the velocity varies over a much shorter radial distance at later times in the numerical experiment. The oscillatory behaviour is clear for the duration of the simulation, however, we observe that this pattern becomes less pronounced in the core region as the global kink mode decays. Meanwhile, within the shell region of the loop, we see the increase in the amplitude of the azimuthal Alfvén waves. As the resonant absorption proceeds, a strong velocity shear develops in the loop's boundary (e.g. at $t \approx 600$ s). As we discuss below, it is this strong gradient

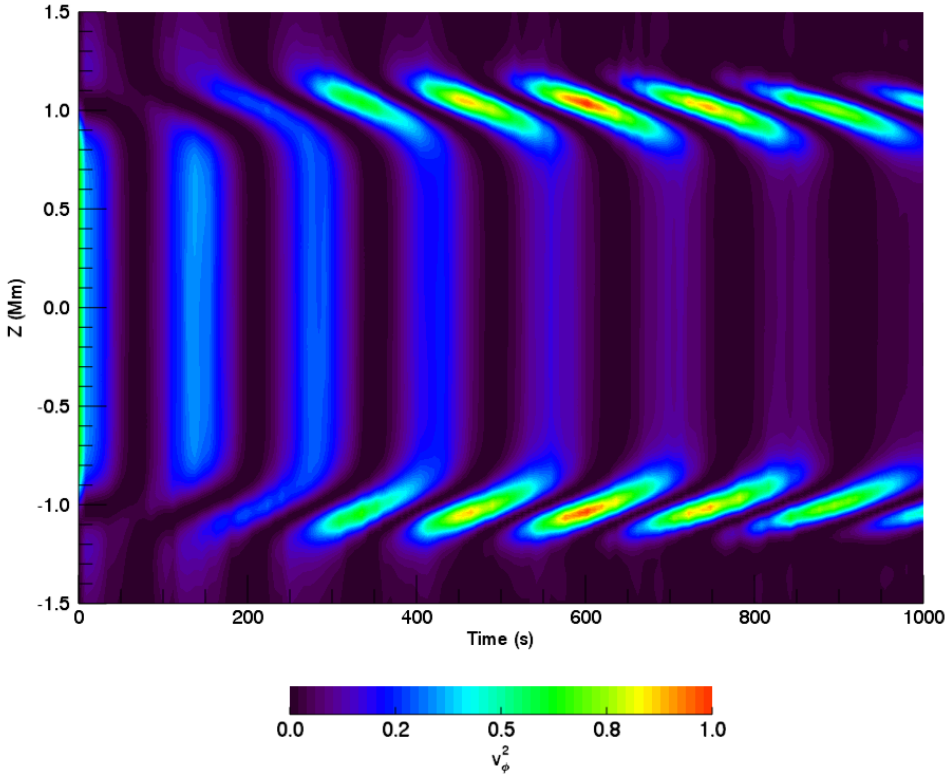

Figure 2.6: Transfer of wave energy during resonant absorption. Distribution of the square of the azimuthal velocity, v_ϕ^2, along a diameter (moving with the transverse oscillation) through the loop apex and as a function of time. We have normalised by the maximum of v_ϕ^2.

that drives the evolution of the Kelvin-Helmholtz instability.

Since the Alfvén frequency is higher within the boundary of the loop than in the core region, any given wave period is observed earlier at $z = \pm 1$ Mm than at $z = 0$ Mm. This explains the form of each wave front as seen in Figure 2.6 and a case in which this behaviour is reversed will be considered in Chapter 4.

The energy associated with the azimuthal Alfvén modes is partitioned between kinetic and magnetic energy. These two energy types oscillate with twice the frequency of the Alfvén waves and are out of phase with each other. Due to the nature of the standing mode, the magnetic energy is greatest at the wave's antinodes (loop foot points) and the kinetic energy is greatest at the wave's node (loop apex). When the loop is at maximum displacement, the wave energy is purely magnetic. On the other hand, when the loop is in the equilibrium position, the wave energy is purely kinetic. In Figure 2.7, we display the kinetic (left-hand panel) energy and magnetic (right-hand panel) energy on the hollow cylinder containing the resonant field lines ($\rho = 2\rho_e$)

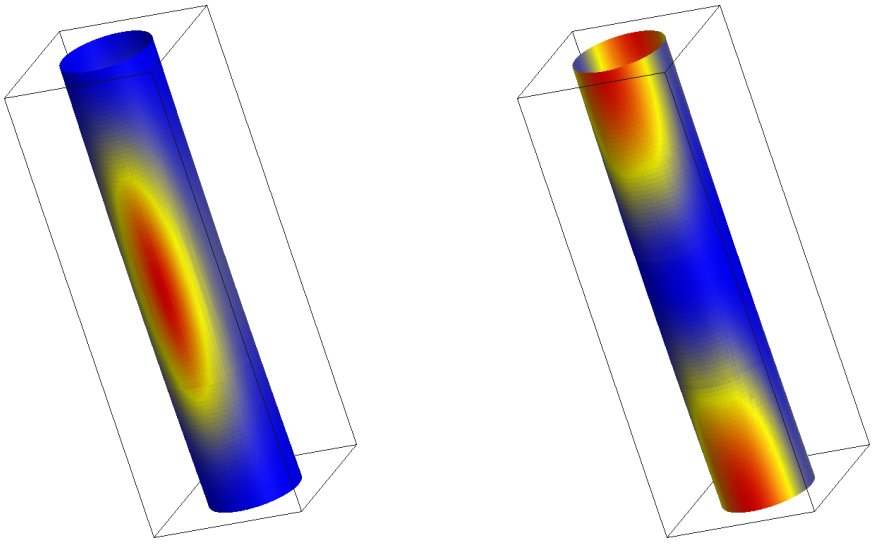

(a) Kinetic wave energy. (b) Magnetic wave energy.

Figure 2.7: Components of azimuthal Alfvén wave energy on the resonant cylinder; $\rho = 2\rho_e$. The figures are generated by integrating in time over a wave period and are produced once significant energy has been transferred from the kink mode.

after significant energy transfer has occured. In order to compare the two components of energy, we have integrated over a wave period. We note that in the azimuthal direction, the second harmonic is generated. This ensures that the azimuthal wave is weakly compressible and is in contrast to the purely torsional (fundamental) mode, which is perfectly incompressible.

2.3.1 Phase Mixing

The azimuthal Alfvén waves that develop within the boundary region of the loop exist on a radial density gradient. This non-uniformity in density is associated with a variation in the natural frequency of magnetic field lines and consequently, Alfvén waves on neighbouring field lines gradually become out of phase. This leads to phase mixing and in a non-ideal regime will enhance the dissipation of wave energy (Heyvaerts and Priest, 1983).

In Figure 2.8, we highlight the formation of out of phase Alfvén waves. In the left-hand panel, we show velocity vectors overplotted on a contour of the density profile. There is a clear velocity shear in the azimuthal flows in the boundary region of the loop. The right-hand panel shows the azimuthal velocity (red line) along a loop diameter perpendicular to the direction of oscillation. Only a small portion of this diameter is depicted. We see from the density profile (dashed blue line) that the out of phase behaviour exists over the boundary of the loop. Since energy in an Alfvén

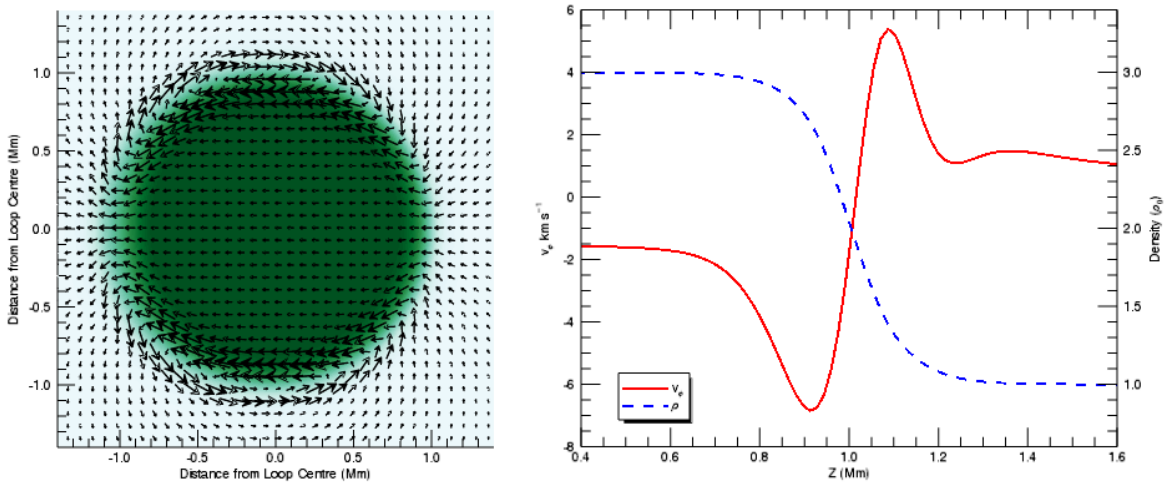

Figure 2.8: Phase mixing of azimuthal Alfvén waves. The left-hand panel depicts horizontal velocity vectors on a contour plot of the density. The right-hand panel shows azimuthal velocity (red line) and the density profile (blue line) along a segment of the loop diameter at the apex (this corresponds to a vertical line through the loop centre in the left-hand plot).

wave is partitioned between kinetic and magnetic energy, similar behaviour can also be observed (a quarter of a period later) in the azimuthal component of the magnetic field. However, as the Alfvén wave is a fundamental, standing mode, the largest radial gradients in B_ϕ are observed close to the loop footpoints, rather than at the loop apex. This phenomenon is discussed in more detail later.

We note that in both panels of Figure 2.8, we can see that the amplitude of the wave within the boundary region is significantly larger than the velocities associated with the kink mode. This is indicative of the transfer of energy between the two wave modes associated with resonant absorption. In the presence of non-zero transport coefficients, the small spatial scales associated with the phase-mixed Alfvén wave enhance energy dissipation above the level that is experienced by the global kink mode. However, it must be noted that this energy dissipation only occurs over a narrow region within the boundary of this loop and hence, in this model, phase mixing alone is unable to heat the entirety of the coronal structure (a more detailed discussion of the implications and limitations of coronal heating by phase mixing can be found in Cargill et al., 2016).

The distance between the minimum ($z \approx 0.9$ Mm) and maximum ($z \approx 1.1$ Mm) can be viewed as a phase mixing length scale, λ_{pm}. If the wave amplitude remains constant, a reduction in this length scale will induce a greater heating rate. In a perfectly ideal regime, λ_{pm} can become infinitely small as phase mixing progresses. However, in any finite difference, numerical scheme, this scale is limited by the resolution of the domain.

In particular, the numerical (or any user-imposed) diffusion will only permit λ_{pm} to decrease until the dissipation length scale is reached. Beyond this, wave energy is simply dissipated and no smaller scales are accessed. In general, this effect means phase mixing is very difficult to track numerically in simulations of a high Reynolds number plasma.

2.4 Development of the KHI

In the previous section, we described the formation of large radial gradients in the azimuthal velocity that form as a result of resonant absorption and phase mixing. As we shall see in this section, this velocity shear can become unstable to the magnetic Kelvin-Helmholtz instability.

The KHI causes the deformation of the loop's radial density profile. The most profound effects are observed at the loop apex ($y = 0$) as this is the plane in which the initial velocity is greatest. In Figure 2.9, we display the evolution of the density in the cross-section of the loop ($y = 0$ plane) at four different stages during the formation of the instability.

The asymmetry observed in the top left panel of Figure 2.9 is evidence of plasma compression at the leading edge of the loop (Antolin et al., 2016). Much of this effect is caused by the nature of the initial velocity profile. A larger velocity is imposed in the core region than within the shell of the loop and so we naturally see a compression of the plasma at the leading edge and an expansion at the trailing edge. Additionally, since the core is denser than the shell region, it has greater inertia and so a larger restoring force is required to decelerate this plasma. This is a reversible process and an equal and opposite effect is observed half a wave period later. In addition, the generation of fluting modes can be observed within the oscillating loop and will also contribute to compressional effects (Magyar and Van Doorsselaere, 2016).

In our simulations, we note that, initially, three major vortices form in the upper and lower half domains. This corresponds to the most unstable azimuthal mode (see eq. 1 in Terradas et al., 2008a). Following the breakdown of these large vortices, we observe that by the end of the simulation, a turbulent-like regime has developed in which the length scales present are very small. Indeed, the simulation is ended once the various plasma properties begin to vary across lengths of the order of the grid size. As we discuss later, similar variation is also observed in the horizontal velocity field (see Figure 2.10) and the horizontal magnetic field.

In order to consider the evolution of the velocity shear as the instability proceeds,

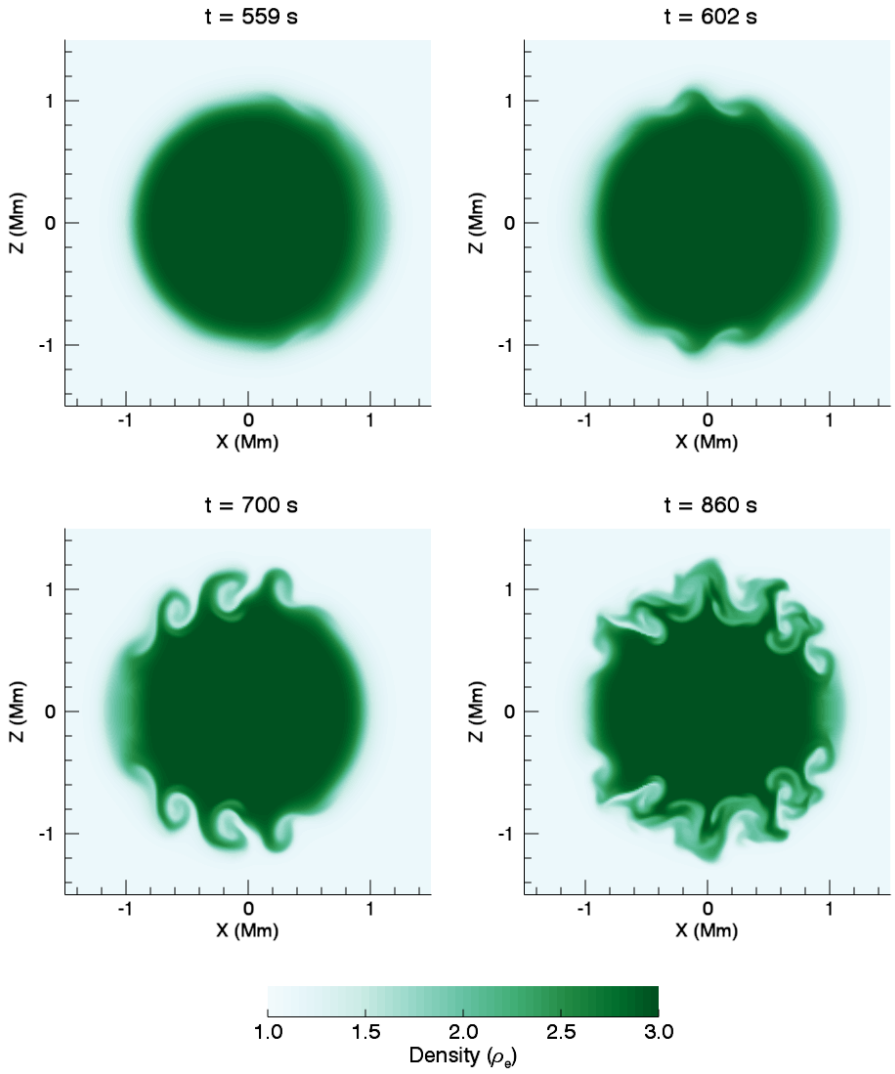

Figure 2.9: The density profile in the horizontal cross-section at the loop apex at four different times during the development of the Kelvin-Helmholtz instability. The initial formation of three dominant vortices (on both sides of the loop) corresponds to the growth of the most unstable mode.

in Figure 2.10 we display vectors corresponding to a small section of the horizontal velocity field, $\mathbf{v}_h = (v_x, v_z)$. For comparison with Figure 2.9, the density profile is also shown. The first panel indicates the strong velocity gradient along the loop's boundary that is responsible for triggering the KHI. Subsequently, Kelvin-Helmholtz vortices begin to deform the boundary region of the oscillating loop. A significant velocity shear persists on the boundary of these large scale vortices and smaller vortices then begin to develop (lower right panel). The devolpment of the instability is associated with strong flows along regions of large density contrast. Ultimately, the regions of enhanced density in the shell of the loop lose any coherent structure. Beyond this stage, any subsequent development of the instability may become unphysical due to a

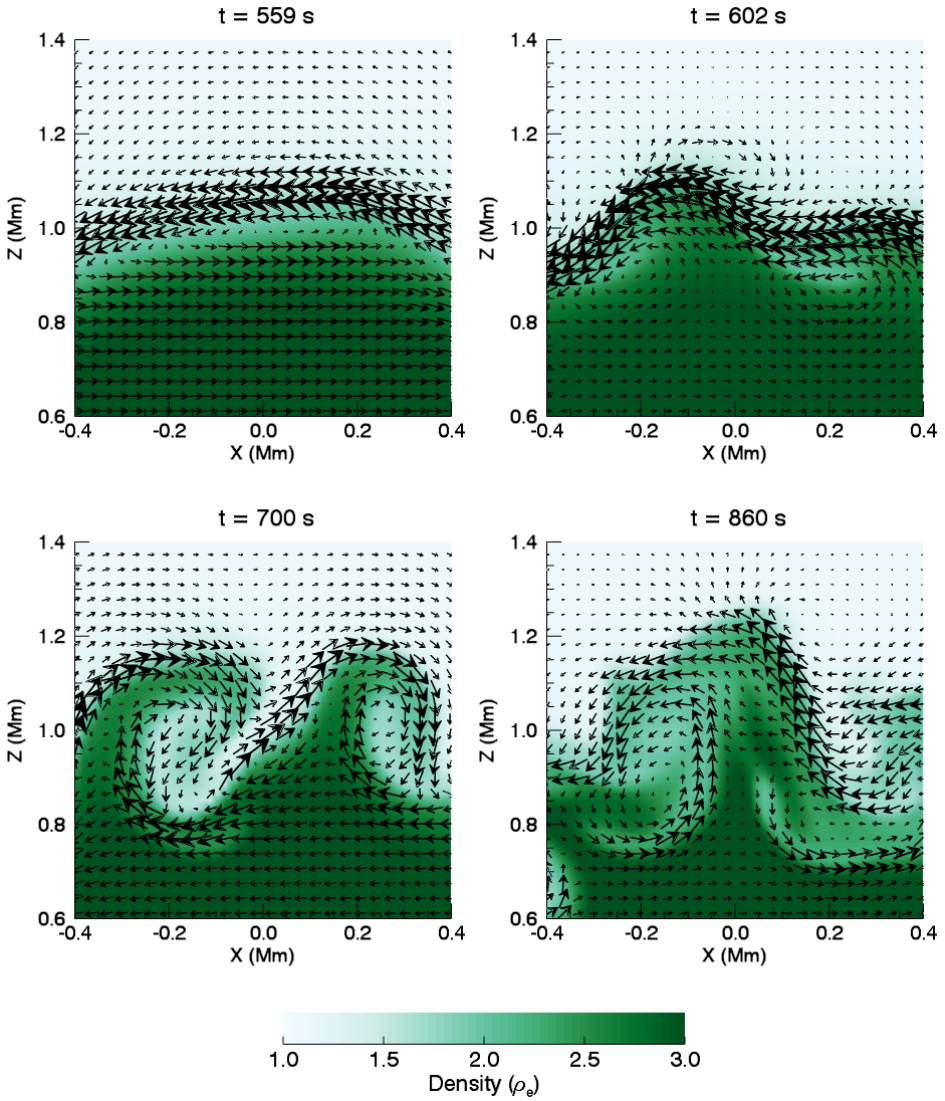

Figure 2.10: The development of the density profile (contour plot) and the horizontal velocity field (arrows) at the loop apex for a small portion of the deforming cross-section.

lack of spatial resolution.

Since the initial perturbation is largest at the loop apex, the radial velocity shear that develops during resonant absorption is most significant at this height. Consequently, we expect the deformation effects of the KHI to be greatest at this location. In order to confirm this, in Figure 2.11, we display an isosurface of $\rho = 2$ (corresponding to the resonant surface in the initial conditions) at three different times during the development of the instability. Indeed, we see that the deformation of the density structure is greatest at the loop apex. Furthermore, we note that the KH-vortices form long, vertical strands along magnetic field lines. The magnetic tension force promotes

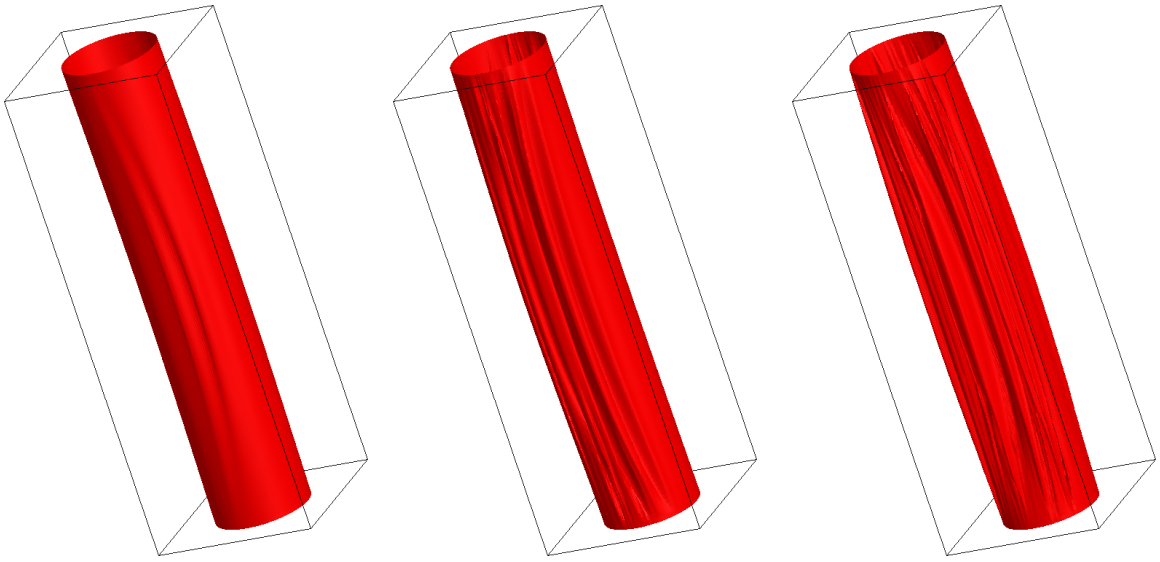

(a) 560 s. (b) 705 s. (c) 850 s.

Figure 2.11: Deformation of resonant layer during the formation of the magnetic Kelvin-Helmholtz instability.

this structuring and in Chapter 3 we shall show that this has an important effect in the presence of twisted fields.

2.4.1 Formation of Small Scales

The development of the KHI accelerates the formation of small spatial scales in the velocity field beyond the rate associated with phase mixing. Since the magnetic Reynolds number, R_M is much larger than unity, the magnetic field is approximately *frozen* into the plasma. As such, small length scales in the velocity field are associated with small length scales in the magnetic field. We can monitor the development of these scales by considering the vorticity, $\boldsymbol{\omega} = \nabla \times \mathbf{v}$, and the current density, $\mathbf{j}$.

In Figure 2.12, we show the magnitude of the vorticity at the loop apex ($y = 0$ Mm) and in Figure 2.13, we show the magnitude of the current density close to one of the loop foot points ($y = -90$ Mm). The selected height differs in each case because, as we shall show shortly, during the simulation, the vorticity dominates at the loop apex and the currents dominate close to the loop foot points. For the current density plots we chose a plane slightly removed from the lower foot point to minimise any spurious boundary effects. In both figures, the top left panel highlights the small scales that form during the growth of the azimuthal Alfvén wave. We immediately see that the gradients associated with this wave mode are significantly larger than those produced by the kink mode. This helps to explain why resonant absorption is an

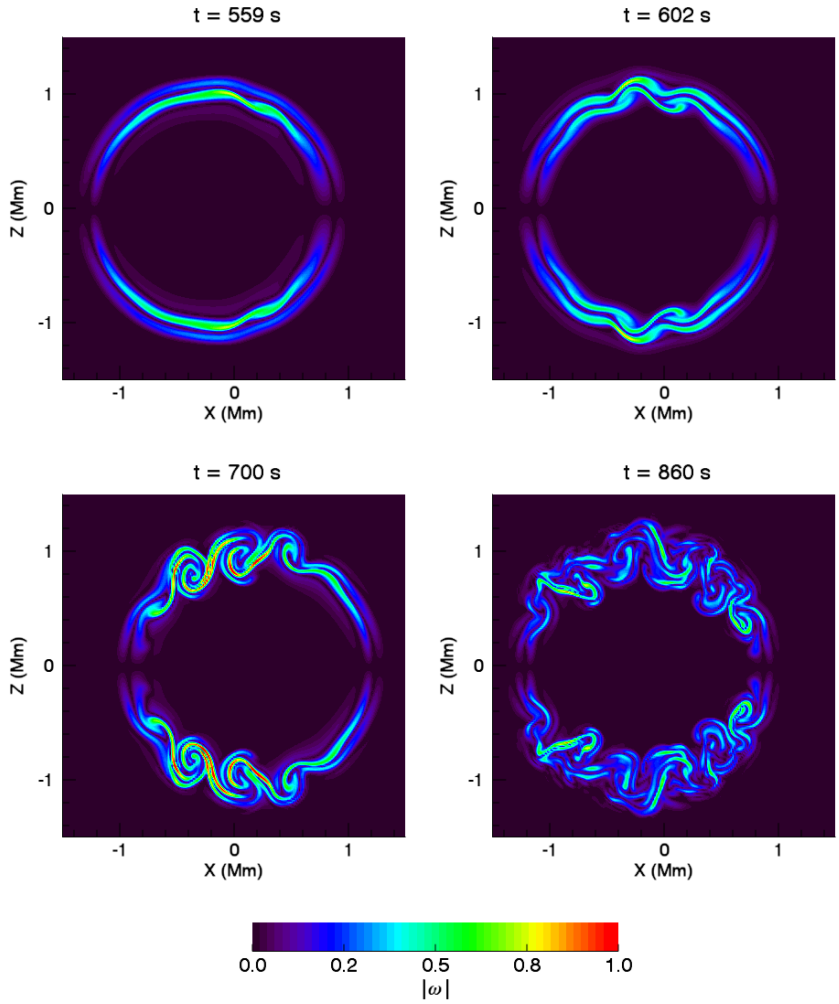

Figure 2.12: Evolution of small scales in the velocity field during the development of the KHI. Magnitude of vorticity at the loop apex is displayed at four stages during the formation of the instability. We have normalised to the maximum of $|\boldsymbol{\omega}|$.

attractive mechanism for enhancing wave energy dissipation. In subsequent panels, we can clearly see the formation of vortices and the corresponding proliferation of small scales in both the magnetic and velocity fields throughout the shell region of the loop.

We note two important effects of the KHI that can be observed in these contour plots. Firstly, we see that the instability enhances the magnitude of both vorticities and currents and therefore may further enhance the rate of wave energy dissipation. Secondly, we notice that as the instability deforms the structure of the loop, small scales spread over a much larger region in the loop's cross-section. This may provide some answer to the criticism of wave heating models that suggests energy dissipation can only occur over a narrow layer close to the resonant field lines (see Karampelas et al., 2017; Karampelas and Van Doorsselaere, 2018). Whilst, in this simulation, small

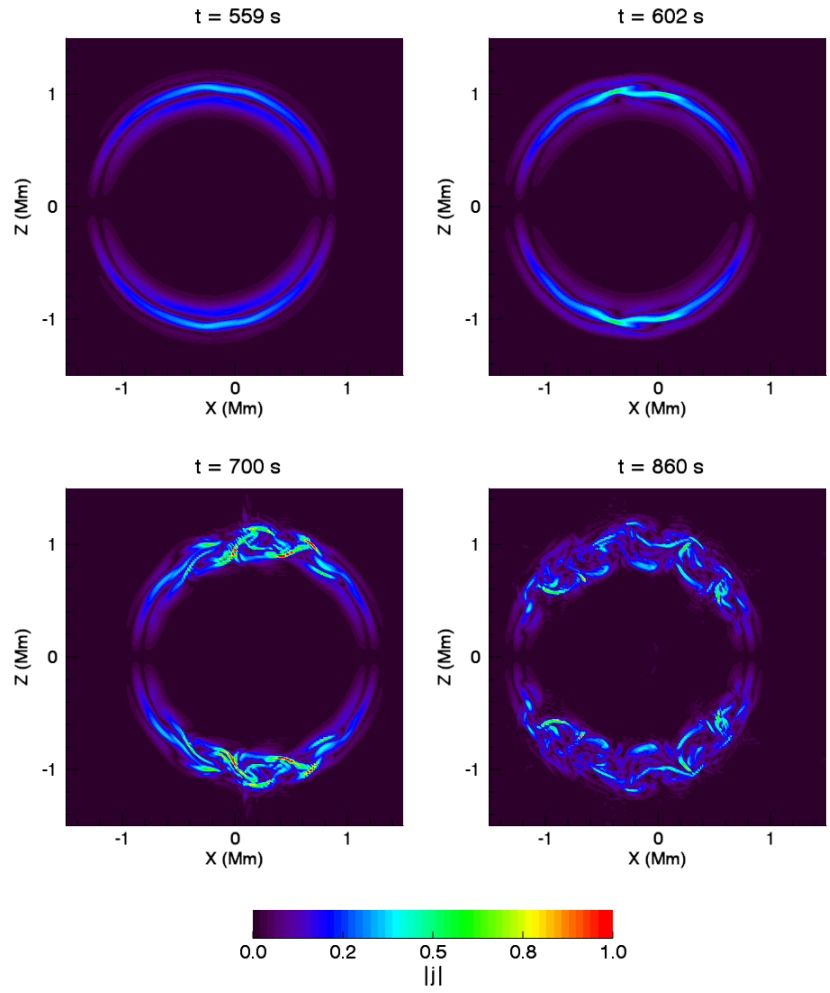

Figure 2.13: Evolution of small scales in the magnetic field during the development of the KHI. Magnitude of current density close to a loop foot point ($y = -90$ Mm) is displayed at four stages during the formation of the instability. We have normalised to the maximum of $|\mathbf{j}|$.

scales do not pervade through the entirity of the loop, Magyar and Van Doorsselaere (2016) presented a similar model and demonstrated that a larger amplitude oscillation can lead to density deformation, and hence the generation of small scales, across the entirity of the loop structure. This suggests that, contrary to many earlier models, if the instability does develop, wave energy could be dissipated as heat throughout the entirity of an oscillating coronal loop.

Since the distribution of magnetic and kinetic wave energy is not uniform along the length of the loop, we might expect the size of vorticities and currents to vary in height too. Indeed, in Figure 2.14, we show that this is the case. From the top panel, we see that vorticity is much larger at the loop apex than at the loop foot points. The high vorticity coincides with the regions of high kinetic wave energy close to the antinode of

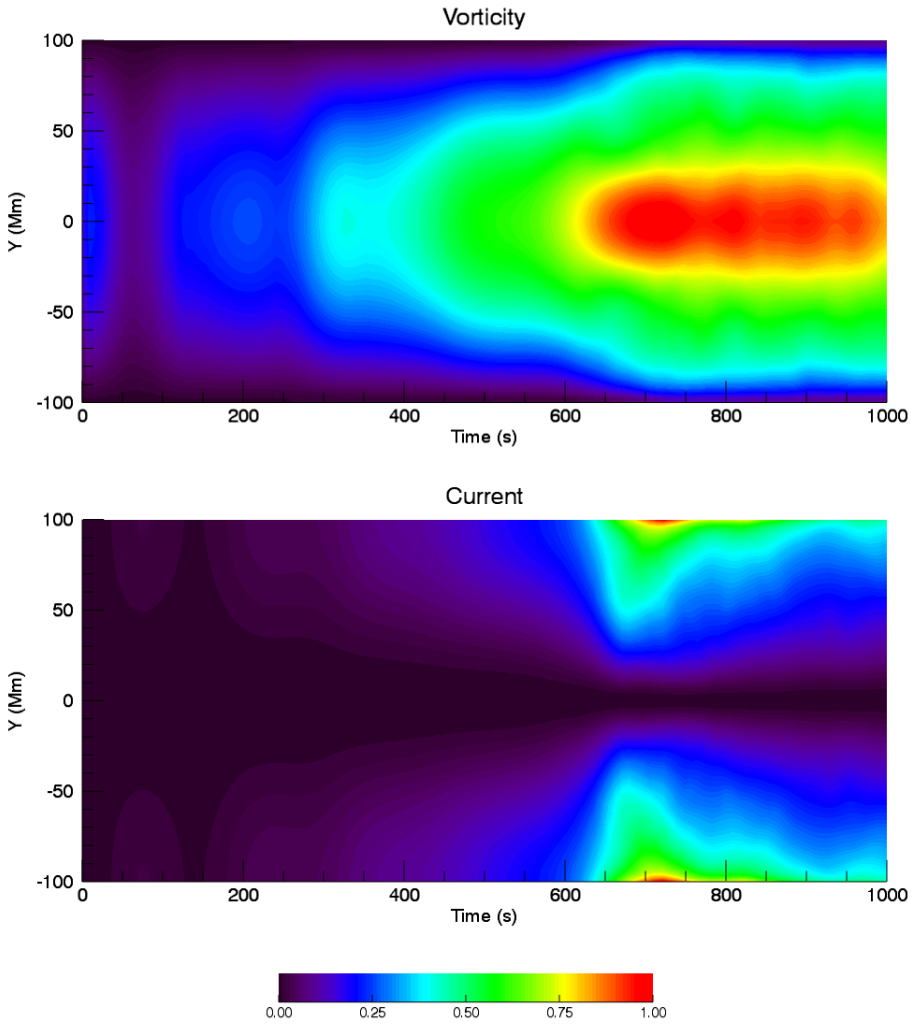

Figure 2.14: Growth of vorticity (upper panel) and current density (lower panel) along the length of the loop (y-axis) and throughout the simulation (time along x-axis). At each time, the variable in question is integrated across the loop cross-section at the specified height. In both cases, we have normalised the plotted data by the maximum value observed.

the standing wave. Analogously, the currents are largest close to the foot points, in the regions of high magnetic wave energy. There may be implications of this phenomenon for observing coronal heating in oscillating loops. In particular, if resistivity is the dominant transport coefficient, then we can expect heating to occur close to the foot points whereas if viscosity dominates, we might expect apex heating. This is discussed in detail by Karampelas et al. (2017).

In Figure 2.14, we see a large increase in both the vorticity and current density at around $t = 600$ s. This coincides with the onset of the KHI and is the time we begin to see deformation in the density profile (see upper right panel of 2.10). Consequently, tracking the formation of vorticities and currents within numerical simulations could

provide a proxy for the growth rate of the KHI. We shall explore this idea further in the following section.

2.5 The Effects of Dissipation

The formation of the KHI depends critically on the velocity shear across the shell region of the coronal loop. Therefore, provided that the width of the loop boundary remains unchanged, modifying the amplitude of the azimuthal Alfvén wave will affect the observed growth rate of the instability. Since the magnitude of the Alfvén wave depends on the magnitude of the kink mode, we can see that increasing the size of the initial perturbation will lead to the KHI developing more readily. Indeed, Magyar and Van Doorsselaere (2016) consider the impact of the oscillation amplitude on the instability and use similar models to verify this proposition.

Another manner in which the amplitude of the azimuthal Alfvén wave can be modified is by implementing different transport coefficients within the numerical domain. As we discussed in Chapter 1, resonant absorption and phase mixing can enhance wave energy dissipation in a non-ideal regime. This transfer from kinetic and magnetic wave energy to thermal energy will decrease the amplitude of the Alfvén mode. As a consequence, in the presence of significant diffusion, the radial velocity shear will decrease and the system will stabilise with respect to the KHI. Furthermore, viscosity can act directly to resist the formation of the Kelvin-Helmholtz vortices (see the velocity field in Figure 2.10). In the remainder of this section we aim to quantify the effects of the transport coefficients and consider the implications for wave energy dissipation within the corona.

2.5.1 Density evolution

Since the effects of the KHI within our simulations are easily observed by the deformation of the loop structure, we begin our consideration of the η-ν-parameter space by examining the evolution of the density profile at the loop apex. In Figure 2.15, we show the development of the instability for various transport coefficients and for a lower resolution simulation (final row).

We see that the suppression of the KHI is so great in the $\eta = \nu = 10^{-4}$ case (first row), that the characteristic KHI vortices do not form at all within the duration of the simulation. For the remaining three of the high resolution simulations displayed in Figure 2.15 (rows 2, 3 and 4), we see an increase in the effects of the instability at lower

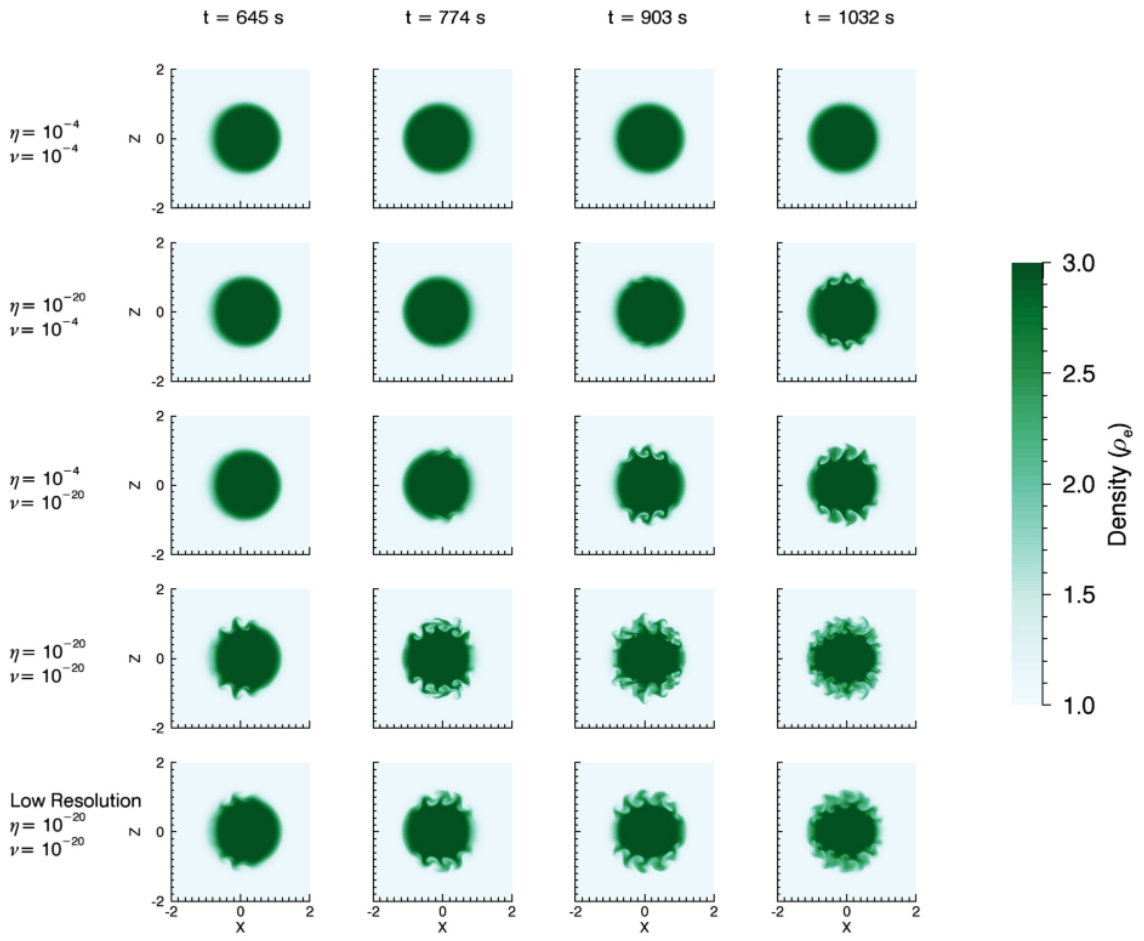

Figure 2.15: Effects of resistivity and viscosity on the development of the KHI. The density profile in the horizontal cross-section at the loop apex is shown for various transport coefficients at 4 stages during the numerical experiments.

levels of dissipation. Higher values of η and/or ν delay the onset time of the KHI and restrict the formation of small scales once the instability does develop. We note that the final row shows that lower resolution (and consequently larger numerical dissipation) will also inhibit the formation of small scales by the KHI. In this case however, the formation time of the first vortices is not delayed (compared to the penultimate row) which suggests that the resolution effects only become significant once the instability develops.

In each case that the KHI does form, we notice that the same azimuthal mode is always observed first. In the subsequent development we also find differences in the presence of higher azimuthal wave numbers which are seen in the unsuppressed cases but are not present in the stronger viscosity cases (e.g. row 2). The smaller scales

associated with the higher number modes are more sensitive to dissipative effects and consequently, are unable to form in the high η and ν cases.

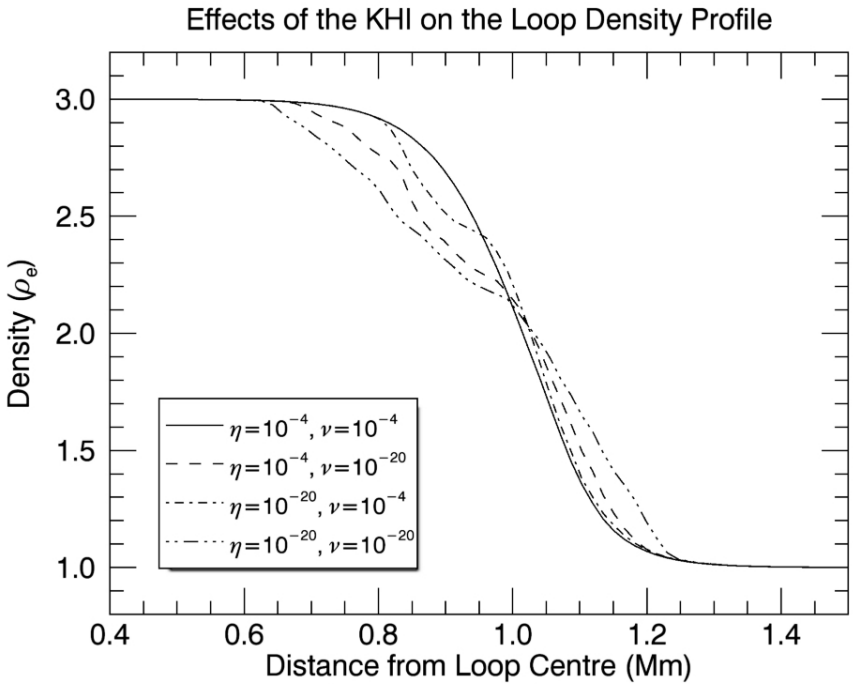

Figure 2.16: Average density along radii of the loop apex cross-section at $t = 1032$ s. The KHI is well-developed in three of the cases and is completely suppressed in the $\{\eta = 10^{-4}, \nu = 10^{-4}\}$ simulation (solid line).

The density deformation associated with the KHI acts to increase the average width of the boundary layer of the loop. In Figure 2.16, we examine this effect by plotting the average radial density profile of the loop for the high resolution simulations displayed in Figure 2.15. The figure was generated using many radial cuts of the loop, each forming a different angle with the direction of oscillation. The mean of these profiles is then calculated to find an average density structure across the radius of the loop. The plot shows the simulation state after a time of 1032 s (final column of Figure 2.15), once the instability is well developed in the least dissipative simulation. Since the effects of the KHI is approximately symmetric, we only show half of the loop cross-section.

The effect of the instability is to broaden the boundary region and so reduce the average density gradient between the interior and exterior of the loop. We note the asymmetric effects of viscosity and resistivity in limiting the density deformation which can also be observed by comparing rows 2 and 3 in Figure 2.15. This behaviour may be expected because the development of the KHI is critically dependent on the velocity shear which is more directly affected by viscous forces than resistive effects. The solid

line corresponds to a case in which the instability is suppressed completely and so the loop averaged density profile is unchanged from the initial equilibrium (Figure 2.2a).

It is important to note that the changing density structure will affect the natural frequency of field lines within the deforming region of the loop. Consequently, any subsequent transfer of energy from the kink mode by resonant absorption will be modified by the KHI. Further, any phase mixing will occur in a much more dynamic and turbulent regime which will change the rate of energy dissipation and possibly lead to heating over a larger fraction of the loop cross-section.

2.5.2 Velocity Shear

As we mentioned above, the effects of dissipation on the growth rate of the KHI can easily be understood by considering the relative amplitude of the Alfvén wave in each simulation. Resistivity and viscosity will both act to remove energy from the wave mode that forms during resonant absorption and thus will restrict the magnitude of the azimuthal velocity. This, in turn, will reduce the radial velocity shear and diminish the growth rate of the instability.

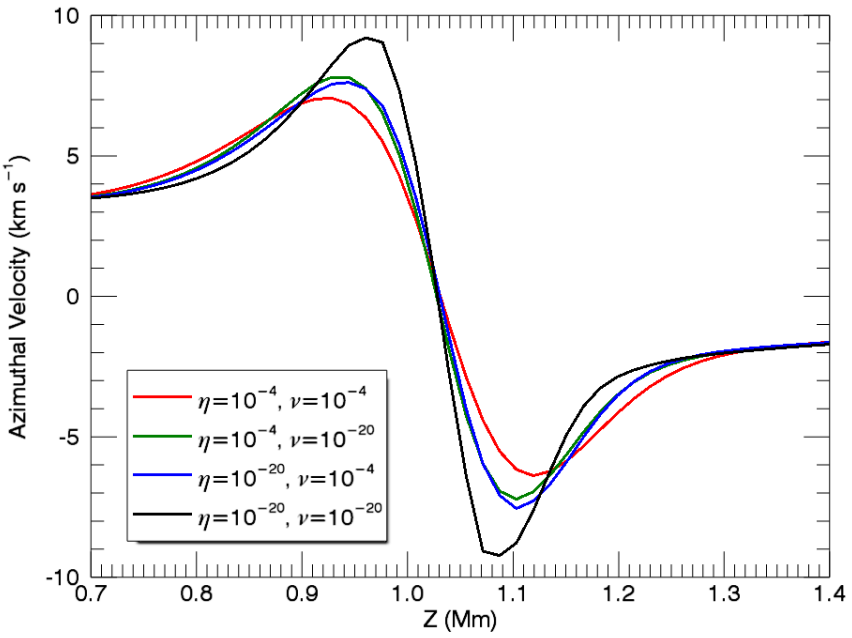

Figure 2.17: Relative magnitudes of the Alfvén waves that form with various transport coefficients. In each of the four curves, we display the azimuthal velocity, v_ϕ, prior to the development of the KHI in any of the simulations. The profiles are shown along a loop radius as a function of position across the boundary region.

We can see this clearly by comparing radial cuts (at the loop apex) of the azimuthal velocity in high resolution simulations with various values of η and ν. In Figure 2.17, we display the azimuthal velocity across the boundary region of the loop before the KHI has developed in any of the simulations. Although the differences in observed velocities are not especially large, we certainly see that increasing dissipation levels causes a decrease in the magnitude of the velocities observed. Further, a secondary effect can be detected by comparing the distance between the maximum and minimum for each of the four curves. We can adopt this as a measure of the phase-mixing length scale, λ_{pm}. Whilst the differences of this value between the simulations appears to be small, we do see that increasing the dissipation coefficients has the effect of increasing λ_{pm}.

When these two changes are considered in conjunction, we can clearly see that there is a greater velocity shear associated with the Alfvén wave in cases of lower resistivity and/or viscosity. This explains the important manner in which the transport coefficients will modify the growth rate of the instability.

2.5.3 Instability Onset Times

In order to quantify the suppression associated with high values of η and ν, in this section we aim to calculate an onset time for the instability in each numerical experiment. We would like this to correspond to the earliest time at which the effects of the KHI can be observed in various plasma quantities, such as the density profile. Unfortunately, identifying the earliest moment that the loop structure begins to deform by simply looking at contour plots can be an unreliable measure of the onset time (see for example row 2, column 3 of Figure 2.15 - can we see deformation at this point? Should we look earlier? Or later?). Instead, we seek an objective method for finding the KHI onset time in each simulation.

To this end, in each simulation, we monitored the maximum distance of plasma with density equal to $\rho = \frac{\rho_e+\rho_i}{2} = 2\rho_e$ from the centre of the loop. In the initial conditions, this corresponds to the cylindrical shell of resonant field lines located within the boundary layer, 1 Mm from the loop centre. In Figure 2.18, we show the evolution of this maximum distance for four simulations with different transport coefficients. These are the same simulations as used for rows 1-4 in Figure 2.15.

The rapid rise seen in three of the simulations (red, green and blue lines) corresponds to the onset of the KHI, when some of the plasma from the resonant shell begins to move radially outwards. In the experiment for which no sharp rise is observed (black

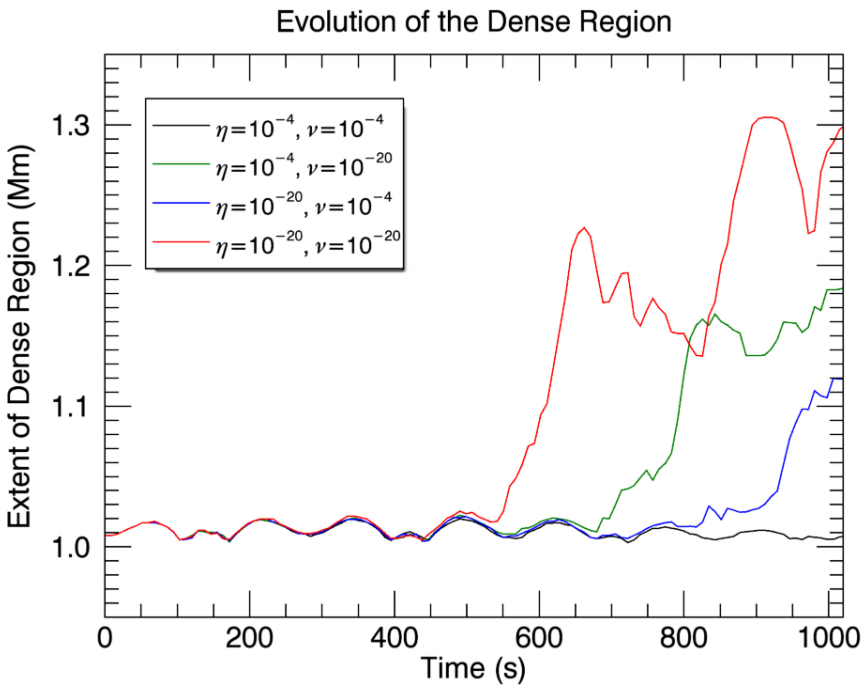

Figure 2.18: Maximum distance of plasma with density, $\rho = 2\rho_e$ from the loop centre for four different simulations. We use the time of the sharp rise as a measure for the onset time of the KHI (see Table 1).

line), the instability did not form. We note that not only can the start of the rise be identified with the onset of the instability, but the gradient of the initial rise acts as a proxy for the early growth rate. We see that larger transport coefficients act to both delay the onset time of the KHI and restrict subsequent development.

We highlight the small amplitude periodic behaviour that can be observed prior to the steep rise in all four of the curves. This corresponds to the periodic compression of plasma at the $z = 0$ line by both the kink mode and the azimuthal Alfvén wave. As we discussed previously, we can see the compressional effects of the transverse oscillation in Figure 2.9. Furthermore, since the Alfvén wave is not simply the torsional mode (it oscillates with a higher harmonic), the azimuthal velocity is oppositely signed in both halves of the $y = 0$ plane. Consequently, the oscillation is weakly incompressible and we observe a periodic change in density at the resonant layer. In Figure 2.18, we see that this behaviour is largely independent of the transport coefficients, and so we conclude that the compression by the kink mode, which is almost completely unaffected by the low levels of dissipation, is the dominant mechanism.

We can also see from Figure 2.18 that once the KHI does form, the motion of dense material away from the loop centre does not continue indefinitely. For example, the

decrease we observe for the unsuppressed case (red line) at around $t = 600$ s corresponds to the folding over of the vortices (see Figure 2.10; lower left panel) during the reversal of motion in the kink mode.

Using Figure 2.18, we can identify the onset time of the instability as the moment there is noticeable deviation of the simulation curve with the black line (no instability). Whilst this still allows some possibility for different interpretations, we see that values of 540 s, 680 s and 820 s for the red, green and blue lines respectively can be used as estimates for onset times. Using this method, we are able to deduce onset times for simulations throughout the parameter space. These are displayed in Table 2.1.

		ν				
		10^{-3}	10^{-4}	10^{-5}	10^{-6}	10^{-20}
η	10^{-3}					X
	10^{-4}		X	X	680	680
	10^{-5}					550
	10^{-6}					540
	10^{-20}	X	820	550	540	540

Table 2.1: Approximate onset times (seconds) of the Kelvin-Helmholtz instability for the completed simulations in the parameter space. The symbol X denotes that the instability was suppressed for the duration of the experiment and a blank entry signifies no data; the simulation was not conducted.

For the results displayed in Table 2.1, we notice that changing the value of the viscosity or the resistivity below 10^{-6}, has no effect on the onset time of the instability. This behaviour can also be confirmed by considering contour plots such as those displayed in 2.15. We therefore conclude that (for the high resolution simulations), the effective numerical viscosity and resistivity are approximately 10^{-5} – 10^{-6} (Reynolds numbers of $10^5 - 10^6$). These are similar to the values obtained in the model presented in Antolin et al. (2014).

In the approximately non-dissipative case $\{\eta = 10^{-20}, \nu = 10^{-20}\}$, the instability begins to form after just under two wave periods. Meanwhile, in the suppressed simulations, the onset time is delayed by (approximately) some multiple of half the oscillation period (140 s). This is because the magnitude of the velocity shear does not increase uniformly throughout the wave period. Instead, it oscillates (with increasing amplitude) at twice the frequency of the global mode. The KHI is most likely to form at times where the velocity shear has a maximum and hence, it is typically delayed by a factor of half the wave period.

2.5.4 Vorticity

As we demonstrated in the ideal case, the vorticity measured within the numerical domain increases substantially during the development of the KHI. The onset of the instability is associated with the growth of unstable, high azimuthal wave number, Alfvén modes. These waves are particularly sensitive to dissipative forces and are readily suppressed in simulations with high values of η and ν. These wave modes are observed as vortices in the shell region of the oscillating loop and hence we expect to see vorticity suppression in cases where the growth of high number wave modes is prevented by large dissipation.

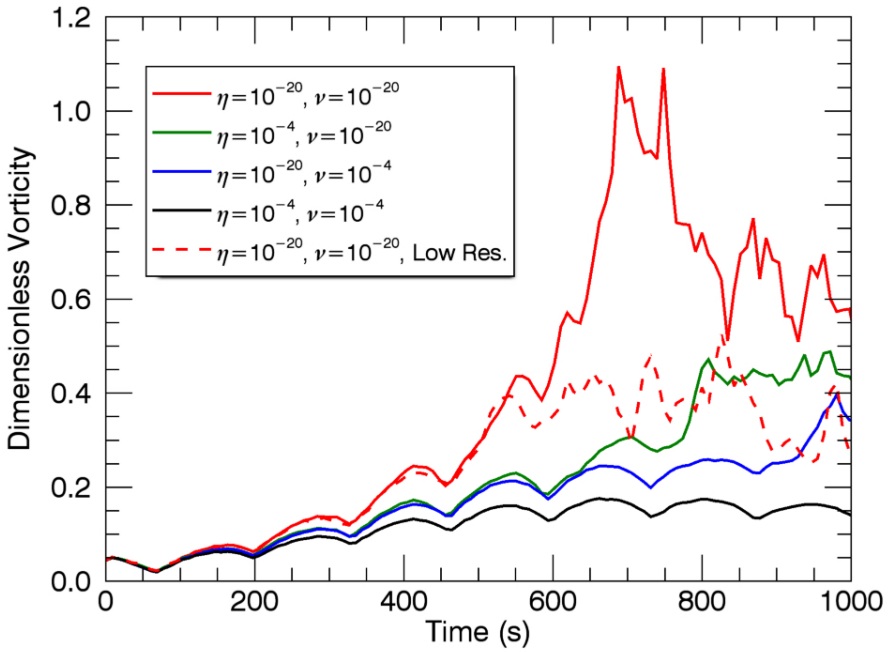

Figure 2.19: Evolution of the mean of $|\omega_y|$, the component of vorticity perpendicular to the cross-section of the plane, for five simulations.

In Figure 2.19, we examine the evolution of the mean magnitude of the vorticity component perpendicular to the loop cross-section. We average $|\omega_y|$ across the cross-section at the loop apex and track this quantity through time. In these simulations, this component of vorticity is initially dominated by radial gradients in v_ϕ and represents the growth of azimuthal wave power in the shell region of the loop. Subsequently, azimuthal gradients of radial velocities can become significant as the KHI develops and these contribute to the plotted curves. Indeed, in the lower panels of Figure 2.10, we observe the formation of the small scale vortices that coincide with the rapid vorticity

increase following the onset of the instability. Additionally, since velocities parallel to the loop tend to be small in comparison to those in the loop cross-section, we have $|\omega| \approx |\omega_y|$. We note that unsigned vorticity is used because the motions in each of the z half-planes contribute equal and opposite vorticities.

By considering the black line (instability totally suppressed), we see that the unsigned vorticity oscillates with twice the frequency of the kink mode. This periodic behaviour occurs because the energy transfer from the kink mode into Alfvén modes varies throughout each wave period. Energy transfer is more efficient when the kink mode is at maximum displacement and so the vorticity increase is greatest at these times. Since two displacement maxima occur for each wave period, we see that $|\omega_y|$ oscillates with half the period. For this case, the mean vorticity (averaged over one period) increases until around $t \approx 700$ s. From this point, energy extracted from the Alfvén wave by dissipation exceeds energy injected through resonant absorption. This suggests that the largest velocity shear has been obtained and since this did not induce the KHI, it is likely that the system will remain stable even beyond the end time of the simulation.

In the remaining simulations, we observe an appreciable increase in the vorticity as the KH-vortices form. Indeed, we see that in the near-ideal, high resolution case (solid red line), the mean vorticity reaches a level six times larger than the case in which the instability is suppressed (black line). The delay in the rise in the vorticity for the green and blue curves is caused by the later onset time of the KHI that is observed in the associated simulations. Whilst we could use the rise in vorticity as a measure of the KHI onset time, this method seems less precise than using the density evolution as described above. For this reason, we did not choose to use vorticities to find the times displayed in Table 2.1.

The minimum observed in all simulations at around $t = 70$ s, is associated with the first displacement maximum in the kink oscillation. At this time, the global mode has zero velocity associated with it and there has been little energy transferred to the Alfvén wave in the loop boundary. Consequently spatial gradients of the velocity components, and hence vorticities, are very small. Following this minimum, Alfvén wave modes are always present in the loop boundary and so no repeat of the vorticity minimum at $t \approx 70$ s is observed.

Even before the formation of the KHI in any of the simulations ($t \approx 540$ s), there are η and ν-dependent differences in the mean vorticity. As was shown in the previous section, greater dissipation has the effect of suppressing the growth of the Alfvén mode, and hence the vorticity, present within the domain. These differences are sim-

ply enhanced by the onset of the instability and the formation of the Kelvin-Helmholtz vortices.

The asymmetry of the effects of η and ν on the instability is again highlighted by comparing the simulations corresponding to the green and blue lines in Figure 2.19. We see that before the onset of the KHI, the mean vorticity is remarkably similar, suggesting there is little difference in the nature of the Alfvén wave between the two simulations. This is confirmed in Figure 2.17 in which there is little difference in wave amplitude in the $\{\eta = 10^{-4}, \nu = 10^{-20}\}$ and the $\{\eta = 10^{-4}, \nu = 10^{-20}\}$ simulations. However, once the KHI forms in the green line simulation (approximately $t = 680$ s) the vorticity behaviours diverge. This suggests that the value of ν is more pertinent than η for the development of the Kelvin-Helmholtz vortices.

Furthermore, by comparing the solid and dashed red lines in Figure 2.19, we see that the vorticity is also a function of the spatial resolution. The enhanced numerical dissipation that is present in the low resolution simulation will also act to restrict the vorticity levels. Interestingly, this effect only becomes apparent when the KHI forms and energy begins to cascade to length scales comparable to the coarser spatial resolution in the dashed line simulation. This behaviour is in agreement with the previous discussion concerning the near-identical behaviour of the (ideal) high and low resolution simulations prior to the development of the instability.

2.5.5 Energetics

In this section, we continue our analysis by considering volume integrated energies to identify the important energy transfer mechanisms that occur during the simulations. Since resonant absorption is essentially an ideal process, provided that the dissipation levels are not large enough to cause significant direct damping of the kink mode over a few wave periods, the transfer of energy to the Alfvén mode will proceed largely independently of the values of η and ν.

In Figure 2.20, we show the energy integrated over the core region of the loop (see Figure 2.1) as a function of time. The core is tracked through time as the loop axis is shifted by the kink mode. We see that both the oscillation and the loss of kinetic energy from the core region of the loop do not depend on the values of η and ν. This confirms that the kink mode does not experience significant damping (in the loop core) due to the effects of resitivity and viscosity. Certainly, the initial velocity profile has no horizontal velocity gradient within the loop's core and so we expect the only effects of viscosity to occur within the boundary layer. We note that the apparent unresolved

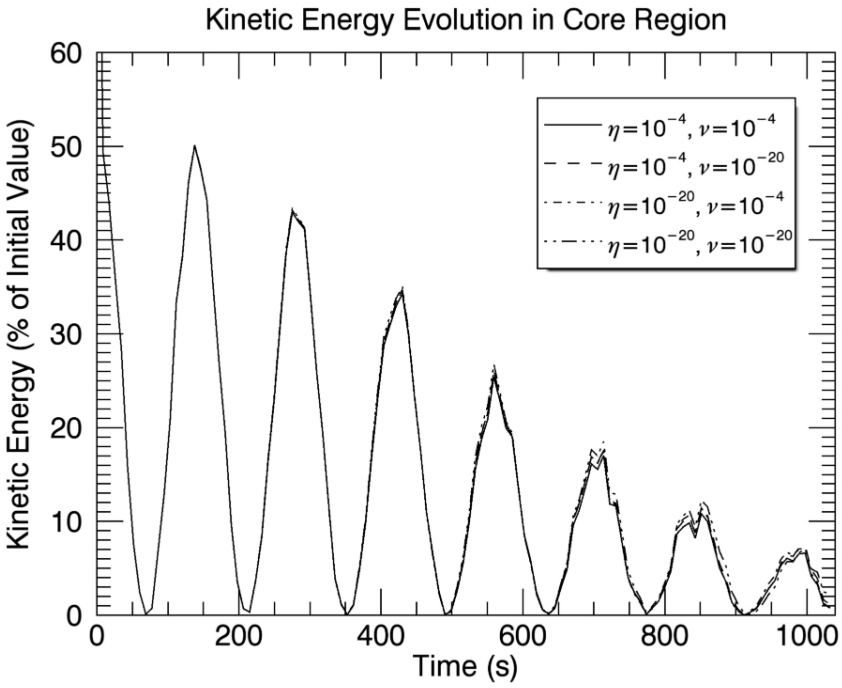

Figure 2.20: Evolution of the volume integrated kinetic energy in the core region of the loop for four simulations.

nature of the oscillation in Figure 2.20 is caused by an insufficient frequency of data outputs from the Lare3d code and is not indicative of poor temporal resolution in the underlying numerical scheme.

As we highlighted earlier (red envelope in Figure 2.5), the energy lost from the core region through this process follows a Gaussian damping profile (see e.g. Hood et al., 2013; Pascoe et al., 2013). At later times (after $t = 600$ s), small differences in the kinetic energy profiles of the four simulations are noticeable. These coincide with the onset of the KHI and reflect difficulty in tracking the core region once the density profile begins to deform. We also expect some additional damping due to the development of small scales in the velocity and magnetic fields. This effect was also noticed by Magyar and Van Doorsselaere (2016).

In Figure 2.21, we now consider the evolution of the kinetic energy within the shell region of the loop. For clarity we have only included the essentially ideal and the fully suppressed ($\eta = \nu = 10^{-4}$) simulations. The remaining experiments are constrained by the two curves. Initially, we see the maxima decay as a function of the dissipative coefficients; larger values of η and ν cause greater Ohmic and viscous heating and thus a greater reduction in the kinetic energy. However, even in the approximately ideal case, we see a small loss of kinetic energy from the shell region. This loss is grid

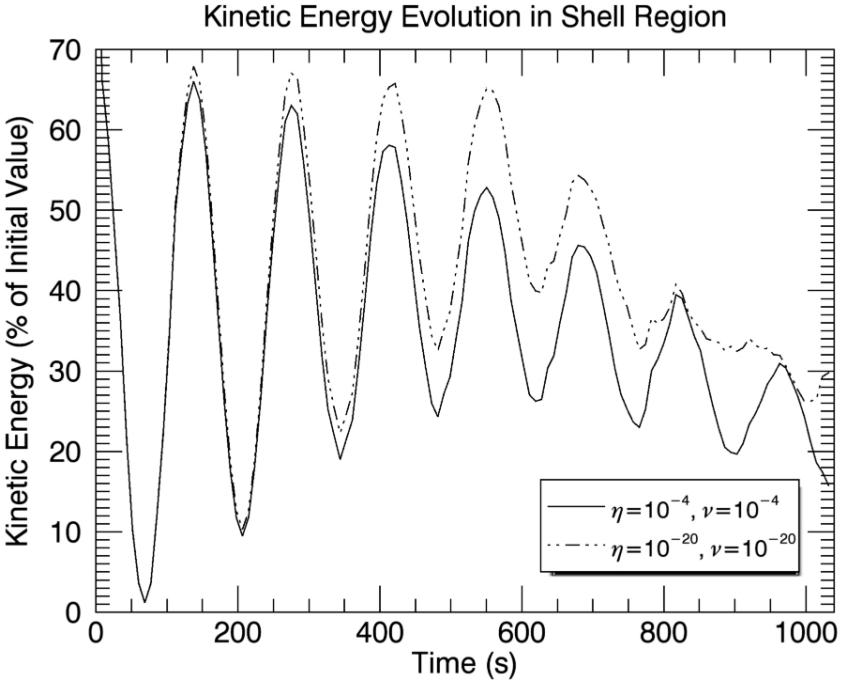

Figure 2.21: Evolution of the volume integrated kinetic energy in the shell region of the loop. The results of two extreme simulations (no suppression for the dotted-dashed line and total suppression for the solid line) are shown. The results of other simulations are bounded by the two curves.

dependent and is enhanced in the lower resolution simulation. We therefore conclude that this energy decrease is due to numerical dissipation and so does not coincide with an increase in thermal energy. It is important to note that this result differs from similar models implementing different MHD codes in which the numerical energy loss can be tracked and deposited as heat (e.g. Karampelas et al., 2017).

At the same time, kinetic energy is constantly being transferred into the shell region from the decaying kink mode. This enhances the time average kinetic energy associated with the Alfvén wave. Further, due to the phase mixing of the azimuthal mode, some part of the loop boundary is in constant motion. These two effects explain the increasing minima seen until $t \approx 600$ s.

Beyond this time, two significant events occur within the loop boundary; the rate of wave energy dissipation begins to exceed the energy injected by resonant absorption and the KHI develops in the non-suppressed case ($\eta = \nu = 10^{-20}$). The former effect is observed as a decrease in kinetic energy within the shell region. Since the rate of energy input follows a Gaussian profile, as the simulation progresses, less energy is converted from the kink wave mode. Further, as the amplitude of the Alfvén mode increases, the

process of phase mixing becomes more effective at dissipating energy. When combined, these two effects result in the decrease in Alfvén wave energy from the loop boundary.

Additionally, we begin to observe the effects of the instability in the non-suppressed case in Figure 2.21 (dot-dashed line) beyond $t = 600$ s. As we have detailed previously, the instability decreases typical length scales in both the magnetic and the velocity fields. This amplifies the effects of η and ν and increases the rate of wave energy dissipation. The formation of small scale vortices will enhance viscous effects and the braiding of magnetic field by the turbulent plasma will generate small scale currents and increase the amount of Ohmic heating. Inevitably, the formation of these small scales also increases the magnitude of numerical effects. As a result, even in the approximately ideal case, we observe enhanced kinetic energy loss following the formation of the instability. However, the energy transfer may be tracked more accurately using a locally enhanced resistivity (discussed below).

We should also note that as with the kinetic energy of the core region plot, uncertainties in defining and tracking the shell region following the onset of the instability will also contribute to the behaviour of the dot-dashed curve. However, since these only resulted in small errors in Figure 2.20, we expect a similar, limited, effect in this case.

We can consider the contribution of magnetic energy dissipation to the heating of the plasma by monitoring the Ohmic heating term in the energy equation. From equation 1.18, we see that the rate of Ohmic heating is proportional to ηj^2. Therefore, to obtain comparable Ohmic heating with a resistivity that is an order of magnitude smaller, the size of j must be approximately $\sqrt{10} \approx 3.2$ times larger.

In Figure 2.22, we plot ηj^2 integrated over the shell region of the loop apex during the growth of the KHI for two simulations with different resistivities (blue line: $\eta = 10^{-4}$, red line: $\eta = 10^{-5}$). We observe that despite having a lower resistivity value, heating occurs earlier for $\eta = 10^{-5}$ (red line) as the small length scales associated with the KHI develop earlier. For larger values of resistivity, the development of the instability is delayed. However, once it forms, the rate of Ohmic heating is higher (blue line) due to the higher value of the resistivity. Despite η being an order of magnitude larger for the blue curve, the Ohmic heating is not ten times larger due to the inhibitive effect that higher values of dissipation have on the generation of small scales.

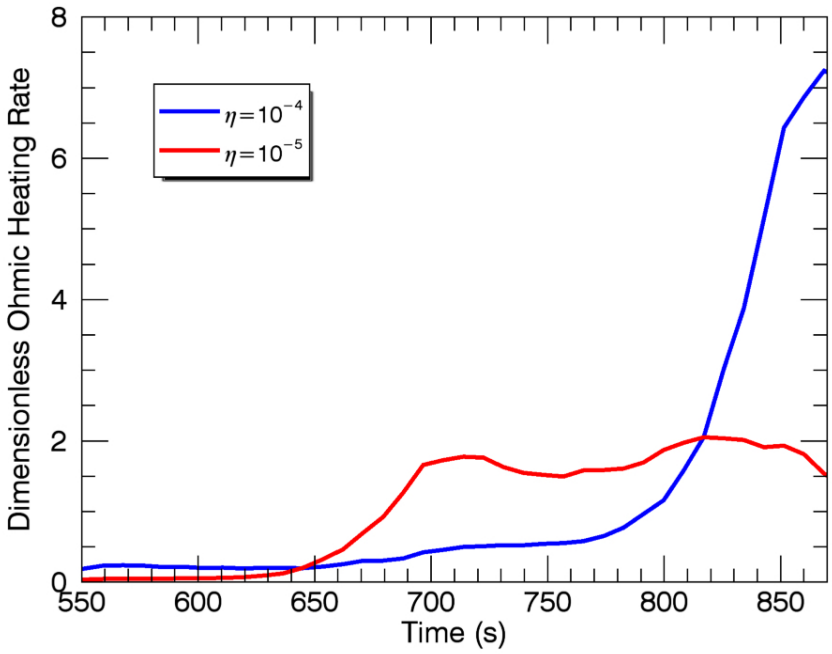

Figure 2.22: Volume integrated Ohmic heating rate within the shell region at the loop apex for two values of η during the formation of the KHI.

2.5.6 Anomalous resistivity

The turbulent-like regime that is associated with the KHI may have implications for heating coronal plasma as wave energy is more readily dissipated at the small scales that are generated. As the instability develops, the energy cascade quickly reaches scales on the order of the grid resolution and inevitably cannot be accurately tracked using a finite difference scheme. When this happens, wave energy will be lost from the domain as a result of numerical dissipation.

In order to mitigate this resolution problem, it is common practice to use anomalous dissipation coefficients that are only triggered if certain criteria are satisfied, e.g. the plasma parameters begin to vary on a scale that is comparable to the grid size. In the case of resistivity, this condition is typically dependent on a threshold current. If such currents form, an enhanced resistivity, η^*, will ensure that the associated magnetic energy is dissipated as heat at length scales that can be resolved by the numerical grid. Within our model, implementing a locally enhanced resistivity allows the instability to develop without the usual suppression caused by high η, but will limit the resolution effects in the turbulent aftermath. Such an approach may be physically valid as the formation of very small length scales (which would be associated with enhanced Ohmic

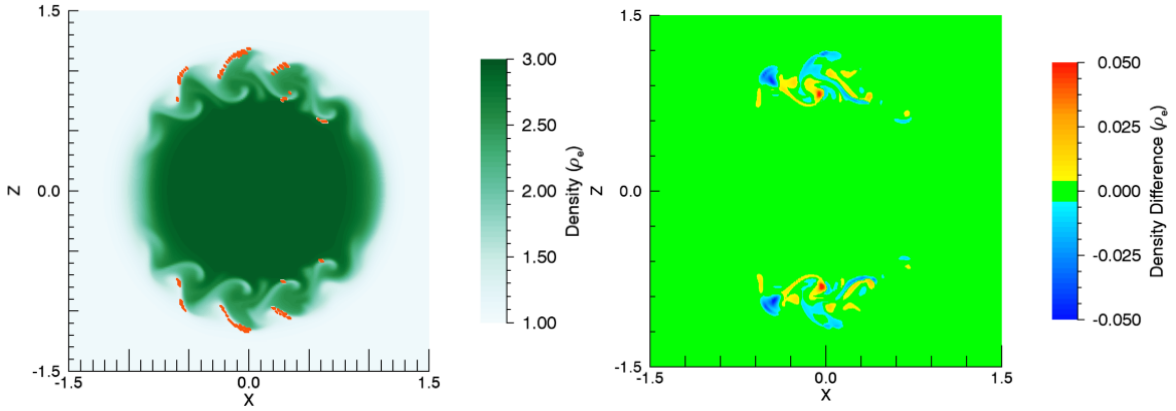

Figure 2.23: *Left* - Density profile in the cross-section at the loop apex for the simulation with $\{\eta = 10^{-20}, \nu = 10^{-4}\}$ and a critical resistivity, $\eta^* = 10^{-4}$. Regions in which the critical resistivity, is triggered are overplotted in red. *Right* - Difference plot between the density in the $\{\eta = 10^{-20}, \nu = 10^{-4}\}$ simulation and the case in which η^* is considered. Red regions indicate larger densities in the simulation including η^* and blue regions indicate larger densities in the original case.

heating) is artificially restricted by the finite resolution of the numerical grid during the development of the KHI.

As we described earlier, in these simulations, the currents are dominated by those close to the loop foot points and not by the small scales in the magnetic field that form at the loop apex in the region of largest density deformation. The magnitude of the horizontal components of the currents are, however, typically largest at the loop apex once the instability forms. We track the Ohmic heating associated with these apex currents by imposing a critical resistivity that is triggered when the magnitude of the horizontal currents exceeds a certain threshold.

This threshold is selected such that no horizontal currents exceed this value prior to the onset of the instability. This ensures that the early development of the KHI will coincide with the observed growth in the ideal ($\eta = \nu = 10^{-20}$) simulation. Subsequently, the threshold is attained by currents that form within the Kelvin-Helmholtz vortices. Since the horizontal currents are largest at the loop apex, the resistivity is only enhanced close to $y = 0$ Mm and only at a small number of grid points within the boundary region of the loop.

Even once the critical resistivity, η^*, is triggered, the large-scale behaviour of the plasma remains unchanged. In the left-hand panel of Figure 2.23, we display the density profile at the loop apex obtained in the critical resistivity simulation. We see that it is almost identical to the corresponding images in Figure 2.9. In this panel, the red regions denote grid cells in which the critical resistivity is triggered. A more detailed

comparison considering the density difference between the two simulations is shown in the right-hand panel of Figure 2.23. We find that there are only minor ($\leq 5\%$ change in density at any given location) differences close to the KHI vortices in the shell region. Further, in contrast with the $\{\eta = 10^{-4}, \nu = 10^{-20}\}$ simulation, in which the formation of the instability was delayed, we find little evidence to suggest that the triggering of this critical resistivity leads to significant suppression. This is unsurprising when we consider the very small area that is affected by the anomalously enhanced η^*.

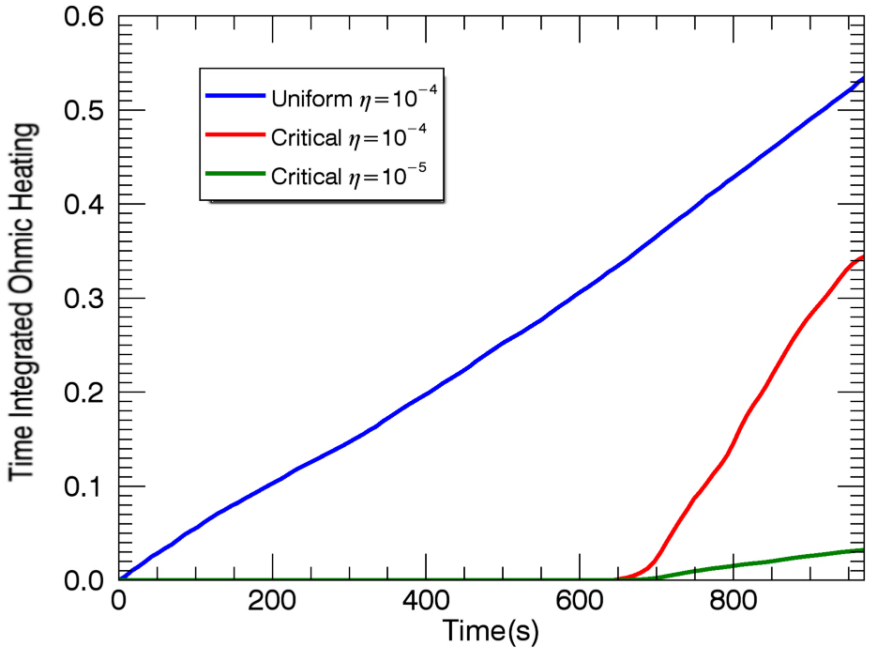

Figure 2.24: Time integrated Ohmic heating at the loop apex for the $\{\eta = 10^{-4}, \nu = 10^{-4}\}$ case (blue), the $\{\eta = 10^{-20}, \nu = 10^{-20}, \eta^* = 10^{-4}\}$ case (red) and the $\{\eta = 10^{-20}, \nu = 10^{-20}, \eta^* = 10^{-5}\}$ case (green).

The inclusion of an η^* that is many orders of magnitude larger than the background resistivity, induces a dramatic increase in the rate of Ohmic dissipation. In Figure 2.24, we display the cumulative Ohmic heating integrated over the loop apex for the fully suppressed simulation (blue; uniform η and ν), and two simulations with anomalous resistivities (red; $\eta^* = 10^{-4}$ and green; $\eta^* = 10^{-5}$). The integral is calculated over a circle of radius 2 Mm that tracks the cross-section of the loop at $y = 0$ Mm.

For the simulations that include the critical η^*, it is clear that the enhanced resistivity is first triggered at around $t \approx 650$ s. Once $\eta^* = 10^{-4}$ is triggered, the rate of Ohmic heating observed (derivatives of the displayed curves) exceeds the rate in the $\{\eta = 10^{-4}, \nu = 10^{-4}\}$ simulation in which the KHI is suppressed. Whilst this is not the

case along the entire loop (the current density is particularly small at the loop apex in the suppressed case), it is remarkable that $\eta = 10^{-4}$ at such a low number of grid points generates more Ohmic dissipation than the uniform η case once the KHI has formed.

2.6 Excitation by External Pulse

Thus far, we have restricted our consideration to the wave dynamics associated with a spontaneously excited coronal loop. In particular, in order to generate a fundamental standing kink mode, we have imposed a velocity profile on the density structure within the initial conditions of our simulations. Whilst this simplifies the analysis of the plasma evolution, it is not representative of the generation of transverse waves within the solar corona.

The standing waves presented within this chapter may form as the result of the reflection of propagating kink waves that are induced at one (or both) of the loop foot points. This mechanism has been studied extensively by, for example, Magyar and Van Doorsselaere (2016); Karampelas et al. (2017); Karampelas and Van Doorsselaere (2018). In each case, the authors find that the Kelvin-Helmholtz instability develops in a qualitatively similar manner to the results described above. We also note that kink waves may be generated internally by the collision of asymmetric, loop-aligned flows (Antolin et al., 2018), however, a study of whether the instability forms in such cases is beyond the scope of this thesis.

Alternatively, transverse oscillations of coronal loops have been frequently observed to be excited by a propagating (blast) wave emanating from a nearby impulsive event, e.g. a solar flare or the destabilisation of a filament (e.g. Nakariakov et al., 1999; Schrijver et al., 2002; Verwichte et al., 2004). Therefore, in this section, we examine the wave dynamics associated with a kink mode that is generated by an external pulse. This problem has previously been considered (e.g. Pascoe et al., 2009; De Moortel and Pascoe, 2009) for a coronal arcade in the context of coronal seismology. However, in these publications the authors focussed on the observed decay of the kink mode (in order to evaluate seismological estimates of the magnetic field strength) and the possible formation of the Kelvin-Helmholtz instability was not investigated.

Whilst a blast wave will excite transverse oscillations in a coronal loop, it will also generate wave modes within the external plasma. Therefore, since the development of the KHI is sensitive to the form of the velocity shear across the boundary of a flux tube, we may expect different dynamical behaviour in this case. Despite this, we will

show that for a small amplitude kink mode, the characteristic vortices will still form in this regime. Resonant absorption still permits the transfer of wave energy from the transverse mode to localised Alfvén waves and the instability is able to develop as a result of the radial gradient in the azimuthal velocity.

2.6.1 Initial Conditions

For this model, we maintain the form of the flux tube presented earlier, however, we no longer impose the velocity profile within the loop structure. Instead, we mimic the generation of a propagating fast wave (for example as a result of a solar flare) by imposing a large gas pressure in the external plasma. In order to minimise any direct interaction (beyond the generated fast wave) between this pressure enhancement and the modelled loop, the location of the flare is assumed to be far removed from the boundary of the flux tube. The inclusion of this large pressure generates a fast magnetoacoustic wave which ultimately displaces the density structure and excites a transverse oscillation of the coronal loop.

Since the pressure wave propagates isotropically in the horizontal directions (although not in the loop-aligned directions), the size of the computational grid is increased to avoid boundary effects when the wave reaches the edges of the domain. As such we extend the non-uniform region (see Figure 2.3) of the numerical grid. This is achieved by increasing the number of grid points in both of the horizontal directions to 550. The uniform region in the centre of the domain remains unchanged. A damping layer close to each of the upper and lower x and z boundaries is also included to reduce the amplitude of the propagating fast wave in these volumes. This is designed to minimise energy transfer across the periodic boundaries. The form of the y-axis (loop-aligned) remains unchanged. For the duration of the simulation, $\eta = \nu = 10^{-20}$ throughout the domain.

Pressure Enhancement

We impose a pressure enhancement at a significant distance from the boundary of the flux tube. We would like the pressure to remain continuous and thus, we use a three-dimensional Gaussian profile for the enhancement. Therefore, including the original background pressure, P_0, we impose

$$P(x, y, z) = P_0 \left(\lambda e^{-a(x-x_0)^2 - b(y-y_0)^2 - c(z-z_0)^2} + 1 \right). \tag{2.6}$$

Here, λ is a parameter that defines the magnitude of the pressure enhancement. Further, x_0, y_0, z_0, a, b and c are constants that define the centres and the widths of the Gaussian profiles in the x, y and z directions. We immediately see that for large $|x - x_0|, |y - y_0|$ and $|z - z_0|$, the pressure reduces to P_0, the gas pressure in the original model. Since we wish to maintain the density profile used previously, this new pressure profile is associated with a change in the plasma temperature. This inevitably leads to extremely high (non-coronal) temperatures in the enhanced pressure region, however, these are well-removed from the interesting wave dynamics and are not considered further.

For the purpose of our simulation we set $\lambda = 150$, $x_0 = -18$ Mm, $y_0 = z_0 = 0$ Mm. The location of the pressure enhancement ensures that the loop is displaced in the x direction. Furthermore, the amplitude of the propagating fast wave will be largest at the loop apex. We select $a = c = 0.25$ Mm^{-2} and $b = 37.5$ Mm^{-2} in order to ensure that the Gaussian profile in the y-direction (loop-aligned) is wide in comparison to the horizontal profiles. This ensures that a large proportion of the loop axis is displaced by the blast wave. Whilst this will not generate a purely fundamental standing mode, it will ensure that the entire loop oscillates and that we do not simply excite a localised perturbation close to the loop apex.

2.6.2 Wave Excitation

Due to the inclusion of the pressure enhancement, the initial conditions are no longer in equilibrium. Instead, a gas pressure force acts outwards from the centre of the high pressure region and causes a rapid expansion of the plasma. This induces a propagating fast magnetoacoustic wave (see Chapter 1), which we show in Figure 2.25. In the upper left-hand panel, we show the density (background colours) and velocity magnitude in a horizontal cut through the loop apex and maximum pressure enhancement. We see that, in this plane, the wave propagates isotropically. We also highlight the evacuation of plasma (at $x \approx -18$ Mm) caused by the large gas pressure forces.

In the right-hand panel of Figure 2.25, we show the plasma dynamics in the $z = 0$ Mm (vertical) plane and observe two distinct wave phenomena. Firstly, we see the fast wave (at $x \approx -6$ Mm) propagating towards the density structure. The velocity perturbation is primarily in the x direction. We see that in this plane, the fast wave does not propagate isotropically. We also identify loop-aligned flows originating from the pressure enhancement ($x \approx -18$ Mm). These are associated with a slow magnetoacoustic mode which travels along the direction of the magnetic field. However, this

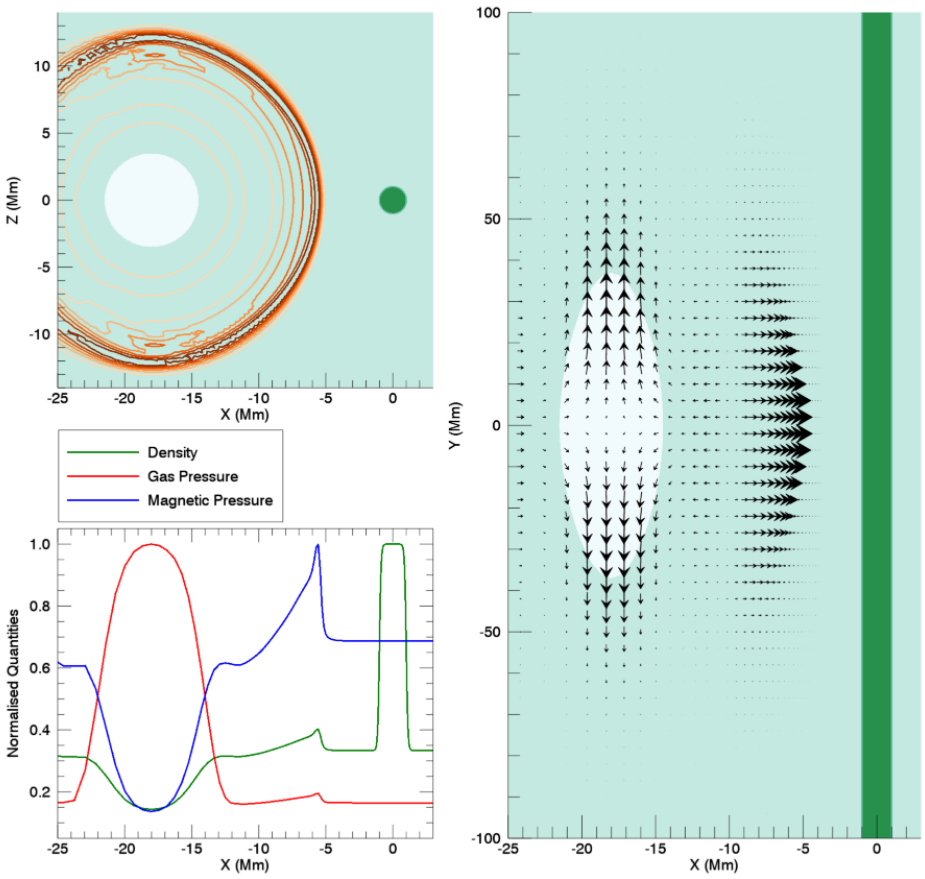

Figure 2.25: Propagating fast wave excited by the pressure enhancement. *Upper left*: Horizontal cut through the loop apex. Background colour shows the density profile and the line contours correspond to the magnitude of the horizontal velocity. *Right*: Vertical cut showing the density profile and velocity projected onto this plane (vectors). *Lower left*: Profile of the density (green) and the magnetic (blue) and gas (red) pressures along a horizontal line between the pressure enhancement and the loop. In each case we have normalised by the maximum value observed.

wave behaviour is not relevant to our present study of the dynamics of the flux tube and is not discussed further.

In the lower left-hand panel of Figure 2.25, we plot the density (green), gas pressure (red) and magnetic pressure (blue) in a line between the source of the blast wave and the loop apex. At $x = -18$ Mm, we can see that the force associated with the pressure enhancement has expelled both plasma and magnetic field. We can also identify the location of the blast wave by the magnetic and gas pressure enhancements at $x \approx -6$ Mm. We see that these are in phase and that the wave is compressible as the density also increases at this point.

Upon collision with the flux tube, the fast wave excites a transverse oscillation of

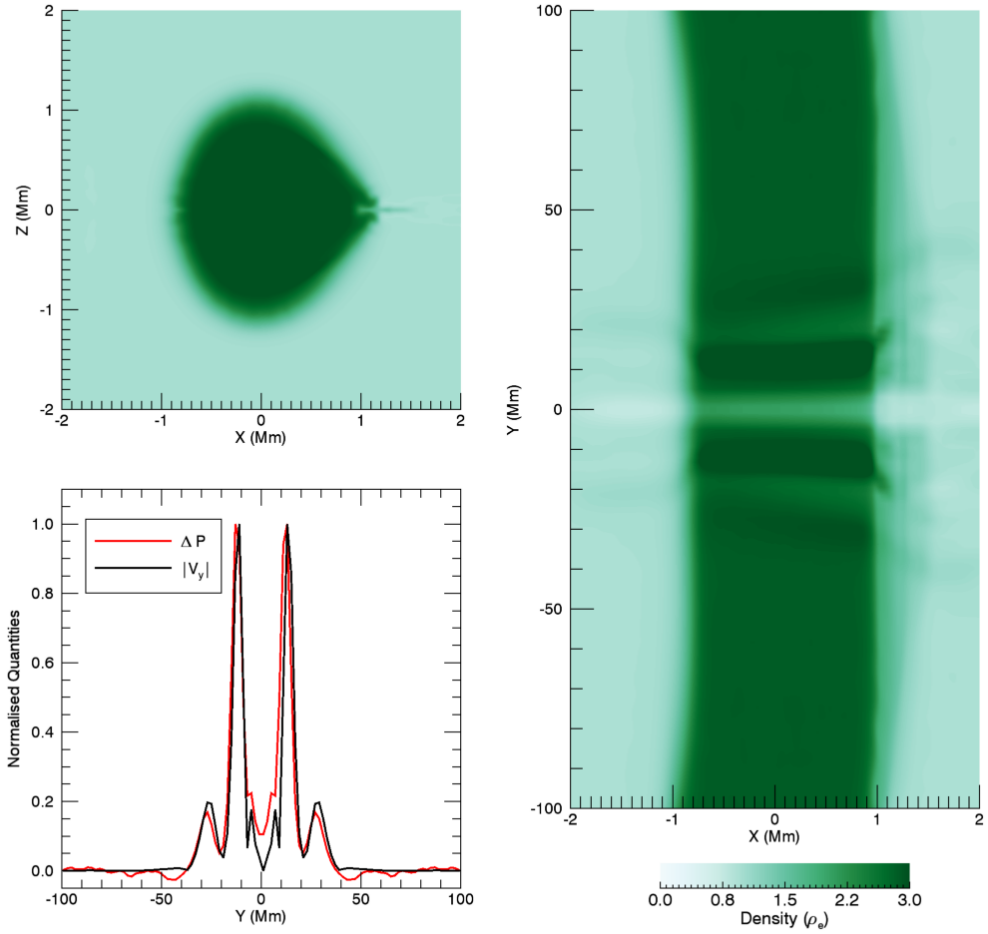

Figure 2.26: Waves excited by the propagating fast wave. *Upper left*: Density profile in the horizontal cross-section at the loop apex. *Right*: Vertical cut showing the kink mode and propagating slow mode. *Lower left*: Normalised pressure enhancement (compared to the initial conditions) and magnitude of the loop-aligned velocity along the length of the flux tube.

the loop structure and a standing kink mode is generated. Again, zero velocities are enforced at the loop foot points and thus we ensure that nodes are located at the upper and lower y boundaries. However, since the blast wave does not induce the exact form of the original velocity profile (see Figure 2.4), higher harmonics (in addition to the fundamental mode) are generated. Furthermore, a propagating slow magnetoacoustic wave is excited at the loop apex. This propagates from the loop apex towards both foot points of the flux tube.

In the right-hand panel of Figure 2.26, we can see the manifestation of this slow wave as a small enhancement in the plasma density (at $y \approx \pm 10$ Mm). This is also associated with the evacuation of plasma at the loop apex which is not normally observed in

models of standing kink waves. Indeed, typically the ponderomotive force will increase the plasma density at the loop apex. It remains unclear whether this phenomenon is representative of transverse waves generated by an external pulse. Alternatively, it may simply be a characteristic of the specific manner in which this blast wave interacted with the flux tube. In the lower left-hand panel, we show the pressure and loop-aligned velocity perturbations to confirm that these are in phase. We note that the generation of loop-aligned variation may result in the selected spatial resolution along the y axis becoming insufficient.

Returning to the right-hand panel of Figure 2.26, we can also see the excited transverse oscillation. The maximum displacement of the loop centre is small when compared to the radius of the flux tube. Despite this, in the top left-hand panel, we highlight that considerable compression of the flux tube cross-section is observed. We also note the excitation of additional, higher, harmonics due to the vertical form of the pressure enhancement. These have also been detected in observations of transverse oscillations in the corona (e.g. Verwichte et al., 2004; De Moortel and Brady, 2007; Duckenfield et al., 2018).

2.6.3 Resonant Absorption

The density profile of the flux tube is unchanged from the original model and, as such, we expect the conversion of kink mode energy into azimuthal Alfvén wave energy as a result of resonant absorption. In Figure 2.27, we show the transfer of kinetic wave energy from the core region to the boundary of the loop. This is plotted in the same manner as Figure 2.6. However, due to the large velocities observed at $t \approx 250$ s, in this case we plot $|v_\phi|$ instead of v_ϕ^2 .

We see that the energy conversion proceeds as before with wave energy quickly becoming concentrated in the shell region of the loop. However, we also notice that (compared to Figure 2.6) the wave fronts are not well defined, and the external plasma, in particular, is in turbulent motion. This behaviour is partly associated with the rapid formation of the Kelvin-Helmholtz instability (see below). Further, small amplitude propagating fast waves are continuously generated from the region containing the initial pressure enhancement. These are reflected by the flux tube boundary and contribute to the generation of turbulent-like flows in the external plasma.

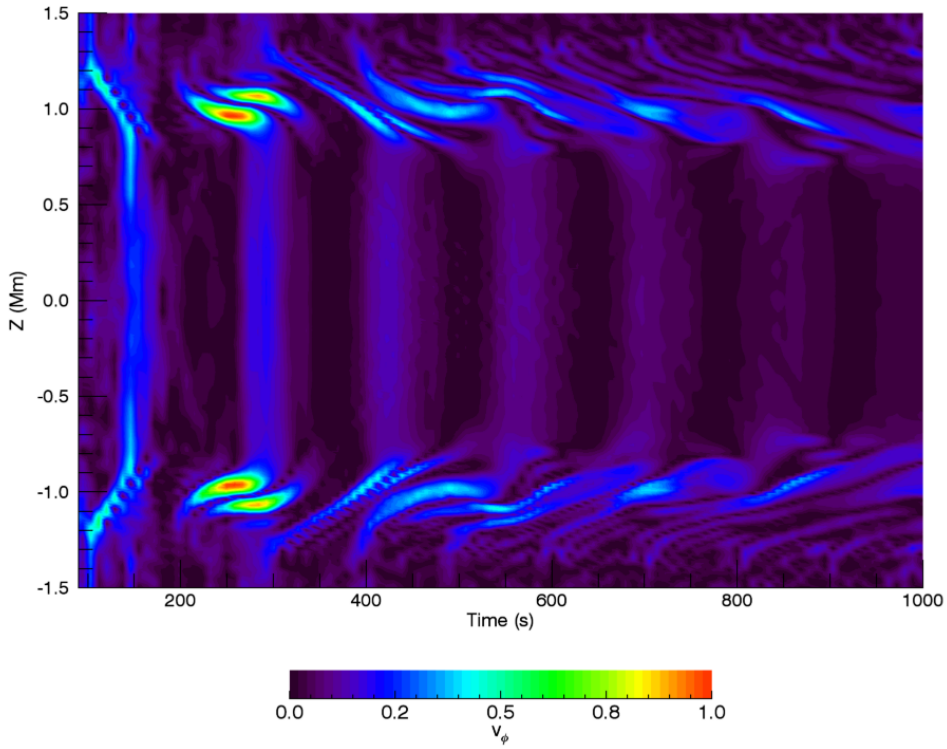

Figure 2.27: Transfer of wave energy during resonant absorption. Distribution of the azimuthal velocity, v_ϕ, along a diameter through the loop apex and as a function of time. We have normalised by the maximum of v_ϕ.

2.6.4 Development of the KHI

The existence of a significant external flow in this regime enhances the velocity shear across the loop boundary (Yu and Van Doorsselaere, 2016). As such, we see an earlier onset time ($t \approx 318$ s) for the development of the Kelvin-Helmholtz vortices than in the original (ideal) simulation ($t \approx 540$ s).

In Figure 2.28, we show the deformation in the density profile during the development of the KHI. We show a horizontal cut close to the loop apex but not exactly in the midplane due to the evacuation of the density at $y = 0$ Mm (see right-hand panel of Figure 2.26). We notice that the vortices develop sooner on the half of the loop that is closest to the origin of the blast wave. On this front edge, the flows in the adjacent plasma are large and thus a significant velocity shear is present, even at early times. The opposite side of the loop, however, is more sheltered and consequently, the radial velocity gradients are smaller. As such, the growth rate of the KHI is reduced.

We also note that in all of the panels in Figure 2.28, the compressibility of the excited wave mode is apparent and we can see that the density varies ($\sim 15\%$) much

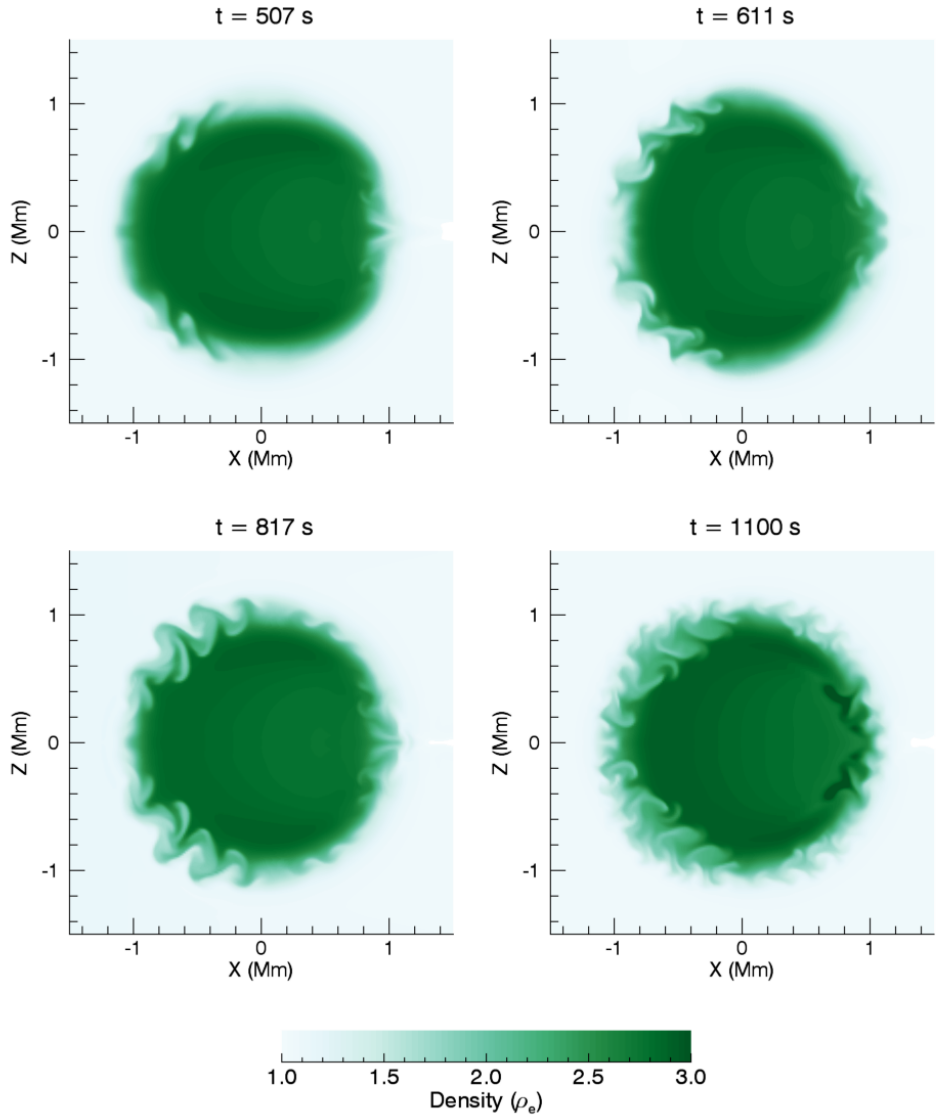

Figure 2.28: Density profile in a horizontal cross-section close to the loop apex is shown at four stages during the development of the KHI.

more within the core region than in the original simulations. The formation of this substructure within the flux tube will modify the conversion of energy between the transverse and azimuthal wave modes and may affect the damping rate of the kink oscillation. Further, the plasma compression, together with the density enhancement associated with the propagating slow mode, may have observational signatures that could be detected with high spatial resolution imaging instruments.

Finally, in Figure 2.29, we show the $\rho = 2\rho_e$ surface at two times during the formation of the instability. In the left-hand panel, we can see that the density deformation is limited to one half of the flux tube. However, at the later time presented in the right-hand panel, the vortices have formed around the full circumference of the struc-

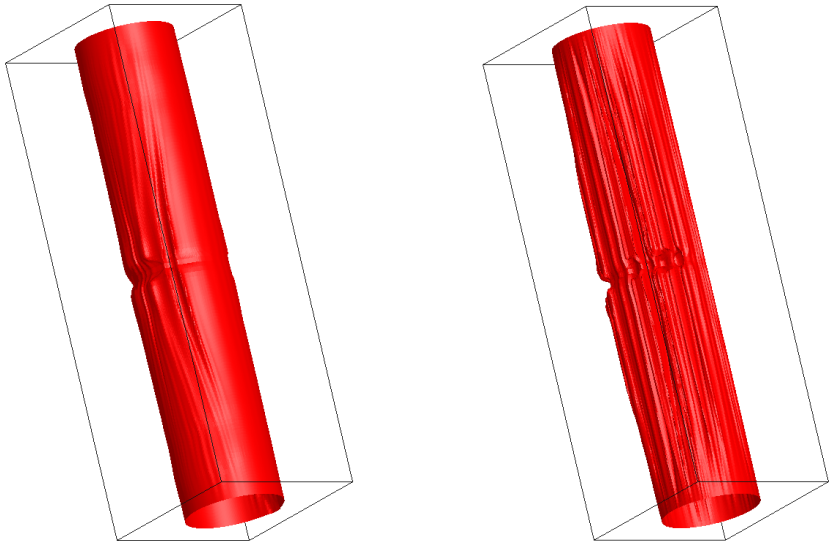

(a) $t = 550$ s. (b) $t = 1053$ s.

Figure 2.29: Deformation of the resonant layer ($\rho = 2\rho_e$) during the development of the Kelvin-Helmholtz instability.

ture.

Despite the formation of additional harmonics, we note that the Kelvin-Helmholtz vortices still form along the entire length of the magnetic flux tube, with the most signficant density deformation occurring close to the loop apex. In the midplane of the simulation, we can clearly see the evacuation of plasma at the location of greatest interaction between the pressure pulse and the coronal loop. This decrease in density might not be directly observable in the solar atmosphere due to resolution limitations and line-of-sight effects. However, we may expect to see a small decrease in the intensity at the location a blast wave first encounters (not necessarily the loop apex) a coronal density structure.

2.7 Discussion and conclusions

In this chapter we have described the self-consistent development of a dynamic instability from the decay of a standing kink mode in a coronal magnetic flux tube. We modelled a transversely oscillating, density-enhanced loop using a 3-D, resistive, MHD code and demonstrated the rapid transfer of energy from the global wave to localised Alfvén modes within the boundary of the flux tube. These Alfvén modes were observed to be associated with a radial velocity shear which, in a weakly non-ideal setting, was unstable to the Kelvin-Helmholtz instability. The KHI was observed to generate small scales in both the velocity and magnetic fields and enhance the rate of wave energy dis-

sipation. We conducted a parameter study to highlight the significance of dissipation coefficients on the stability of the system.

The role of resonant absorption in the decay of standing kink modes has been extensively studied by previous authors and the underlying process is well understood. In the analysis presented within this chapter, we were able to confirm that the energy transfer during the decay of the kink mode is essentially ideal and does not depend on the dissipation coefficients. The resulting azimuthal Alfvén waves exhibit much smaller length scales that are sensitive to both resistivity and viscosity. Through the process of phase mixing, both of these dissipative plasma properties act to remove energy from the Alfvén waves more efficiently than from the kink mode. Since the energy injected into the azimuthal waves is independent of transport coefficients, we see that these dissipative mechanisms reduce the amplitude of the Alfvén wave and hence restrict the magnitude of radial velocity shear. This, in turn, stabilises the system with respect to the KHI. Whilst both η and ν were observed to reduce the velocity gradients, viscosity has a greater effect on the suppression of the instability due to the direct forces exerted upon the characteristic Kelvin-Helmholtz vortices.

The development of the KHI causes the transfer of energy from shear, azimuthal waves in the boundary of the oscillating loop to vortical motions that deform the loop's density structure. By tracking the motion of high density plasma away from the loop's centre of mass, we were able to measure the instability onset time and the growth rate. Employing this method allowed the suppressive effects of η and ν to be quantified. Since the largest spatial velocity gradients occur at the loop apex, it is here that the greatest effects of viscosity are observed. Analogously, the effects of η are largest close to the loop foot points, corresponding to the locations of largest current density. Therefore, if coronal dissipation is dominated by one of these transport coefficients, we might expect to observe wave energy being dissipated non-uniformally along the loop (Karampelas et al., 2017). In addition, we may expect temporal variation in the heating rate as the gradients in the velocity and magnetic fields oscillate out of phase with each other.

Naturally, the formation of the Kelvin-Helmholtz vortices enhances the vorticity and the vortical flows stress the magnetic field. The instability is known to transfer energy from shear flows (associated with the azimuthal Alfvén waves) to compressive flows that enhance energy release through the generation of current sheets and encouraging magnetic reconnection (Lapenta and Knoll 2003; Figure 2 in Antolin et al. 2014). We highlight that studies on magnetic reconnection triggered by the KHI can be found in Nykyri and Otto (2001, 2004). Since the velocity and magnetic field gradients are subject to dissipation by viscosity and resistivity, respectively, the formation of the

instability is associated with an increase in the thermal energy of the plasma. Indeed, we have shown that the onset of heating can occur earlier for lower values of η and ν due to the earlier formation of the instability. Further, if the dissipation is sufficiently low that the energy cascade reaches the grid scale, then enhancing the numerical resolution will produce an increased heating rate.

A cautionary note must be provided when considering the heating rate within these simulations. In particular, since the size of the initial perturbation is small (and only occurs once), the magnitude of irreversible plasma heating is also small. Indeed, the Ohmic/viscous heating observed is much less than the increase in temperature within the loop caused by the inflow of hot plasma from the surroundings during the formation of the KHI. This effect is examined in detail in Magyar and Van Doorsselaere (2016). Having said this, in a constantly driven system it is likely that more energy would be available for heating and the KHI would still be able to form. A more detailed analysis of the actual energy dissipation associated with continuously driven (propagating) kink modes in an inhomogeneous flux tube can be found in Pagano and De Moortel (2017). Further, in this work, the authors are able to compare the obtained wave heating with estimated coronal radiative losses.

Although the effective values of resistivity and viscosity within the corona are not well constrained, they are estimated to be many orders of magnitude below the levels of η and ν that we have found to suppress the formation of the KHI. Hence, we might expect the instability to form very rapidly in a similar flux tube within the coronal volume. Although the levels of dissipation within the corona are currently unobtainable in 3D numerical MHD simulations, these results may be directly applicable to regions of the Sun's atmosphere with reduced Reynold's numbers. In particular, our findings may be pertinent for oscillations with chromospheric structures or within prominences. In these locations, the typical temperatures are much lower and so particle species are often only partially ionised. The presence of neutral atoms within the fluid will modify the dissipation terms and enhance the effective dissipation rates. We direct the reader to Forteza et al. (2007); Soler et al. (2009, 2015); Khomenko and Collados (2012) for a more detailed discussion on the effects of partial ionisation on chromospheric/prominence heating.

The work presented within this chapter highlights that artificially high dissipation, such as the values necessarily used within 3D numerical MHD models, can have significant effects on plasma dynamics as well as estimated heating rates. Since, the spatial resolution required to accurately model coronal dissipation is prohibitively expensive, non-ideal models typically implement artificially large dissipation to prevent

the formation of unresolved small scales. This technique allows energy dissipation to be accounted for despite coarse spatial resolution. However, as we have shown, this does not just affect the estimated heating rate. In particular, plasma dynamics can be significantly affected, e.g. by the suppression of instabilities, which can impede investigations into the suitability of a heating model. In our model, the modified method of implementing a large, localised resistivity demonstrates that the Ohmic heating rate associated with the KHI may be more significant than that associated with phase mixing in an instability-suppressed regime. Unfortunately, the inability to accurately track the formation of small scales during the development of the instability has ramifications for investigating the KHI, and indeed other drivers of MHD turbulence, as coronal heating mechanisms. At best, we can hope to infer a plasma heating rate by the extrapolation of results from a spatially resolved regime, however the reliability of this method remains unclear.

Many previous authors (e.g. Aschwanden et al., 1999; Goddard et al., 2016; Pascoe et al., 2016a) have recorded observations of transversely oscillating coronal loops that, according to our model, should become unstable to the KHI. Indeed, when the model was modified to take into account a more realistic wave excitation mechanism, the instability was still generated. Despite this, there has been a lack of direct evidence of the formation (in this manner) of the KHI within the solar corona. It may be the case that this is because the observational signatures of the KHI are beyond the current capabilities of coronal imagers. However, the results of forward modelling of a similar model by Antolin et al. (2016), suggest that observations of decayless oscillations (Anfinogentov et al., 2013, 2015) may be evidence of the spatially unresolved Kelvin-Helmholtz instability.

An alternative, perhaps simpler, explanation for the lack of evidence of the instability is that coronal loop conditions are not consistent with our model and the evolution of the KHI may be suppressed in this regime. One possibility is that the magnetic field is not perfectly loop-aligned, but is instead twisted; it has a (possibly small) azimuthal component. As we shall see in the following chapter, twist within the magnetic field can restrict the formation of the KHI and even a relatively small B_ϕ can reduce the size of vortices and ensure the instability is even more difficult to observe. Until our knowledge of the form and structure of coronal loops improves, it is difficult to determine the suitability of our model for understanding wave behaviour within the Sun's atmosphere. Hopefully, the advent of new solar telescopes (e.g. DKIST and EST) within the next few years will allow solar physicists to improve constraints on coronal conditions and determine whether the KHI is truly a viable mechanism for enhancing

wave energy dissipation.

Chapter 3

The Kelvin-Helmholtz Instability Induced by Transverse Waves in Twisted Coronal Loops

3.1 Introduction

Within this chapter, we modify the model presented previously to consider the effects of weakly twisted magnetic field on the development of the magnetic Kelvin-Helmholtz instability. As in the previous chapter, we model the decay of a transversely oscillating coronal loop using the Lare3d code and we will investigate the development of small scales in the velocity and magnetic fields following the onset of the KHI. Whilst the process of resonant absorption and the growth of the azimuthal Alfvén mode is only weakly modified by the inclusion of helical field, we shall show that the formation of Kelvin-Helmholtz vortices is sensitive to the magnitude of B_ϕ. Despite this, significant currents and vorticities are still able to form in numerical simulations in which the density deformation is reduced.

Many wave heating models suffer from an inability to dissipate energy at a sufficiently high rate, particularly if the high Reynolds and Lundquist numbers expected in the corona are considered. As such, the suitability of these models remains contentious (e.g. Arregui, 2015; Cargill et al., 2016). Despite this, in the previous chapter, we argued that the rate of wave heating within the corona may be enhanced by the formation of the KHI. Indeed, the potential for waves to drive turbulent flows is interesting in the context of heating the corona (for example, van Ballegooijen et al., 2011; Woolsey and Cranmer, 2015). As wave power seems to be abundant in the solar

atmosphere (for example Aschwanden et al., 1999; Okamoto et al., 2007; Parnell and De Moortel, 2012), the development of the instability remains a plausible mechanism for dissipating this energy and heating the coronal volume.

Unfortunately, despite the aid of the improved spatial and temporal resolution provided by contemporary observing instruments, direct evidence of transverse wave-driven dynamic instabilities remains elusive. Furthermore, even the azimuthal Alfvén waves which may trigger the instability are difficult to detect due to their weak compressibility. Whilst this may be a result of telescope limitations (Antolin et al., 2017, claim that some signatures of the instability are observable given current constraints), it may also be the case that the instability does not form as readily as is suggested by the results presented within the previous chapter. In particular, analytic investigations of the stability of similar models have concluded that magnetic twist can stabilise the system (Soler et al., 2010) and, as such, prevent the formation of Kelvin-Helmholtz vortices.

The presence of twist within the Sun's magnetic field has been reported throughout the solar atmosphere such as in prominences (and their subsequent eruption e.g. Rust and Kumar, 1996) and in active regions (e.g. Démoulin et al., 2002; Guo et al., 2013), or predicted through numerical simulations of photospheric motions (e.g. Török and Kliem, 2003) and flux emergence (e.g. Magara and Longcope, 2003; Fan, 2009). Indeed, it is widely expected that shear flows at the photosphere will introduce magnetic twist into the corona and many studies have considered how the release of energy in these stressed, non-potential fields can contribute to heating the corona (e.g. Wilmot-Smith et al., 2011; Bareford et al., 2013; O'Hara and De Moortel, 2016). If coronal loops typically contain helical field, then investigations into the effects of magnetic twist on the decay of kink mode oscillations are important.

Several studies have demonstrated that the process of resonant absorption continues to occur in a variety of coronal loop configurations. For example, Van Doorsselaere et al. (2004); Terradas et al. (2006) find that the energy transfer is robust in the context of curved loops and Ruderman (2003) considers the mode conversion in the case of loops with elliptical cross-sections. Furthermore, studies considering more general loop shapes (Pascoe et al., 2011) and multi-stranded sub-structuring within the loop (Terradas et al., 2008b) confirm that resonant absorption is able to progress in these conditions. Additionally, studies find that gravitational stratification along the length of the loop (Andries et al., 2005; Soler et al., 2011) does not inhibit the conversion of kink mode energy into azimuthal motions on resonant field lines. Finally, and importantly in the context of this thesis, the presence of magnetic twist (Karami and

Barin, 2009; Ebrahimi and Karami, 2016) does not prevent the transfer of energy to azimuthal Alfvén modes. The interested reader will be able to find a more thorough exploration of resonant absorption and mode coupling in a diverse range of geometries in reviews presented by Ruderman and Erdélyi (2009) and Goossens and Ruderman (2011).

One important effect of the inclusion of magnetic twist within a coronal flux tube can be seen by considering the natural Alfvén frequencies of field lines within the loop structure. In the straight field case, the length of each field line and hence the loop aligned wave number of a fundamental standing mode is simply determined by the length of the flux tube. However, in the case of twisted field, increasing the azimuthal component, B_ϕ, will increase the length of magnetic field lines and hence modify the natural Alfvén frequencies present within the flux tube.

To illustrate this point, we consider a magnetic field within some cylinder of length L and radius a expressed in cylindrical co-ordinates as

$$\mathbf{B}\left(R\right) = \left(0, \psi R, \sqrt{B_0^2 - \psi^2 R^2}\right), \tag{3.1}$$

where ψ and B_0 are constants with $B_0^2 > \psi^2 a^2$. We immediately see that the field is divergence free and has a constant field strength, B_0. In the case $\psi = 0$, this reduces to the straight field case and the length of each field line within the flux tube is simply L. However, if $0 < \psi^2 a^2 \ll B_0^2$, we are in a weakly twisted regime (the vertical component, B_z is much larger than the non-zero, azimuthal component B_ϕ) and the field lines are no longer constant in length. Instead, the length of each field line, $\Lambda\left(R\right)$, is given by

$$\Lambda\left(R\right) = \sqrt{L^2\left(1 + \frac{B_\phi^2}{B_z^2}\right)} = \frac{LB_0}{\sqrt{B_0^2 - \psi^2 R^2}}. \tag{3.2}$$

Clearly, the central field line has length L, however field lines increase in length away from the loop centre. Therefore, the inclusion of magnetic twist can modify the location of resonant field lines within a flux tube. However, provided the density and magnetic field remain continuous, then a resonance will still exist and allow the transfer of energy between the kink and Alfvén wave modes.

Within the remainder of this chapter, we aim to quantify the effect of magnetic twist on the non-linear evolution of kink modes by conducting a parameter study on the size of B_ϕ.

3.2 Initial configuration

As in the previous chapter, we model a coronal loop as a straight flux tube that is denser than the surrounding plasma. We retain the same loop length ($L = 200$ Mm), density profile (Figure 3.1 shows this as a function of R), and labels for different regions of the cross-section (core, shell, external; see Figure 2.1). As previously, all variables are independent of height and we implement the same axis orientation as in the preceeding chapter (y-axis is loop aligned).

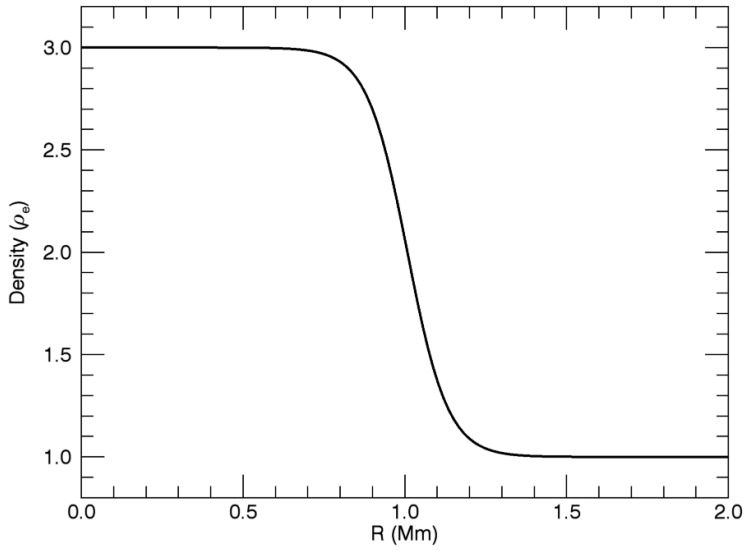

Figure 3.1: Initial density profile for all cases. We display a radial cut through the cross-section of the loop. Here, we have normalised the density profile with the initial external density, $\rho_e = 8.4 \times 10^{-13}$ kg m^{-3}.

Three different cases were considered for the nature of the magnetic field. In the following we describe these three cases using cylindrical co-ordinates with the origin located at the centre of the loop apex.

- *Case 1: Straight field* - We include a uniform magnetic field of strength 21 G aligned with the loop axis (y direction). This is identical to the model described in the previous chapter. As before, in order to implement an initial equilibrium, we ensure that the gradient in the total pressure is zero by defining the temperature as

$$T = \frac{P_0}{\rho}, \tag{3.3}$$

where P_0 was set to ensure the plasma-$\beta = 0.05$ throughout the numerical domain.

- *Case 2: Twisted field; $|B_\phi|$ largest at the boundary between the core and the shell regions* - Once again, we include a magnetic field of strength 21 G throughout the domain. However, in this case the field is not aligned with the y-axis everywhere. Instead, a radially-dependent azimuthal component of the field is included and is defined as

$$B_\phi(R) = \begin{cases} \tau R, & \text{if } R \leq a, \\ \tau(b - R), & \text{if } a < R \leq b, \\ 0, & \text{if } R > b. \end{cases} \tag{3.4}$$

Here, τ is a parameter that quantifies the magnetic twist, a is the radius of the core region and b is the radius of the loop (including the boundary region). We immediately note that in the case, $\tau = 0$, the first (straight field) case is recovered. Further, the azimuthal field is continuous for all R. Three levels of twist are considered; $\tau = \{0.1, 1.0, 2.0\}$ and are labelled as case 2a, 2b and 2c, respectively. The amount of magnetic twist that these values correspond to is presented in Table 3.1.

In order to maintain a constant field strength of 21 G, the loop aligned component of the magnetic field must also be a function of R. As with the field defined in the introduction of this chapter (equation 3.1), we set

$$B_y^2(R) = B_0^2 - B_\phi^2(R), \tag{3.5}$$

where $B_0 = 21$ G. We note that in the external plasma ($R > b$), the field is completely straight ($B_\phi = 0$). Since the magnetic pressure is uniform throughout the domain, in this geometry, the only non-zero component of $\mathbf{j} \times \mathbf{B}$ is the radially inwards component of the tension force, T_R. This is given by

$$T_R = \frac{B_\phi^2}{R}. \tag{3.6}$$

Therefore, in order to balance this tension force, we define the gas pressure, P, as

$$P = \int \frac{B_\phi^2}{R} \, \mathrm{d}R, \tag{3.7}$$

and the constant of integration is selected to ensure the plasma-$\beta = 0.05$. With

Table 3.1: Magnetic twist parameter space. The angle is the largest any field line moves through between the lower and upper boundaries of the domain. Further, the distance $L_{\max}$ is the length of the longest field line and $L_0 = 200$ Mm.

Case	Field	Angle (°)	$L_{\max} - L_0$ (km)
1	Straight	0	0.0
2a	$\tau = 0.1$	0.39	0.8
2b	$\tau = 1.0$	39	81.7
2c	$\tau = 2.0$	78	327.3
3	$\psi = 1.0$	78	327.3

the gas pressure in this form, we see that there are no net forces in the equation of motion. We can then use the ideal gas law to find the required form of the temperature.

- *Case 3: Twisted field; $|B_\phi|$ largest at the boundary between the shell region and the external plasma* - As with the previous two cases, we include a magnetic field of strength 21 G throughout the domain. In a similar manner to case 2, we introduce a radially-dependent azimuthal component of the magnetic field defined as

$$B_\phi(R) = \begin{cases} \psi R, & \text{if } R \leq b, \\ \psi(2b - R), & \text{if } a < R \leq 2b, \\ 0, & \text{if } R > 2b. \end{cases} \tag{3.8}$$

Again b is the radius of the loop (including the boundary region) and ψ is a parameter that quantifies the amount of magnetic twist. In this case, the magnetic twist extends into a region beyond the density-enhancement of the loop. We include this case in order to determine whether the location of twisted field within a loop affects the development of the KHI and the subsequent formation of small scales. Once again, we note that the profile is continuous for all values of R and we see that if $\psi = 0$, this regime reduces to the straight field case. For the purpose of this parameter study, we only consider the case of $\psi = 1.0$. The corresponding level of twist is included in Table 3.1.

As with the case 2 experiments, the loop-aligned field profile is prescribed by equation 3.5 and, in order to maintain an initial equilibrium, the gas pressure is defined using equation 3.7.

In each of the cases outlined above, we have $B_R = 0$ everywhere and azimuthal and loop-aligned invariance. Hence, we can immediately see that $\nabla \cdot \mathbf{B} = 0$ is satisfied. We

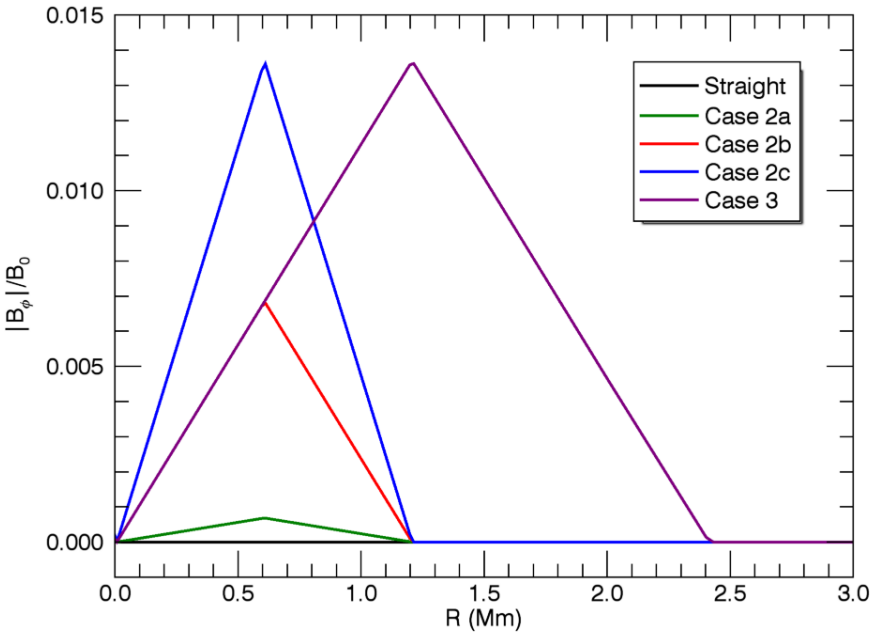

Figure 3.2: Magnitude of initial azimuthal magnetic field, $|B_\phi|$, through the cross-section of the loop for each case. Here, B_ϕ is normalised to $B_0 = 21$ G. We see that in all cases, $|B_\phi| \ll |B_0|$.

also note that, although the total magnetic energy within the domain is identical in each simulation, case 1 represents a potential field, whilst all other cases do not. Since the potential field is the lowest energy state for some prescribed boundary conditions, no magnetic energy can be extracted from the initial field configuration in case 1. For all remaining cases, however, the presence of currents implies that the field is non-potential and, consequently, some free magnetic energy may be extracted. This can be achieved, for example, by implementing a large resistivity throughout the domain. However, additional topological constraints may prevent the potential magnetic field being obtained on the dynamical time scale and thus limit the accessible energy (e.g. Yeates et al., 2010). We shall consider the consequences of this free magnetic energy later within this chapter.

We are able to quantify the magnetic twist within the flux tube in each simulation by calculating the largest angle that any field line moves through between the lower and upper boundaries of the domain. The cases considered are displayed in Table 3.1. For reference, we also include the length of the longest field line, calculated using equation 3.2. Since $B_y \gg B_\phi$, we see that the length of field lines does not vary significantly between each simulation.

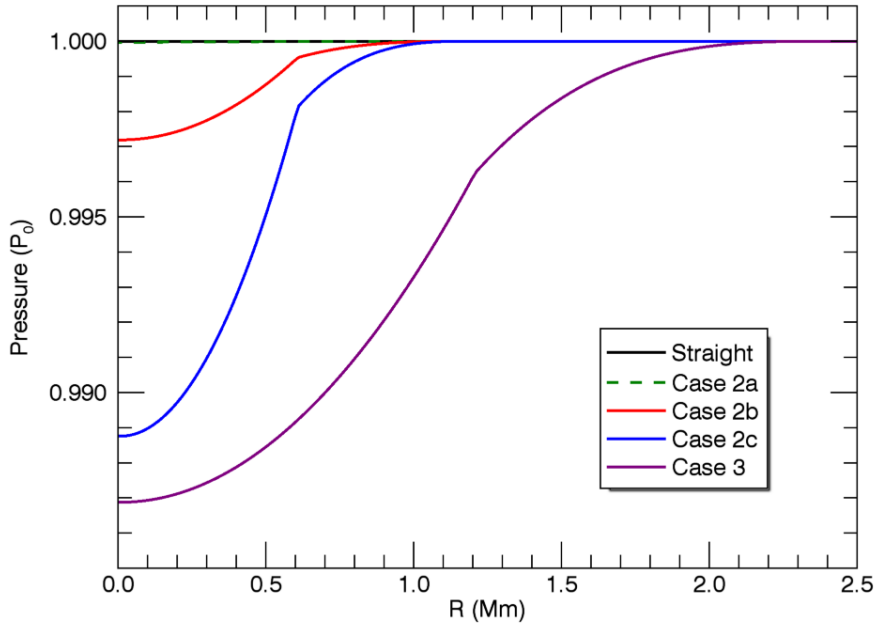

Figure 3.3: Initial gas pressure profile through the cross-section of the loop for each case. Here, we have normalised the pressure to the external pressure, P_0.

In Figures 3.2 and 3.3, we display the initial radial profiles of the azimuthal field strength and the gas pressure, respectively. We see that even in the numerical experiments with the most significant azimuthal field, $|B_\phi|$ is much smaller than the loop-aligned field strength, $|B_y|$. Since the magnetic twist is weak in all cases, the corresponding radially inward tension force, T_R (see equation 3.6), is very small. Consequently, the gas pressure does not have to decrease significantly in order to support an equilibrium. In particular, throughout the initial conditions in each simulation, it remains above 98% of the maximum (external) pressure. As such, we are able to maintain a temperature profile that, in all cases, is nearly identical to the form implemented within the previous chapter (see Figure 2.2b).

As previously, we excite a fundamental, standing, kink mode using the velocity profile described in equation 2.3 and displayed in Figure 2.4. We recall that the maximum velocity of 8.3 km s $^{-1}$ is introduced at the loop apex ($y = 0$ Mm). Once again we note that this is a relatively low amplitude kink mode and is commonly observed within the solar corona (e.g. Anfinogentov et al., 2015).

For the simulations presented here, the evolution of the plasma is again tracked with the Lare3d code and we use the non-uniform grid described in the previous chapter. We implement the same boundary conditions as before and we note that since the

azimuthal field is weak in all of our simulations, this is sufficient to ensure a standing mode is generated. However, if cases with more significant twist were to be considered, it may become necessary to use line-tying boundary conditions.

For our initial study, we mimic the essentially ideal simulations presented in Chapter 2 by using values of resistivity, $\eta = 10^{-20}$, and viscosity, $\nu = 10^{-20}$. These coefficients remain significantly smaller than the estimated numerical values which we recall are of the order $10^{-5} - 10^{-6}$. In the final part of this chapter, we consider the effects of including larger values of η, however, this is described in more detail later.

3.3 Resonant Absorption

In all of the simulations, we induce a fundamental, standing kink mode that has a very similar form to the wave described in the previous chapter. For all twisted field cases, the period of the wave (approximately 280 s) and the maximum displacement of the loop (approximately 0.27 Mm) remain unchanged from the straight field case. In Figure 3.4, we track the displacement of the centre of the loop (at the apex) as a function of time for both the straight field case 1 (solid black line) and the twisted field case 2b (dashed black line). We have also included an estimate of the damping rate (red envelopes) which, as expected, follows a Gaussian profile (Ruderman and Terradas, 2013; Pascoe et al., 2013). We observe that, at least in the weakly twisted regime, the damping rate is largely independent of the magnitude of the azimuthal field present.

Since we have maintained the same field strength (21 G) and density profile as the model presented in Chapter 2, the radial Alfvén speed profile is identical in all of the cases considered within this parameter study. However, since the magnetic field lines are no longer uniform in length, the natural Alfvén frequencies are modified within each simulation. Thus, the location of the resonant field lines is (slightly) displaced in the twisted field simulations. However, we cannot expect to be able to detect this effect within our numerical results as a quick calculation shows that, even in the most twisted cases, the expected shift is smaller than the grid resolution. Regardless, the existence of a resonance is sufficient for the purposes of this study (Terradas et al., 2008b; Pascoe et al., 2011) as we simply require the formation of azimuthal Alfvén waves to determine whether the magnetic Kelvin-Helmholtz instability develops.

To confirm that the transfer of wave energy from the kink mode to the Alfvén mode proceeds as expected, in Figure 3.5 we plot the square of the azimuthal velocity along a diameter through the loop centre for case 2c. This corresponds to Figure 2.6 which was

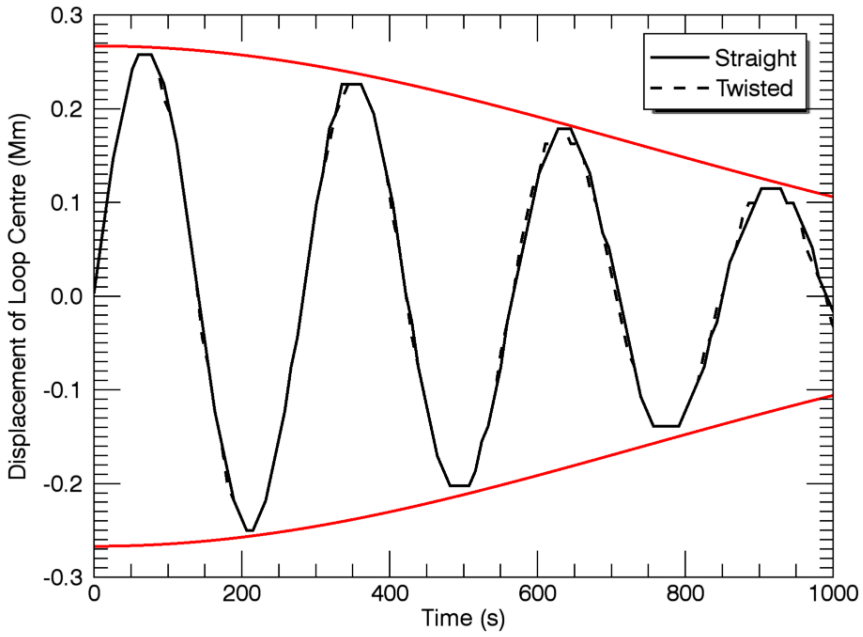

Figure 3.4: Displacement of the loop apex during the simulation for the straight case and a twisted case (case 2b). The red lines are given by $y = \pm 0.267 e^{-\left(\frac{t}{1040}\right)^2}$.

produced using a straight field case. Despite the inclusion of magnetic twist we note that the energy transfer from the core region to the shell region is largely unchanged. We observe that the disruption of the periodic behaviour beyond $t = 650$ s corresponds to the formation of the KHI. This phenomenon is not observed in Figure 2.6 as this figure was produced with results from a non-ideal simulation in which the instability was suppressed.

Although the damping of the kink mode still progresses in the presence of weak magnetic twist, the azimuthal component of the velocity is no longer perpendicular to the magnetic field lines. Therefore, the pure Alfvén mode for field lines in the shell region of the loop is no longer generated by a velocity perturbation in (purely) the $\mathbf{e}_\phi$ direction. In particular, as we described in Chapter 1, we require $\mathbf{B}_0 \cdot \mathbf{v}_1 = 0$; the background field and the velocity perturbation are perpendicular. Hence, a perturbation that is constrained within a horizontal plane (no v_y component) will excite additional wave modes within the flux tube.

In order to detect this effect, in Figure 3.6, we plot the azimuthal velocity as a function of time (x-axis) and of position along the loop (y-axis). In particular, we show the evolution of v_ϕ along the line

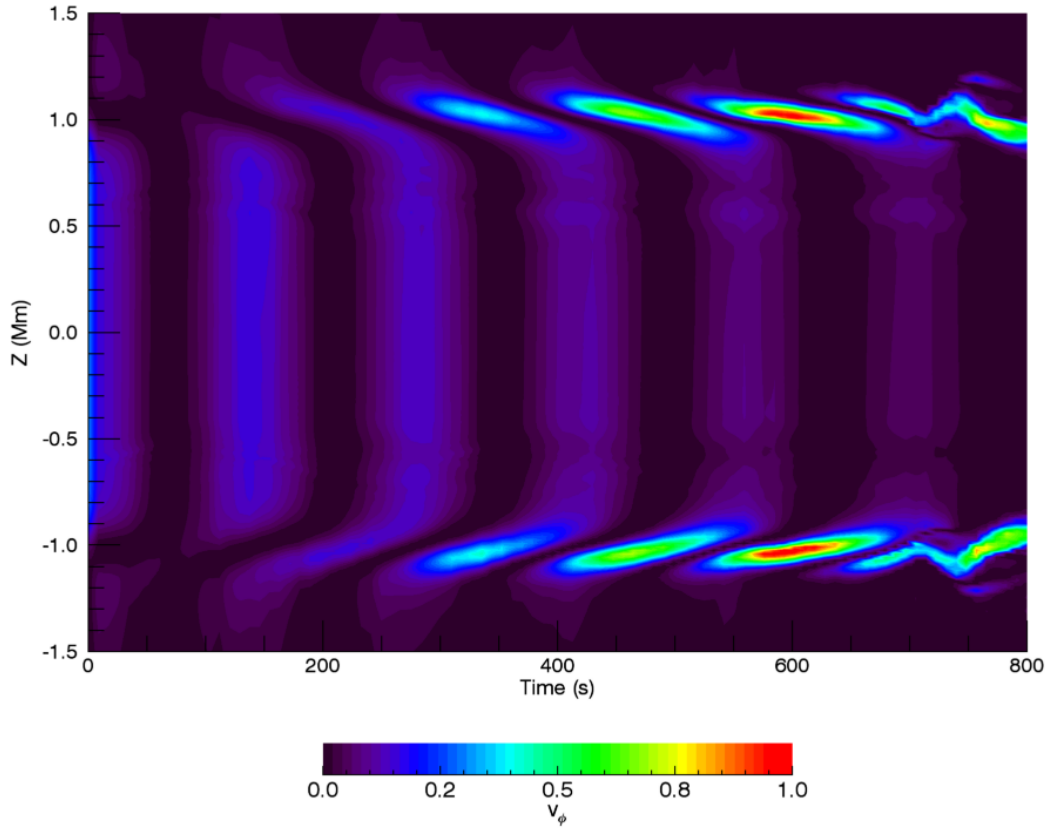

Figure 3.5: Evolution of the square of the azimuthal velocity along the line $y = 0$ (through the loop apex), $z = 0$. Here v_ϕ^2 is normalised to the maximum value obtained during the simulation. The figure is produced from case 2c, a twisted field simulation.

$$x = c_x(y, t),$$

$$z = c_z - \zeta,$$

where $c_x(y, t)$ and c_z are the x and z coordinates of the loop centre, respectively and $\zeta = 1$ Mm. At all heights, this tracks the global kink mode and is always contained within the shell region of the loop. Indeed, it aims to track a resonant field line in the straight field case. Further, in order to allow comparison across the length of the flux tube, at each height, we normalise the observed azimuthal velocity by the maximum of the initial velocity perturbation at the corresponding height. We generate this plot for both the straight field case 1 (upper panel), and for the twisted field case 2c (lower panel).

In both panels we are able to observe an oscillatory pattern in the azimuthal velocity which corresponds to the periodic reversal of the Alfvén waves. As we track resonant

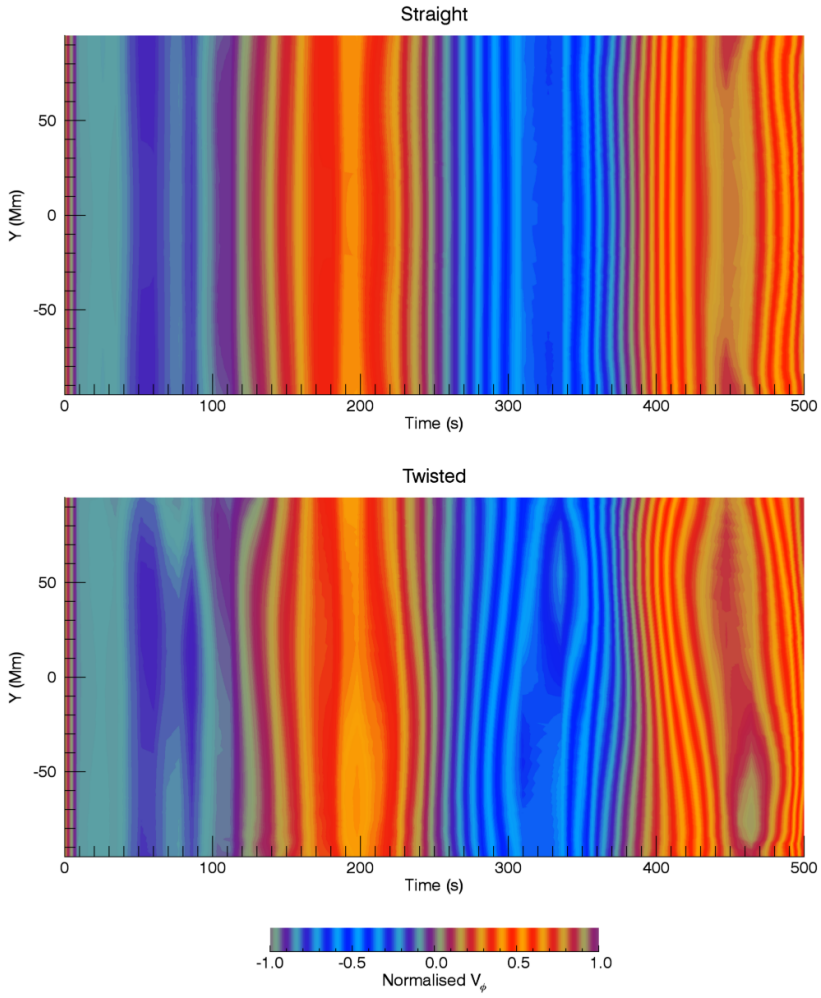

Figure 3.6: Time evolution of the azimuthal component of the velocity v_ϕ, along a line parallel to the loop axis and within the shell region. The azimuthal velocity is normalised to the maximum initial velocity perturbation at that particular height. The upper panel shows the simulation with a straight magnetic field (case 1) and the lower panel shows case 2c.

field lines, we can see that the period of these waves match the period of the kink mode (≈ 280 s). For the purpose of our analysis, we have selected a colour bar that optimises the detection of small variations but masks larger scale changes. Despite this, careful scrutiny of the colour table reveals a gradual increase of the amplitude of the azimuthal flows in both cases. This is indicative of the increase in the power of the Alfvén mode as resonant absorption progresses. We note that we do not observe any effects of the Kelvin-Helmholtz vortices as the figure does not consider times beyond the onset of the instability.

A more interesting feature can be observed by considering the vertical structuring of the oscillations in both cases. For the upper panel (straight field), the Alfvén wave

has approximately the same structure at all heights. This is confirmed by the height-normalised azimuthal velocity being similar along the length of the flux tube. In other words, once the magnitude of the initial perturbation is accounted for, the amount of energy injected into the Alfvén mode is roughly constant at all heights. In the lower panel (twisted field), however, we observe that the azimuthal Alfvén wave does not demonstrate the same vertical invariance. As we discussed above, the presence of twisted magnetic field excites additional wave modes as the velocity perturbation is not perpendicular to the background field. Indeed, the magnetic twist within the flux tube will enhance the non-linearity of the system and is known to generate fluting modes (Terradas et al., 2018). Although the vertical uniformity is violated in the lower panel, some symmetry can still be observed within the loop. In particular, if Figure 3.6 is reproduced for the line $x = c_x, z = c_z + \zeta$, then we will recreate the lower panel of the figure albeit with a reflection in $y = 0$ and a change of sign for v_ϕ.

Notwithstanding the formation of helical fluting modes, the nature of the observed Alfvén waves is modified by the inclusion of magnetic twist. We can see this by considering a field line oscillating with a fundamental, standing Alfvén mode. In case 1, this field line is parallel to the central axis of the flux tube. In all other cases, this is no longer true and instead, the field line's azimuthal location changes with height. Therefore, a wave on a single field line that is observed at a particular value of ϕ at the loop apex, will not be observed at the same value of ϕ close to the loop foot points.

In Figure 3.7, we highlight this behaviour by displaying the amplitude of the Alfvén wave on the $\rho = 2\rho_e$ surface for two twisted field cases. In the left-hand panel, the magnetic field is very weakly twisted, and indeed we see that the structure of the kinetic wave energy appears to be aligned with the longitudinal direction. However, in case 2c, the magnetic field is more significantly twisted and we are able to detect the helical form of the standing Alfvén wave.

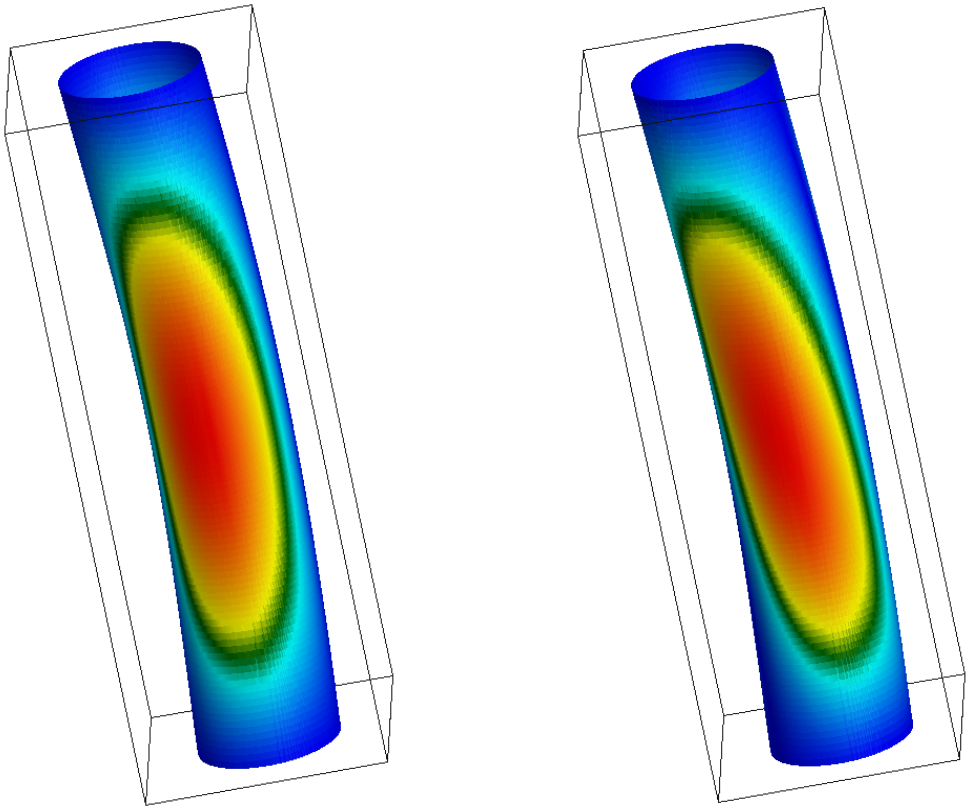

(a) Case 2a. (b) Case 2c.

Figure 3.7: Azimuthal velocity profile on the surface defined by $\rho = 2\rho_e$. The figures are generated using a time at which significant energy has been transferred to the Alfvén wave mode.

3.4 Development of the KHI

The helical nature of field lines in the simulated flux tubes will modify the development of the Kelvin-Helmholtz instability. We can easily understand an important effect of twisted field by considering Figure 3.8. We display two density contours from the straight field case at a time when the initial vortices associated with the instability have formed. Although the density profiles in the two panels appear identical, the horizontal planes are separated by 10 Mm along the height of the loop. This highlights the similarity of the KHI along the y-axis in case 1. In Figure 3.8, the red dots represent the location of a bundle of field lines in a flux tube with helical magnetic field. We see that the field lines are at a different position within the cross-section at the $y = 0$ Mm (left-hand panel) than at $y = 10$ Mm (right-hand panel). Consequently, if the KHI developed in the same manner in the twisted field simulation then these field lines would experience the instability differently at each height. In particular, they lie within

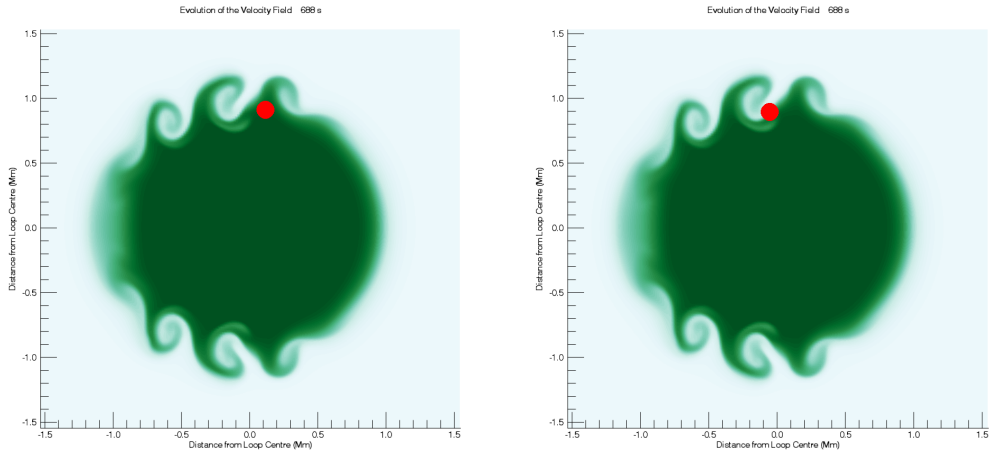

(a) $y = 0$ Mm. (b) $y = 10$ Mm.

Figure 3.8: Schematic demonstrating the effect of twisted field on the evolution of the magnetic Kelvin-Helmholtz instability. The red circles represent the location of a bundle of helical magnetic field lines within the two horizontal cross-sections.

a vortex at the loop apex but not at $y = 10$ Mm. This would cause significant bending of the magnetic field line and lead to a large magnetic tension force which would act to ensure vortices form along field lines instead. In this way, the magnetic tension force will modify vortex formation and, as we shall see, can suppress the development of the characteristic vortices.

In Figure 3.9 we show the density profile in the horizontal cross-section at the loop apex for different stages during the development of the KHI. With the exception of case 2c, in all of the simulations, we first observe the deformation of the density profile at around $t = 600$ s ($t \approx 680$ s for case 2c). The presence of weakly helical field does not change the number of vortices that first form. As in the previous chapter, we observe that the same azimuthal mode has the fastest growth rate. Subsequently, smaller scale, higher wave number vortices develop as the instability progresses and ultimately, a turbulent-like regime is generated. We note that prior to the onset of the KHI, the twisted field cases do not display major differences to the straight case. In particular, these differences would be extremely difficult to detect observationally. However, once the instability begins to form, the azimuthal field component begins to have a profound effect on the dynamic evolution of the loop.

The particularly weak twisted field explored in case 2a, generates almost identical plasma behaviour to that of case 1. This can be expected since $\frac{|B_\phi|}{|B_y|} \leq 10^{-3}$ throughout the computational domain. Beyond this limiting case, increasing the magnitude of B_ϕ

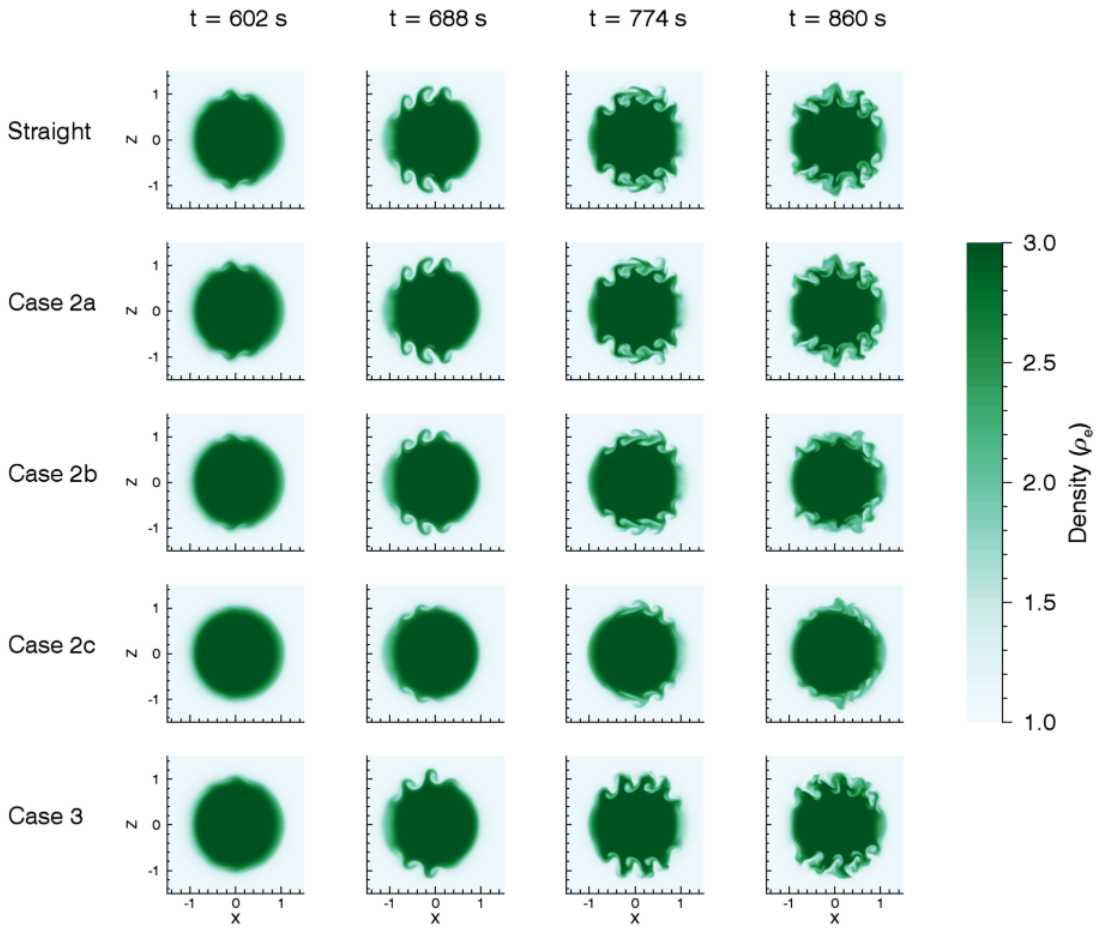

Figure 3.9: Density deformation at the loop apex during the formation of the KHI. The density is normalised to the initial exterior density, $\rho_e = 8.4 \times 10^{-13}$ kg m^{-3}.

clearly impedes vortex formation. As described above, the cause of this suppression is the magnetic tension force (Soler et al., 2010). Since the magnetic field is approximately *frozen* into the plasma, the density deformation in case 1 ensures that straight field lines remain locally straight. Analagously, twisted field lines encourage the development of helical Kelvin-Helmholtz vortices that form along the magnetic field lines.

Additionally, we can also observe that the location of magnetic twist within a loop's cross-section can affect the formation of the KHI. Indeed, in case 3, we include the same maximum twist as case 2c (the largest value of $|B_\phi|$ is the same in both simulations) but it is located at a greater distance from the loop centre. Indeed, this case has a higher quantity of twist when integrated over the entire loop and the resonant field lines have a larger B_ϕ component. Despite this, we see more vortex formation in the case 3 simulation than is observed in case 2c. However, once the first vortices have formed,

there is evidence that the greater radial extent of the twist restricts the development of a turbulent regime at the edge of the shell region (compare the small scales observed in Row 1 Column 3 with those in Row 5 Column 3). In case 3, the vortices that extend into the region of high twist experience an enhanced tension force that arrests the formation of smaller structures. On the other hand, there is little suppression of the KHI where the azimuthal field is weaker, close to the core of the loop.

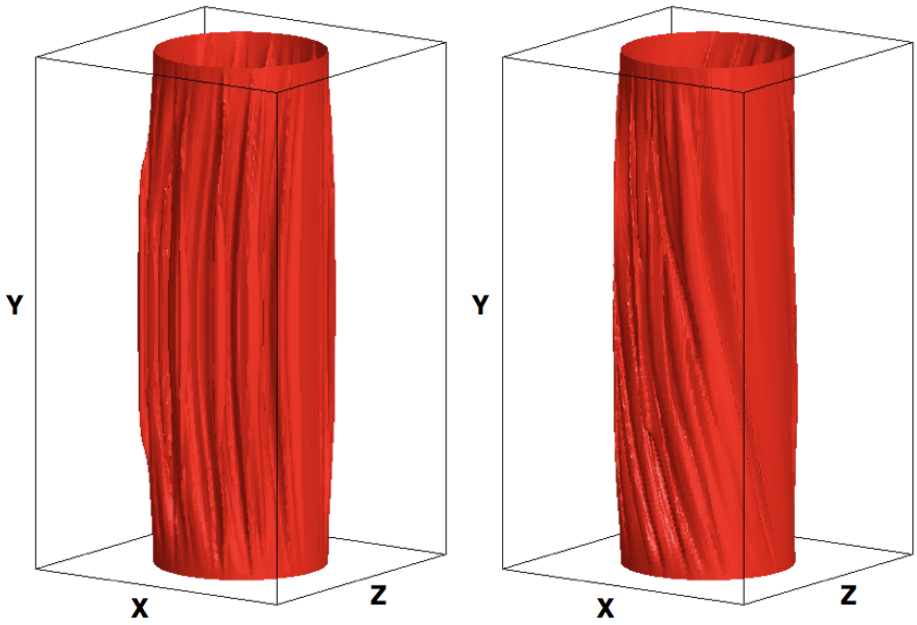

Figure 3.10: Isosurface of density, $\rho = 2\rho_e$ for the straight field case (left-hand panel) and case 2c, a twisted field simulation (right-hand panel). The time shown is 990 s (three and a half wave periods) after the start of the simulation. At this time, the KHI is well-developed in both experiments.

In Figure 3.10, we illustrate the helical nature of the Kelvin-Helmholtz vortices in the twisted field simulations. We show the $\rho = 2\rho_e$ surface for the case 1 (left-hand panel) and case 2c (right-hand panel) simulations once the instability is well-developed. We note that the aspect ratio of the flux tube has been altered in order to allow the reader to easily discern the form of the vortices.

In both cases, the greatest density deformation can be observed at the loop apex (midpoint of the y-axis) as this is the location of the maximum perturbation, largest Alfvén wave amplitudes and hence, most significant velocity shear. Horizontal cuts through the flux tubes at the loop apex correspond to the plots in Figure 3.9. Further, we immediately see that the vortices are more substantial in the straight field case

and that in both simulations they follow magnetic field lines. As a result, in the twisted field experiment (right-hand panel), the vortices develop in helical structures. The azimuthal and vertical nature of these forms has significant implications for the numerical resolution within the computational domain which we will discuss in more detail later. Despite the apparent differences, it is important to note that, in both the twisted and straight field cases, the vortices form approximately uniformly along field lines as a result of the magnetic tension force.

3.4.1 Estimating suppressive effects of twisted field

In the previous chapter, we established several metrics for identifying the onset time of the instability and estimating the subsequent growth rate. We now implement these to quantify the extent of the KHI suppression associated with the azimuthal field. The results are shown in Figures 3.11-3.12. An additional comparison of the vorticity growth which was also considered in Chapter 2 is addressed in the Vorticity section below.

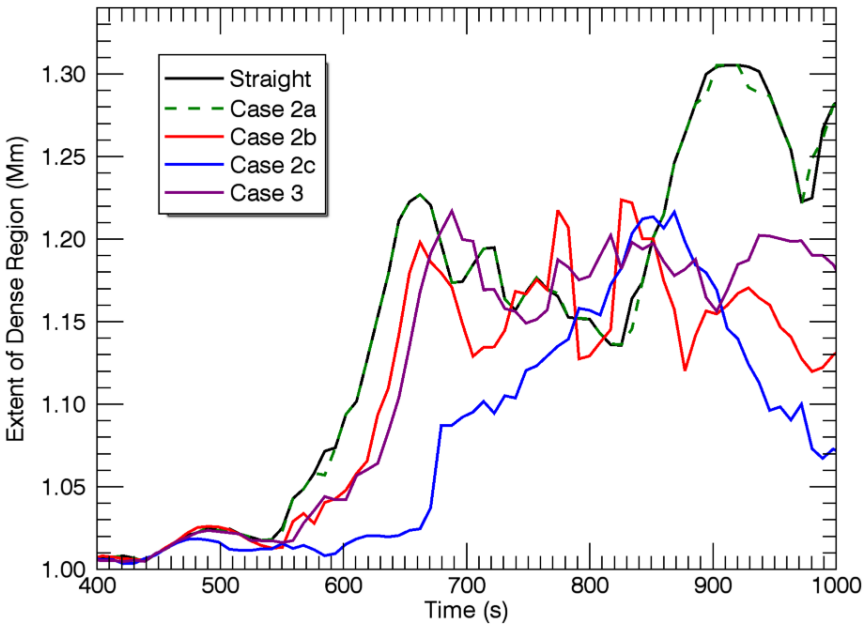

Figure 3.11: Greatest distance of plama with density, $\rho = 2\rho_e$ from the centre of the loop apex during the formation of the KHI. In the straight field case, this plasma is initially located on the resonance layer.

In both figures we can observe that the twist both postpones the onset of the

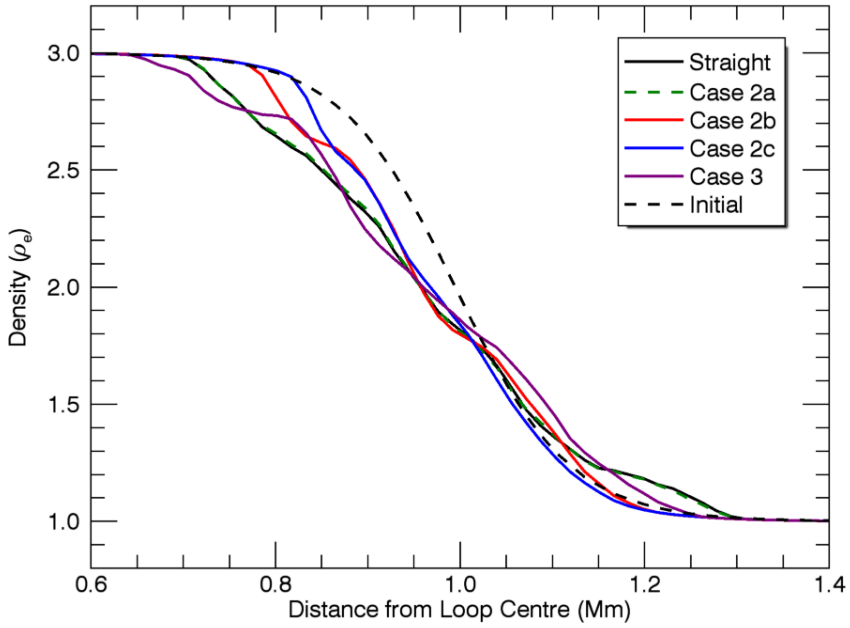

Figure 3.12: Mean density along loop radii in the horizontal cross-section at the apex at $t = 990$ s. By this time, the KHI is well-developed in all cases. For comparison, the initial density profile is also included (black dashed line).

KHI (case 2c; blue line) and inhibits its subsequent growth. For very weak azimuthal magnetic field (case 2a; green dashed line), it is only once the density deformation begins that the suppressive effects of the magnetic tension force can be observed. We note that even after this time the effects are very small (compared to solid black line in both figures).

In Figure 3.11, we aim to summarise the results displayed within the panels of Figure 3.9. We track the largest distance of any plasma with density $\rho = 2\rho_e$ from the loop centre. As the early behaviour of these curves was described in Chapter 2, we omit the early simulation times in Figure 3.11. We compare each numerical experiment to the straight field simulation (black line). The suppressive effects of the azimuthal field are clear and as in Figure 3.9, we note that case 3 exhibits much lower suppression than case 2c. In all cases, since the plasma being tracked corresponds to the approximate location of the resonant layer, we expect that any subsequent energy transfer from the kink mode through resonant absorption will become less azimuthally uniform (Ruderman et al., 2010).

In the previous chapter, we acknowledged that the formation of the instability reduces the mean radial density gradient across the loop boundary. In particular, it

increases the average width of the shell region of the flux tube. Indeed, simulations in which the KHI was partially or totally suppressed generated a mean density profile that remained more similar to the initial conditions. In Figure 3.12, the two limiting cases are the solid black line (no suppression) and the dashed black line (initial conditions; complete suppression). In agreement with the η-ν-parameter study, we observe that the case 2 simulations exhibit successively less smoothing as the magnitude of the azimuthal field was increased.

3.4.2 Currents and field-aligned flows

Although the suppression of vortex formation by twisted magnetic field could result in the instability being difficult to observe in the solar corona, the formation of currents still persists and may have interesting consequences for the energetics of the system. Indeed, as we shall show in this section, the maximum magnitude of the current density that forms during the instability can be significantly larger in the twisted field cases. Ultimately, this may allow the magnetic Kelvin-Helmoltz instability to enhance the rate of wave energy dissipation even if only small vortices are able to form.

As we demonstrated in Chapter 2, the formation of the KHI is associated with the generation of significant currents as the vortices stress the magnetic field. Meanwhile, the inclusion of a background, azimuthal field ensures that there are currents present in the initial conditions. Since B_ϕ is a non-trivial function of R, we see that these currents are loop-aligned. We aim to quantify how the development of the azimuthal wave and subsequent growth of the KHI modifies and enhances the magnitude of these currents.

In Figure 3.13, we display the magnitude of the current density integrated over the cross-section of the loop at different heights and as a function of time for case 2c. The analagous plot for the straight field simulation is shown in the lower panel of Figure 2.14. In both cases, we see the formation of larger currents as the simulation progresses; initially, as resonant absorption injects energy into the azimuthal Alfvén waves and subsequently ($t > 600$ s), as the KHI develops. In the straight field case, the magnitude of the currents remains very small at the loop apex, however, in the twisted field simulations, the presence of currents in the background field ensures that the area integral of $|\mathbf{j}|$ is always non-zero at any value of y along the length of the loop.

Despite this, in Figure 3.13 we can observe that the currents that form during resonant absorption and the growth of the KHI, are much larger than the initial currents. In case 2c, we also see significant current formation at the loop apex as the instability

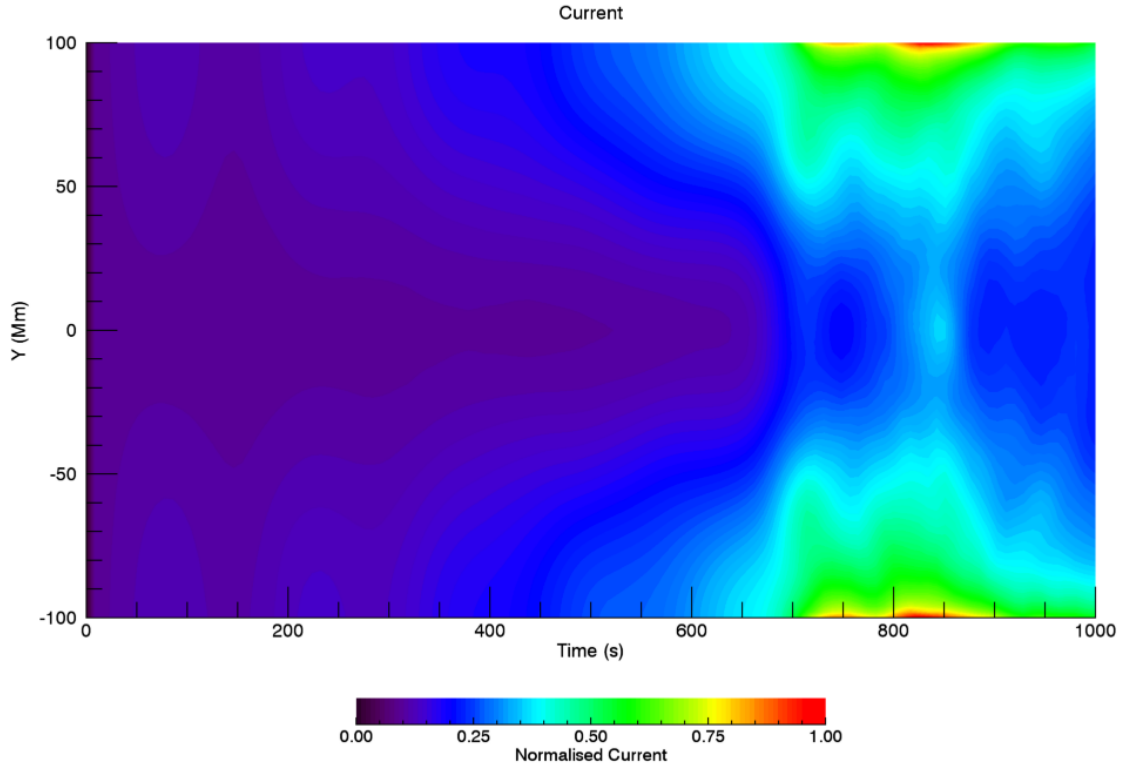

Figure 3.13: Magnitude of current density integrated over loop cross-section as a function of time and position along the length of the loop. The figure was produced using the results of case 2c.

develops. This is a significant departure from the straight field regime. Although we still expect, in a non-ideal simulation, that magnetic wave energy dissipation will be largest at the loop foot points, in the twisted field simulations we might expect some contribution from currents along the entire length of the flux tube, including at the loop apex.

In Figure 3.14, we display the magnitude of the current density that forms on the $\rho = 2\rho_e$ surface for three simulations. The surface plots correspond to a time at which the KHI is well-developed. This can be seen by the deformation of the initially cylindrical surface. In all three cases we see that the currents that form are highly localised and this highlights the difficulty in resolving the turbulent-like aftermath of the KHI on a finite numerical grid.

In the straight field case (first panel), we see a band around the loop apex in which no significant currents have formed. This is not the case, however, in the twisted field simulations. In all three simulations, the large currents tend to form in field-aligned strands, which suggests any Ohmic heating (with $\eta \neq 0$) at a given time would

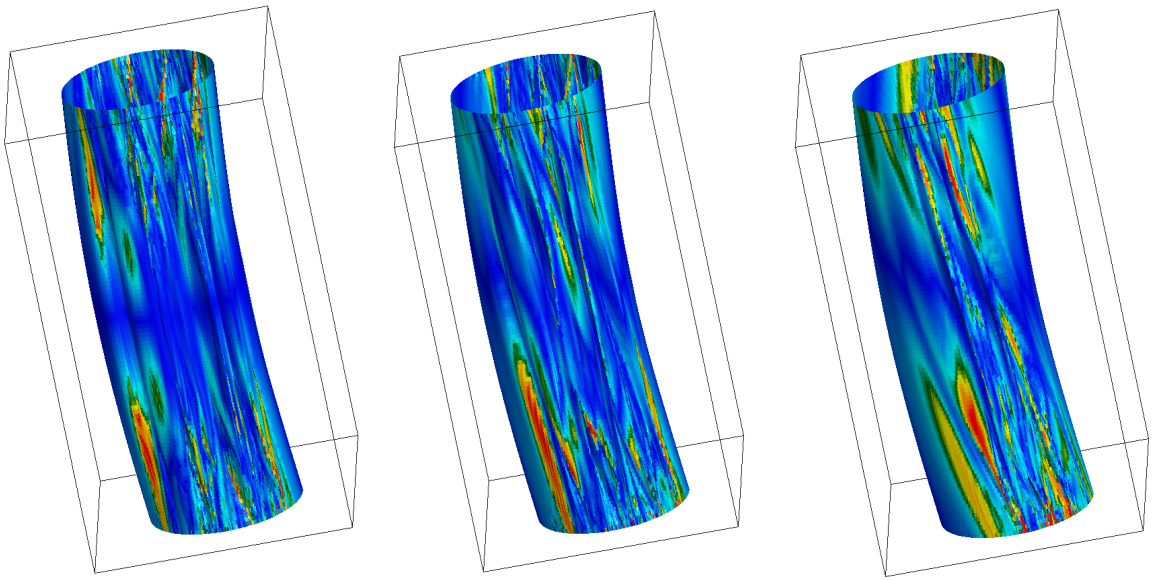

(a) Case 1. (b) Case 2b. (c) Case 2c.

Figure 3.14: Magnitude of current density on the surface defined by $\rho = 2\rho_e$ during the development of the KHI.

cause temperature increases on along individual field lines rather than across the entire surface. Despite this, these figures mask the highly dynamic nature of the small scales that form, and over the course of a wave period, the majority of the surface experiences the formation of energetic current sheets.

In Chapter 2, we argued that, for the straight field case, the currents that do form at the loop apex following the onset of the KHI are dominated by the horizontal components j_x and j_z. However, this is not true for the twisted magnetic field simulations. In Figure 3.15, we show the maximum magnitude of the current density (and each component) at the loop apex for each case as the simulations progress. Each curve displayed in the top left-hand panel has been normalised to the pre-KHI formation current density (at $t = 560$ s) in the respective simulation. In this manner, we aim to represent the relative growth of the current density during the development of the instability.

Despite this normalisation, which is more significant in the simulations with larger magnetic twist (they have greater background current densities), we see that the weakly twisted simulations (case 2a and 2b) exhibit much larger currents than the straight field case. By considering the remaining three panels, we see that this is associated with differences in the loop-aligned current density, j_y. Indeed, in the lower left-hand panel of Figure 3.15, it is clear that the twisted field simulations generate much larger values of $|j_y|$ than the straight magnetic field case. Meanwhile, with the exception of $|j_z|$ in

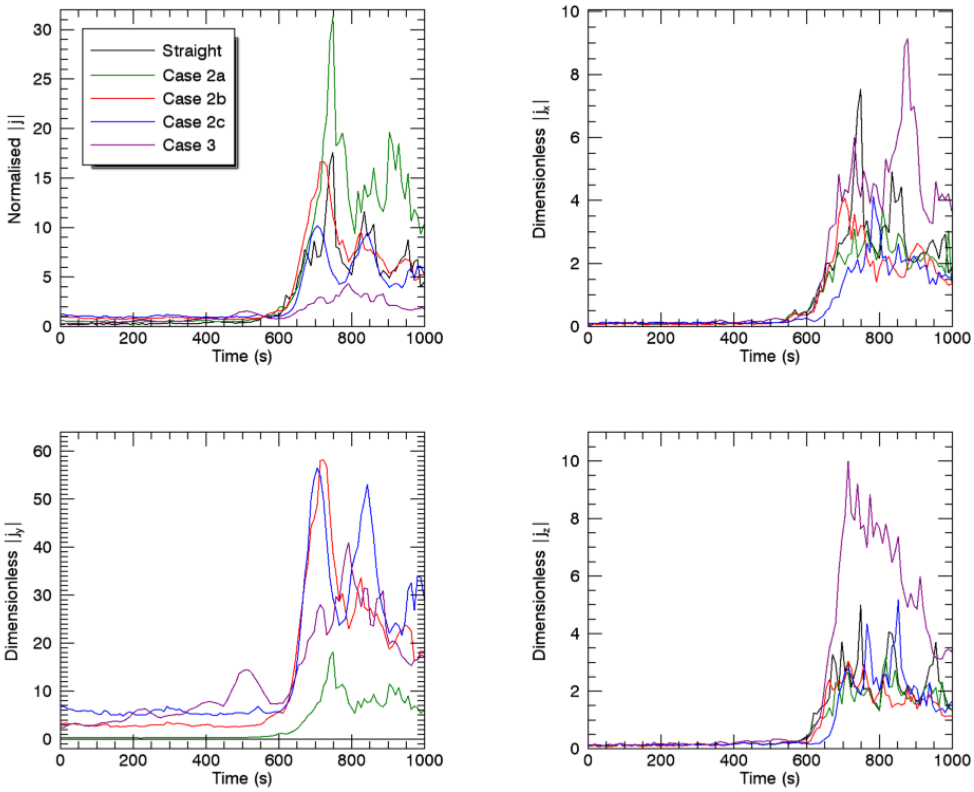

Figure 3.15: Growth of currents during the development of the KHI. The top left-hand panel displays the maximum magnitude of the current density in the horizontal cross-section at the loop apex. For each simulation, it is normalised by the maximum current density in this plane at $t = 560$ s. This corresponds to a time just before the first Kelvin-Helmholtz vortices can be observed. The remaining three panels display the maximum magnitude of each component in the same cross-section. The units are dimensionless but are the same for each of the components.

case 3 (which we discuss below), the horizontal current densities, j_x and j_z, remain similar in magnitude in all simulations.

From Ampère's law (1.7), we see that the y-component of the current density is associated with radial gradients in B_ϕ and azimuthal gradients in B_R. In the case 1 simulation (straight magnetic field), at the loop apex, there is no background horizontal field component. Furthermore, the standing kink and Alfvén wave modes do not induce any horizontal field perturbations in the $y = 0$ plane. Thus, with the exception of small variations induced by the KHI, $|j_y|$ is necessarily small. In the twisted field cases, on the other hand, there is a non-zero component of j_y, even prior to the onset of the instability ($t < 600$ s; Figure 3.15, lower left-hand panel). As the magnitude of the radial gradient is a function of twist factor (τ or ψ) , we see that, for example, Case 2c has more significant currents than Case 2b.

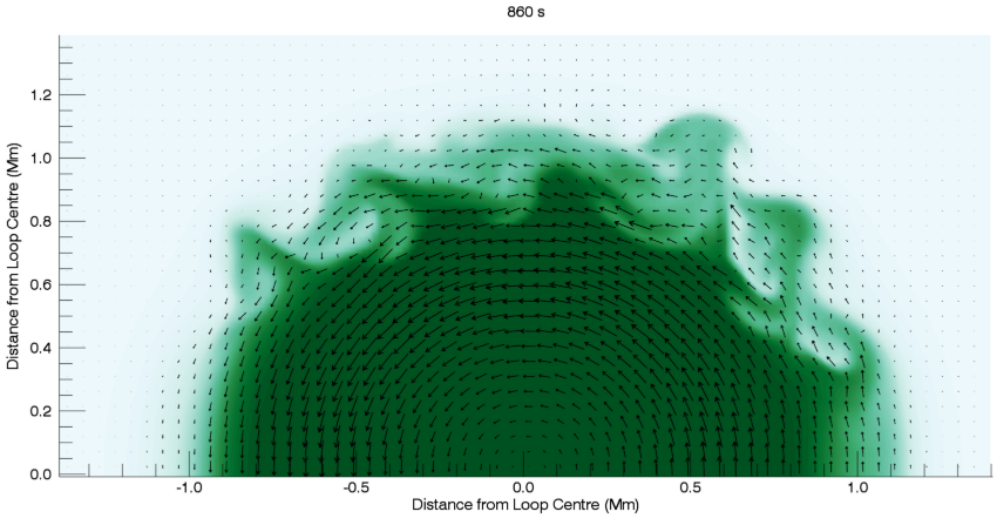

Figure 3.16: Horizontal components of the magnetic field (vectors) and the deformed density profile (coloured contour plot). The plane displayed is the upper half ($z \geq 0$) of the horizontal cross section at the loop apex once the KHI is well-developed. The figure is produced using the results of case 2b.

Subsequently, we see that during the development of the KHI, this difference is enhanced. We attempt to explain this phenomenon in Figure 3.16. Here, we display the horizontal components of the magnetic field along with the deformed density profile for Case 2b. We can clearly see the azimuthal field which is well-structured within the loop's core but has become stressed within the vortex-forming region. We consider a plasma element that is moving radially outwards on account of the instability and recall that the magnetic Reynolds number is much larger than unity. Thus, the motion of this plasma element will advect magnetic field away from the centre of the loop. Hence, field with a large azimuthal component will be transported into a region with lower twist. Therefore, we can see that this process reduces the length scales on which the azimuthal component varies and so increases the current density. Furthermore, vortical motions produced by the KHI introduce radial components of the field and generate additional loop-aligned currents.

Although the presence of azimuthal magnetic field can suppress the formation of vortices, it can also produce locally enhanced currents. Indeed, the lower left-hand panel of Figure 3.15 demonstrates that the KHI can be more energetic over (possibly small) regions of the loop. Consequently, we may expect more powerful Ohmic heating events in the most energetic vortices in a loop with weakly twisted field. We also note that despite the very small magnitude of B_ϕ implemented in case 2a, there are

still significant loop-aligned currents generated. This suggests that even though the magnetic field is locally, almost straight, it may produce different heating signatures than the truly straight field case.

As mentioned above, in the lower right-hand panel of Figure 3.15, we see that the alternative magnetic twist profile explored in case 3 generates larger values of $|j_z|$ than the other simulations. Further, the maximum for j_x (top right-hand panel) occurs later and is larger than the values observed in each of the other simulations. We see more significant values of the horizontal current density in this case because the Kelvin-Helmholtz vortices form in regions of stronger twist than in the case 2 simulations. As a result, the transverse gradients generated during the instability are much larger than those in the other experiments.

Another consequence of the inclusion of azimuthal magnetic field is the excitation of loop-aligned velocities, v_y, at the loop apex. In the straight field case, at $y = 0$, there is no vertical gradient in the gas or magnetic pressures and there is no magnetic tension force. Thus, in the absence of gravity, there are no forces to drive loop-aligned flows at the loop apex (we note that ponderomotive forces will drive vertical flows close to the loop foot points). However, if an azimuthal component of the magnetic field is included, the radial current density (associated the KHI) induces a y-component of the Lorentz force. This effect occurs for even extremely weakly twisted field (case 2a). Both positive and negative radial currents are generated during the KHI and thus both upwards and downward flows are generated.

In Figure 3.17, we display the maximum value of $|v_y|$ at the loop apex for all the simulations within our parameter space. We note that on this scale case 2a (green line) does not seem too different from the straight field simulation (black line). However, the vertical velocities obtained in the weakly twisted case are in fact many orders of magnitude larger than the very small loop-aligned flows observed in the straight case. The velocities observed in the twisted field simulations for $t \leq 600$ s, are associated with the Alfvén mode wave vector not being parallel to the horizontal plane. Thus, any excited Alfvén wave will have a velocity component in the vertical direction. Subsequently, we see the radial current density that forms during the instability generates much larger flows. The stabilising effects associated with the magnetic twist ensure that for a short period the vertical flows are greater in case 2b than case 2c despite the stronger twist component present in the latter simulation.

In theory the excitation of these loop-aligned velocities could act as a proxy for detecting magnetic twist within a transversely oscillating coronal loop. Indeed, there is a significant difference between the vertical flows observed in each case. However,

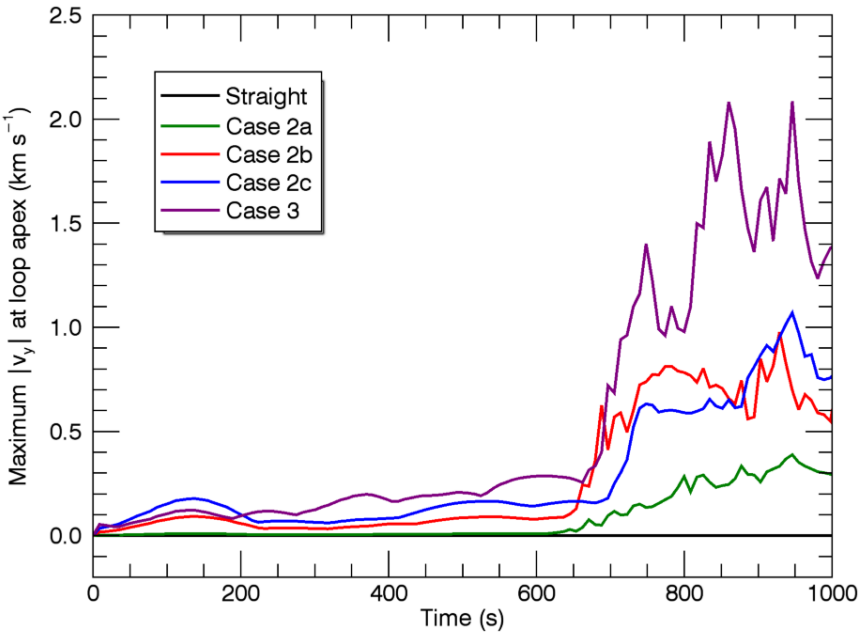

Figure 3.17: Maximum value of $|v_y|$ at the loop apex as a function of time for all simulations.

the velocities are highly localised and will likely exist over scales significantly beyond current observing capabilities. Furthermore, the differences are only significant at the loop apex for a fundamental standing mode. The ponderomotive force excites loop-aligned flows along much of the rest of the loop in all cases. Therefore difficulties in identifying the loop apex, flux tube asymmetries and the existence of higher harmonics will likely further impede the applicability of this proxy.

3.4.3 Vorticity

As we discussed in Chapter 2, the development of the KHI also produces small scales in the velocity field which can be monitored by considering the vorticity, ω. In non-ideal regimes, gradients in the velocity are susceptible to the effects of viscosity which, in turn, lead to the dissipation of wave energy. In the straight field case, we highlighted that the excitation of azimuthal Alfvén waves enhances the loop-aligned component of vorticity, ω_y. Additionally, the subsequent development of Kelvin-Helmholtz vortices further increases the magnitude of velocity gradients.

In Figure 3.18, we display the magnitude of the vorticity, $|\omega|$ in the horizontal cross-section at the loop apex. We show two different stages during the simulation for the

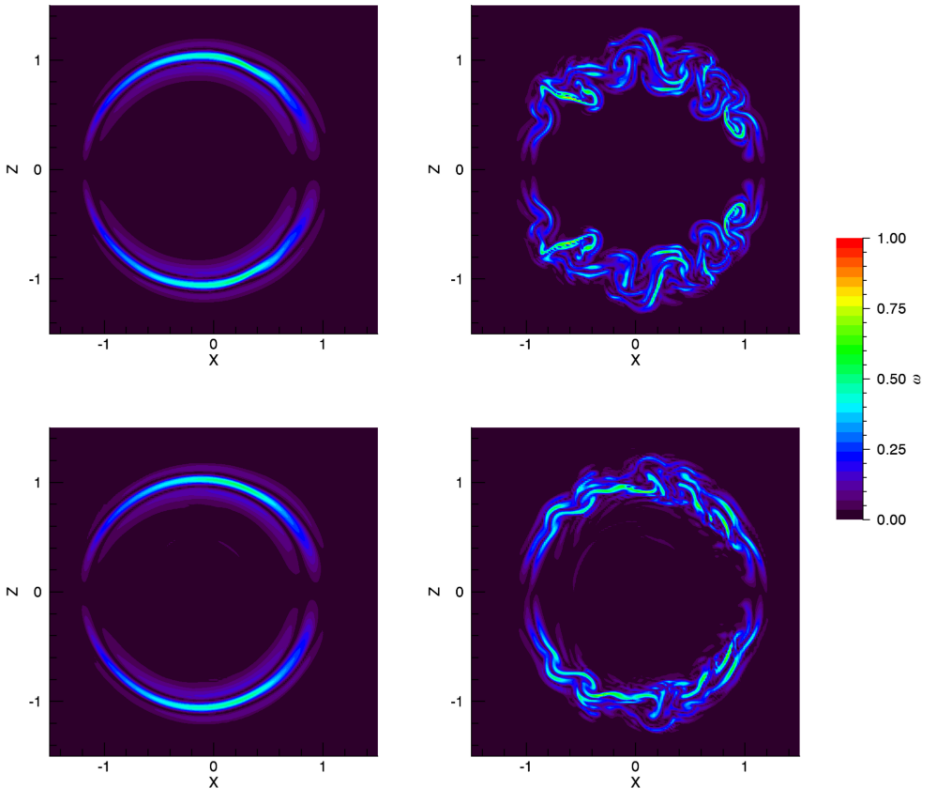

Figure 3.18: Magnitude of the vorticity at two different times, $t = 420$ s (left) and $t = 990$ s (right) in the horizontal cross-section through the loop apex. The first row corresponds to case 1, the straight field simulation, and the second row corresponds to case 2c. Here we have normalised the vorticity by the same value for both simulations.

straight field case (first row) and the twisted field case 2c (final row). In the left-hand column, significant resonant absorption has occurred, however, no vortices have formed in either simulation. In the right-hand column, on the other hand, we can see that the instability has developed. Prior to the formation of the KHI, since resonant absorption is only weakly modified by the azimuthal field, the profiles of $|\omega|$ are very similar. Once the KHI forms, however, differences become apparent as the characteristic vortices are suppressed in the twisted field case. Despite this, the maximum magnitude of the vorticity is very similar in both of these simulations, suggesting that the vortices that form in case 2c are at least as energetic as those observed in the straight field simulation.

In Figure 3.19, we consider the three components of vorticity in more detail. In the top row, we display the three components of ω integrated over the loop cross-section. In particular, at each time we calculate,

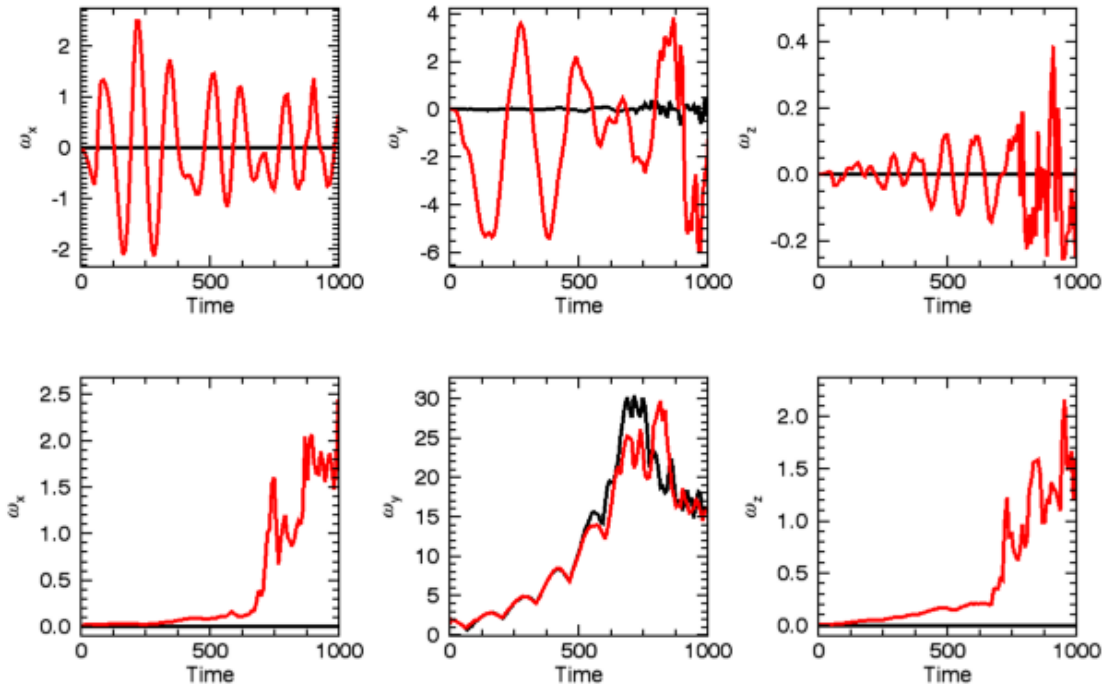

Figure 3.19: First row - the three components of the vorticity integrated over the horizontal plane at the loop apex. Second row - maximum size of each component of the vorticity in this plane. For both of the rows, the black line corresponds to the straight field simulation (case 1) and the red line corresponds to a twisted field simulation (case 2c).

$$\int_A \omega_x \, \mathrm{d}A = \int_A \frac{\partial v_z}{\partial y} - \frac{\partial v_y}{\partial z} \, \mathrm{d}A, \tag{3.9}$$

$$\int_A \omega_y \, \mathrm{d}A = \int_A \frac{\partial v_x}{\partial z} - \frac{\partial v_z}{\partial x} \, \mathrm{d}A, \tag{3.10}$$

$$\int_A \omega_z \, \mathrm{d}A = \int_A \frac{\partial v_y}{\partial x} - \frac{\partial v_x}{\partial y} \, \mathrm{d}A, \tag{3.11}$$

for the panels from left to right. Here, A is a circle of radius 1.5 Mm that tracks the cross-section of the flux tube as it moves with the global kink mode. For all three components of ω, the straight field simulation (black lines) displays very little net vorticity when integrated across the loop cross-section. In other words, any contributions from regions with positive vorticity are cancelled by regions with negative vorticity. On the other hand, the inclusion of magnetic twist permits the non-linear generation of additional harmonics that are associated with the oscillating profiles in the panels

in the top row of Figure 3.19.

The most significant effect is observed in ω_y (second column). In the case 1 simulation, the azimuthal Alfvén modes in the upper z half-plane have an equal and opposite contribution to those in the lower z half-plane. Consequently, there is no net vorticity. Meanwhile in the case 2c simulation, the magnetic tension force associated with the azimuthal field has a positive contribution to one of the half-planes and has an inhibiting effect in the other. This causes the ω_y contribution from the Alfvén waves in one half of the x-z-plane to be slightly larger than in the opposite half of the domain. The effect of the tension force reverses as the direction of motion changes, thus causing the area integral of ω_y to oscillate with the same period as the kink mode.

For the remaining two components of vorticity, the area integrals oscillate with half the period of the kink wave. For both ω_x and ω_z, the associated panels in Figure 3.19 are dominated by the contribution of loop-aligned gradients; $\frac{\partial v_z}{\partial y}$ and $\frac{\partial v_x}{\partial y}$, respectively. These gradients are associated with additional, higher-harmonic waves that are generated in case 2c but are not observed in the straight field case.

The second row of Figure 3.19 displays the maximum magnitude of each component of the vorticity in the $y = 0$ plane. The central panel corresponds to a proxy used for the growth rate of the KHI in the Chapter 2. We see that the small differences observed in the loop-aligned vorticity (central column) arise due to the later formation of KHI vortices in the twisted field simulation. However, once the KHI does form, ω_y reaches a similar value to the maximum observed in the straight field case. This supports the claim that some of the vortices in case 2c would be (in a non-ideal regime) as effective at dissipating energy as those that form in case 1. There is a marked difference in the growth of the other two components of vorticity. In particular, the maximum size of $|\omega_x|$ and $|\omega_z|$ is around an order of magnitude larger in the twisted field case. This is caused by the Alfvén waves and, later, the Kelvin-Helmholtz vortices having a significant helical component (see Figure 3.10).

3.5 Loop-aligned numerical resolution

In the straight field simulations examined in Chapter 2, small scales typically develop within the horizontal plane. Thus, the profile of the numerical domain was selected to reflect this. In particular, a high spatial resolution was implemented along the x and z axes. The loop-aligned resolution was less crucial and thus we accepted a coarser grid in the y direction. However, the inclusion of magnetic twist generates small scales in the loop-aligned direction and, as such, the spatial resolution in the y direction can

become critical.

As we have highlighted throughout this chapter, one effect of twisted field on the model is that azimuthal Alfvén waves and the Kelvin-Helmholtz vortices are helical in nature. Furthermore, as more magnetic twist is included, vertical non-uniformity in the density and velocity field becomes more profound in the case 2 simulations. Consequently, with increasing azimuthal field, the vertical resolution becomes more important. Since, in our model, the loop-aligned resolution is much coarser than the horizontal resolution, we investigate whether the number of grid points we have used in the y direction is sufficient.

In all of the simulations, the most unstable wave vector satisfies $\mathbf{k}\cdot\mathbf{B}=0$ such that the inhibiting effect of the magnetic tension force is eliminated (see right-hand side of equation 4.7 in Cowling (1976)). Thus, a consequence of the inclusion of azimuthal field is the modification of the direction of this wave vector, $\mathbf{k}$. In particular, it is no longer confined to the horizontal, x-z-plane as in the straight field case.

We can provide an estimate of the required vertical resolution as follows. Since $\mathbf{k}\cdot\mathbf{B}=0$ and $B_R\approx 0$ prior to the onset of the instability, we have

$$\frac{|k_y|}{|k_\phi|}\approx\frac{|B_\phi|}{|B_y|}. \tag{3.12}$$

In order to prevent the vertical resolution limiting the effective Reynolds number (accounting for numerical dissipation), we wish to resolve the vertical component of $\mathbf{k}$ at least as well as we resolve the horizontal component. Therefore, we require

$$\Delta_y\leq\frac{\lambda_y\Delta_\phi}{\lambda_\phi}=\frac{k_\phi\Delta_\phi}{k_y}=\frac{B_y\Delta_\phi}{B_\phi}, \tag{3.13}$$

where Δ_y and Δ_ϕ are the vertical and azimuthal numerical resolution (grid widths) and $\lambda_y=\frac{2\pi}{k_y}$ and $\lambda_\phi=\frac{2\pi}{k_\phi}$ are the vertical and azimuthal wave lengths, respectively. Further, Δ_ϕ is constrained by the horizontal grid widths Δ_x and Δ_z such that

$$\Delta_x\leq\Delta_\phi\leq\sqrt{\Delta_x^2+\Delta_z^2}. \tag{3.14}$$

Since equation (3.13) must be satisfied throughout the entire instability forming region, we obtain

$$\Delta_y\leq\frac{B_y\Delta_x}{B_\phi}. \tag{3.15}$$

Using this restriction, we immediately see that the larger the magnitude of B_ϕ, the more refined the vertical grid must be in order to ensure the simulation is not limited

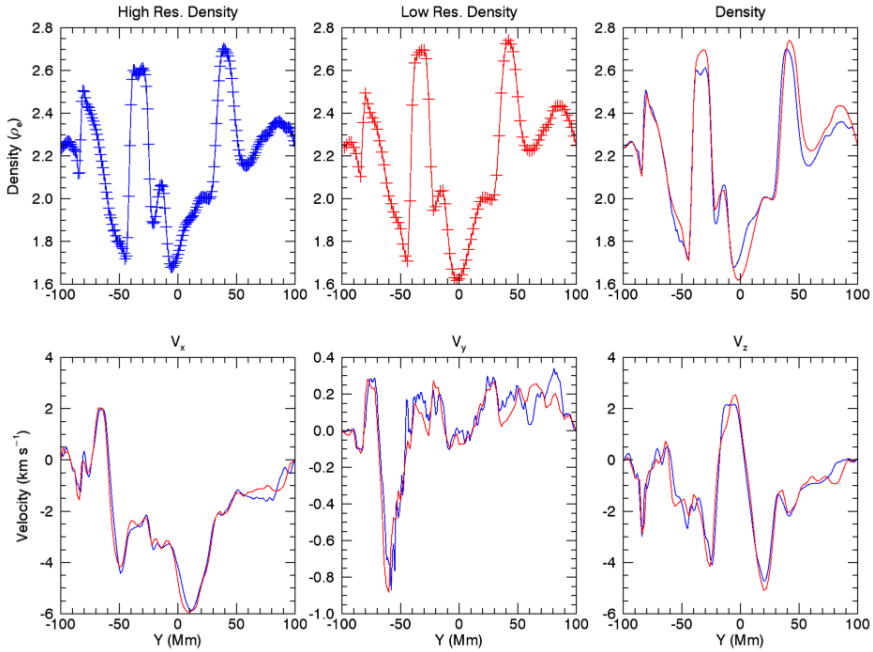

Figure 3.20: First row - density profile along the most under-resolved vertical line at $t = 900$ s for the high resolution (blue) and low resolution (red) simulations. In the first two panels, the position of grid points are denoted with a cross, and the third panel shows a comparison between the two simulations. Second row - comparison of the three velocity components along the same line for the two different spatial resolutions.

by the loop-aligned resolution. We also note this is only one restriction on Δ_y, and in the opposite limit, $B_\phi \to 0$, more restrictive bounds are required in order to spatially resolve the standing kink and Alfvén modes, for example.

In our model, for the most twisted cases, equation 3.15 yields $\Delta_y \lesssim 1200$ km. Since we have $\Delta_y = 2000$ km in our model, this suggests that the vertical component of the wave vector $\mathbf{k}$ is less well resolved than the horizontal component. As the spatial resolution is critical for the development of the KHI, this suggests that any suppression found for case 2c could be associated with a lack of grid points in the y direction and not, as we have claimed, the azimuthal field.

In order to determine whether the low vertical resolution did produce significant numerical artefacts in our simulations, we re-used the set-up of case 2c but with twice the number of grid points in the y direction. This then sets $\delta_y = 1000$ km, which satisfies the restriction obtained with equation 3.15.

In Figure 3.20, we display the density and velocity profiles along the most under-resolved vertical line in the low resolution (original) simulation at a time when the instability is well-developed. The selected line is found within the vortex-forming region

in the boundary of the loop. We notice that for -45 Mm $\leq y \leq$ -35 Mm, the density profile is approaching the limit of the spatial resolution, particularly in the 100 grid point simulation. Despite this, there is little difference between the density profile (first row, third panel) and the velocity field (second row) produced by the two simulations. Further, we found that there was no significant increase in the growth rate of the Kelvin-Helmholtz vortices or indeed any change in the results of the analysis presented within this chapter. However, we note that these resolution effects are expected to become more pronounced in regimes with greater magnetic twist and thus, care should be taken when considering models with a more significant azimuthal field component.

3.6 Heating considerations

Hitherto, within this chapter, we have only considered ideal simulations in which the only dissipation of magnetic and kinetic energy occurs because of numerical effects. In particular, no irreversible heating has been considered. We now extend our model by introducing a non-zero resistivity, η, in order to determine whether the twisted field simulations can produce any additional plasma heating. Although the energy in the initial perturbation is small, the introduction of magnetic twist and background currents ensures that there is additional magnetic energy in the non-potential background field. As such, in this section, we aim to identify whether any of this additional magnetic energy can be dissipated during the evolution of the KHI.

3.6.1 Modified equilibrium

Thus far, we have ensured that the gas pressure is constant throughout the initial conditions by allowing the temperature within the flux tube to be lower than the exterior plasma. As the KHI progresses, the cold, internal plasma mixes with the hot, external plasma and causes a mean temperature increase within the loop. This effect masks any temperature increase associated with Ohmic or viscous heating. Therefore, in order to mitigate this problem, we modify our initial equilibrium such that the plasma is isothermal throughout the domain. Since the internal plasma density is high in comparison to the surroundings, this will mean that there is an enhanced gas pressure force that acts radially outwards. We can still achieve force balance by adjusting the magnetic pressure accordingly and we must, therefore, relax the requirement of a constant field strength throughout the domain.

We begin by maintaining the same magnetic twist profile as in the case 2 simula-

tions:

$$B_\phi(R) = \begin{cases} \tau R, & \text{if } R \leq a, \\ \tau(2a - R), & \text{if } a < R \leq 2a, \\ 0, & \text{if } R > 2a. \end{cases} \tag{3.16}$$

Since the gas pressure is no longer constant, it must be balanced by the Lorentz force. As we have azimuthal and vertical invariance, in cylindrical co-ordinates, we require

$$\frac{\mathrm{d}P}{\mathrm{d}R} = -\frac{B_\phi^2(R)}{R} - \frac{\mathrm{d}}{\mathrm{d}R}\left(\frac{B^2}{2}\right) = \underbrace{-\frac{B_\phi^2(R)}{R}}_{\text{Magnetic Tension}} - \underbrace{B\frac{\mathrm{d}B}{\mathrm{d}R}}_{\text{Magnetic Pressure}}. \tag{3.17}$$

We note that only the azimuthal component of the magnetic field appears in the tension term, whereas the total magnetic field strength appears in the magnetic pressure term. Rearranging equation (3.17) yields

$$\int B\ \mathrm{d}B = \int \left(-\frac{B_\phi^2(R)}{R} - \frac{\mathrm{d}P}{\mathrm{d}R}\right)\ \mathrm{d}R, \tag{3.18}$$

$$\implies \frac{B^2}{2} + P = -\int \frac{B_\phi^2(R)}{R}\ \mathrm{d}R. \tag{3.19}$$

We see that the total (magnetic and gas) pressure balances the radially inward magnetic tension force. This is in contrast with the original (cold loop) case in which the magnetic pressure is uniform and only the thermal pressure balanced the tension force.

We now consider the solution to equation (3.19) for each of the three sections of the twist profile described in equation (3.16).

Case 1: $R \leq a$.

In this case, the integral in (3.19) reduces to

$$-\int \tau^2 R\ \mathrm{d}R = C_1 - \frac{\tau^2 R^2}{2}, \tag{3.20}$$

where the integration constant C_1 will be calculated below.

Case 2: $a < R \leq 2a$.

In this case, the integral in (3.19) reduces to

$$-\int \frac{\tau^2(2a-R)^2}{R}\,\mathrm{d}R = C_2 - \tau^2\left(4a^2\ln R - 4aR + \frac{R^2}{2}\right), \tag{3.21}$$

where the integration constant C_2 will be calculated below.

Case 3: $R > 2a$.

In this case, the integral in (3.19) reduces to

$$-\int 0\,\mathrm{d}R = C_3, \tag{3.22}$$

where the integration constant C_3 will be calculated below.

In order to find the constants of integration, we begin with C_3. For $R > 2a$, we have a constant pressure, P_0, and the magnetic field is prescribed by $\mathbf{B} = (0, B_0, 0)$. Therefore, we can use the desired (external) plasma-$\beta = 0.02$ to define P_0 as

$$P_0 = \frac{B_0^2\beta}{2}. \tag{3.23}$$

Now we have

$$C_3 = \frac{B_0^2}{2} + P_0 = \frac{B_0^2}{2}(1+\beta). \tag{3.24}$$

In order to ensure the continuity of total pressure, we require the solutions in equations (3.21) and (3.22) to coincide at $R = 2a$. Hence

$$C_2 = C_3 + 2a^2\tau^2\left\{2\ln(2a) - 3\right\}. \tag{3.25}$$

Similarly, we require that the solutions in equations (3.20) and (3.21) are equal at $R = a$. Therefore, we obtain

$$C_1 = C_2 + 4a^2\tau^2(1 - \ln a) = C_3 + 2a^2\tau^2(2\ln 2 - 1). \tag{3.26}$$

Returning to equation (3.19), we consider a magnetic field of the form (in cylindrical co-ordinates) $\mathbf{B} = (0, B_\phi, B_y)$ and $B = |\mathbf{B}|$. We have

$$B^2(R) = \begin{cases} 2\left(C_1 - P\right) - \tau^2 R^2, & \text{if } R \leq a, \\ 2\left(C_2 - P\right) - \tau^2\left(8a^2 \ln R - 8aR + R^2\right), & \text{if } a < R \leq 2a, \\ 2\left(C_3 - P\right), & \text{if } R > 2a. \end{cases} \tag{3.27}$$

Finally, we can use equation (3.27) to find $B_y(R) = \sqrt{B^2 - B_\phi^2}$. We note that since $B_R = 0$ and is azimuthally and vertically uniform, the solenoidal constraint is automatically satisfied. In this equilibrium, the density profile is unchanged and the temperature is 2.5 MK everywhere. We note that it is not possible to preserve the uniformity of the plasma-β, but it remains less than 0.065 throughout the computational domain.

3.6.2 Ohmic Heating

In order to consider the dissipation of magnetic energy, we implement various resistivity profiles in simulations of the modified equilibrium (static loop) and of the loop perturbed by the velocity profile used throughout this chapter. We only investigate the level of twist corresponding to case 2c ($\tau = 2$). For the value of $\eta = 10^{-4}$, we investigate energy dissipation for uniform resistivity and for an anomalous resistivity which is only triggered by currents that form following the onset of the KHI. As with the previous chapter, it is only activated within the vortex-forming region. In this case, however, it is triggered by large values of the total current density, rather than simply by the horizontal components. This ensures that the critical η is activated at many points along the entire length of the loop and not only at the loop apex.

Magnetic energy

In simulations in which the kink mode is induced, we observe that any temperature increase caused by irreversible heating is masked by adiabatic effects. These are associated with the compressive nature of the Kelvin-Helmholtz vortices and, to a lesser extent, the azimuthal Alfvén waves (we recall that these are not totally incompressible). Therefore, in order to examine the implications of the KHI on the dissipation of magnetic energy, we directly monitor changes in the azimuthal field. In particular we calculate

$$W(t) = \int_V \frac{B_\phi^2}{2\mu_0}\, \mathrm{d}V, \tag{3.28}$$

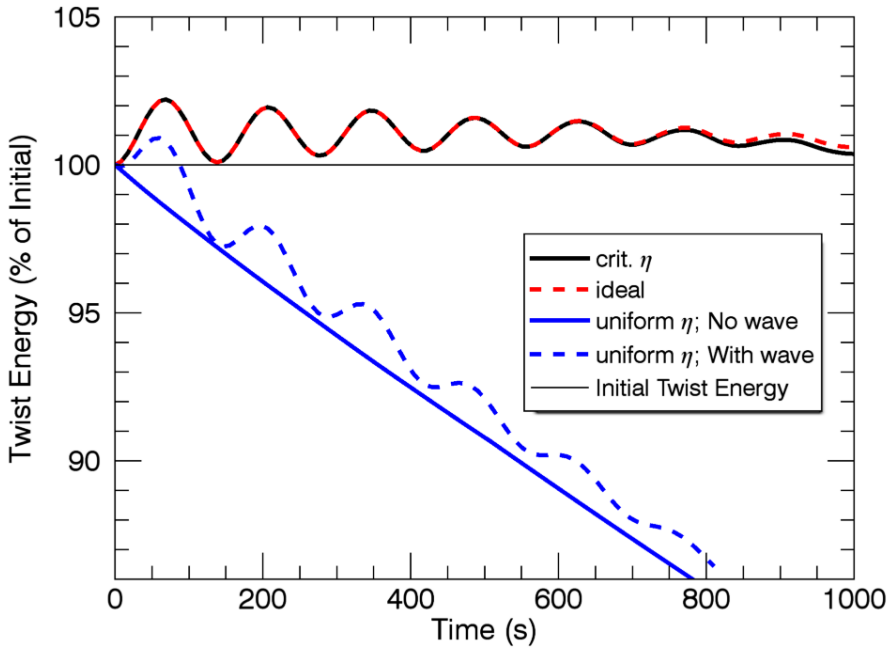

Figure 3.21: Azimuthal magnetic energy integrated over the volume of the loop.

where V is the volume of the loop. The value of this integral is displayed as a function of time for each simulation in Figure 3.21. In all wave simulations we observe oscillatory behaviour in this quantity which corresponds to the periodic transfer between kinetic and magnetic energy during the kink and Alfvén wave periods. We also see that the largest decrease in azimuthal magnetic energy is found in the uniform η cases (blue lines). In these simulations, the resistivity is acting on the currents in the initial conditions and dissipating the magnetic energy in the background field. The inclusion of a wave adds a perturbation to the azimuthal energy which is itself dissipated. However, the wave does not increase the transfer of the background magnetic energy into heat.

The threshold for triggering the critical η was selected such that the anomalous resistivity is only active within the Kelvin-Helmholtz vortices. In particular, it is designed such that it only dissipates energy in the turbulent-like plasma and not simply the background magnetic twist. This represents the cascade of energy to the dissipation scale during the KHI whilst maintaining a long (in comparison to the length of the simulation) diffusion time scale for the initial magnetic field. We aimed to test whether the KHI accessed any of the background magnetic energy as is suggested by the larger currents that form in the twisted field simulations.

In Figure 3.21, we do see a small enhancement in dissipation in the critical η case when compared to the ideal simulation (the difference between the solid black line and the dashed red line). However, despite the significant currents that form, we do not observe significant dissipation of the energy within the initial magnetic twist. In particular, the azimuthal magnetic energy is always at least as large as the value at $t = 0$. We see that when resistivity only acts on the Kelvin-Helmholtz vortices, we are only able to dissipate wave energy and not the background magnetic twist.

3.6.3 Volume integrated currents

We now consider the implications of this behaviour by returning to the original simulations presented within this chapter. In particular, we show that if the energy in the background magnetic field cannot be accessed then we should expect more significant Ohmic dissipation in the straight field simulations.

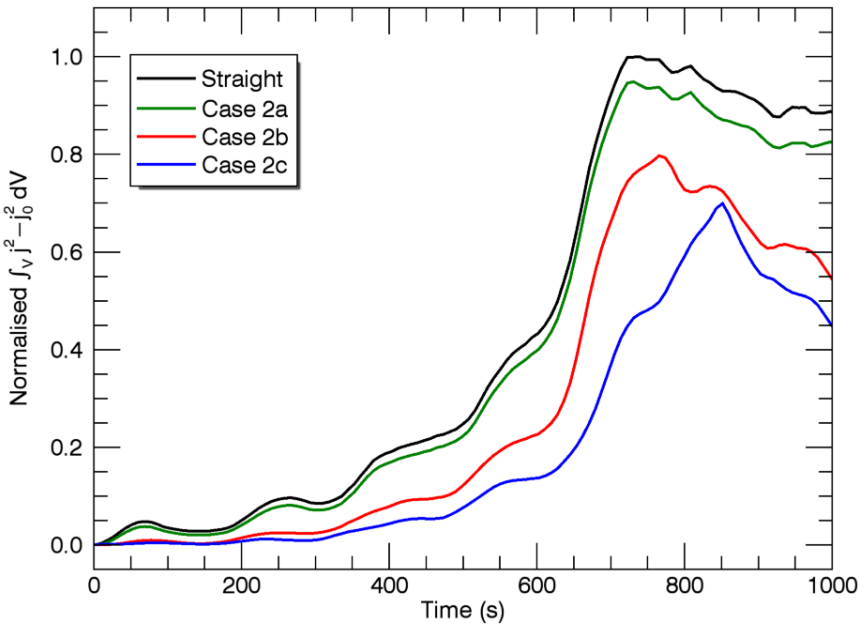

Figure 3.22: Estimated enhancement of volume integrated Ohmic heating associated with development of the Kelvin-Helmholtz instability.

To this end, in Figure 3.22, we display the volume integrated enhancement of j^2 (proportional to the Ohmic heating) above the level found in the initial conditions. In particular we calculate

$$H(t) = \int_V j^2 - j_0^2 \, \mathrm{d}V, \tag{3.29}$$

as a function of time. Again, V is the volume of the loop and j_0 denotes the initial current density in the respective simulation. In our analysis of this figure, we assume that within the corona, the diffusion time scale for the background field is very long. Therefore, the only currents of interest, in the context of coronal heating, are associated with the azimuthal Alfvén waves and the development of the KHI. We see that once the background current density is removed, the loop-integrated Ohmic heating (proportional to j^2) is larger in the simulations with lower levels of magnetic twist. This suggests that despite very localised, strong currents forming in the twisted field simulations, overall the inclusion of magnetic twist reduces the rate of wave energy dissipation as the volume integrated Ohmic heating is smaller.

3.7 Discussion and conclusions

Within this chapter, we have presented the results of an investigation into the effects of magnetic twist on the dynamics of a transversely oscillating coronal loop. We restricted the study to numerical simulations in which the level of magnetic twist was weak. As such, $B_\phi \ll B_y$ and we ensured that the loop was stable with respect to the kink instability.

As in the previous chapter, a fundamental standing kink wave was induced using a low amplitude velocity profile. In all simulations, the oscillation was observed to decay with a Gaussian profile as a result of resonant absorption. In this manner, energy is transferred from the standing kink mode to azimuthal Alfvén waves confined within the boundary region of the loop. This process proceeds largely independently of the amount of magnetic twist present within the flux tube. The inclusion of an azimuthal component of the field modifies the observed Alfvén modes by permitting additional, higher harmonic waves that contribute to an oscillating net vorticity at the loop apex. However, the global dynamics remain largely unchanged when compared to the straight field case.

The significant radial shear associated with the azimuthal Alfvén wave persists and can become unstable to the Kelvin-Helmholtz instability. In all of the non-ideal cases presented, the instability formed after a few wave periods. However, the density deformation that is associated with the KHI is partially suppressed in cases with twisted magnetic field. Furthermore, we note that, for the extent of the parameter space considered within this chapter, greater magnetic twist will induce greater suppression of the instability. In contrast with the suppression associated with dissipation (see Chapter 2), we note that the magnitude of magnetic twist does not significantly delay

the onset of the KHI. Instead, the azimuthal field simply limits the subsequent growth. This is in concordance with the observation that the velocity shear (associated with the resonant absorption) develops largely independently of the twist.

Despite the apparent suppression of the density deformation, the KHI in twisted fields may still have significance for the coronal heating problem. Indeed, we observed that the instability can generate (locally) larger currents than an analagous straight field simulation. Since the twisted cases have an azimuthal component that is radially non-uniform, the characteristic, radial movement of plasma, and hence magnetic field (since it is approximately *frozen* into the plasma), associated with the KHI will generate large currents. Meanwhile, analysis of the vorticity at the loop apex reveals that although the density deformations produced in the twisted cases are smaller in size, they can be as energetic as in the straight case. However, although smaller scales are observed in simulations with azimuthal field, we see that the KHI does not access the energy in the background magnetic field and thus does not enhance loop-integrated heating. Indeed, once the initial currents are accounted for, the total heating is expected to be lower in the twisted field simulations.

Once the KHI currents develop, the azimuthal field produces a vertical component of the Lorentz force that induces the formation of loop-aligned flows at the apex of the flux tube. These are not observed in the completely straight case but are significant even in weakly twisted regimes. This raises the possibility of detecting magnetic twist in coronal structures by searching for loop-aligned flows at the apex during decaying kink oscillations.

Finally, a major criticism of previous work considering the Kelvin-Helmholtz instability as a driver of MHD turbulence in the solar atmosphere is that even weak magnetic twist will suppress the development of the instability. Whilst we have demonstrated that, to some extent, this is indeed the case, large currents are still induced in the presence magnetic twist. Although it seems that the rate of wave dissipation may be reduced by the presence of azimuthal field, we still observe an increase in the volume integrated heating as the instability forms. This ensures that the KHI remains relevent as a mechanism for enhancing wave energy dissipation. The ultimate effect of the azimuthal field is an increase in the difficulty of directly observing the Kelvin-Helmholtz vortices rather than a significant decrease in its efficiency as a heating mechanism.

Chapter 4

Resonant Absorption in an Expanding Magnetic Flux Tube

4.1 Introduction

Many coronal wave models, including those presented in the previous chapters, assume a flux tube which is associated with a density enhancement above the level of the external plasma. In such cases, if there is a continuous transition across the boundary of the loop, then resonant absorption will permit the transfer of wave energy from the kink mode to azimuthal Alfvén waves. As we have discussed previously, this process, along with the potential for phase mixing and the development of the Kelvin-Helmholtz instability, can enhance the rate of wave energy dissipation.

Previous studies (e.g. Pagano and De Moortel, 2017) have highlighted that wave heating may require dissipation coefficients that are many orders of magnitude larger than the expected coronal values in order to balance atmospheric energy losses. Despite this, it remains feasible that the generation of turbulent-like behaviour during the development of dynamic instabilites may enhance wave energy dissipation to the required levels. However, Cargill et al. (2016) identified additional, critical issues with wave heating models. The authors argued that any expected heating is unable to self-consistently generate or sustain the density profile that is typically assumed within the models. Moreover, the expected evaporation of dense plasma from the chromosphere following heating events would *detune* the resonant field lines and limit any subsequent heating. With this in mind, in this chapter, we explore the potential for resonant absorption and phase mixing to proceed without the density profile that is typically assumed in coronal flux tube models. Whilst we do not directly address the

issues presented by Cargill et al. (2016), we highlight that a non-uniform density profile is not a prerequisite for resonant absorption, phase mixing and, potentially, wave heating to occur.

The existence of resonant field lines simply relies on the existence of a transverse gradient in the natural Alfvén frequency. Whilst this gradient can be associated with a change in density, a difference between the internal and external magnetic field strength will also suffice. To this end, we investigate the transfer of energy between a fundamental standing kink mode and azimuthal Alfvén waves within an expanding coronal magnetic flux tube.

We introduce MHD waves to a flux tube in which the internal magnetic field strength is larger than the external value. Due to the expansion of the flux tube, the field strength contrast is largest at the foot points and is very small along the central portion of the flux tube (close to the loop apex). Despite this near-uniformity between the internal and external Alfvén speeds for much of the height of the flux tube, we show that resonant absorption is still able to proceed.

Whilst such a model is not well-studied in terms of coronal physics, in the context of magnetospheric waves, previous investigations have demonstrated the existence of resonances associated with varying magnetic field strength and changes in field line length. In particular, an analytic treatment of resonances forming in fields with an invariant direction can be found in Wright and Thompson (1994). Furthermore, more recent studies (e.g. Wright and Elsden, 2016; Elsden and Wright, 2017) have explored the existence of resonant regions in fully three-dimensional (no invariant direction) magnetic fields.

Within the Earth's approximately dipolar magnetosphere, the field strength falls with height. Therefore, the natural frequency of magnetic field lines are modified in comparison to those in a uniform field regime. An analogy may be drawn with the solar atmosphere in which flux tubes emerging in dense patches from the lower levels of the solar atmosphere might be expected to expand rapidly within the coronal volume. A similar regime is explored in Khomenko et al. (2008), in which the authors explore the dynamics of propagating magnetoacoustic waves in small, expanding photospheric flux tubes.

In the remainder of this chapter, we aim to establish the possibility of resonant absorption occuring in magnetic loop-like structures that are bereft of any density enhancement. We initially explore the possible forms of such a flux tube and describe the selected model. Subsequently, we investigate the nature of the energy transfer in this regime and detail the formation of small scales as the mode conversion progresses.

Additionally, we present comparisons to simulations of straight field, density-enhanced flux tubes (the experiments discussed in Chapter 2) to highlight the differences between this model and the classical case.

4.2 Numerical Method

Before presenting initial conditions for our model, we begin by considering an azimuthally invariant cylindrical structure with uniform density and an internal enhancement of the magnetic field strength. The magnetic field is aligned with the axis of the flux tube throughout the domain. This configuration is associated with a radial magnetic pressure force and, in order to find an initial equilibrium, we consider solutions to the equation of motion (1.9), with $\mathbf{v} = \mathbf{0}$. Hence, we find

$$\nabla P = \mathbf{j} \times \mathbf{B} = \underbrace{(\mathbf{B} \cdot \nabla)\,\mathbf{B}}_{\substack{\text{Magnetic} \\ \text{Tension}}} - \underbrace{\nabla \left(\frac{B^2}{2\mu_0} \right)}_{\substack{\text{Magnetic} \\ \text{Pressure}}}. \tag{4.1}$$

We explore three cases for satisfying equation 4.1.

1. *External gas pressure enhancement* - We can balance the radial magnetic pressure force with an equal and opposite gas pressure force. Since we require the density to be uniform, this will be associated with an enhancement in the temperature of the external plasma. Further, this configuration requires $\beta > 1$ in the external medium which is not suitable for a coronal investigation. We therefore reject this case. However, it may be appropriate for representing a flux tube located within the lower layers of the solar atmosphere (see, for example, Yu et al., 2017).

2. *Twisted field* - The radially outwards magnetic pressure force can be balanced by an inwards magnetic tension force that is associated with twisted field. This is similar to the second equilibrium presented in the previous chapter (although the tension is now balancing magnetic pressure instead of thermal pressure). However, as we demonstrated, the inclusion of an azimuthal component of the magnetic field can complicate the wave dynamics (also see Karami and Barin, 2009, for example) and so is not suitable for this initial study.

3. *Field expansion* - Alternatively, an initially straight flux tube can be allowed to (numerically) relax to a state with $\mathbf{j} \times \mathbf{B} = \mathbf{0}$. In this regime, the original field is maintained at the loop foot points by preventing the expansion of the flux

tube on the boundaries. During the relaxation, the field strength will decrease within the magnetic structure as it expands, however, it can be constrained, to a limited degree, by tension in the field lines. Furthermore, the inclusion of a (weaker) background field in the external plasma will help to further constrain the expansion and ultimately allow a larger field strength within the flux tube to be obtained. In this case, the flux tube is not constant with height and longer loops will permit a greater expansion of the initial magnetic field.

For the remainder of this chapter, we will restrict our consideration to the third case.

4.2.1 Initial Set-up

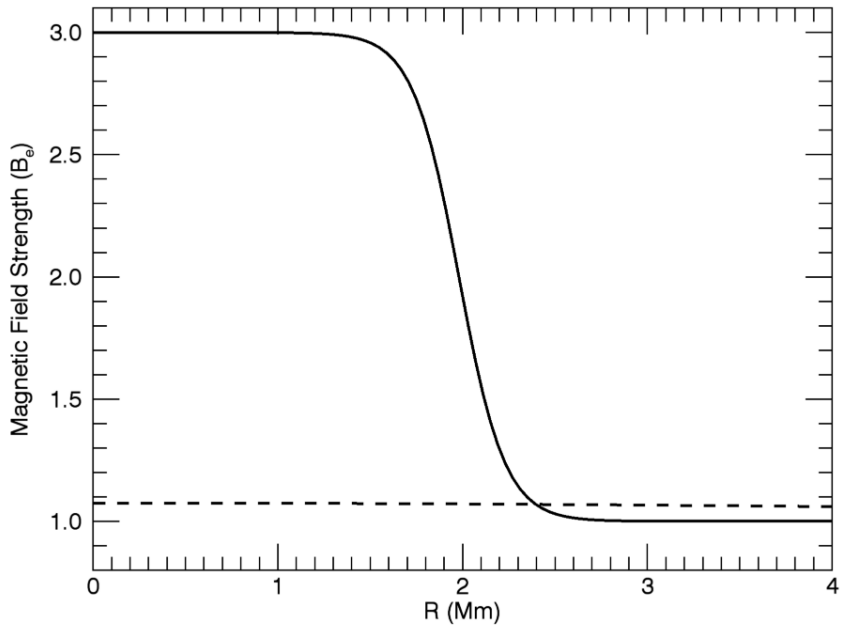

Figure 4.1: Initial magnetic field strength profile through the cross-section of the loop. The solid line shows the pre-relaxation field profile and, equivalently, the post-relaxation field profile at both of the z boundaries. The dashed line shows the field profile at the loop apex following the relaxation. In both cases, we have normalised by the initial, external field, $B_e = 5$ G.

We begin with a straight, vertically and azimuthally invariant magnetic flux tube with a field parallel to the loop axis. We impose an enhanced field strength within

the loop (relative to its exterior) of the form $\mathbf{B} = (0, 0, B_z(R))$ where R and z are the radial and loop-aligned coordinates, respectively. Furthermore,

$$B_z(R) = B_e + \frac{(B_i - B_e)}{2}\left(1 - \tanh\left\{\frac{R - r_a}{r_b}\right\}\right). \tag{4.2}$$

Here, $B_e = 5$ G and $B_i = 15$ G. They are the exterior and interior field strength, respectively. The parameters, r_a and r_b are set to produce a loop radius (prior to numerical relaxation) of approximately 2 Mm and a smooth transition from the exterior field to the interior field of approximately 0.8 Mm in width. The radial profile of this field is shown (solid line) in Figure 4.1. The loop length is 20 Mm. We note that this is short for a coronal structure and may be more representative of a transition region loop. The length of the structure is important for the observed wave dynamics and we explore this in more detail below.

We implement a numerical domain of $512 \times 512 \times 200$ grid cells and in order to minimise boundary effects, we adopt a non-uniform resolution profile in the x and y directions. This is similar to the non-uniform domain discussed in the previous chapters. In particular, the grid profile has a region of uniform resolution in the centre of the domain in which the important wave dynamics (e.g. resonant absorption) occur. However, since the flux tube (especially once expanded) has different dimensions, the exact nature of the non-uniformity is modified. The horizontal axes remain 32 Mm in length, however, the most refined resolution obtained in the central, uniform, region is 40 km (15.9 km previously). The coarser resolution ensures that the expanded, oscillating loop can be confined within the (larger) uniform region throughout the simulation, without increasing the number of grid points used in the horizontal directions. We note that the horizontal spatial resolution is less critical for this simulation as the small scales associated with the Kelvin-Helmholtz instability are not relevant for this study. The large displacement of the x and y boundaries from the centre of the flux tube is sufficient to ensure that, during relaxation (see below), the magnetic field is not artificially constrained by the boundaries of the domain. Meanwhile, the z direction has 200, equally-spaced, grid points in order to resolve the vertical gradients that form as a result of the flux tube expansion.

Numerical relaxation

Whilst maintaining a density of 1.67×10^{-12} kg m^{-3}, and a temperature of 1.8 MK, throughout the computational domain, we allow the magnetic field to relax towards a numerical equilibrium. A high value of viscosity is implemented in order to damp

the amplitude of the oscillations that form. However, the associated viscous heating is removed by overwriting the temperature (and density) at each time step. During the numerical relaxation, we maintain the initial magnetic field profile on the upper and lower z boundaries. Following this process, the magnetic field (numerically) satisfies $\mathbf{j} \times \mathbf{B} = \mathbf{0}$ with the exception of a narrow layer close to the top and bottom of the domain where the boundary conditions are associated with non-parallel currents.

Following the relaxation, the high viscosity is reduced to ensure that no significant flows are generated before the simulation is continued. The relaxation is considered complete once the velocities that form during this testing period are less than 0.5% of the amplitude of the introduced kink mode (see below).

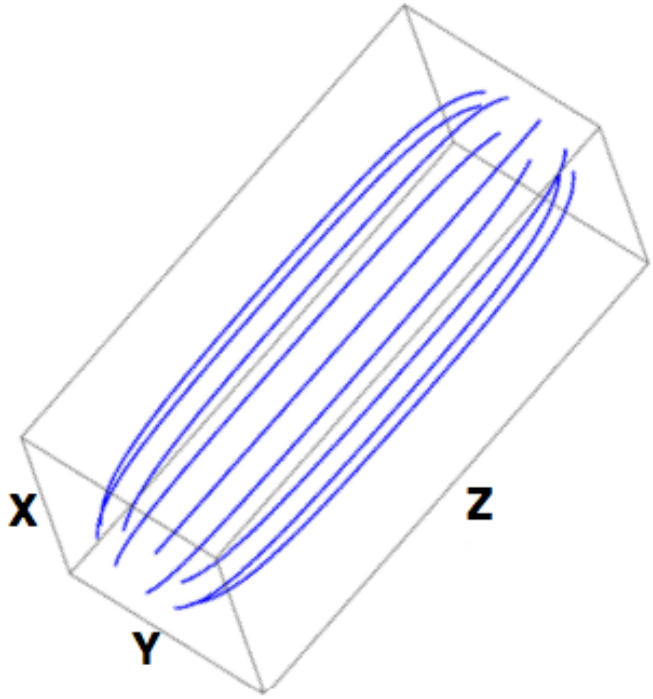

Figure 4.2: Magnetic field lines traced from $R = 2$ Mm on the lower z boundary after the numerical relaxation. Only a subsection of the full domain is shown; $|x| \leq 4$ Mm, $|y| \leq 4$ Mm, $|z| \leq 10$ Mm

In Figure 4.2, we display magnetic field lines (after relaxation) within the boundary region (traced from $R = 2$ Mm at $z = -10$ Mm) of the flux tube. We note that the box does not represent the full numerical domain and, as mentioned above, the flux tube expansion is not significantly restricted by boundary effects. Although the field expansion seems limited, in Figure 4.1 (dashed line) we see that the field strength does decrease significantly at the loop apex. Despite this, the magnetic flux lost from the central region of the loop structure is simply redistributed throughout the grid rather

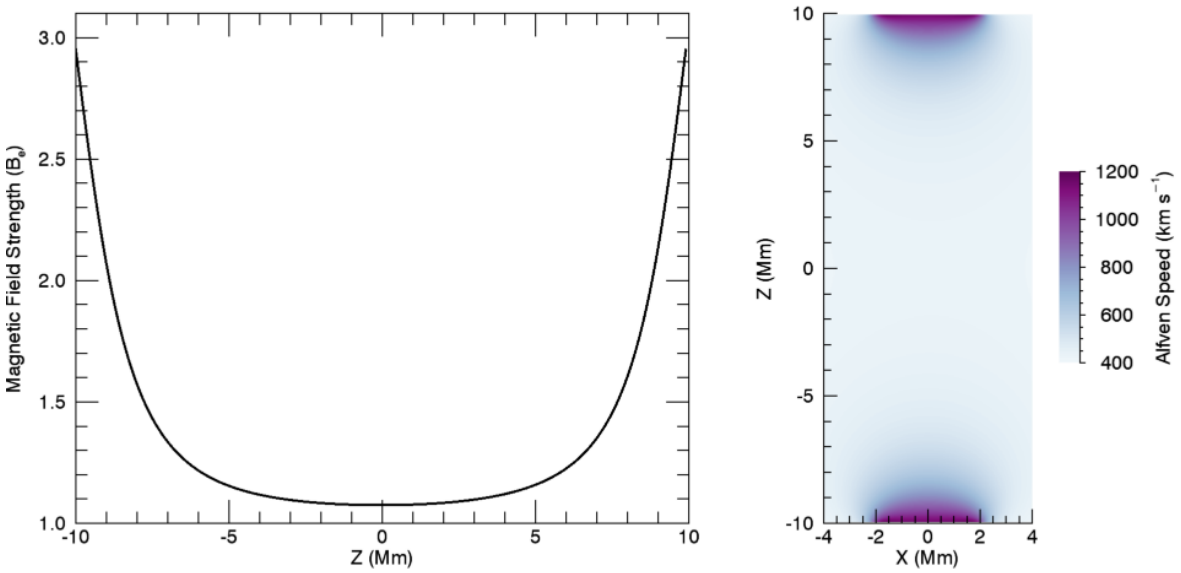

Figure 4.3: *Left*: Field strength variation along the flux tube axis (central field line). *Right*: Alfvén speed in a vertical cut through the loop axis ($x = 0$ plane). Both plots represent the conditions within the domain following the numerical relaxation.

than being lost from the computational domain.

In Figure 4.3, we consider the change in magnetic field strength along the loop axis (left-hand panel) and a vertical cut of the Alfvén speed (right-hand panel), following the numerical relaxation. Prior to the relaxation, these variables are uniform with height and thus the vertical gradients we see are associated with the expansion of the magnetic flux tube. We note that since the density is initially uniform, the Alfvén speed is simply proportional to the magnitude of the field. We observe that the majority of the expansion occurs close to both foot points and the central portion (-5 Mm $\leq z \leq$ 5 Mm) of the loop is almost uniform. We highlight that at the loop apex, the field strength within the flux tube is close (within 10 %) to that of the initial external field. Furthermore, we also note that the numerical relaxation conserves the azimuthal symmetry of the flux tube.

Since the magnetic field strength and the length of field lines vary along the radius of the loop, we see that there is a non-uniform profile of the natural Alfvén frequency across the structure. If we are able to find an estimate for the time period, τ, of a fundamental, standing Alfvén wave, then we can use the formula

$$\text{wave frequency } = \frac{2\pi}{\tau} \tag{4.3}$$

to find an estimate of the natural Alfvén frequency of a given field line. Since we have,

$$\tau = \text{ wave number } \times \text{ wave speed,} \tag{4.4}$$

we can find estimates for τ. In particular, we can use the Alfvén speed at the foot point of a field line and at the loop apex to find an upper and a lower bound, respectively, for the period of an Alfvén wave. Alternatively, we can recognise that the Alfvén speed varies along a field line and find an additional estimate of the wave period by calculating

$$\tau \approx 2 \int_L \frac{\mathrm{d}s}{v_A}. \tag{4.5}$$

Here, we integrate along a field line, $\mathrm{d}s$ is an infinitesimal line element and v_A is the local Alfvén speed. The factor of 2 is included as the length of the loop is only half of the wave length for a fundamental, standing mode.

In Figure 4.4, we show the estimates of the natural Alfvén frequencies of field lines across the cross-section of the loop calculated using this method. The solid line uses the position of field lines when traced from the lower z boundary and the dashed line shows their position at the loop apex. Clearly, the same field lines are identified in both cases and the difference between the two lines is simply indicative of the flux tube expansion.

Following the numerical relaxation, we impose a transverse velocity of the form $\mathbf{v} = (v_x, 0, 0)$ where

$$v_x = v_0 e^{-\left(\frac{R}{r_v}\right)^2} \cos\left(\frac{\pi z}{2L}\right). \tag{4.6}$$

Here, $v_0 \approx 13$ km s^{-1} is the maximum amplitude of the initial perturbation , r_v is a parameter that ensures the width of the velocity profile is approximately the radius of the apex of the expanded flux tube (see Figure 4.2) and $L = 20$ Mm is the length of the loop. We observe that the maximum velocity perturbation is much smaller than the local Alfvén speed throughout the flux tube. The cosine term generates a fundamental standing mode with the velocity set to zero at the footpoints and maximal at the loop apex ($z = 0$). We also note that the initial velocity profile in the loop cross-section was selected to reflect the magnetic field variation at the loop apex and is therefore different from the form described in the previous chapters. In Figure 4.5, we show the initial velocity profile in vertical (left-hand panel) and horizontal (upper right panel) cuts and along the central axis (lower right panel).

Since the flux tube does not have a constant radius (it expands with height), this

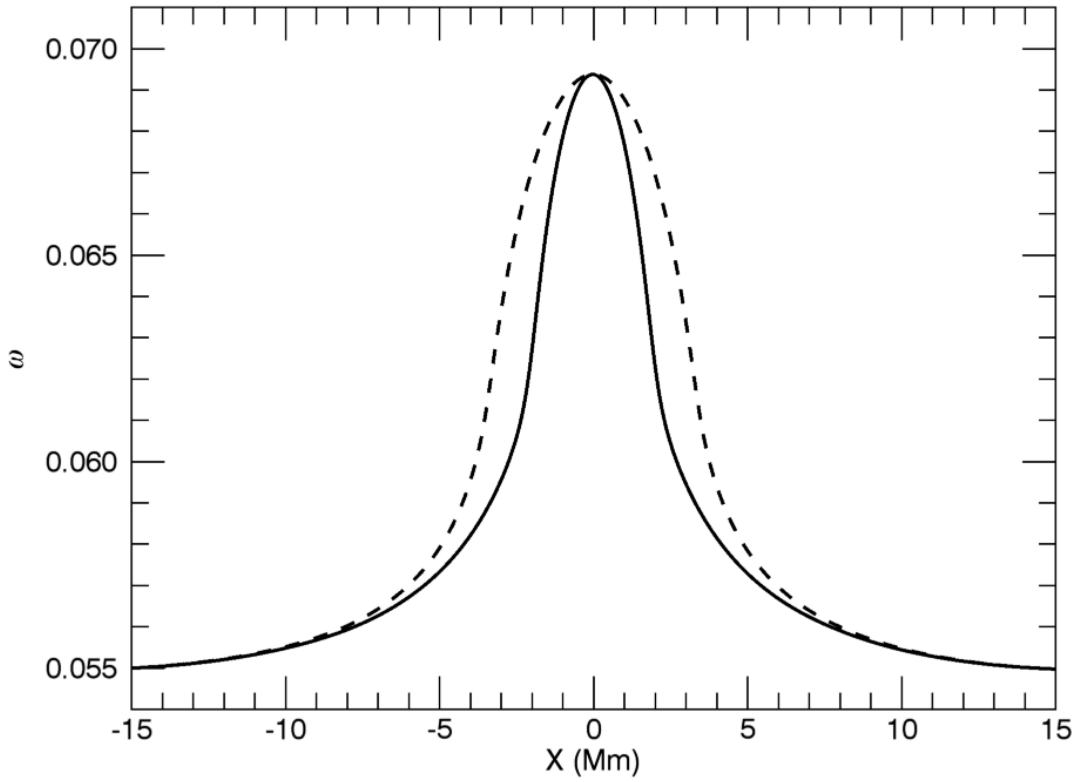

Figure 4.4: Natural frequencies of the fundamental standing Alfvén mode for magnetic field lines across the diameter of the flux tube. The solid line shows field lines traced from the lower z boundary and the dashed line shows field lines traced from the horizontal plane containing the loop apex.

velocity profile does not exactly coincide with the width of the loop along the entire height of the structure. However, previous studies (e.g. Pascoe et al., 2011, and the externally excited kink mode described in Chapter 2) have highlighted that the initial location of wave energy does not inhibit mode conversion. In particular, energy from both the internal and external plasma is readily transferred to Alfvén wave energy associated with resonant field lines. The main effect of the velocity profile not coinciding with the exact form of the magnetic flux tube is that higher wave harmonics are excited.

Boundary conditions

Throughout the simulations, we ensure that a node is located on both the upper and lower z boundaries by enforcing zero velocities in these locations. Meanwhile, all other variables have zero gradients at the loop foot points. The x and y boundaries are

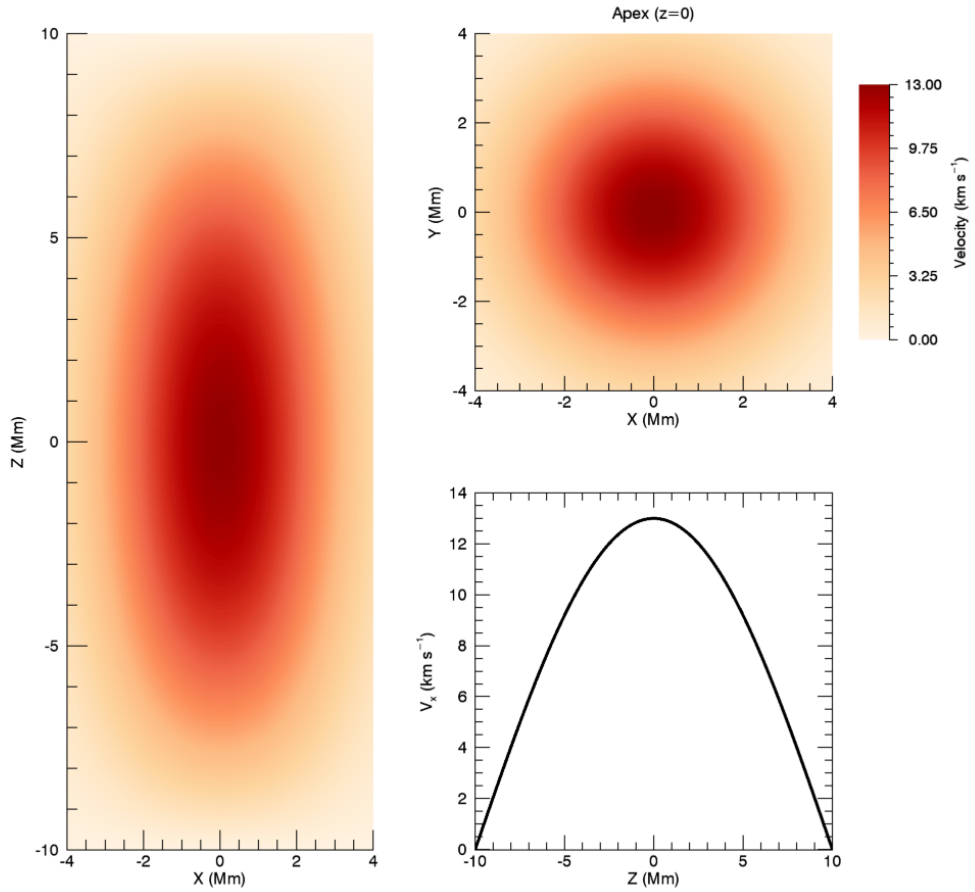

Figure 4.5: Initial velocity profile. Cuts in a vertical plane through the loop axis (left), a horizontal plane throught the loop apex (upper right) and a plot of v_x as a function of height along the loop axis (lower right).

periodic, however, in practice, flows are very small across these boundaries as a damping region is implemented at large $|x|$ and $|y|$ in order to minimise domain boundary effects on the oscillation. Throughout the duration of the simulation, the damping layers are well removed from the wave dynamics that are discussed hereafter.

The damping close to the boundaries is implemented within the regions satisfying $|x| \geq 25$ Mm or $|y| \geq 25$ Mm. In particular, for the positive x boundary, at each time step we multiply the velocity by a factor $a(x) \leq 1$ defined by

$$a(x) = 1 - d\left(\frac{x - x_{\min}}{x_{\max} - x_{\min}}\right), \tag{4.7}$$

where $d = 10^{-3}$ is a damping factor, $x_{\min} = 25$ Mm and $x_{\max} = 32$ Mm.

Within the remainder of the domain, low levels of user-implemented shock viscosities (see Chapter 1) are included in order to enhance numerical stability. As we shall see, these transport coefficients are associated with a slow dissipation of the azimuthal Alfvén waves that form as a result of resonant absorption.

4.3 Results

Following the imposition of the initial velocity profile, a standing kink wave is generated. As with the models presented in previous chapters, magnetic tension, and to a much lesser extent magnetic (and gas) pressure, act as the restoring forces. The period of the wave is observed to be approximately 106 s.

Using this time period, we find that the observed kink frequency is $\omega_k = 0.0593$. In a straight and slender flux tube with loop-aligned invariance, the kink speed, v_k can be expressed as (e.g. Nakariakov and Verwichte, 2005)

$$v_k = \sqrt{\frac{\rho_i v_{A,i}^2 + \rho_e v_{A,e}^2}{\rho_i + \rho_e}}, \tag{4.8}$$

where a subscript i denotes a variable within the flux tube and a subscript e denotes a variable within the external plasma. We see that equation 4.8 corresponds to a density-weighted average of the internal and external Alfvén speeds. In our model, in which the equilibrium density is constant, $\rho_0 = 1.67 \times 10^{-12}$ kg m^{-3}, this reduces to

$$v_k = \sqrt{\frac{B_i^2 + B_e^2}{2\mu_0 \rho_0}}, \tag{4.9}$$

Whilst the assumptions used in deriving this wave speed are not completely valid for the flux tube presented here, we can use the relations in equations 4.4 and 4.9, to find an estimate of the expected kink frequency. We note that more sophisticated expressions for the kink frequency in a flux tube with a loop-aligned variation in the Alfvén speed are presented by Andries et al. (2005) and Dymova and Ruderman (2006). However, in these cases, the ratio between the internal and external Alfvén speeds are constant and thus the derived formulae are not directly applicable here.

Since the kink speed varies with height, we find three estimates for the expected frequency. Firstly, we use the maximum kink speed (located at the foot points of the flux tube), secondly, we use the minimum kink speed (located at the apex of the flux tube) and thirdly, we track the change in kink speed along the loop. For this third

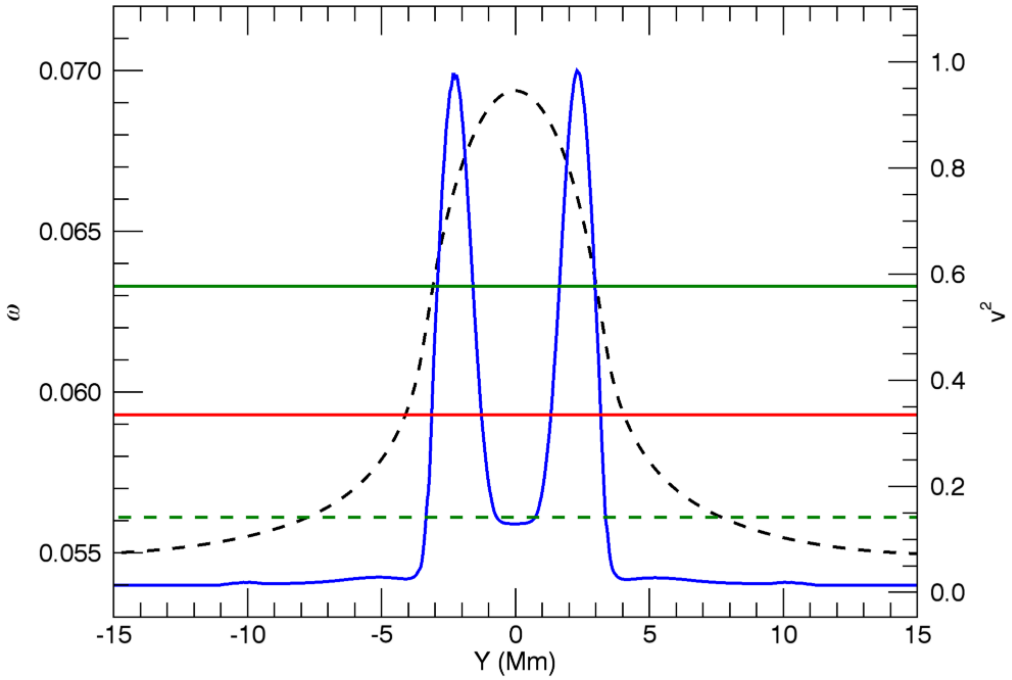

Figure 4.6: *Black dashed line*: Estimates of the natural Alfvén frequencies of field lines at the loop apex. *Red line*: Observed kink frequency. *Green lines*: Theoretical estimates of the frequency of the fundamental kink mode using the kink speed, v_k, at the loop apex (dashed line) and tracking v_k as a function of position along the loop axis (solid line). The estimate calculated using the kink speed at the loop foot points is significantly larger and is thus omitted from the figure. *Blue line*: Square of azimuthal velocity integrated over a wave period once significant energy has been transferred through resonant absorption (see below). This is normalised to the maximum value observed.

method, as with the Alfvén frequency estimates in the previous section, we approximate the time period as

$$\tau_k \approx 2 \int_{z_{min}}^{z_{max}} \frac{dz}{v_k}. \tag{4.10}$$

In this case, we note that we integrate along the z axis and not along individual field lines.

In Figure 4.6, we show the second (dashed green line) and third (solid green line) estimates compared to the observed frequency of the kink mode. The first estimate (employing the kink speed at the loop foot points) yields a frequency of 0.121 which is not displayed in order to improve the clarity of the figure. For reference, we also include the natural Alfvén frequencies of field lines at the loop apex (dashed black

line). This is identical to the curve shown in Figure 4.4. The nature of the solid blue curve will be considered in the next section. As expected, the observed kink frequency is bounded by the first and second estimates which represent the extrema of the kink speed within the domain.

4.3.1 Resonant Absorption

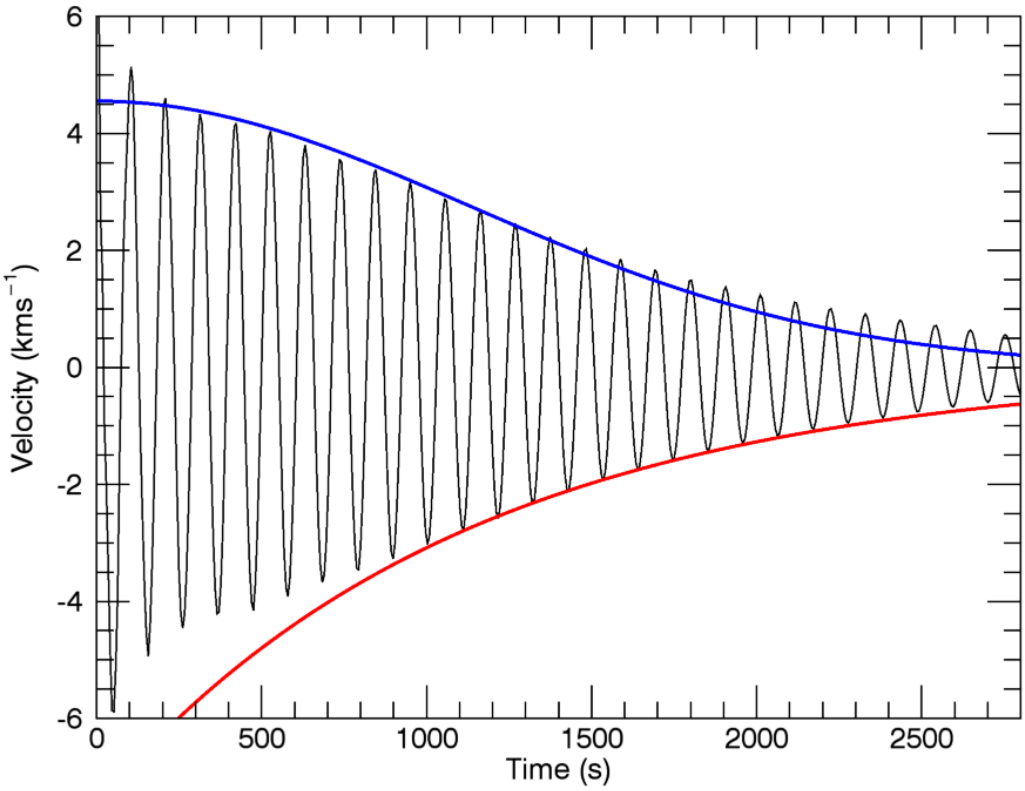

Figure 4.7: Velocity at the centre of the flux tube cross-section indicating the damping rate of the kink mode. Two damping profiles are also displayed. Upper: Gaussian (blue) profile. Lower: exponential (red) profile.

In Figure 4.7, we track the kink mode oscillation by plotting the velocity in the centre of the flux tube (at the loop apex) as a function of time. We see that the maximum velocity in the initial perturbation is much larger than the amplitude of the kink mode that is ultimately excited. We conclude that much of the energy associated with the initial velocity profile is transferred to the external dipole flow (see upper right-hand panel of Figure 4.8) and does not remain within the centre of the flux tube.

Subsequently, we observe that, even in ideal conditions, the kink wave experiences damping at a significantly higher rate than can be accounted for by the small amount of dissipation included within the simulation. We interpret this behaviour as evidence of resonant absorption even though the usual density contrast is absent. The required gradient in the Alfvén frequency is instead associated with a radial change in the magnetic field strength and the length of field lines.

In Figure 4.7, we have included two decay profiles; the more typical exponential decay (blue) and a Gaussian curve (red). We note that the Gaussian fit is more suitable until around $t = 1200$ s, at which time the exponential curve becomes more appropriate. This is in agreement with Pascoe et al. (2013), in which the authors demonstrate that resonant absorption is associated with an initial phase of Gaussian damping before exponential decay dominates at later times.

In the aforementioned work, the time of the switch between the damping profiles is shown to critically depend on the width of the boundary layer of the flux tube. This allows the potential for coronal seismology to deduce information regarding the structure of the flux tube (Pascoe et al., 2016b). However, it remains unclear whether the vertical structuring of the Alfvén speed profile will permit the implementation of this technique with the current model.

As in the previous chapters, the process of resonant absorption transfers energy from the kink mode into energy associated with azimuthal Alfvén waves. This is readily observed in the velocity field displayed in Figure 4.8. In the left-hand panel we show the initial velocity profile (corresponds to Figure 4.5). This demonstrates that the majority of the initial kinetic energy is contained within the central region of the flux tube. As this plasma moves, it is replaced by external plasma (and magnetic field) and thus a dipole flow forms immediately. This persists over many wave periods (second panel) as the kink mode decays. Throughout the simulation, resonant field lines are excited by the kink mode and begin to oscillate as part of an azimuthally polarised Alfvén wave which can be observed in the lower panels of Figure 4.8. At these times, we see that there is little kinetic energy remaining within the central region of the flux tube.

The mode conversion transfers wave energy from the central region of the flux tube, to the boundary between the internal and external plasma. This boundary is well-defined close to the loop foot points, however, due to the expansion of the flux tube, it is much less apparent close to the loop apex. Indeed, we can easily see this by comparing the solid and dashed line in Figure 4.1. In particular, at the loop apex, there is very little change in the magnetic field strength between the interior and exterior of

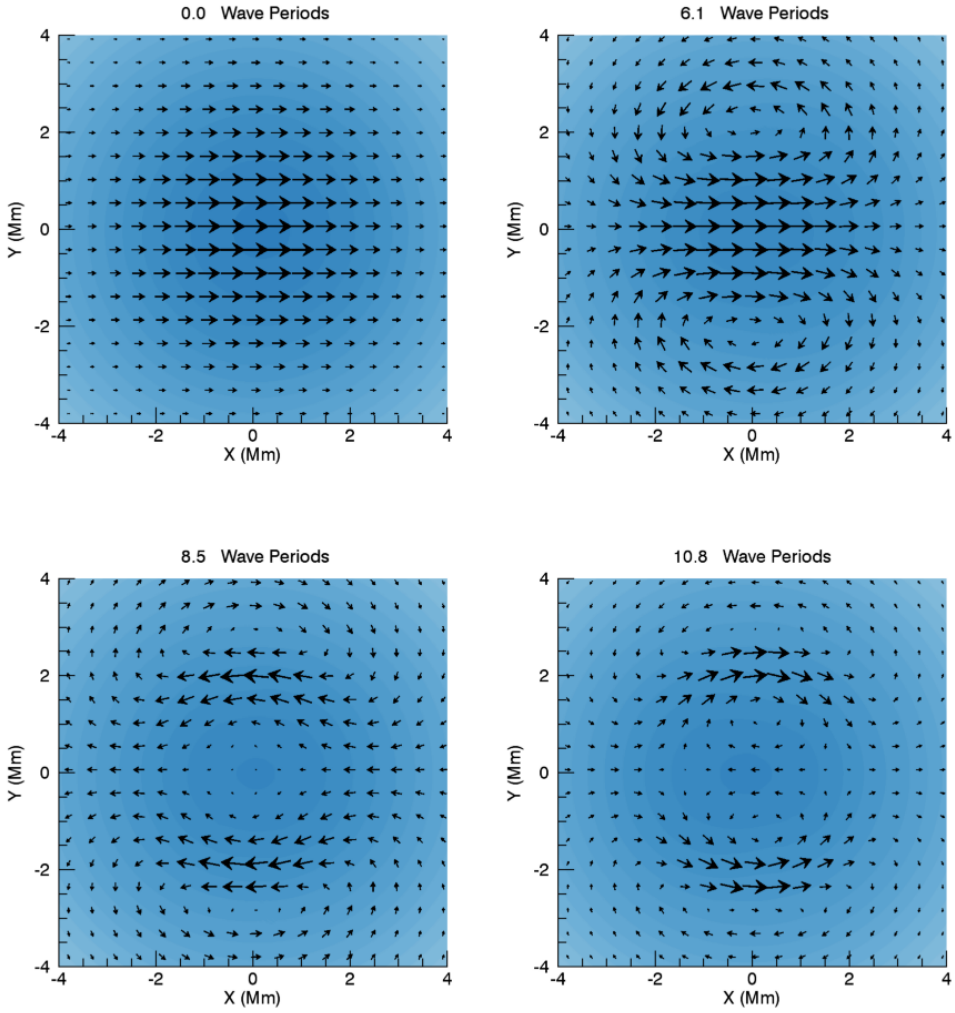

Figure 4.8: Velocity vectors in the horizontal plane at the loop apex. The background contour plots depict the magnetic field strength. *Upper left*: The initial velocity profile. *Upper right*: A dipole flow has formed. *Lower*: Resonant absorption gradually transfers the kink mode energy into the azimuthal Alfvén wave located within the boundary of the flux tube.

the flux tube. We highlight the result that resonant absorption can still occur even if there is no gradient in Alfvén speed along large sections of a magnetic flux tube.

As with the previous models presented within this thesis, the process of resonant absorption will deposit wave energy on resonant field lines within the boundary of the flux tube. As such, if we integrate in time over several wave periods once significant energy conversion has occured, then we expect that wave power will be greatest on resonant field lines. Since the density is uniform throughout the domain, this integral is proportional to the blue curve in Figure 4.6. We see that the estimate of the natural Alfvén frequency of the field lines at the locations of peak wave power ($y \approx \pm 2.5$ Mm) does not coincide with the observed kink frequency. This difference will be partially

due to equation 4.5 providing a poor estimate for the exact period of the Alfvén wave. In particular, this may be associated with the present model violating the thin flux tube assumption (e.g. Nakariakov and Verwichte, 2005). Additionally, the generation of higher harmonics by the initial velocity perturbation will also modify the energy conversion.

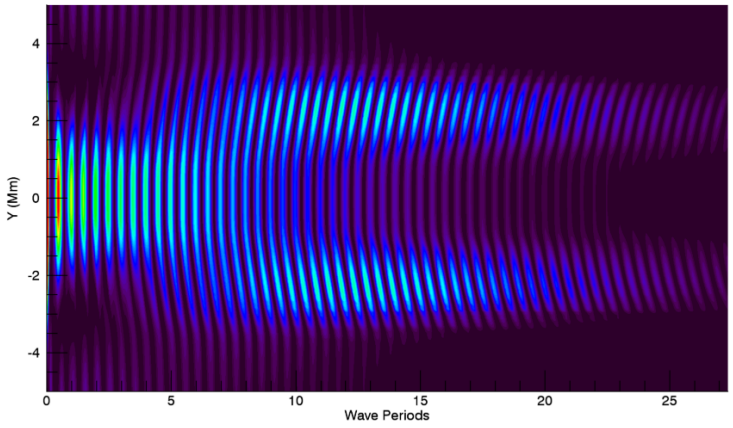

(a) Non-uniform magnetic field, uniform density.

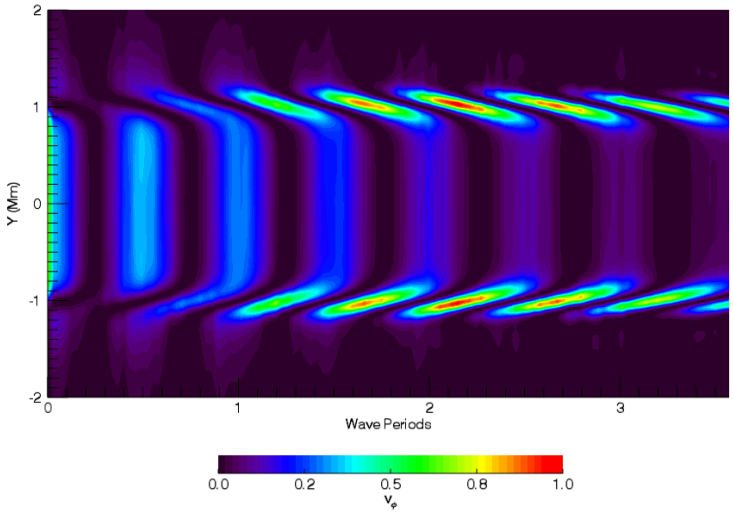

(b) Uniform magnetic field, non-uniform density.

Figure 4.9: Transfer of wave energy during resonant absorption. We show the square of the azimuthal velocity, v_ϕ^2, along a diameter through the loop apex and as a function of time. In each case, we have normalised by the maximum value observed during the simulation.

In Figure 4.9, we show how the location of kinetic energy along the line $x = z = 0$ (a vertical line through the loop centre when viewed in the panels in Figure 4.8) changes throughout the course of the simulation. We show the simulation described within this chapter (upper panel) and, for comparison, the $\eta = \nu = 10^{-4}$ simulation outlined in Chapter 2. We note that the flux tube is significantly longer than in the case presented

within this chapter. Since the observed kink frequency is different in both experiments, we display the energy transfer as a function of the number of wave periods.

In both simulations, we see that energy is transferred from the core region to the boundary of the loop as time progresses. It is clear that resonant absorption occurs much more quickly (in terms of wave periods) in the straight field simulation. This is intuitive given that the Alfvén speed gradient (a critical requirement for resonant absorption to proceed) is significant along the entire length of the flux tube in the straight field case, but not in the expanding structure. Indeed, in the simulation described here, the Alfvén speed is almost constant throughout the cross-section at the loop apex. Importantly, there is a larger contrast between the natural Alfvén frequencies of field lines inside and outside of the flux tube in the straight field case than in the expanding magnetic field simulation.

Another important difference between the two simulations can be observed by considering the orientation (direction) of the wave fronts in the two panels of Figure 4.9. In the upper panel, an Alfvén wave front appears to propagate away from the centre of the loop, whereas in the lower panel, this behaviour is reversed. This phenomenon is associated with the relative interior and exterior Alfvén frequencies in the two simulations. In the flux tube with the density enhancement, the Alfvén speed (and thus the natural frequency) within the loop is lower than in the exterior plasma. Hence, a standing Alfvén wave will be first observed on field lines at the edge of the boundary region. The lower frequency field lines closer to the loop centre will oscillate at a slightly later time, and hence the wave front appears to propagate towards the centre of the loop. In the simulation corresponding to the upper panel, the natural Alfvén frequencies of field lines within the flux tube are higher than in the external plasma and thus, the opposite effect is observed. This inversion (with respect to the typically modelled case) might be expected in chromospheric flux tubes (if the internal frequency is higher than the external frequency) but is unusual for a coronal simulation.

At the apex, the radial Alfvén frequency gradient is much more pronounced across the diameter of the loop in the straight field simulation than in the expanding field case. Therefore, oscillating field lines will become out of phase at a faster rate for the density-enhanced loop. As such, we expect phase mixing to occur more readily in this regime. Indeed, by considering vertical lines in the two contour plots in Figure 4.9, we can see that radial gradients in the azimuthal velocity are typically larger in the lower panel. However, in the new model, close to the loop foot points, the gradients in the magnetic field remain significant. Therefore, we can expect significant phase mixing close to the z boundaries. Whilst the velocity field is small in these locations,

the magnetic field perturbation is more significant and phase mixing in a non-ideal regime could lead to wave energy dissipation through Ohmic heating. This effect could enhance heating close to the loop foot points and is considered in more detail below.

Additionally, the late time behaviour displayed in the upper panel of Figure 4.9 shows a slow decrease in wave amplitude. This occurs for two main reasons. Firstly, the amount of energy being injected into the azimuthal Alfvén mode decreases as the majority of the initial kink mode energy has been exhausted. Secondly, the wave amplitude is damped by the shock viscosities and numerical diffusion as phase mixing progresses.

4.3.2 Alfvén Wave Structure

On account of the expansion of the flux-tube with height, a narrow resonant layer of field lines at the loop foot point, maps to a much wider layer close to the loop apex. Accordingly, the width of the Alfvén wave varies with height along the flux tube. In particular, it exists over a much smaller horizontal extent close to the upper and lower z boundaries than at the loop apex.

In Figure 4.10, we display the vertical form of the Alfvén wave once significant energy has been transferred from the kink wave. The upper panels correspond to the kinetic (left) and magnetic (right) wave energy, integrated over a wave period. The lower left-hand panel is simply the sum of the two upper panels. The lower right-hand panel corresponds to the straight field simulations presented in Chapter 2. As with the lower left panel, it shows the sum of the magnetic and kinetic wave energy integrated over a wave period.

In the top left panel of Figure 4.10, we observe that the magnitude of the kinetic energy is largest at the loop apex which coincides with the location of the maximum speed in the initial velocity profile (left-hand panel of Figure 4.5). Meanwhile, the magnetic component (upper right panel) of the wave energy is largest at the loop foot points as this is where the perturbation of the magnetic field is greatest. Since we generate a standing wave, the velocity and magnetic field perturbations are out of phase, however, integrating over a wave period means we might expect the wave energy to be approximately constant along a field line. This is indeed the case in the straight flux tube case (lower right panel) as the resonant layer does not change along the length of the loop axis (notwithstanding any density deformation associated with the development of the Kelvin-Helmholtz instability). At a radius of $R \approx 1$ Mm, we see that the integrated Alfvén wave energy is approximately constant with height.

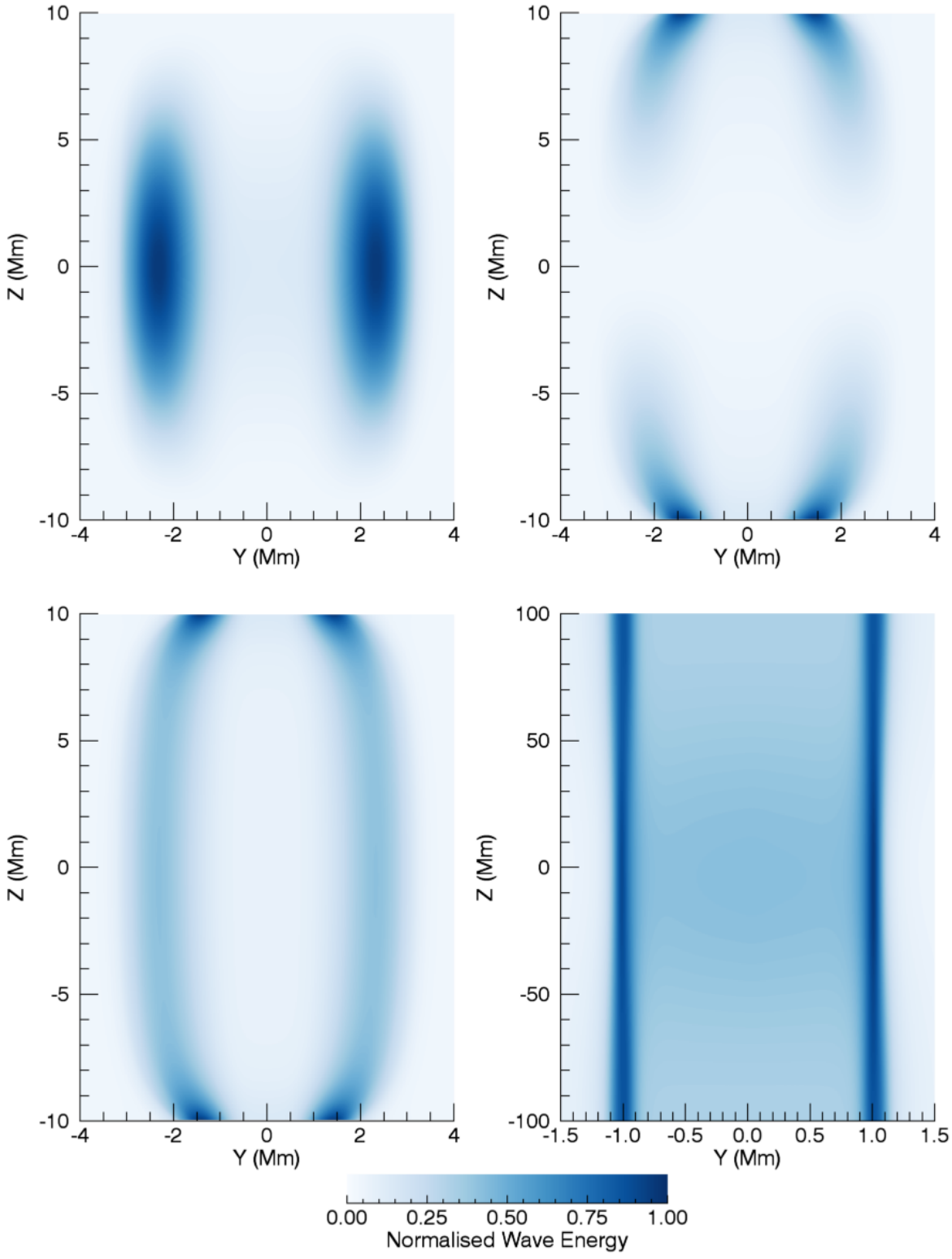

Figure 4.10: Vertical cuts through the flux tube highlighting the structure of the Alfvén wave. The upper two panels show the kinetic (left) and magnetic (right) wave energy, integrated in time over a full period. The lower left panel is the sum of the two components of wave energy and the lower right panel is an analogous plot using data from straight field (no magnetic expansion) simulations. In each case, we have normalised by the maximum value in the respective cut.

However, this is not the case in the expanding field simulation, even when the shape of the field lines is accounted for. Whilst the energy integrated over the cross-section of the flux tube is approximately constant with height, we see that wave energy becomes more concentrated close to the foot points. This phenomenon is associated with the density of magnetic field lines increasing close to the upper and lower z boundaries. We note that the generation of smaller scales at the loop foot points may be important in the context of wave energy dissipation. We shall explore this in more detail below.

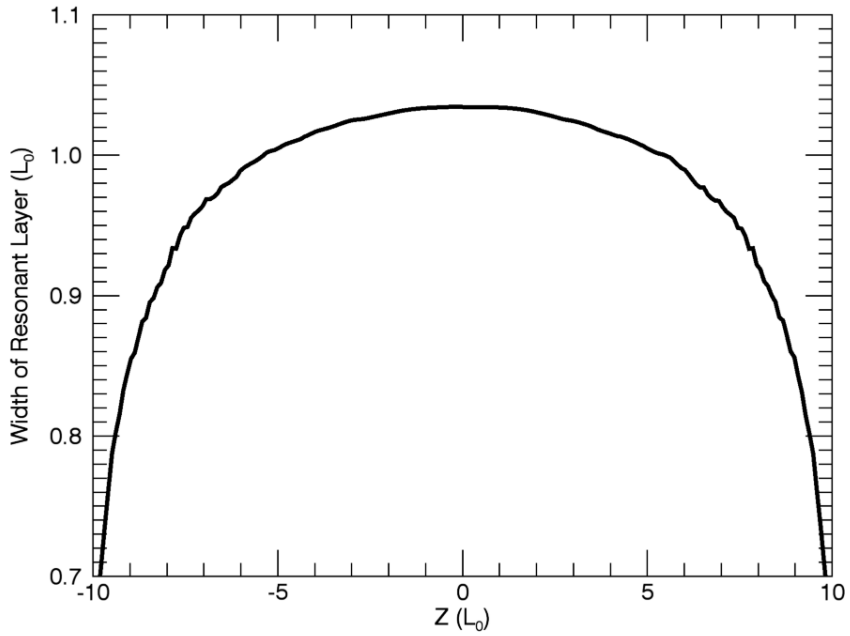

Figure 4.11: Width of the resonant layer as a function of height along the flux tube.

The uniform (with height) flux tube is able to sustain a narrow region of resonant field lines along the entire length of the structure. However, the field expansion considered here results in the resonant layer being much wider in comparison to the loop length. The width of this layer as a function of height is shown in Figure 4.11. Here, the width is calculated using the full width at half maximum of the azimuthal velocity profile for one wing of the Alfvén wave at each height within the domain. Since most of the expansion of the flux tube occurs close to the foot points (see Figure 4.3), we observe that the greatest change in the width of the resonant layer occurs closes to the upper and lower boundaries of the domain.

The smaller (in relation to the kink mode) length scales of the Alfvén wave are important in the context of wave energy dissipation, and hence coronal heating. The

gradients in the velocity and magnetic fields are larger for the localised wave mode and hence the effects of viscosity (on the velocity field) and resistivity (on the magnetic field) are more significant. In the case presented within this paper, the horizontal length scales associated with the Alfvén wave change with height (this is not true for the straight field case). As such, we may expect the Alfvén wave energy to be more sensitive to transport coefficients away from the apex of the flux tube. Indeed, as mentioned previously, this may encourage a greater rate of energy dissipation close to the loop foot points and further enhance the Ohmic heating identifed by Van Doorsselaere et al. (2007); Karampelas et al. (2017). However, a rigorous consideration of the system in a non-ideal regime is beyond the scope of this thesis and will be considered in subsequent work.

The expansion of the magnetic flux tube reduces the radial non-uniformity in natural field line frequency and thus, we observe a slower rate of wave energy conversion in the magnetically defined flux tube than in the straight field case (see Figure 4.9). Furthermore, the lower right-hand panel of Figure 4.10 exhibits a very narrow Alfvén wave along the entire length of the flux tube and thus we expect a higher rate of wave energy dissipation in the straight field case. Since the rate of resonant absorption and the rate of Alfvén wave dissipation are both lower in the expanded field regime, we anticipate that this model would be (in non-ideal simulations) less efficient at converting the initial kink mode energy into heat.

4.3.3 Current and Vorticity

As with the simulations presented in the previous chapters, the small scales associated with the Alfvén wave manifest in the form of currents (for the magnetic field) and vorticities (for the velocity field). Furthermore, the radial non-uniformity in natural Alfvén frequency will induce out-of-phase wave behaviour on neighbouring field lines. This leads to an enhanced rate of small scale formation through phase mixing.

In Figures 4.12 & 4.13, we display the current density and vorticity, respectively, associated with the azimuthal Alfvén wave, for both the expanding flux tube (left-hand panels) and straight field (right-hand panels) cases. To generate these plots, for both simulations, we consider a time (expanding field; $t = 1900$ s , straight field; $t = 460$ s) after a significant amount of energy has been transferred from the global wave to the localised modes. For the left-hand panels, the shape of the expanded flux tube remains apparent in these plots and corresponds to the Alfvén wave structure (Figure 4.10). For both the current density and the vorticity figures, the plotted quantities are

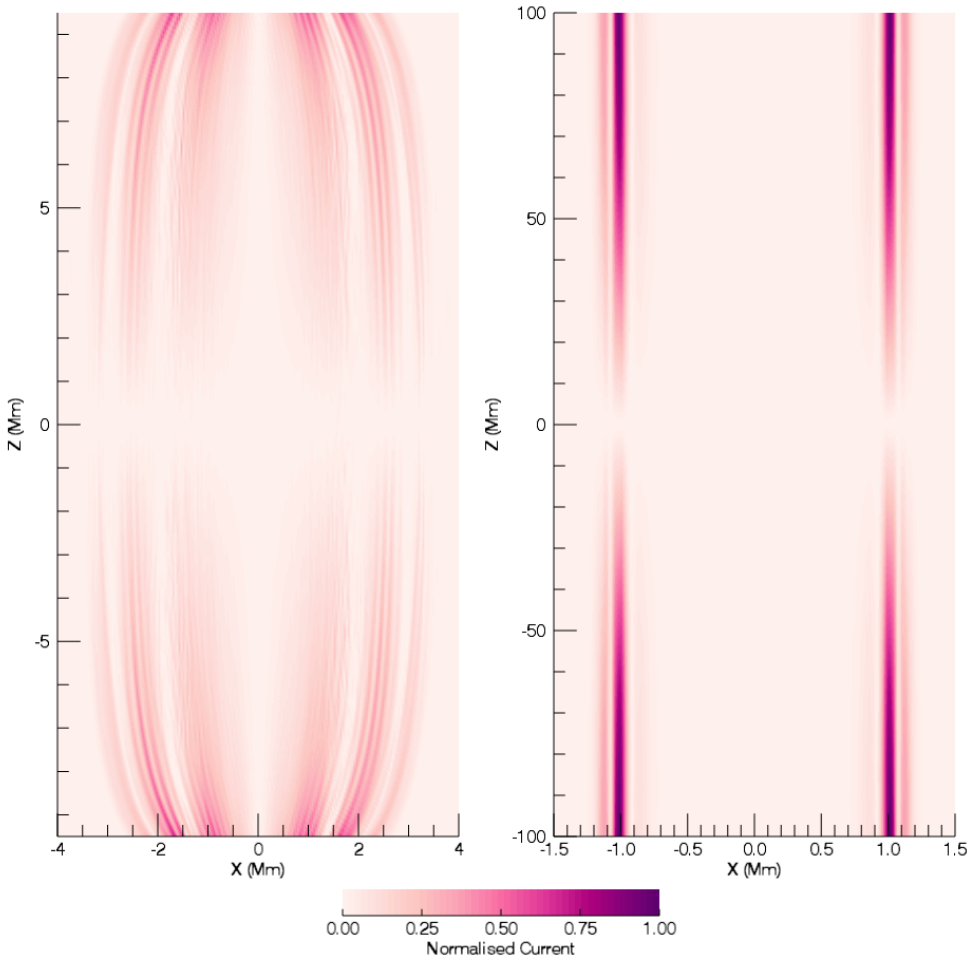

Figure 4.12: Magnitude of the current density, $|\mathbf{j}|$, associated with the azimuthal Alfvén wave. We show a vertical cut through the flux tube for the expanding field case (left) and straight field case (right). In both cases, we have normalised by the maximum current density observed in the respective plane.

dominated by the field-aligned component. This is simply given by j_z and ω_z for the straight field case, however, away from the loop apex, there is a horizontal component in the expanding flux tube simulation.

As discussed previously, over the course of a wave period, the energy in a standing Alfvén wave is partitioned into kinetic energy (located close to the antinode) and magnetic energy (located close to the nodes). This ensures that the largest currents form close to the foot points of the magnetic flux tube and the largest vorticities form close to the loop apex. This phenomenon is independent of the form of the flux tube and is discussed in more detail by Karampelas et al. (2017). In this case, it can be observed by comparing the location of the largest current density and vorticity (for

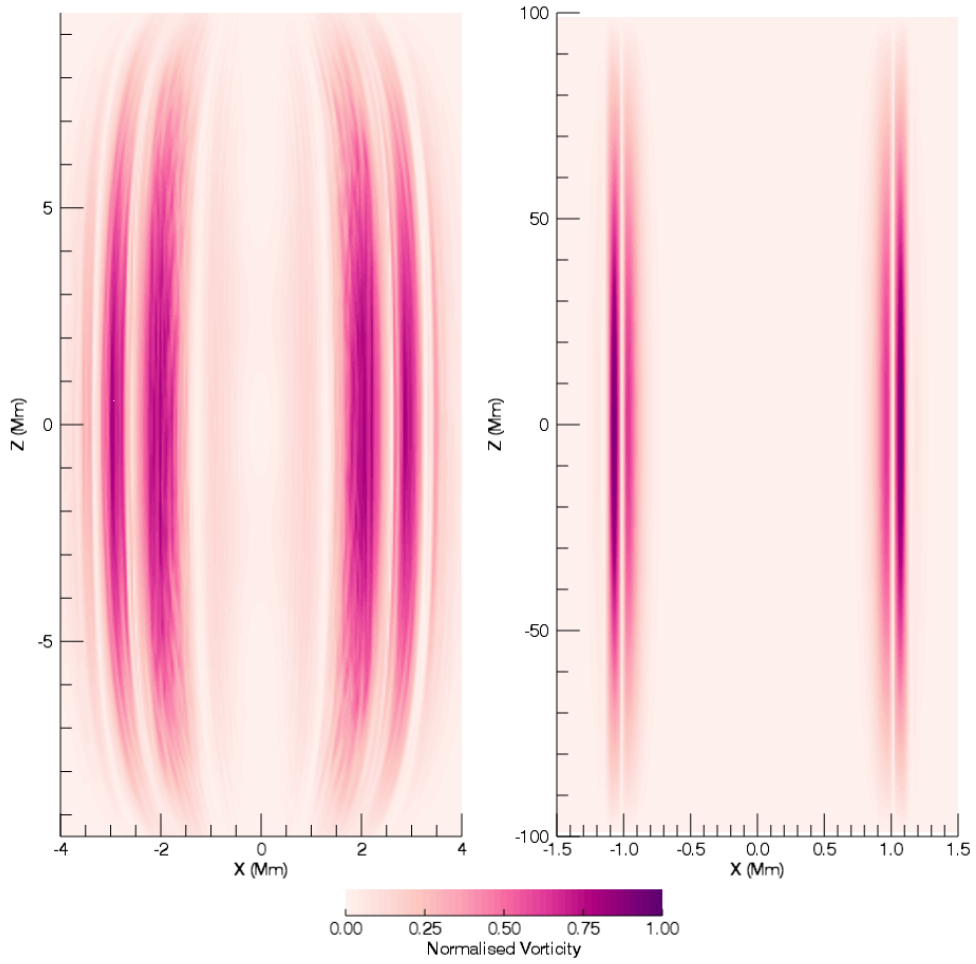

Figure 4.13: Magnitude of the vorticity, $|\boldsymbol{\omega}|$, associated with the azimuthal Alfvén wave. We show a vertical cut through the flux tube for the expanding field case (left) and straight field case (right). In both cases, we have normalised by the maximum vorticity observed in the respective plane.

both simulations) in Figures 4.12 & 4.13.

The large-scale, strand-like structures that appear in all of the contour plots are indicative of phase mixing. As time progresses, the largest gradients associated with the out-of-phase Alfvén waves move across radial shells and thus, in a non-ideal regime, energy will be deposited throughout the phase mixing layer. Additionally, we note that, for both simulations, these large scale structures are out of phase between the current density and vorticity plots (comparing the left-hand panels of Figures 4.12 & 4.13, for example). This is because the magnetic and velocity perturbations of the standing Alfvén waves, and hence their associated gradients, are also out of phase.

As resonant absorption transfers energy from the global mode to localised waves,

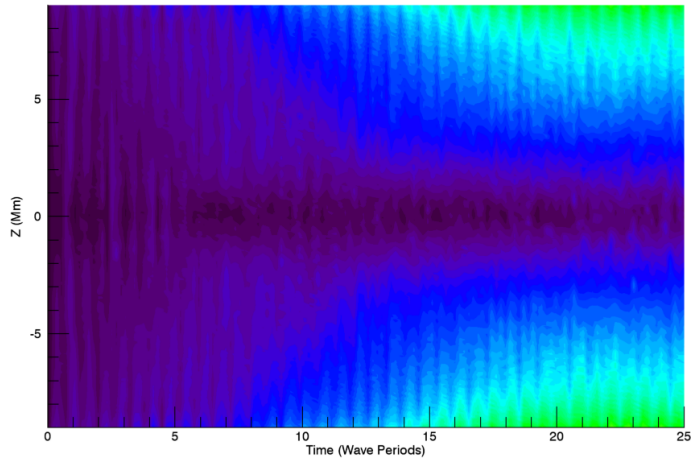

(a) Current.

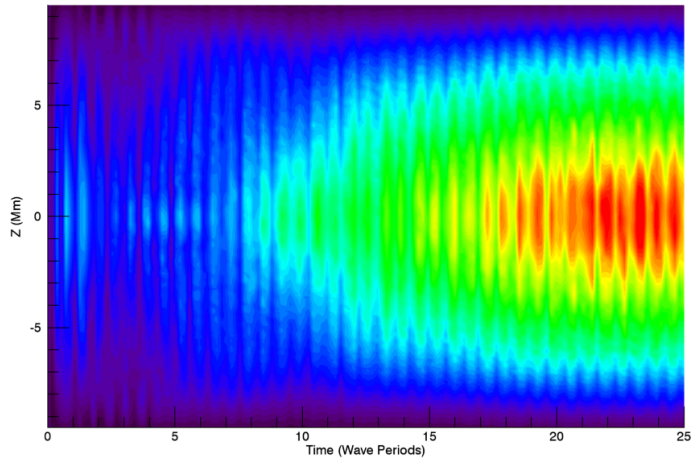

(b) Vorticity.

Figure 4.14: Total current (upper panel) and vorticity (lower panel) across loop cross-section as a function of distance along the loop and time

the magnitude of currents and vorticities within the numerical simulation will increase. This can be observed in Figure 4.14 for the currents (upper) and vorticities (lower), respectively. In each case we integrate the magnitude of the vectors over the loop cross-section at each height and display this quantity as a function of time. The corresponding plots for the (ideal) straight field simulation are displayed in Figure 2.14, however, in this case we note that the small scales are dominated by the development of the Kelvin-Helmholtz instability. We observe that the KHI does not form within this simulation as the large width of the resonant layer at the loop apex ensures that the radial velocity shear is too low.

In Figure 4.14, the formation of small scales as resonant absorption progresses can be observed and once again we note that vorticity dominates at the loop apex and

currents dominate at the loop foot points. The small peak in vorticity at the beginning of the simulation corresponds to velocity gradients associated with the initial kink mode. Since the magnetic energy is concentrated over a smaller region than the kinetic energy (see Figure 4.10), the associated spatial gradients are typically larger. As such, we anticipate that for comparable values of resistivity and viscosity, Ohmic heating (acting at the loop foot points) will be the more significant dissipation mechanism.

4.4 Discussion and Conclusions

Within this chapter, we have presented a model of an expanded magnetic flux tube oscillating with a standing, transverse, kink mode. Many previous studies (including the models presented in Chapters 2 & 3) have considered similar MHD waves in coronal loops with an internal density enhancement. However, in this case, the density is constant throughout the initial conditions, and instead we rely on a radial gradient in the magnetic field strength to allow resonant absorption to occur. In either case, it is widely accepted that the presence of a transverse Alfvén frequency gradient will permit resonant absorption to augment the decay of the fundamental kink mode as energy is transferred to localised, azimuthal Alfvén waves.

We have confirmed that, even in this modified case, the mode conversion leads to an initial phase of Gaussian decay in the amplitude of the kink wave before a subsequent period of exponential damping occurs. The induced azimuthal waves exist over much smaller spatial scales than the global mode and are associated with larger gradients in the magnetic and velocity fields. As with the straight field simulations, these gradients correspond to currents and vorticities that increase in magnitude as the resonant absorption progresses. The expansion of the flux tube ensures that the width of the Alfvén wave is much smaller close to the foot points than at the loop apex. Hence, given comparable resistivity and vorticity coefficients, in a non-ideal regime we can expect Ohmic heating to be the dominant cause of wave energy dissipation (Van Doorsselaere et al., 2007).

The absence of any density enhancement implies that the waves described within this chapter would be very difficult to detect even with the increased capabilities of contemporary observational instruments. Indeed, the initial flux tube is invisible to all but sensitive magnetic field measurements which are not currently possible within the coronal volume. Detecting the wave itself may be possible using Doppler velocities and line widths, however, favourable conditions are required as flows within dense structures along the line of sight will likely dominate any observed signal. Despite this,

the next generation of solar telescopes such as DKIST and EST, will hopefully provide insight into such magnetic structures within the Sun's atmosphere.

Regardless of observational difficulties, it could be expected that such flux tube structures exist throughout the corona. Magnetic field within the outer solar atmosphere is typically connected to small scale flux patches in the photosphere/chromosphere, and as the field emerges into a low plasma-β, regime, in order to maintain an equilibrium, it must become approximately force free. Thus, if we assume low levels of magnetic twist, it is reasonable to expect the field to expand significantly with height. As we have shown, in order to fully explain the damping behaviour of fundamental standing waves at high altitude, the expansion of the magnetic field closer to the solar surface should be considered. In particular, the global frequency of the field line is critically important and cannot simply be inferred from the local frequency at the loop apex. It is not possible to accurately predict the decay of a standing kink mode unless the Alfvén speed is well constrained along the entire length of the flux tube. Ultimately, we have shown that resonant absorption can still occur even if there is little change in the Alfvén speed across the cross-section of the loop apex.

Since the flux tube presented here is short (in comparison to the loop radius), it may be more representative of transition region loops than the long coronal structures that are frequently modelled with radial density enhancements. The rapid expansion of the flux tube presents numerical difficulties as a large number of grid points parallel to the loop axis is required to resolve the spatial gradients that exist close to the foot points. This is in contrast with the straight loops that are typically uniform along their length and thus can be modelled numerically with much coarser spatial resolution along the loop-aligned axis. Since the rate of expansion with height only weakly depends on the length of the loop, the number of grid points required along the z axis may be prohibitive for modelling significantly longer structures. However, we expect that resonant absorption will transfer energy at a slower rate for longer flux tubes that are almost uniform (with the external plasma) over a larger proportion of their length.

A major criticism of wave heating models (see e.g. Cargill et al., 2016), is that the density profile typically assumed for resonant absorption/mode coupling and phase mixing models cannot be self-consistently generated, or sustained, by the dissipation of MHD waves alone. In a partial response to this criticism, the model presented here provides a proof of principle suggesting that the density profile is not essential for wave heating to occur within the corona. However, in this chapter, we have not considered the potential for the evaporation of chromospheric plasma during heating events to

modify subsequent wave dynamics. Given the spatial distributions of the currents and vorticities that develop, we speculate that the formation of two thinner, density-enhanced loops within the boundary of the original flux tube could be an observational signature of this model.

Chapter 5

The Effects of Heat Transport on the Energetics of a Flux Tube Tectonics Model

In this chapter, we depart from simulations of MHD waves and consider the effects of thermal conduction and optically thin radiation on the heating associated with the braiding of two magnetic flux tubes. Thus far, our consideration of coronal heating has focussed on the dissipation of magnetic and kinetic wave energy. However, an alternative mechanism for energy release involves the reconnection of stressed magnetic field. We will present a model that allows the build up of magnetic energy within the coronal volume before magnetic reconnection and Ohmic dissipation allows the conversion of this energy into heat.

Magnetic flux tubes within the Sun's atmosphere emerge from the photosphere and are subject to plasma flows at the solar surface. In the low atmosphere, the plasma-β is typically larger than unity and the evolution of the plasma is usually dominated by fluid (and not magnetic) forces. The foot points of the coronal magnetic field are embedded in this environment and are advected by the photospheric flows associated with the turbulent convection that occurs beneath the surface. This leads to the complex buffeting of coronal field and magnetic flux tubes can become highly intertwined throughout the atmosphere. If the time scales associated with the foot point motions are long in comparison to the Alfvén travel time along a coronal loop, then the magnetic stress will gradually increase as the structure slowly evolves through stages of quasi-equilibrium.

The braiding of flux tubes inevitably leads to the development of large gradients in the magnetic field and can form significant currents within the corona. Despite the low

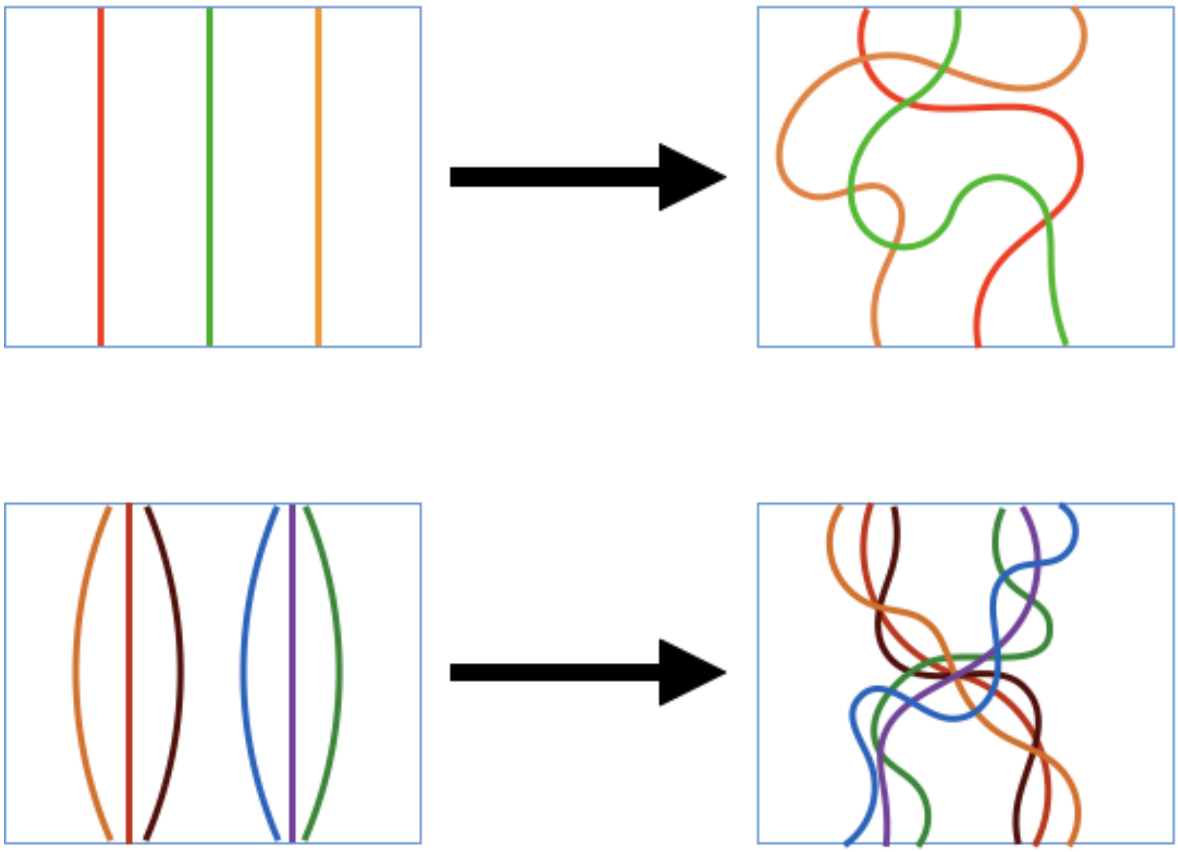

Figure 5.1: Schematic of braiding by complex motions (top) and flux tube tectonics (bottom). In the classical braiding regime, a simple magnetic field configuration (upper left panel) is braided into a stressed field (upper right panel) by complex photospheric motions. Flux tube tectonics, on the other hand, explains how simple footpoint motions (such as the rotation of a loop footpoint or the rotation of two footpoints around each other) can create the stressed field required for coronal heating. Two expanded flux tubes (lower left panel) become twisted around each other and generate current sheets at their interface (lower right panel).

value of η, very narrow current sheets may form and cause significant heating of the solar atmosphere. We note that small scales in the magnetic field are able to form as a result of the complex braiding motions of a simple magnetic field or, alternatively, by simple motions of complex magnetic field. In the model presented within this chapter, we see that relatively simple (albeit coherent) motions acting on expanding magnetic flux tubes are able to induce significant heating. We shall see that current sheets form at the boundary of the structures and, in the literature, this regime is known as flux tube tectonics (see e.g. Priest et al., 2002).

In Figure 5.1 we display a schematic of two mechanisms for stressing the coronal magnetic field. In the upper row we see how complex photospheric motions can generate

small scales within an initially simple, straight field. However, as we expect magnetic flux tubes to emerge in concentrated patches from the lower atmosphere, in the lower row we show the manner in which simple photospheric motions can generate small scales in the coronal field. In the depicted regime, large currents will form between the two flux tubes and magnetic reconnection is able to release the stress stored by the twisted field.

For the remainder of this chapter, we describe and analyse numerical simulations that investigate flux tube tectonics. We show that a simple rotational driver imposed at the loop foot points can produce intense currents within the coronal volume. As a result, Ohmic dissipation and magnetic reconnection will lead to significant plasma heating. Furthermore, outflows from a central region form shocks that can (irreversibly in a non-ideal regime) also increase the plasma temperature.

This configuration has been studied previously in publications by De Moortel and Galsgaard (2006a,b); O'Hara and De Moortel (2016). However, we describe the inclusion of additional physics in the form of thermal conduction and optically thin radiation. These heat transfer processes will modify the levels of thermal energy and typically reduce the high temperatures that are observed at the flux tube interface. Additionally, we shall show that by reducing the gas pressure, they also have subtle effects on the evolution of the magnetic field.

5.1 Model and Numerical Method

Following the set-up of O'Hara and De Moortel (2016), we permit the relaxation of two, initially straight, magnetic flux tubes to obtain a numerical equilibrium. The flux tubes are initially defined by a two-dimensional Gaussian distribution and are uniform in height. Prior to the relaxation, the field is parallel to the z-axis and the non-zero component is given by

$$B_z = B_0 \left\{ \exp\left(\frac{-(x-x_0)^2 - (y-y_0)^2}{r_0^2} \right) + \exp\left(\frac{-(x-x_1)^2 - (y-y_1)^2}{r_1^2} \right) \right\}. \quad (5.1)$$

Here, $B_0 = 100$ G, (x_0, y_0) and (x_1, y_1) are the centres of the two flux tubes and r_0 and r_1 define the initial radii of the two flux tubes. The simulation domain is a cube with edges of length 75 Mm. For the purposes of the simulations described within this chapter, we set $x_0 = 22.5$ Mm, $x_1 = 52.5$ Mm, $y_0 = y_1 = 37.5$ Mm and $r_0 = r_1 \approx 5$ Mm. Since the radius of each flux tube is much smaller than the separation between the two

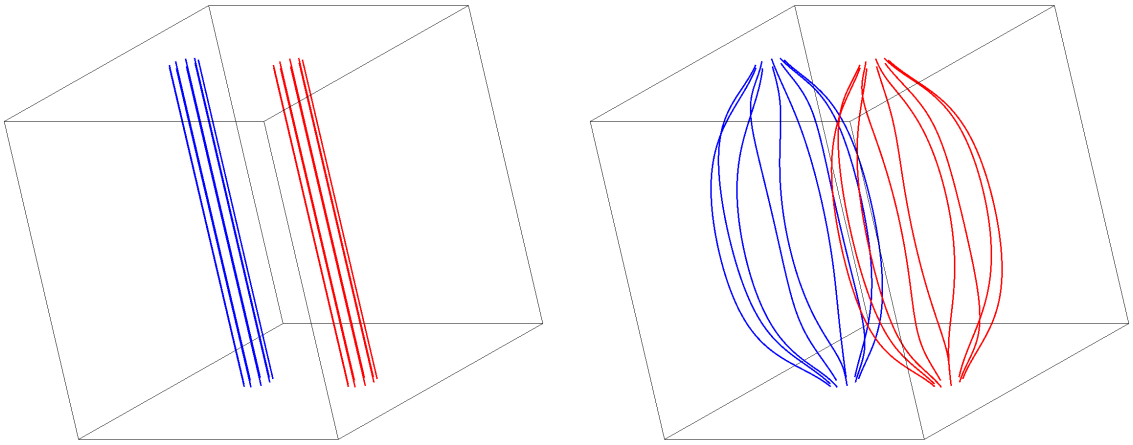

(a) Before relaxation. (b) After relaxation.

Figure 5.2: Magnetic field lines traced from the two flux tube sources on the $z = 0$ Mm (lower) boundary. The blue and red field lines are used to differentiate between the two structures.

flux tubes, we see that the maximum field strength within the domain is approximately $B_0 = 100$ G. We note that 100 G is much larger than a typical coronal field strength, however, the expansion of the flux tubes during the numerical relaxation (see below) ensures that an acceptable value is obtained throughout the majority of the domain (away from the loop foot points).

The simulations described below employ a numerical grid of $512 \times 512 \times 256$ cells. The z-axis uses fewer grid points as the smallest spatial scales typically develop in the horizontal x-y-plane (perpendicular to the flux tube axes in the initial conditions). Shock viscosities (see Chapter 1) are included in order to accurately track the strong outflows (see below) that emerge from the reconnection region between the two flux tubes. The effects of resistivity are also included within the simulations and the form of η is described in more detail below.

Numerical Relaxation

Initially, the density $\left(\rho_0 = 1.67 \times 10^{-12} \text{ kg m}^{-3}\right)$ and temperature ($T_0 = 1.9$ MK) are uniform. Consequently there is no gas pressure force within the domain. However, since the magnetic pressure is much larger inside the flux tubes than in the surrounding plasma, there is a magnetic pressure force that acts to cause the expansion of the field. As in Chapter 4, we therefore allow the field to relax to obtain a numerical equilibrium

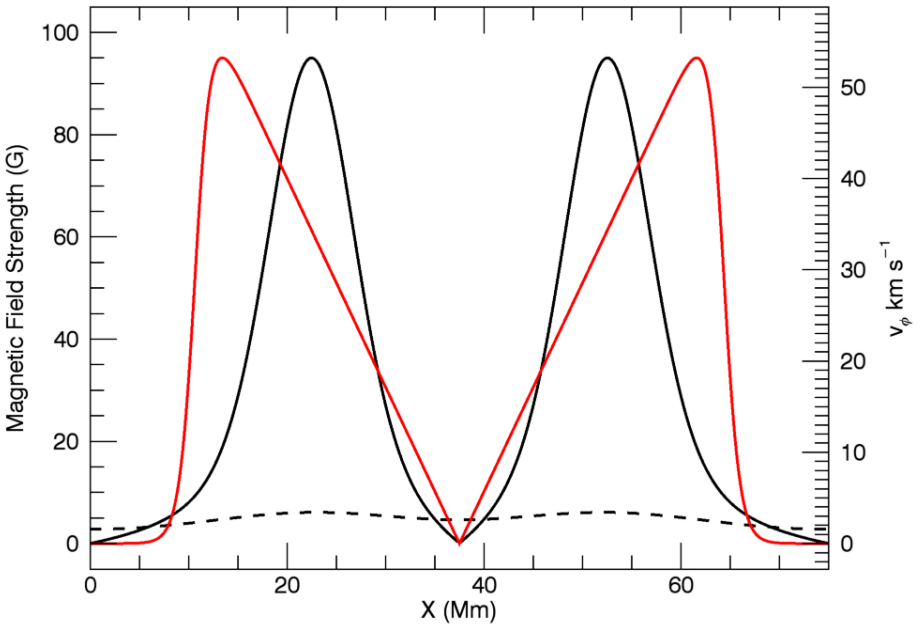

Figure 5.3: Profile of the magnetic field strength (black curves) following the numerical relaxation in cuts through the flux tubes at the lower boundary (solid) and at the apex (dashed). We also show the azimuthal velocity profile (red curve) for the imposed driver.

for use as initial conditions. As previously, a high viscosity is implemented to reduce the amplitude of the oscillations that form and, in order to maintain a constant gas pressure, the temperature and density are overwritten at each time step. We consider the relaxation to be complete once the largest velocities that form once the viscosity is reduced are much smaller ($\leq 1\%$) than the driving velocity (discussed below).

The flux tubes expand (and oscillate) until $\mathbf{j} \times \mathbf{B} = \mathbf{0}$ is numerically satisfied with the exception of a narrow layer close to the loop foot points which are held in place by the boundary conditions (see also Chapter 4). In the centre of the domain, the expansion of each flux tube is limited by the presence of the neighbouring structure. The field profiles before (left) and after (right) the relaxation are depicted in Figure 5.2. We note that, at this stage, the flux tubes remain distinct, however, this is no longer the case once magnetic reconnection begins to occur during the driving phase. This is discussed in more detail below.

We also note that the expansion of the flux tubes is associated with a significant decrease in the magnetic field strength observed in the midplane. In Figure 5.3 we see that the maximum field strength at the apex (dashed black line) is around 5% of the

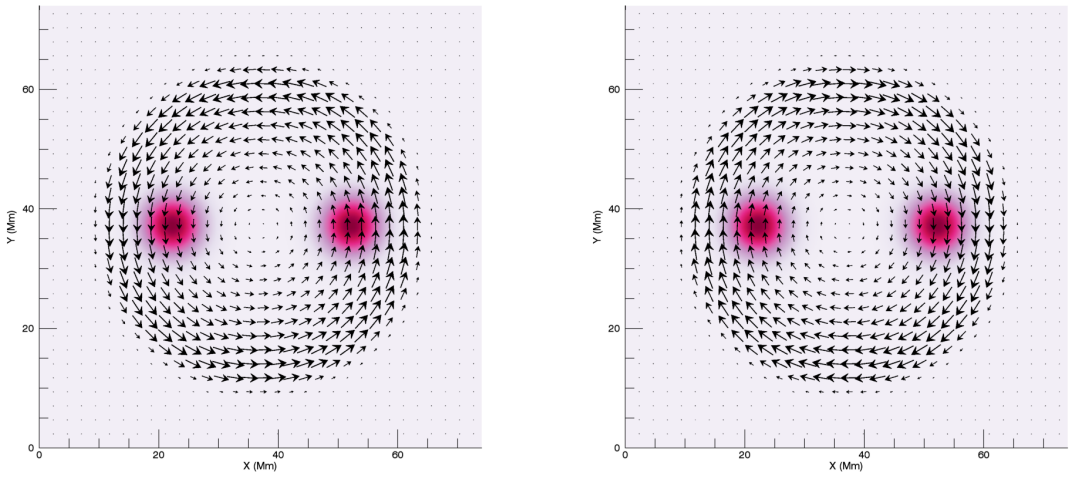

(a) $z = 0$ Mm. (b) $z = 75$ Mm.

Figure 5.4: Driving velocity vectors and the magnetic flux tube foot points on the lower and upper z boundaries.

maximum field strength at the upper and lower z boundaries (solid black line).

Foot Point Driving

Once the relaxation of the flux tubes is complete, we inject Poynting flux (see equation 1.18) into the domain by driving the upper and lower z boundaries with an imposed velocity field. The flow is purely azimuthal and rotates the flux tubes clockwise on the $z = 75$ Mm boundary and anti-clockwise on the $z = 0$ Mm boundary. This has the effect of twisting the flux tubes around each other.

A co-ordinate transform moving the origin to the centre of the lower z boundary ($x = 37.5$ Mm, $y = 37.5$ Mm, $z = 0$ Mm) allows us to define the azimuthal component of the velocity driver as

$$v_\phi = v_0 R \left(1 + \tanh\left\{A - BR\right\}\right). \tag{5.2}$$

Here, v_0 sets the maximum driving velocity $\left(v_{\max} \approx 54 \text{ km s}^{-1}\right)$, and A and B are constants used to define the spatial extent of the driver. We note that the driving velocity is slow in comparison to the Alfvén speed within the flux tubes and thus the magnetic structures will evolve quasi-statically as opposed to generating torsional waves within the domain.

In Figure 5.3 we display the relative locations of the peak driving velocity (red curve)

and the magnetic field strength associated with the two flux tubes (black curves; solid at the lower boundary and dashed at the loop apex). Further, in Figure 5.4, we show the rotational nature of the driver on the lower (left) and upper (right) z boundaries. For reference, we also include the location of the magnetic flux tube foot points (coloured contours).

Additionally, in order to start the rotation smoothly, the magnitude of the imposed velocity is increased gradually at the onset of the driving phase. This is achieved by multiplying the velocity profile described in equation 5.2 by a time-dependent factor, $f(t)$ defined as

$$f(t) = \frac{1}{2}\left(1 + \tanh\left\{\frac{t - 4t_r}{t_r}\right\}\right). \tag{5.3}$$

Here, t_r is a parameter set to ensure a smooth increase of the velocity magnitude from the start of the driving phase at $t = 0$. We note that at $t = 0$, $f(t) \approx 0$ and for $t \gg 4t_r$, then $f(t) \approx 1$.

Resistivity

The action of the driver twists the magnetic flux tubes around each other and generates large currents at the interface of the structures. In order to dissipate these currents as heat, we wish to impose a resistivity, $\eta \approx 2.1 \times 10^4\,\mathrm{m^2\,s^{-1}}$ (for these simulations, this corresponds to a magnetic Reynolds number of $R_M \approx 10^4$), which will lead to a significant increase in thermal energy within the domain. However, the velocity profile also creates very large currents at the upper and lower z boundaries. Therefore, in the presence of any finite resistivity, significant Ohmic heating will occur at the foot points of the flux tubes. This heating will increase the gas pressure and cause the evacuation of plasma from these locations.

Since the Lare3d code uses a time step that is limited by the inverse of the Alfvén speed, we have

$$\Delta t \leq \frac{C\sqrt{\rho}}{B}, \tag{5.4}$$

where C is some constant. We note that, if $\rho \to 0$, then $\Delta t \to 0$ and the simulation will not advance in time. Therefore, in order to prevent this scenario, the value of resistivity, η is set to zero near the $z = 0$ Mm and $z = 75$ Mm boundaries. It increases with a Gaussian profile in the z direction, to the maximum value ($\eta_{\max} \approx 2.1 \times 10^4\,\mathrm{m^2\,s^{-1}}$) in the centre of the domain. At any height, the resistivity is uniform within the horizontal plane.

5.1.1 Heat Transfer

The driving phase is repeated for two cases

1. Without thermal conduction and optically thin radiation (NCR).
2. With both of these processes included (WCR).

Thermal Conduction

In magnetized plasmas thermal conduction is dominated by heat being transferred parallel to the magnetic field (with the obvious exception of at magnetic null points). The effects of thermal conduction are included within the right-hand side of equation 1.10 and in Lare3d are calculated by advancing the following equation

$$\rho \frac{\partial \epsilon}{\partial t} = \nabla \cdot \mathbf{q}. \tag{5.5}$$

Here, ϵ denotes the specific internal energy density and $\mathbf{q}$ is the heat flux vector defined by

$$-\mathbf{q} = \left(\frac{\kappa_{\parallel}}{B_{min}^2 + B^2} \right) (\mathbf{B} \cdot \nabla T)\, \mathbf{B} + \frac{\kappa_{\parallel} B_{min}^2}{B_{min}^2 + B^2} \nabla T. \tag{5.6}$$

The variable $\kappa_{\parallel} = 10^{-11} T^{-5/2}$ W m^{-1} K^{-1} is the parallel thermal conductivity and B_{min} is some small number, chosen according to typical values of the magnetic field. The first term in (5.6) dominates when the magnetic field strength is large. This implies that away from null points, heat will be transferred parallel to the field. Meanwhile, when the field strength is small, the second term dominates. Thus, at magnetic null points, conduction reduces to the isotropic case. We note that in the corona, the transfer of thermal energy parallel to the field is typically much more efficient than perpendicular conduction.

Optically Thin Radiation

Additionally, coronal plasma is also subject to heat loss due to the effects of optically thin radiation. In Lare3d the energy loss is calculated using the equation

$$\rho \frac{\partial \epsilon}{\partial t} = n_e^2 \chi T^{\alpha}, \tag{5.7}$$

where n_e is the number density of the plasma and χ and α are piecewise, continuous functions of temperature. The form of the right-hand side of equation 5.7 is described in detail by Klimchuk et al. (2008) and is displayed in Figure 5.5.

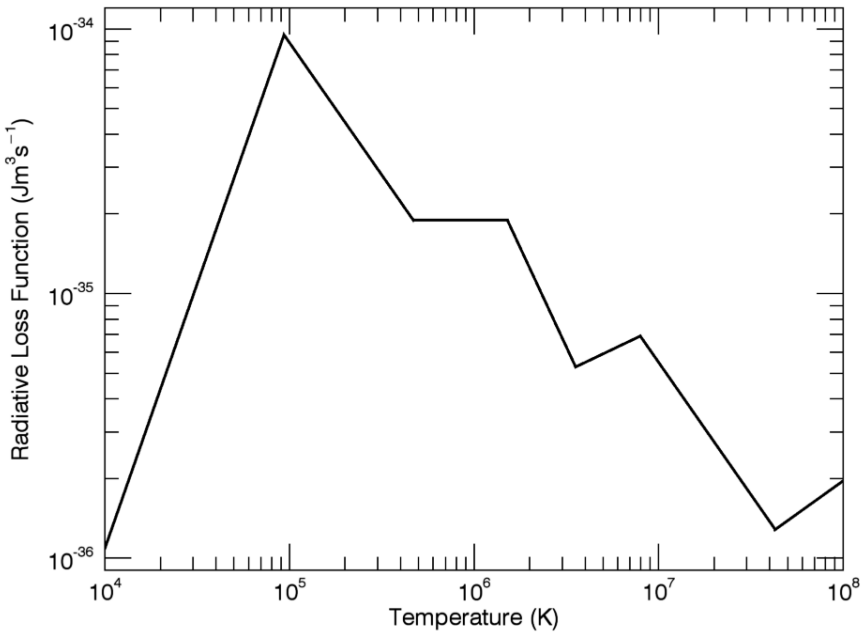

Figure 5.5: Klimchuk et al. (2008) optically thin radiative loss function.

This optically thin radiative loss function is derived from non-trivial atomic physics and can be associated with complicated thermodynamic behaviour. For example, plasma at a temperature of 0.4 MK will radiate more rapidly as it cools. This can create thermal instabilities and can lead to the formation of coronal rain (e.g. Karpen and Antiochos, 2008; Xia et al., 2017; Auchère et al., 2018).

It is also important to note that as a result of the n_e^2 term in equation 5.7, heat loss due to optically thin radiation is highly sensitive to the plasma density. For much of the coronal volume, the loss of energy to the cooler, lower atmosphere by thermal conduction will be more significant than radiative losses. However, in dense, (relatively) low temperature, coronal structures (e.g. prominences), optically thin radiation can be the dominant transfer process.

Thermodynamics of the Initial Equilibrium

Following the relaxation of the two magnetic flux tubes (described above), we obtained a numerical equilibrium satisfying $\mathbf{j} \times \mathbf{B} = \mathbf{0}$. However, this process did not consider the two heat transfer processes considered in the WCR simulation. We now briefly discuss the manner in which an equilibrium is maintained when thermal conduction and optically thin radiation are included.

In the corona, thermal conduction typically acts as an energy loss mechanism as heat is transferred to the cooler transition region and chromosphere. During heating events (e.g. flares, nanoflares), this process, (along with other energy transfer phenomena, such as the transmission of non-thermal electrons) can inject significant energy into the chromosphere and lead to the evaporation of plasma into the corona. This process is difficult to model correctly (Bradshaw and Cargill, 2013) and is completely neglected in these coronal simulations. As such, by enforcing zero gradients in the temperature at the edges of the computational grid, we do not allow thermal conduction to act across the domain boundaries.

As a consequence, since the numerical equilibrium is isothermal, conduction has no effect in the initial conditions. However, radiation does remove some energy from the domain. Therefore, in order to maintain the temperature of the plasma, we must add the lost heat back into the simulation. This can be done by including a background heating term which is a common technique in both one (e.g. Klimchuk et al., 2008; Longcope, 2014; Johnston et al., 2017) and three (e.g. Reale et al., 2016) dimensional coronal simulations. In general this should be a function of the initial density ρ_0 and the initial temperature, T_0. Given these are both uniform in the initial conditions, it is not difficult to calculate a uniform heating profile that will balance the initial radiative losses throughout the domain.

5.2 Results

In both cases, the velocity driver acts to braid the two flux tubes around each other, generating a current sheet in the centre of the numerical domain. The evolution of magnetic field lines associated with the two structures is highlighted in Figure 5.6. For all panels, we trace field lines from the lower ($z = 0$ Mm) boundary and identify the source using either blue or red.

We immediately see that during the course of the simulation, the flux tubes become highly twisted and ultimately (by the time of the lower right-hand panel), become kink unstable. For the purpose of this investigation, we are not interested in the kink instability (Hood and Priest, 1979) as a heating mechanism (see, for example Browning et al., 2008; Reid et al., 2018) and thus we terminate the simulations at this time.

Since $\eta \neq 0$, as the current sheet develops at the interface of the two flux tubes, we encourage the reconnection of magnetic field lines in the centre of the domain. Unfortunately, a small amount of numerical resistivity allows for the diffusion of field lines through the imposed driver and thus precludes the possibility of monitoring the

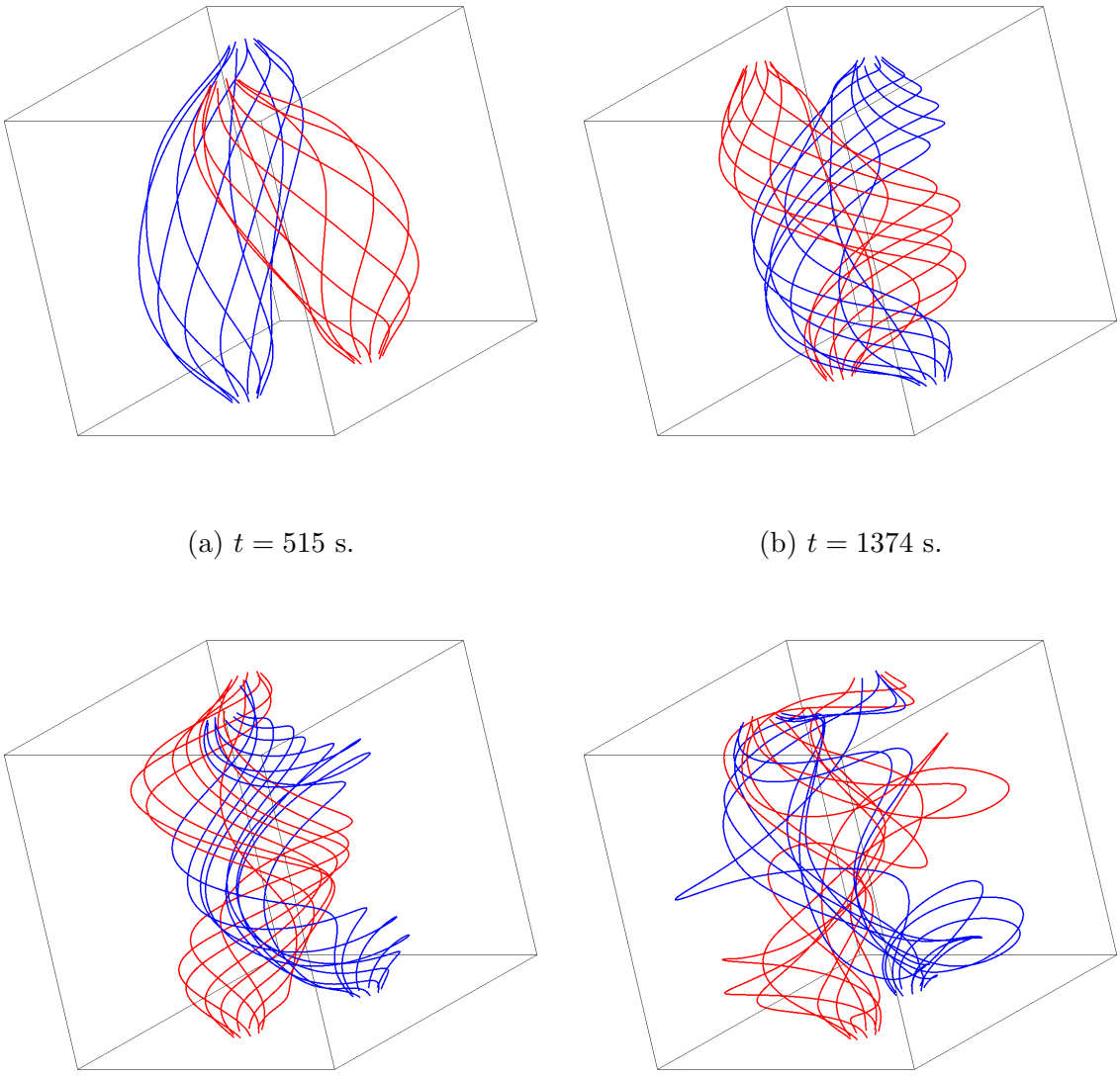

(a) $t = 515$ s.

(b) $t = 1374$ s.

(c) $t = 1890$ s.

(d) $t = 2450$ s.

Figure 5.6: Magnetic field lines traced from the two flux tube sources on the $z = 0$ Mm (lower) boundary at four times during the driving phase of the simulation.

(a) $t = 2078$ s. (b) $t = 2577$ s.

Figure 5.7: Isosurfaces of current density at two stages during the driving phase of the NCR simulation. In the right-panel, the kink instability is beginning to develop.

connectivity of a single field line for the duration of the simulation. However, we can monitor the magnetic reconnection by examining the connectivity of a number of field lines traced from the two sources on the $z = 0$ Mm plane. In the lower left-hand panel of Figure 5.6, we see that on the upper boundary, some of the field lines are connected with the source of different colour. This change in field line connectivity is indicative of magnetic reconnection.

Currents

The driving of field lines at the upper and lower z boundaries is associated with the injection of magnetic energy (Poynting flux) into the domain. Meanwhile, Ohmic heating (proportional to ηj^2) allows the conversion of this magnetic energy into thermal energy as the simulation progresses. As field lines become twisted around each other, large currents are generated throughout the domain. In Figure 5.7, we show isosurfaces of the current density at two different times within the simulation. The foot point currents are not included as these do not contribute to the heating of plasma (see the discussion on the chosen form of η above). We see that currents are generated between the two flux tubes as the driving progresses and, ultimately, once the kink instability develops (right-hand panel of Figure 5.7), Ohmic heating will occur throughout a large volume of the domain.

Reconnection Outflows

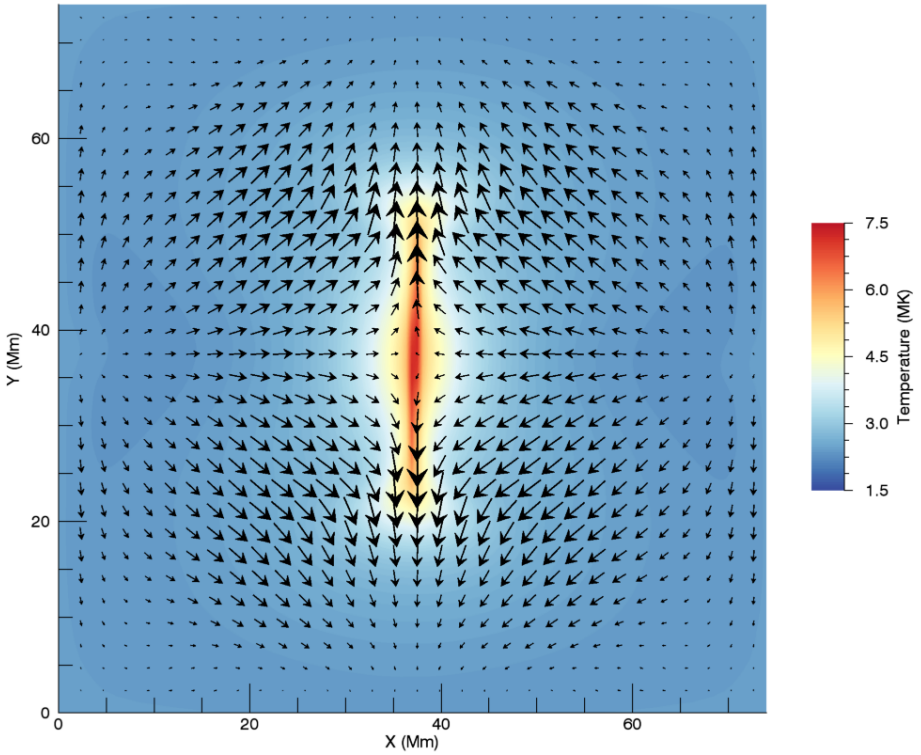

Figure 5.8: Horizontal velocity (v_x, v_y) vectors and a contour plot of the temperature in the midplane of the NCR simulation.

The tension force associated with the twisted field lines causes the migration of magnetic flux into the magnetic reconnection region. Subsequently, fast outflows are generated as a result of the retraction of reconnected field lines and the effects of the gas pressure force. We can see these two effects by tracking the evolution of the velocity field in the horizontal, $z = 37.5$ Mm plane.

On this midplane, the oppositely orientated rotational velocities imposed at the upper and lower z boundaries have equal effect and thus the location of the flux tubes does not change (in this plane) until the structures become kink unstable. We can confirm this by considering the midplanes of the first three panels of Figure 5.6. As such, an inflow into the reconnection region is observed as a velocity in the x direction, and analogously, an outflow will be seen as a velocity in the y direction.

In Figure 5.8, we show the horizontal velocity field (vectors) in the midplane of the simulation. We also show a contour plot of the temperature. We immediately see that, in this simulation without thermal conduction and optically thin radiation, the maximum temperatures obtained are extremely high ($> 10^7$ K). As we shall see, the

action of these heat transfer processes will reduce the temperature in the centre of the domain and, in the case of conduction, distribute the thermal energy across a larger volume.

The plasma flows into and out of the reconnection region are also clearly visible in Figure 5.8. The magnetic tension force acts towards the centre of the domain and is responsible for the acceleration of plasma and (since $R_M \gg 1$) magnetic flux towards the reconnection region. We note that the large ouflow velocities carry heated plasma away from the centre of the domain, in part explaining the elongated (in the y direction) high temperature region. Furthermore, these large velocities generate additional plasma heating due to the effects of the artificial shock viscosities.

5.2.1 Thermal Conduction and Optically Thin Radiation

The most apparent difference between the NCR and WCR simulations is the change in temperature in the centre of the domain. In both experiments, Ohmic heating significantly increases the temperature of the plasma, particularly within the reconnection region (see the contours in Figure 5.8). In the WCR simulation, however, conduction acts to transfer thermal energy along field lines, reducing the temperature of the plasma in the centre of the domain and heating the surrounding fluid. Meanwhile, optically thin radiation acts throughout the domain but is most significant in dense and relatively cool regions (see Figure 5.5). Together, these processes will reduce the temperature, and consequently, the gas pressure within the reconnection region. In the NCR simulation, on the other hand, the only method in which heat can be transferred is through the advection of hot plasma. As we shall see, the enhanced gas pressure observed the NCR simulation ensures that the outflows from the reconnection region are significantly larger when conduction and radiation are neglected.

In Figure 5.9, we display isosurfaces of the temperature difference between the simulations at two different times during the driving phase. In particular, at every grid cell within the numerical domain, we calculate $T_d = T_{\rm NCR} - T_{\rm WCR}$, where $T_{\rm NCR}$, and $T_{\rm WCR}$ are the temperatures in the respective simulations. In the left-hand column of Figure 5.9, we display an isosurface of $T_d = 0$. In other words, all points within the displayed surfaces are hotter in the NCR simulation than in the WCR simulation (at the respective time). By the same argument, the plasma outside the isosurfaces is hotter when conduction and radiation are included. In the right-hand column, we show an isosurface of $T_d = 2$ MK, or equivalently, all points within the displayed surfaces are at least 2 MK hotter in the NCR simulation. Additionally, in Figure 5.10, we display a

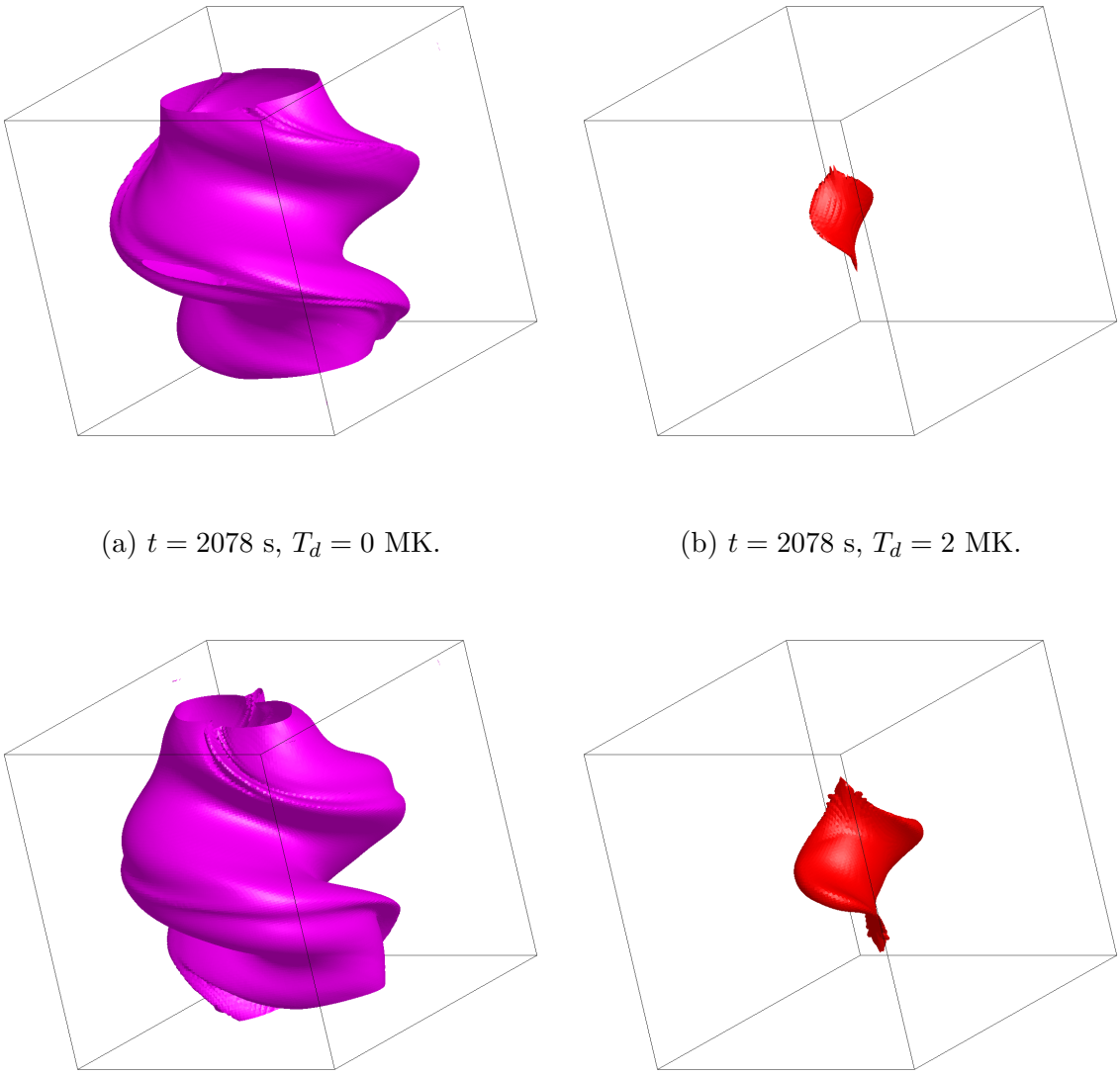

(a) $t = 2078$ s, $T_d = 0$ MK.

(b) $t = 2078$ s, $T_d = 2$ MK.

(c) $t = 2577$ s, $T_d = 0$ MK.

(d) $t = 2577$ s, $T_d = 2$ MK.

Figure 5.9: Isosurfaces of temperature difference between the NCR and WCR simulations at two stages during the driving phase. The left-hand column displays the surface on which the temperature difference is 0. Within this volume, the NCR simulation generates higher plasma temperatures. The right-hand column displays the surface containg plasma which is at least 2 MK hotter in the NCR simulation.

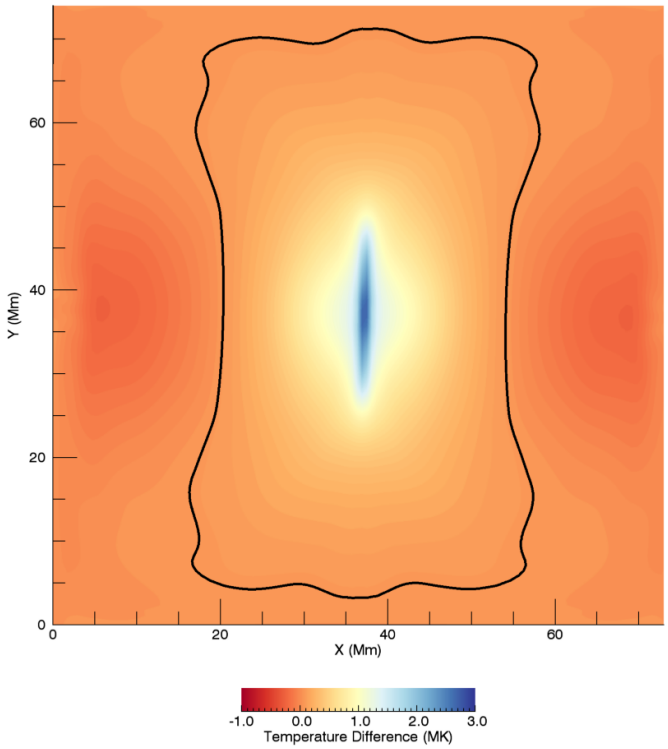

Figure 5.10: Temperature difference between the NCR and WCR simulations in the midplane. Positive values indicate locations in which the NCR simulation is hotter. The solid black line represents the intersection of the $T_d = 0$ MK surface (see left-hand column of Figure 5.9) with this horizontal plane.

contour plot of the temperature difference in the horizontal midplane ($z = 37.5$ Mm). The black line shows the intersection of the $T_d = 0$ surface with this plane.

In the left-hand panel of Figure 5.11, we show the maximum temperature attained by plasma as the simulations progress. We see that the plasma is heated above typical coronal values (with the exception of flaring active region loops) when conduction and radiation are not included (blue curve). We reiterate that the only manner in which heat can be redistributed in the absence of these energy transfer processes is via the motion of hot plasma. Since the tension force associated with the magnetic field lines is directed towards the reconnection region, this is typically inefficient in this regime. As a result, very large temperatures form in the centre of the domain. The right-hand panel of Figure 5.11, displays the evolution of the volume integral of ρ^2 for the two simulations. We discuss the implications of this plot later.

Returning to Figure 5.9, we observe that there is a clear boundary between the regions that are hotter when conduction and radiation are not included and those that have higher temperatures when the heat transfer mechanisms are considered. Despite

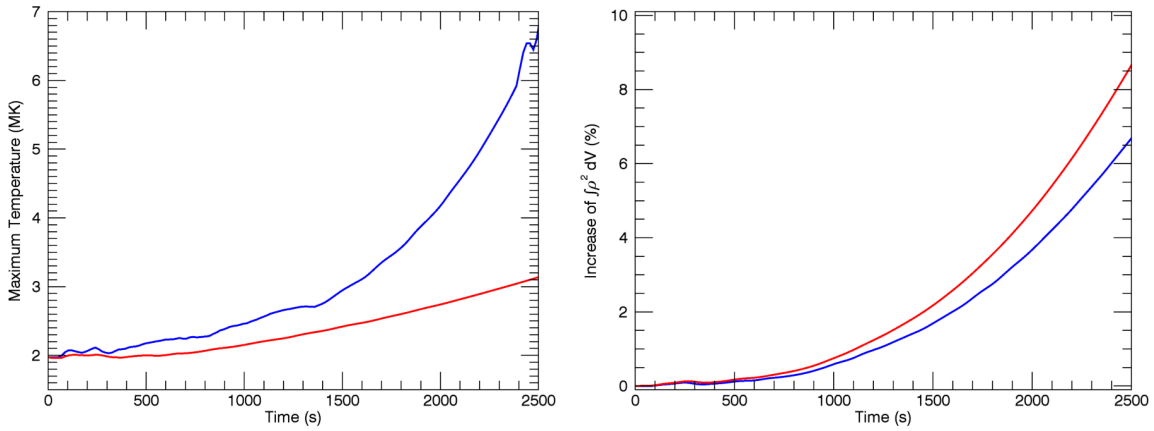

Figure 5.11: *Left:* The maximum temperature observed within the domain as a function of time for the NCR (blue) and WCR (red) simulations. *Right:* Percentage increase in the volume integral of ρ^2 for the two experiments.

the energy lost from the domain due to optically thin radiation in the WCR simulation, there is a large volume in which higher temperatures are observed because of the redistribution of heat caused by thermal conduction. In the initial conditions, the field is largely aligned with the z axis (see right-hand panel of Figure 5.2) and thus we might expect thermal conduction to primarily transfer heat in this direction. Indeed, in the corona we expect energy to be conducted along loop structures. However, by the time significant Ohmic dissipation begins to occur in this model, the field lines are very twisted (see Figure 5.6) and thus conduction transfers heat along helical structures. This may have interesting observational implications as we may observe an *apparent* heating of the entire cross-section of the flux tube.

In Figure 5.12, we trace magnetic field lines from within the reconnection outflow (see Figure 5.8). We have coloured the field lines using the plasma temperature in order to show how thermal energy is distributed for the WCR (left) and NCR (right) simulations. As these field lines exist within the outflow, they have already been heated. Again we see that much hotter temperatures are attained in the NCR simulation, however there are significant temperature gradients along the field lines. We can see that for the WCR simulation, the heat has been redistributed (by conduction) and there are no longer large variations in temperatures along magnetic field lines.

Whilst the total mass is conserved (to machine precision) within both experiments, it is redistributed within the domain during the driving phase of the simulations. In particular, magnetic tension forces exerted by the twisted flux tubes act to enhance the density within the centre of the domain. Since the density is initially constant, this redistribution of mass increases the volume integral of ρ^2 in both simulations. We show

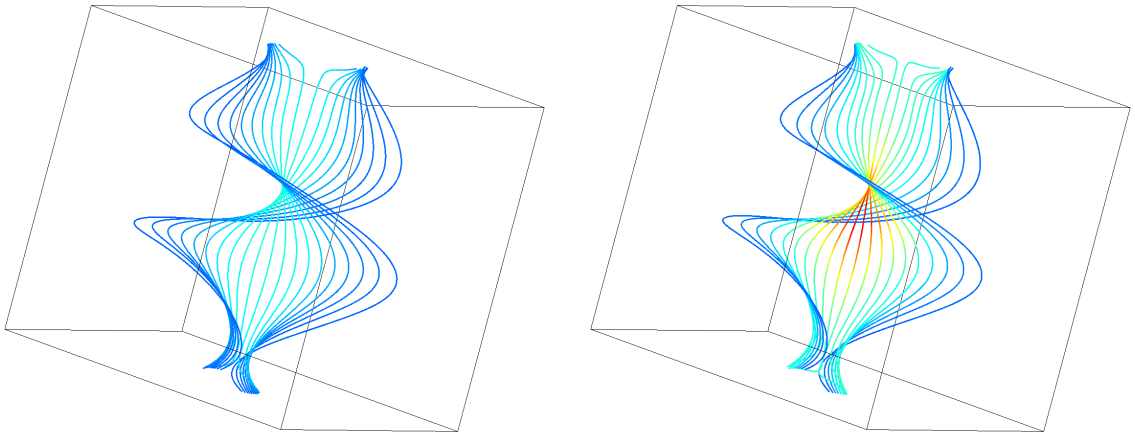

(a) WCR. (b) NCR.

Figure 5.12: Magnetic field lines traced from the line $y = 37.5$ Mm in the midplane of the simulation. The displayed lines are coloured using the temperature. Within both figures, the minimum temperature (dark blue) is 1.8 MK and the maximum temperature (red) is 6.2 MK.

the evolution of this integral for both the NCR (blue) and WCR (red) simulations in the right-hand panel of Figure 5.11. We see an increase in both cases and, as such, we might expect the radiation to increase throughout the simulation (see equation 5.7). On the other hand, the heating of the plasma will decrease the effectiveness of optically thin radiation (see Figure 5.5) and thus it is not immediately clear whether the heat loss from the domain becomes more or less significant as the driving progresses.

In the left-hand panel of Figure 5.13, we resolve this question by showing the normalised, volume integrated optically thin radiation as a function of time. We see that radiation is nearly 50% more effective as a mechanism for removing energy from the domain at the end of the simulation than it was at the start of the driving phase. The red curve is the volume integrated radiative losses from the WCR simulation. This corresponds to the energy lost from the domain. The blue curve, on the other hand, is the same integral calculated for the NCR simulation. Clearly, this energy is not removed in this case as radiative losses are not included. In the right-hand panel of Figure 5.13, we display the density profile at a late time through the reconnection region for the WCR (red) and NCR (blue) simulations.

We see that the WCR experiment is able to support a larger plasma density within the reconnection region due to the reduced temperatures (and therefore gas pressure).

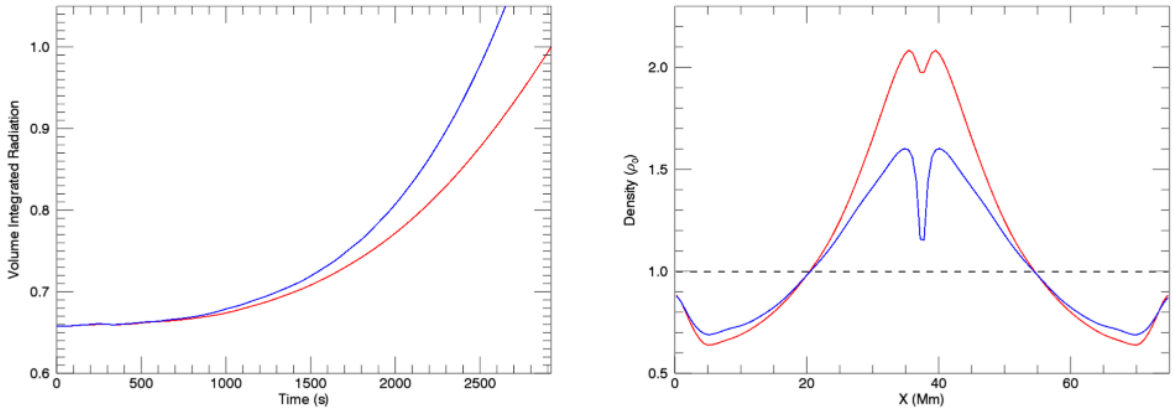

Figure 5.13: *Left*: Volume integrated radiative losses for the WCR simulation (red) and expected losses for the NCR simulation (blue). We have normalised both curves by the maximum radiative losses for the WCR simulation. *Right*: Late time density profile for the WCR (red) and NCR (blue) simulations through the reconnection region in the horizontal midplane.

This also explains the difference in behaviour observed in the volume integral of ρ^2 (see the right-hand panel of Figure 5.13). The plasma evacuation observed in the very centre of the domain (in both cases), is associated with the formation of the large reconnection outflows. Whilst they are significant in both cases they are larger in the NCR simulation due to the higher gas pressure forces. As such, in the right-hand panel of Figure 5.13, for $x \approx 37.5$ Mm, we see a larger decrease in the density in the reconnection region.

The higher density observed in the centre of the WCR domain would suggest that we should anticipate that the actual/expected volume integrated radiative losses should be larger for this simulation. However, in the left-hand panel of Figure 5.13, we actually see that the opposite is true. Although optically thin radiation is very inefficient for the exceptionally high temperatures attained in the NCR reconnection region, much of the domain contains cooler plasma which experiences more significant radiative losses. As such, the slightly higher density, and slightly cooler temperatures away from the centre of the domain in the NCR simulation, contribute to the (expected) more significant losses displayed in the left-hand panel of Figure 5.13.

In Figure 5.14, we display the gas pressure (upper left), magnetic pressure (upper right), plasma-β (lower left) and velocity (lower right) in cuts through the reconnection region along the direction of the plasma outflows. As we mentioned earlier, this is parallel to the y-axis (see Figure 5.8). In the first panel, we observe that the higher temperatures observed in the centre of the NCR simulation, are clearly associated with higher gas pressures (upper left). We note that whilst the plasma-$\beta < 1$, in the

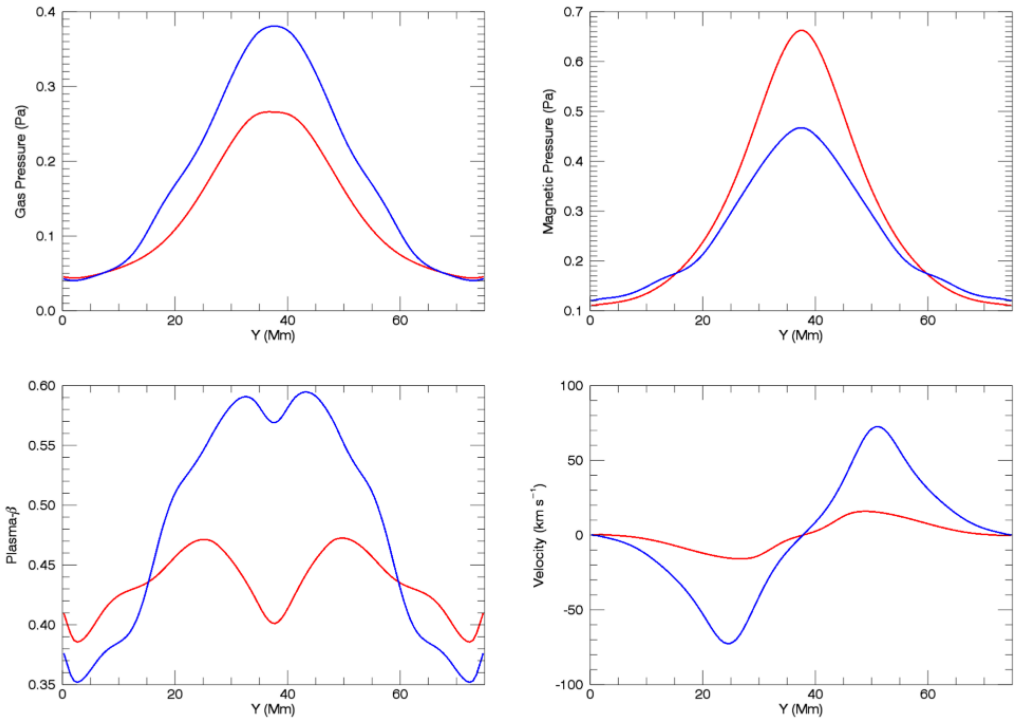

Figure 5.14: *Upper left*: Gas pressure. *Upper right*: Magnetic pressure. *Lower left*: Plasma-β. *Lower right*: Outflow velocities. All panels show profiles through the centre of the midplane, parallel to the reconnection outflows (y direction).

midplane, it is not particularly small. As such, gas pressure forces will have some, non-negligible, influence on the plasma dynamics. Thus, the larger gas pressures resist the inflow of magnetic flux (caused by the tension force) into the reconnection region and consequently, we observe a larger magnetic pressure in the centre of the WCR simulation. We highlight that due to lower plasma-β observed in the WCR simulation, the Lorentz force has greater significance for the evolution of the plasma in this case. It is important to note that the inclusion of heat transfer processes has implications on the evolution of the field and not simply the temperature of the plasma within the domain.

We also note that the velocity outflows are much larger in the simulation without conduction and radiation. These large velocities transport heated plasma away from the centre of the domain and we can clearly see their influence in the shape of the temperature isosurface in the lower right-hand panel of Figure 5.9 and in the horizontal cut shown in Figure 5.10. In particular, we notice the elongation of the higher temperature plasma (in the NCR simulation) in one horizontal direction (y) but not in the other (x).

These outflow velocities have an additional effect in terms of further plasma heating.

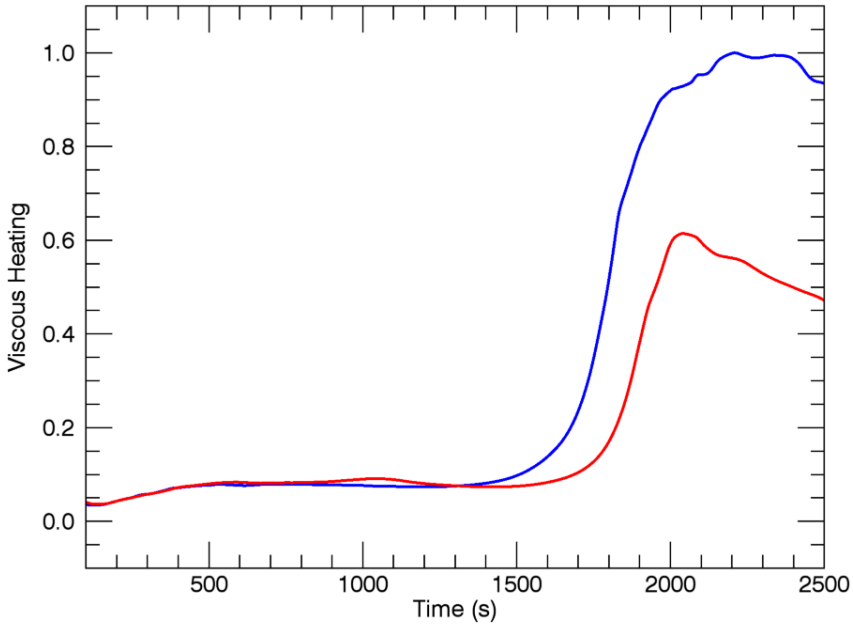

Figure 5.15: Volume integrated viscous heating rate during the driving phase of the WCR (red) and NCR (blue) simulations. Here we have normalised both curves by the maximum rate observed in either experiment.

The large flows occur over a narrow layer (in the x direction) and as such are subject to significant frictional effects. As a result, we expect the viscous dissipation included within both simulations to be more significant in the NCR case. Indeed, in Figure 5.15, we show the volume integrated viscous heating rate for both the WCR (red) and NCR (blue) simulations. Whilst the viscous heating rate is very similar at early times, once magnetic reconnection begins to occur, the outflows generate significant further heating, particularly in the NCR case.

Volume Integrated Energy

We conclude our analysis by considering the components of the volume integrated energies in each of the two simulations. In Figure 5.16, we show the increase (above post-relaxation quantities) of the magnetic (blue), thermal (red) and kinetic (green) energies for the NCR (solid) and WCR (dashed) simulations. In each case, we have normalised by the maximum increase of the total energy (black) observed in the NCR experiment.

The increase in the total energy in the NCR case (solid black line) corresponds to the Poynting flux injected into the domain by the driving of the upper and lower z

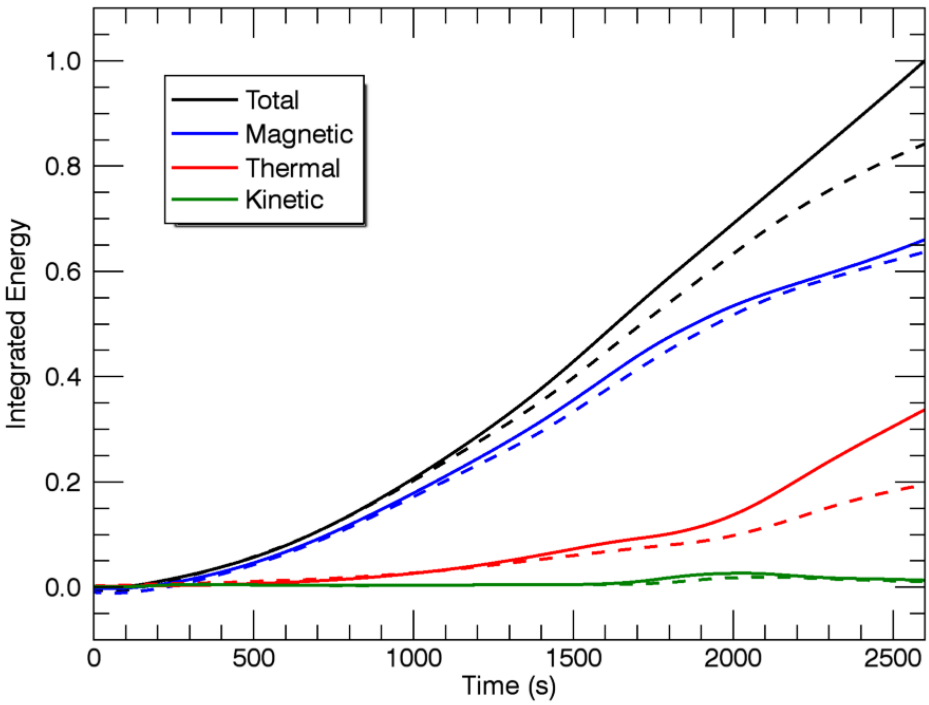

Figure 5.16: The change in the volume integrated energy during the driving stage of both the NCR (solid lines) and WCR (dashed lines) simulations. We also show how much of the total increase is associated with increases in each component of the energy.

boundaries. The analagous curve for the WCR case (dashed black line) shows a smaller increase in total energy. The majority of this difference corresponds to the optically thin radiative losses. There is also a very small difference that arises from a change in the Poynting flux. Although the driver is identical in both cases, as we have discussed, the field configuration is not exactly the same in the two simulations. This change results in a small difference in the energy introduced by the driver (see equation 1.113 fore more details).

It is not surprising to observe the difference in thermal energy between the two simulations. Whilst conduction does not result in any thermal energy loss from the domain, optically thin radiation does directly lead to a reduction in the total energy. Although radiation is not especially efficient in this coronal regime, over the course of 2500 s, it can cause a significant reduction in the plasma temperature. We note that most of the difference in the total integrated energy (black lines) arises from the loss of thermal energy.

At any particular instant, we notice that between 60% and 80% of the introduced

energy is magnetic in nature. Most of the remaining increase is observed as thermal energy with a much smaller amount being kinetic. This remains relatively constant throughout the duration of the experiment although there is a small change in behaviour as Ohmic heating becomes more efficient around $t \approx 2000$ s. We also observe that there is a small, but noticeable difference in the total magnetic energy between the two cases. This difference confirms that conduction and radiation are having an impact on the evolution of the magnetic field as well as the temperature of the plasma.

In the upper right-hand panel of Figure 5.14, we see that the WCR simulation permits a larger increase in magnetic pressure within the reconnection region than in the NCR case. This redistribution of magnetic flux within the domain modifies the integral of B^2 and thus the magnetic energy. Confusingly, if we were to consider Figure 5.14 in isolation, we would expect the magnetic energy to be larger in the WCR experiment. However, we note that the increase of magnetic flux within the reconnection region allows larger currents to form and thus supports a small enhancement in Ohmic heating. Ultimately this decreases the total magnetic energy within the WCR simulation.

5.3 Discussion and Conclusions

In this chapter, we have presented the results of numerical simulations that consider the heating of coronal plasma by the braiding of expanding magnetic structures. In this flux tube tectonics model, large currents are generated at the interface of the magnetic loops and, in a non-ideal regime, this allows magnetic reconnection and significant Ohmic heating to occur. The driving of flux tube foot points by oppositely-orientated, rotational velocities acts to braid the two structures around each other. This, in turn, generates magnetic tension forces which act towards the centre of the domain. As a result, we observe the migration of flux into a high current region, Ohmic heating and, ultimately, the ejection of hot plasma in reconnection outflows.

We have considered the effects of thermal conduction and optically thin radiation on the evolution of both the plasma and the magnetic field. Both processes act to reduce the very high temperatures and gas pressures that are observed in the centre of the domain when these heat transfer mechanisms are not included. Thermal conduction acts to transfer heat along the highly twisted field lines and thus increases the plasma temperature in a large volume of the domain. As the field lines twist around the magnetic flux tubes, line-of-sight effects may imply that the heating of a few field lines would be observed as the heating of the entire cross-section of the structure. The generation of synthetic observations as part of a forward modelling study should clarify

whether this is indeed the case.

In these simulations, no energy is allowed to pass directly through the domain boundaries and thus conduction does not result in a total energy loss. Optically thin radiation, on the other hand, does remove energy from the domain. Although it is typically less efficient for very high temperature plasmas, the high density structures generated in the centre of the numerical grid (particularly for the WCR simulation) do enhance the thermal energy losses as the simulation progresses. As expected, the integrated thermal energy is lower when radiation is included and, together with the effects of thermal conduction, we see that the heat transfer processes actually allow coronal temperatures to be maintained in this regime. In particular, the very high temperatures (> 6 MK) are no longer observed in the reconnection region, but a larger volume of the domain is heated.

In the absence of thermal conduction and optically thin radiation, the only way in which heat can be redistributed throughout the domain is by the advection of hot plasma. With the exception of in the reconnection outflows, this is typically an inefficient process as magnetic tension acts to restrict the expansion (particularly in the x direction) of the heated plasma. Despite this, the high velocity reconnection outflows do allow for the advection of some high temperature plasma throughout the domain. In particular, the outflows are significantly larger in the simulation without the inclusion of conduction or radiation.

As with the model presented in Chapter 4, the initial conditions contain no density structuring and thus will not be identifiable by contemporary observing instruments. In the next few years, magnetic field measurements within the corona may become available (e.g. using the DKIST instrument) and thus the evolution of flux tubes similar to those described in this chapter could be tracked. Regardless, detecting the central density enhancement, the heating of plasma and the formation of Doppler velocities associated with the twisting motions should be possible given current observing capabilities. As such, forward modelling of the described simulations should be able to identify signatures of the heating mechanism to determine whether the current experiments are relevant to the solar corona.

Chapter 6

Conclusions and Future Work

In this thesis we have presented the results of three dimensional MHD simulations examining the dynamics and energetics of coronal flux tubes. In the context of coronal heating, we have investigated energy dissipation mechanisms for waves in magnetic structures (Chapters 2 - 4) and in a flux tube tectonics model (Chapter 5). We have evaluated the formation of small scales in both the magnetic (currents) and velocity (vorticities) fields in order to establish the expected rates and locations of plasma heating.

In Chapters 2 - 4, we investigated the evolution of fundamental standing kink waves in a variety of magnetic flux tubes. In each case we were able to identify the effects of resonant absorption by monitoring the conversion of the kink mode into azimuthal Alfvén waves. This process, together with phase mixing and potentially the development of the Kelvin-Helmholtz instability, promotes the formation of small scales and ultimately enhances the rate of wave energy dissipation.

In Chapter 2, we conducted a parameter study to identify the effects of dissipation on the development of the Kelvin-Helmholtz instability in a transversely oscillating coronal loop. The imposed values of resistivity (η) and viscosity (ν) have a direct effect on the amplitude of the azimuthal Alfvén wave that forms as a result of resonant absorption. In both cases, increasing the dissipation will suppress the formation rate of the instability and for particularly high transport coefficients, the system may stabilise completely. These results are consistent with the findings of Magyar and Van Doorsselaere (2016) in which the authors highlight that increasing the amplitude of the initial kink mode (and therefore the Alfvén wave) will enhance the development of the KHI.

We recognise that the values of η and ν considered within this thesis are many orders of magnitude larger than expected coronal values. This is an inevitable conse-

quence of the prohibitive computational cost associated with modelling high (magnetic) Reynolds number plasmas. As such, our conclusions may not be directly applicable to the solar corona (although they may be more relevant to the lower layers of the solar atmosphere). Indeed, we might expect that the Kelvin-Helmholtz instability will form more readily than suggested in our simulations. However, it is important to note the implications of these results for the numerical modelling of dynamic instabilities within the solar atmosphere. In particular, the inclusion of (possibly numerical) artificially large dissipation can suppress important dynamics that would exist in realistic coronal plasma.

In Chapter 3, we addressed an important criticism of simulations of the Kelvin-Helmholtz instability in straight magnetic flux tubes. In particular, analytic investigations (e.g. Soler et al., 2010) had suggested that magnetic twist would stabilise the system with respect to the KHI. To this end, we presented results examining the nature of the instability in a transversely oscillating flux tube which was threaded with helical magnetic field.

In comparison to the ideal, straight field simulation discussed in Chapter 2, we observed short delays in the onset time of the instability and a reduction in the subsequent growth rate. These were especially noticeable when we considered the spatial extent of the Kelvin-Helmholtz vortices. In particular, the density deformation was significantly reduced in cases with weak magnetic twist. Despite this, we believe that the KHI remains energetically relevant in this regime as the currents that form are locally larger than in the straight field case. We observed a small decrease in the loop integrated Ohmic heating (if the background currents are excluded) compared to the straight field case, however, the onset of the instability was still associated with a significant enhancement in wave energy dissipation. It seems that the most critical impact of including helical field is that it increases the difficulty in detecting the KHI observationally and not that it prevents the associated energy dissipation.

Despite the extensive body of literature (e.g. Terradas et al., 2008b; Antolin et al., 2014; Magyar and Van Doorsselaere, 2016; Karampelas et al., 2017; Terradas et al., 2018) that has discussed the formation of the KHI in transversely oscillating loops, no conclusive evidence of the development of the instability has been observed in these coronal structures. It is certainly possible that observing the KHI is beyond the capabilities of contemporary instruments, although Antolin et al. (2017) identified detectable observational signatures of the instability. The advent of more powerful solar telescopes in the coming years (e.g. DKIST, EST) should provide a clearer insight into whether the instability does develop in coronal loops. Furthermore, the ability to directly mea-

sure the coronal magnetic field for the first time should provide further insight into the nature of these structures. In particular, we should be able to place new constraints on numerical models of oscillating loops.

In Chapter 4, we considered MHD wave dynamics in an expanding magnetic flux tube with no density contrast between the internal and external plasma. This is a departure from typical models of coronal oscillations in which the density profile is critical for allowing resonant absorption to proceed. Instead, we observe that the requisite transverse gradient in natural Alfvén frequency can be associated with a magnetic field strength contrast and the length of field lines. The existence of resonances in a similar regime have been studied in the magnetosphere (e.g. Wright and Thompson, 1994; Wright and Elsden, 2016; Elsden and Wright, 2017), however, to our knowledge this model is novel for a coronal-like flux tube.

In this case, the expanding flux tube only weakly constrains the internal field strength and, as such, there is a low contrast between the internal and external Alfvén frequencies. Consequently, resonant absorption occurs less rapidly (in terms of the wave period) than in the straight field regime presented in Chapter 2. Despite this, we are able to generate significant vorticities (at the loop apex) and currents (at the loop foot points) as the azimuthal Alfvén wave forms. Whilst we do not consider non-ideal simulations, we expect that (for equivalent values of η and ν) wave energy dissipation will be enhanced close to the foot points as the concentration of magnetic field increases gradients here. In future experiments, we will consider non-ideal effects in order to verify this hypothesis.

It remains unclear whether the flux tube considered is representative of structures in the corona. In particular, it is short (20 Mm) and may be characteristic of transition region loops. We note that we expect resonant absorption to proceed at a slower rate for longer flux tubes, as the ratio between the internal and external Alfvén frequencies is reduced. Regardless, the model is interesting as a proof of principle that no density enhancement is required for mode conversion and potentially wave heating to progress. This is important in the context of the arguments presented by Cargill et al. (2016) that suggest wave heating mechanisms are not able to create, or sustain, the assumed density profiles.

In comparison with the straight field model presented in Chapter 2, we notice that the Kelvin-Helmholtz instability did not form in the expanding flux tube during the course of the simulation. Indeed we note that the radial velocity shear at the loop apex (critical for the development of the instability) is much less significant in this case. Despite this, analytic investigations conducted by Soler et al. (2010); Zaqarashvili et al.

(2015), suggest that a slender flux tube with any radial velocity shear should permit the formation of the KHI at the apex. We suspect that the numerical dissipation is sufficient to prevent the formation in this case. However, there may be an alternative cause of instability suppresion. In particular, in a short flux tube, we expect that vortex formation at the apex (but not at the foot points) will generate significant magnetic tension forces which may act to stabilise the system. We therefore propose conducting additional simulations with short, straight field flux tubes in order to determine whether the length of the flux tube has a significant effect on the growth rate of the instability.

In Chapter 5, we considered the effects of thermal conduction and optically thin radiation on a flux tube tectonics model previously investigated by De Moortel and Galsgaard (2006a,b); O'Hara and De Moortel (2016). Two magnetic flux tubes were twisted around each other by the action of rotational drivers imposed at the loop foot points. This triggered the development of large currents, magnetic reconnection and Ohmic heating at the interface between the structures. As such, particularly when the heat transfer processes are not included, we see significant temperature increases (to unrealistically high values) in the centre of the domain.

Conduction and radiation both act to lower the observed plasma temperature in the reconnection region. Thermal conduction transfers heat along magnetic field lines and as such redistributes thermal energy throughout the domain. No energy transfer is permitted through the simulation boundaries and, as such, conduction does not constitute an energy loss mechanism. Optically thin radiation, on the other hand does remove thermal energy from the domain. Additionally, we observed that the effects of radiation increase as the simulation progresses due to an increase in density in the reconnection region.

The change in temperature, and consequently gas pressure, associated with conduction and radiation, also has consequences for the plasma dynamics. In the simulation without these processes, we observe large outflows from the reconnection region which advect hot plasma and generate secondary heating due to viscous effects. These are much reduced when conduction and radiation are included. Since the magnetic field is approximately *frozen* into the plasma, the modification of the reconnection outflows also has implications for the evolution of the field. We acknowledge that the simulation was conducted using a relatively (in terms of coronal values) high β plasma and as such, we are interested in to what extent these results are replicated in a lower β regime.

In the simulation that included radiation, in order to establish an initial equilibrium, we implemented a background heating term that exactly balanced the initial radiative

losses. As discussed previously, this is a common technique in numerical simulations that include the effects of radiation (e.g. Reale et al., 2016). However, if we initially neglect the effects of conduction, by considering the radiative loss function (see Figure 5.5), we note that for many initial temperatures, this is unlikely to produce a thermally stable equillibrium. In particular, if we select a starting value of $T = 1.6$ MK, then a small increase in temperature will decrease the radiative losses. Assuming the background heating remains constant, the temperature will increase and a spurious thermal instability will develop. A similar (but opposite) effect may be observed for cooling regions, and indeed this is related to the thermal instabilities that are observed in the corona (e.g. Antolin et al., 2015b; Moschou et al., 2015; Auchère et al., 2018). However, for the purposes of this discussion, we will only consider the increasing temperature case.

The effects of conduction will likely stabilise the initial equilibrium by redistributing heat from any grid cells that become too hot. However, we note that as it does not act isotropically, if a field line experiences an average temperature increase, conduction will not prevent the development of this instability. Within any heating model, we certainly expect some field lines to increase in temperature and as such the radiative losses (assuming the density remains constant) may decrease. Therefore, the background heating term will, in some sense, become too large and contribute to temperature increases which are not associated with the energy release mechanism being investigated. To this end, we suggest extreme care should be taken when evaluating temperature increases in energy dissipation models that include a background heating term. In future investigations, we would like to analyse whether this phenomenon has a significant effect in coronal heating simulations.

Throughout this thesis, we have presented the results of numerical simulations that have examined the formation of small scales, and the subsequent dissipation of magnetic and kinetic energy. In all cases, partially due to numerical considerations, we have treated the corona in isolation from the lower layers of the solar atmosphere. However, it is well established that there is significant mass and energy transfer through the transition region between the chromosphere and the corona (e.g. Withbroe, 1988; De Pontieu et al., 2011). As such, coronal heating mechanisms cannot be fully understood without recognising this connection and we hope that future models will be able to investigate this highly coupled system more thoroughly.

Bibliography

J. Andries, M. Goossens, J. V. Hollweg, I. Arregui, and T. Van Doorsselaere. Coronal loop oscillations. Calculation of resonantly damped MHD quasi- mode kink oscillations of longitudinally stratified loops. *Astron. Astrophys.*, 430:1109–1118, February 2005. doi: 10.1051/0004-6361:20041832.

S. A. Anfinogentov, G. Nisticò, and V. M. Nakariakov. Decay-less kink oscillations in coronal loops. *Astron. Astrophys.*, 560:A107, December 2013. doi: 10.1051/0004-6361/201322094.

S. A. Anfinogentov, V. M. Nakariakov, and G. Nisticò. Decayless low-amplitude kink oscillations: a common phenomenon in the solar corona? *Astron. Astrophys.*, 583: A136, November 2015. doi: 10.1051/0004-6361/201526195.

P. Antolin and K. Shibata. The Role Of Torsional Alfvén Waves in Coronal Heating. *Astrophys. J.*, 712:494–510, March 2010. doi: 10.1088/0004-637X/712/1/494.

P. Antolin, T. Yokoyama, and T. Van Doorsselaere. Fine Strand-like Structure in the Solar Corona from Magnetohydrodynamic Transverse Oscillations. *Astrophys. J. Letts.*, 787:L22, June 2014. doi: 10.1088/2041-8205/787/2/L22.

P. Antolin, T. J. Okamoto, B. De Pontieu, H. Uitenbroek, T. Van Doorsselaere, and T. Yokoyama. Resonant Absorption of Transverse Oscillations and Associated Heating in a Solar Prominence. II. Numerical Aspects. *Astrophys. J.*, 809:72, August 2015a. doi: 10.1088/0004-637X/809/1/72.

P. Antolin, G. Vissers, T. M. D. Pereira, L. Rouppe van der Voort, and E. Scullion. The Multithermal and Multi-stranded Nature of Coronal Rain. *Astrophys. J.*, 806: 81, June 2015b. doi: 10.1088/0004-637X/806/1/81.

P. Antolin, I. De Moortel, T. Van Doorsselaere, and T. Yokoyama. Modelling observed decay-less oscillations as resonantly enhanced Kelvin-Helmholtz vortices from trans-

verse MHD waves and their seismological application. *Astrophys. J.*, 606, October 2016.

P. Antolin, I. De Moortel, T. Van Doorsselaere, and T. Yokoyama. Observational Signatures of Transverse Magnetohydrodynamic Waves and Associated Dynamic Instabilities in Coronal Flux Tubes. *Astrophys. J.*, 836:219, February 2017. doi: 10.3847/1538-4357/aa5eb2.

P. Antolin, P. Pagano, I. De Moortel, and V. M. Nakariakov. In Situ Generation of Transverse Magnetohydrodynamic Waves from Colliding Flows in the Solar Corona. *Astrophys. J. Lett.*, 861:L15, July 2018. doi: 10.3847/2041-8213/aacf98.

T. D. Arber, A. W. Longbottom, C. L. Gerrard, and A. M. Milne. A Staggered Grid, Lagrangian-Eulerian Remap Code for 3-D MHD Simulations. *Journal of Computational Physics*, 171:151–181, July 2001. doi: 10.1006/jcph.2001.6780.

I. Arregui. Wave heating of the solar atmosphere. *Philosophical Transactions of the Royal Society of London Series A*, 373:20140261–20140261, April 2015. doi: 10.1098/rsta.2014.0261.

M. J. Aschwanden, L. Fletcher, C. J. Schrijver, and D. Alexander. Coronal Loop Oscillations Observed with the Transition Region and Coronal Explorer. *Astrophys. J.*, 520:880–894, August 1999. doi: 10.1086/307502.

M. J. Aschwanden, B. de Pontieu, C. J. Schrijver, and A. M. Title. Transverse Oscillations in Coronal Loops Observed with TRACE II. Measurements of Geometric and Physical Parameters. *Solar Phys.*, 206:99–132, March 2002. doi: 10.1023/A:1014916701283.

F. Auchère, C. Froment, E. Soubrié, P. Antolin, R. Oliver, and G. Pelouze. The Coronal Monsoon: Thermal Nonequilibrium Revealed by Periodic Coronal Rain. *Astrophys. J.*, 853:176, February 2018. doi: 10.3847/1538-4357/aaa5a3.

Eugene H. Avrett and Rudolf Loeser. Models of the Solar Chromosphere and Transition Region from SUMER and HRTS Observations: Formation of the Extreme-Ultraviolet Spectrum of Hydrogen, Carbon, and Oxygen. *The Astrophysical Journal Supplement Series*, 175:229–276, March 2008. doi: 10.1086/523671.

M. R. Bareford, A. W. Hood, and P. K. Browning. Coronal heating by the partial relaxation of twisted loops. *Astron. Astrophys.*, 550:A40, February 2013. doi: 10.1051/0004-6361/201219725.

M. R. Bareford, M. Gordovskyy, P. K. Browning, and A. W. Hood. Energy Release in Driven Twisted Coronal Loops. *Solar Phys.*, 291:187–209, January 2016. doi: 10.1007/s11207-015-0824-7.

R. Bowness, A. W. Hood, and C. E. Parnell. Coronal heating and nanoflares: current sheet formation and heating. *Astron. Astrophys.*, 560:A89, December 2013. doi: 10.1051/0004-6361/201116652.

S. J. Bradshaw and P. J. Cargill. The Influence of Numerical Resolution on Coronal Density in Hydrodynamic Models of Impulsive Heating. *Astrophys. J.*, 770:12, June 2013. doi: 10.1088/0004-637X/770/1/12.

P. K. Browning and E. R. Priest. Kelvin-Helmholtz instability of a phased-mixed Alfven wave. *Astron. Astrophys.*, 131:283–290, February 1984.

P. K. Browning, C. Gerrard, A. W. Hood, R. Kevis, and R. A. M. van der Linden. Heating the corona by nanoflares: simulations of energy release triggered by a kink instability. *Astron. Astrophys.*, 485:837–848, July 2008. doi: 10.1051/0004-6361:20079192.

P. J. Cargill, I. De Moortel, and G. Kiddie. Coronal Density Structure and its Role in Wave Damping in Loops. *Astrophys. J.*, 823:31, May 2016. doi: 10.3847/0004-637X/823/1/31.

Subrahmanyan Chandrasekhar. *Hydrodynamic and hydromagnetic stability*. Oxford University Press, 1961.

T. G. Cowling. *Magnetohydrodynamics*. 1976.

I. De Moortel and C. S. Brady. Observation of Higher Harmonic Coronal Loop Oscillations. *Astrophys. J.*, 664:1210–1213, August 2007. doi: 10.1086/518830.

I. De Moortel and P. Browning. Recent advances in coronal heating. *Philosophical Transactions of the Royal Society of London Series A*, 373:20140269–20140269, April 2015. doi: 10.1098/rsta.2014.0269.

I. De Moortel and K. Galsgaard. Numerical modelling of 3D reconnection due to rotational footpoint motions. *Astron. Astrophys.*, 451:1101–1115, June 2006a. doi: 10.1051/0004-6361:20054587.

I. De Moortel and K. Galsgaard. Numerical modelling of 3D reconnection. II. Comparison between rotational and spinning footpoint motions. *Astron. Astrophys.*, 459: 627–639, November 2006b. doi: 10.1051/0004-6361:20065716.

I. De Moortel and D. J. Pascoe. Putting Coronal Seismology Estimates of the Magnetic Field Strength to the Test. *Astrophys. J. Lett.*, 699:L72–L75, July 2009. doi: 10.1088/0004-637X/699/2/L72.

B. De Pontieu, R. Erdélyi, and I. De Moortel. How to Channel Photospheric Oscillations into the Corona. *Astrophys. J.*, 624:L61–L64, May 2005. doi: 10.1086/430345.

B. De Pontieu, S. W. McIntosh, M. Carlsson, V. H. Hansteen, T. D. Tarbell, P. Boerner, J. Martinez-Sykora, C. J. Schrijver, and A. M. Title. The Origins of Hot Plasma in the Solar Corona. *Science*, 331:55, January 2011. doi: 10.1126/science.1197738.

P. Démoulin, C. H. Mandrini, L. van Driel-Gesztelyi, B. J. Thompson, S. Plunkett, Zs. Kovári, G. Aulanier, and A. Young. What is the source of the magnetic helicity shed by CMEs? The long-term helicity budget of AR 7978. *Astron. Astrophys.*, 382:650–665, February 2002. doi: 10.1051/0004-6361:20011634.

T. Duckenfield, S. A. Anfinogentov, D. J. Pascoe, and V. M. Nakariakov. Detection of the Second Harmonic of Decay-less Kink Oscillations in the Solar Corona. *Astrophys. J. Lett.*, 854:L5, February 2018. doi: 10.3847/2041-8213/aaaaeb.

M. V. Dymova and M. S. Ruderman. Resonantly damped oscillations of longitudinally stratified coronal loops. *Astron. Astrophys.*, 457:1059–1070, October 2006. doi: 10.1051/0004-6361:20065051.

Z. Ebrahimi and K. Karami. Resonant absorption of kink magnetohydrodynamic waves by a magnetic twist in coronal loops. *Mon. Not. Roy. Astron. Soc.*, 462:1002–1011, October 2016. doi: 10.1093/mnras/stw1677.

P. M. Edwin and B. Roberts. Wave propagation in a magnetic cylinder. *Solar Phys.*, 88:179–191, October 1983. doi: 10.1007/BF00196186.

T. Elsden and A. N. Wright. The theoretical foundation of 3-D Alfvén resonances: Time-dependent solutions. *Journal of Geophysical Research (Space Physics)*, 122: 3247–3261, March 2017. doi: 10.1002/2016JA023811.

R. Erdélyi and I. Ballai. Heating of the solar and stellar coronae: a review. *Astronomische Nachrichten*, 328:726–733, October 2007. doi: 10.1002/asna.200710803.

Y. Fan. The Emergence of a Twisted Flux Tube into the Solar Atmosphere: Sunspot Rotations and the Formation of a Coronal Flux Rope. *Astrophys. J.*, 697:1529–1542, June 2009. doi: 10.1088/0004-637X/697/2/1529.

P. Forteza, R. Oliver, J. L. Ballester, and M. L. Khodachenko. Damping of oscillations by ion-neutral collisions in a prominence plasma. *Astron. Astrophys.*, 461:731–739, January 2007. doi: 10.1051/0004-6361:20065900.

C. Foullon, E. Verwichte, V. M. Nakariakov, K. Nykyri, and C. J. Farrugia. Magnetic Kelvin-Helmholtz Instability at the Sun. *Astrophys. J. Letts.*, 729:L8, March 2011. doi: 10.1088/2041-8205/729/1/L8.

P. Ghosh and F. K. Lamb. Accretion by rotating magnetic neutron stars. II. Radial and vertical structure of the transition zone in disk accretion. *Astrophys. J.*, 232: 259–276, August 1979. doi: 10.1086/157285.

C. R. Goddard, G. Nisticò, V. M. Nakariakov, and I. V. Zimovets. A statistical study of decaying kink oscillations detected using SDO/AIA. *Astron. Astrophys.*, 585: A137, January 2016. doi: 10.1051/0004-6361/201527341.

E. E. Goldstraw, A. W. Hood, P. K. Browning, and P. J. Cargill. Comparison of Methods for modelling Coronal Magnetic Fields. *ArXiv e-prints*, November 2017.

R. Goossens, M. Erdélyi and M. S. Ruderman. Resonant MHD Waves in the Solar Atmosphere. *Space Science Reviews*, 158:289, 2011. doi: 10.1007/s11214-010-9702-7.

Y. Guo, M. D. Ding, X. Cheng, J. Zhao, and E. Pariat. Twist Accumulation and Topology Structure of a Solar Magnetic Flux Rope. *Astrophys. J.*, 779:157, December 2013. doi: 10.1088/0004-637X/779/2/157.

H. Hasegawa, M. Fujimoto, T. D. Phan, H. Rème, A. Balogh, M. W. Dunlop, C. Hashimoto, and R. TanDokoro. Transport of solar wind into Earth's magnetosphere through rolled-up Kelvin-Helmholtz vortices. *Nature*, 430:755–758, August 2004. doi: 10.1038/nature02799.

J. Heyvaerts and E. R. Priest. Coronal heating by phase-mixed shear Alfven waves. *Astron. Astrophys.*, 117:220–234, January 1983.

A. W. Hood and E. R. Priest. Kink instability of solar coronal loops as the cause of solar flares. *Solar Phys.*, 64:303–321, December 1979. doi: 10.1007/BF00151441.

A. W. Hood, P. K. Browning, and R. A. M. van der Linden. Coronal heating by magnetic reconnection in loops with zero net current. *Astron. Astrophys.*, 506: 913–925, November 2009. doi: 10.1051/0004-6361/200912285.

A. W. Hood, M. Ruderman, D. J. Pascoe, I. De Moortel, J. Terradas, and A. N. Wright. Damping of kink waves by mode coupling. I. Analytical treatment. *Astron. Astrophys.*, 551:A39, March 2013. doi: 10.1051/0004-6361/201220617.

J. R. Hundhausen and B. C. Low. Magnetostatic structures of the solar corona. 1: A model based on the Cauchy boundary value problem. *Astrophys. J.*, 429:876–889, July 1994. doi: 10.1086/174372.

J. A. Ionson. Resonant absorption of Alfvenic surface waves and the heating of solar coronal loops. *Astrophys. J.*, 226:650–673, December 1978. doi: 10.1086/156648.

C. D. Johnston, A. W. Hood, P. J. Cargill, and I. De Moortel. A new approach for modelling chromospheric evaporation in response to enhanced coronal heating. I. The method. *Astron. Astrophys.*, 597:A81, January 2017. doi: 10.1051/0004-6361/201629153.

B. B. Kadomtsev and O. P. Pogutse. Nonlinear helical perturbations of a plasma in the tokamak. *Soviet Journal of Experimental and Theoretical Physics*, 38:575–589, February 1974.

K. Karami and M. Barin. The effects of twisted magnetic field on coronal loop oscillations and dissipation. *Mon. Not. Roy. Astron. Soc.*, 394:521–526, March 2009. doi: 10.1111/j.1365-2966.2008.14360.x.

K. Karampelas and T. Van Doorsselaere. Simulations of fully deformed oscillating flux tubes. *Astron. Astrophys.*, 610:L9, February 2018. doi: 10.1051/0004-6361/201731646.

K. Karampelas, T. Van Doorsselaere, and P. Antolin. Heating by transverse waves in simulated coronal loops. *Astron. Astrophys.*, 604:A130, August 2017. doi: 10.1051/0004-6361/201730598.

J. T. Karpen and S. K. Antiochos. Condensation Formation by Impulsive Heating in Prominences. *Astrophys. J.*, 676:658–671, March 2008. doi: 10.1086/526335.

E. Khomenko and M. Collados. Heating of the Magnetized Solar Chromosphere by Partial Ionization Effects. *Astrophys. J.*, 747:87, March 2012. doi: 10.1088/0004-637X/747/2/87.

E. Khomenko, M. Collados, and T. Felipe. Nonlinear Numerical Simulations of Magneto-Acoustic Wave Propagation in Small-Scale Flux Tubes. *Solar Phys.*, 251: 589–611, September 2008. doi: 10.1007/s11207-008-9133-8.

Elena Khomenko. On the effects of ion-neutral interactions in solar plasmas. *Plasma Physics and Controlled Fusion*, 59:014038, January 2017. doi: 10.1088/0741-3335/59/1/014038.

J. A. Klimchuk. On Solving the Coronal Heating Problem. *Solar Physics*, 234:41–77, March 2006. doi: 10.1007/s11207-006-0055-z.

J. A. Klimchuk, S. Patsourakos, and P. J. Cargill. Highly Efficient Modeling of Dynamic Coronal Loops. *Astrophys. J.*, 682:1351-1362, August 2008. doi: 10.1086/589426.

G. Lapenta and D. A. Knoll. Reconnection in the Solar Corona: Role of the Kelvin-Helmholtz Instability. *Solar Physics*, 214:107–129, May 2003. doi: 10.1023/A:1024036917505.

D. W. Longcope. A Simple Model of Chromospheric Evaporation and Condensation Driven Conductively in a Solar Flare. *Astrophys. J.*, 795:10, November 2014. doi: 10.1088/0004-637X/795/1/10.

T. Magara and D. W. Longcope. Injection of Magnetic Energy and Magnetic Helicity into the Solar Atmosphere by an Emerging Magnetic Flux Tube. *Astrophys. J.*, 586: 630–649, March 2003. doi: 10.1086/367611.

N. Magyar and T. Van Doorsselaere. Damping of nonlinear standing kink oscillations: a numerical study. *Astron. Astrophys.*, 595:A81, November 2016. doi: 10.1051/0004-6361/201629010.

Norbert Magyar, Tom Van Doorsselaere, and Marcel Goossens. Generalized phase mixing: Turbulence-like behaviour from unidirectionally propagating MHD waves. *Scientific Reports*, 7:14820, November 2017. doi: 10.1038/s41598-017-13660-1.

S. W. McIntosh, B. de Pontieu, M. Carlsson, V. Hansteen, P. Boerner, and M. Goossens. Alfvénic waves with sufficient energy to power the quiet solar corona and fast solar wind. *Nature*, 475:477–480, July 2011. doi: 10.1038/nature10235.

Scott W. McIntosh and Stuart M. Jefferies. Observing the Modification of the Acoustic Cutoff Frequency by Field Inclination Angle. *Astrophys. J.*, 647:L77–L81, August 2006. doi: 10.1086/507425.

J. C. McKinney, A. Tchekhovskoy, and R. D. Blandford. General relativistic magnetohydrodynamic simulations of magnetically choked accretion flows around black holes. *Mon. Not. Roy. Astron. Soc.*, 423:3083–3117, July 2012. doi: 10.1111/j.1365-2966.2012.21074.x.

J. W. Miles. On the generation of surface waves by shear flows. *Journal of Fluid Mechanics*, 3:185–204, January 1957. doi: 10.1017/S0022112057000567.

A. Miura. Anomalous transport by magnetohydrodynamic Kelvin-Helmholtz instabilities in the solar wind-magnetosphere interaction. *Journal of Geophysical Research*, 89:801–818, February 1984. doi: 10.1029/JA089iA02p00801.

S. P. Moschou, R. Keppens, C. Xia, and X. Fang. Simulating coronal condensation dynamics in 3D. *Advances in Space Research*, 56:2738–2759, December 2015. doi: 10.1016/j.asr.2015.05.008.

V. M. Nakariakov and E. Verwichte. Coronal Waves and Oscillations. *Living Reviews in Solar Physics*, 2:3, December 2005. doi: 10.12942/lrsp-2005-3.

V. M. Nakariakov, L. Ofman, E. E. Deluca, B. Roberts, and J. M. Davila. TRACE observation of damped coronal loop oscillations: Implications for coronal heating. *Science*, 285:862–864, August 1999. doi: 10.1126/science.285.5429.862.

K. Nykyri and A. Otto. Plasma transport at the magnetospheric boundary due to reconnection in Kelvin-Helmholtz vortices. *Geophys. Res. Lett.*, 28:3565–3568, 2001. doi: 10.1029/2001GL013239.

K. Nykyri and A. Otto. Influence of the Hall term on KH instability and reconnection inside KH vortices. *Annales Geophysicae*, 22:935–949, March 2004. doi: 10.5194/angeo-22-935-2004.

L. Ofman and B. J. Thompson. SDO/AIA Observation of Kelvin-Helmholtz Instability in the Solar Corona. *Astrophys. J. Lett.*, 734:L11, June 2011. doi: 10.1088/2041-8205/734/1/L11.

J. P. O'Hara and I. De Moortel. Impact of flux distribution on elementary heating events. *Astron. Astrophys.*, 594:A67, October 2016. doi: 10.1051/0004-6361/201628913.

T. J. Okamoto, S. Tsuneta, T. E. Berger, K. Ichimoto, Y. Katsukawa, B. W. Lites, S. Nagata, K. Shibata, T. Shimizu, R. A. Shine, Y. Suematsu, T. D. Tarbell, and A. M. Title. Coronal Transverse Magnetohydrodynamic Waves in a Solar Prominence. *Science*, 318:1577, December 2007. doi: 10.1126/science.1145447.

T. J. Okamoto, P. Antolin, B. De Pontieu, H. Uitenbroek, T. Van Doorsselaere, and T. Yokoyama. Resonant Absorption of Transverse Oscillations and Associated Heating in a Solar Prominence. I. Observational Aspects. *Astrophys. J.*, 809:71, August 2015. doi: 10.1088/0004-637X/809/1/71.

A. Otto and D. H. Fairfield. Kelvin-Helmholtz instability at the magnetotail boundary: MHD simulation and comparison with Geotail observations. *Journal of Geophysical Research*, 105:21,175–21,190, September 2000. doi: 10.1029/1999JA000312.

P. Pagano and I. De Moortel. Contribution of Mode Coupling and Phase-Mixing of Alfven Waves to Coronal Heating. *Astron. Astrophys., submitted*, January 2017.

J. C. B. Papaloizou and J. E. Pringle. The dynamical stability of differentially rotating discs. II. *Mon. Not. Roy. Astron. Soc.*, 213:799–820, April 1985. doi: 10.1093/mnras/213.4.799.

Susanna Parenti. Solar prominences: Observations. *Living Reviews in Solar Physics*, 11(1):1, Mar 2014. ISSN 1614-4961. doi: 10.12942/lrsp-2014-1. URL `https://doi.org/10.12942/lrsp-2014-1`.

C. E. Parnell and I. De Moortel. A contemporary view of coronal heating. *Philosophical Transactions of the Royal Society of London Series A*, 370:3217–3240, July 2012. doi: 10.1098/rsta.2012.0113.

D. J. Pascoe, I. de Moortel, and J. A. McLaughlin. Impulsively generated oscillations in a 3D coronal loop. *Astron. Astrophys.*, 505:319–327, October 2009. doi: 10.1051/0004-6361/200912270.

D. J. Pascoe, A. N. Wright, and I. De Moortel. Propagating Coupled Alfvén and Kink Oscillations in an Arbitrary Inhomogeneous Corona. *Astrophys. J.*, 731:73, April 2011. doi: 10.1088/0004-637X/731/1/73.

D. J. Pascoe, A. W. Hood, I. De Moortel, and A. N. Wright. Damping of kink waves by mode coupling. II. Parametric study and seismology. *Astron. Astrophys.*, 551: A40, March 2013. doi: 10.1051/0004-6361/201220620.

D. J. Pascoe, C. R. Goddard, G. Nisticò, S. Anfinogentov, and V. M. Nakariakov. Damping profile of standing kink oscillations observed by SDO/AIA. *Astron. Astrophys.*, 585:L6, January 2016a. doi: 10.1051/0004-6361/201527835.

D. J. Pascoe, C. R. Goddard, G. Nisticò, S. Anfinogentov, and V. M. Nakariakov. Coronal loop seismology using damping of standing kink oscillations by mode coupling. *Astron. Astrophys.*, 589:A136, May 2016b. doi: 10.1051/0004-6361/201628255.

D. I. Pontin, A. L. Wilmot-Smith, G. Hornig, and K. Galsgaard. Dynamics of braided coronal loops. II. Cascade to multiple small-scale reconnection events. *Astron. Astrophys.*, 525:A57, January 2011. doi: 10.1051/0004-6361/201014544.

E. Priest. *Magnetohydrodynamics of the Sun*. Cambridge University Press, May 2014.

E. R. Priest, J. F. Heyvaerts, and A. M. Title. A Flux-Tube Tectonics Model for Solar Coronal Heating Driven by the Magnetic Carpet. *Astrophys. J.*, 576:533–551, September 2002. doi: 10.1086/341539.

F. Reale, S. Orlando, M. Guarrasi, A. Mignone, G. Peres, A. W. Hood, and E. R. Priest. 3D MHD modeling of twisted coronal loops. *Astrophys. J.*, 830:21, October 2016. doi: 10.3847/0004-637X/830/1/21.

J. Reid, A. W. Hood, C. E. Parnell, P. K. Browning, and P. J. Cargill. Coronal energy release by MHD avalanches: continuous driving. *Astron. Astrophys.*, 615:A84, July 2018. doi: 10.1051/0004-6361/201732399.

M. S. Ruderman. The resonant damping of oscillations of coronal loops with elliptic cross-sections. *Astron. Astrophys.*, 409:287–297, October 2003. doi: 10.1051/0004-6361:20031079.

M. S. Ruderman and R. Erdélyi. Transverse Oscillations of Coronal Loops. *Space Sci. Rev.*, 149:199–228, December 2009. doi: 10.1007/s11214-009-9535-4.

M. S. Ruderman and J. Terradas. Damping of coronal loop kink oscillations due to mode conversion. *Astron. Astrophys.*, 555:A27, July 2013. doi: 10.1051/0004-6361/201220195.

M. S. Ruderman, D. Berghmans, M. Goossens, and S. Poedts. Direct excitation of resonant torsional Alfven waves by footpoint motions. *Astron. Astrophys.*, 320: 305–318, April 1997a.

M. S. Ruderman, M. Goossens, J. L. Ballester, and R. Oliver. Resonant Alfven waves in coronal arcades driven by footpoint motions. *Astron. Astrophys.*, 328:361–370, December 1997b.

M. S. Ruderman, M. Goossens, and J. Andries. Nonlinear propagating kink waves in thin magnetic tubes. *Physics of Plasmas*, 17:082108, August 2010. doi: 10.1063/1.3464464.

D. M. Rust and A. Kumar. Evidence for Helically Kinked Magnetic Flux Ropes in Solar Eruptions. *Astrophys. J.*, 464:L199, June 1996. doi: 10.1086/310118.

T. Sakurai, M. Goossens, and J. V. Hollweg. Resonant behaviour of MHD waves on magnetic flux tubes. I - Connection formulae at the resonant surfaces. *Solar Phys.*, 133:227–245, June 1991. doi: 10.1007/BF00149888.

I. C. Santamaria, E. Khomenko, and M. Collados. Magnetohydrodynamic wave propagation from the subphotosphere to the corona in an arcade-shaped magnetic field with a null point. *A&A*, 577:A70, 2015. doi: 10.1051/0004-6361/201424701. URL `https://doi.org/10.1051/0004-6361/201424701`.

C. J. Schrijver, M. J. Aschwanden, and A. M. Title. Transverse oscillations in coronal loops observed with TRACE I. An Overview of Events, Movies, and a Discussion of Common Properties and Required Conditions. *Solar Phys.*, 206:69–98, March 2002. doi: 10.1023/A:1014957715396.

R. Soler, R. Oliver, and J. L. Ballester. Resonantly Damped Kink Magnetohydrodynamic Waves in a Partially Ionized Filament Thread. *Astrophys. J.*, 707:662–670, December 2009. doi: 10.1088/0004-637X/707/1/662.

R. Soler, J. Terradas, R. Oliver, J. L. Ballester, and M. Goossens. Kelvin-Helmholtz Instability in Coronal Magnetic Flux Tubes due to Azimuthal Shear Flows. *Astrophys. J.*, 712:875–882, April 2010. doi: 10.1088/0004-637X/712/2/875.

R. Soler, J. Terradas, G. Verth, and M. Goossens. Resonantly Damped Propagating Kink Waves in Longitudinally Stratified Solar Waveguides. *Astrophys. J.*, 736:10, July 2011. doi: 10.1088/0004-637X/736/1/10.

R. Soler, M. Carbonell, and J. L. Ballester. On the Spatial Scales of Wave Heating in the Solar Chromosphere. *Astrophys. J.*, 810:146, September 2015. doi: 10.1088/0004-637X/810/2/146.

D. J. Southwood and W. J. Hughes. Theory of hydromagnetic waves in the magnetosphere. *Space Sci. Rev.*, 35:301–366, 1983. doi: 10.1007/BF00169231.

L. Stella and R. Rosner. Magnetic field instabilities in accretion disks. *Astrophys. J.*, 277:312–321, February 1984. doi: 10.1086/161697.

H. R. Strauss. Nonlinear, three-dimensional magnetohydrodynamics of noncircular tokamaks. *Physics of Fluids*, 19:134–140, January 1976. doi: 10.1063/1.861310.

J. Terradas, R. Oliver, and J. L. Ballester. Damping of Kink Oscillations in Curved Coronal Loops. *Astrophys. J.*, 650:L91–L94, October 2006. doi: 10.1086/508569.

J. Terradas, J. Andries, M. Goossens, I. Arregui, R. Oliver, and J. L. Ballester. Nonlinear Instability of Kink Oscillations due to Shear Motions. *Astrophys. J. Lett.*, 687:L115, November 2008a. doi: 10.1086/593203.

J. Terradas, I. Arregui, R. Oliver, J. L. Ballester, J. Andries, and M. Goossens. Resonant Absorption in Complicated Plasma Configurations: Applications to Multistranded Coronal Loop Oscillations. *Astrophys. J.*, 679:1611-1620, June 2008b. doi: 10.1086/586733.

J. Terradas, N. Magyar, and T. Van Doorsselaere. Effect of Magnetic Twist on Nonlinear Transverse Kink Oscillations of Line-tied Magnetic Flux Tubes. *Astrophys. J.*, 853:35, January 2018. doi: 10.3847/1538-4357/aa9d0f.

S. Tomczyk, S. W. McIntosh, S. L. Keil, P. G. Judge, T. Schad, D. H. Seeley, and J. Edmondson. Alfvén Waves in the Solar Corona. *Science*, 317:1192, August 2007. doi: 10.1126/science.1143304.

T. Török and B. Kliem. The evolution of twisting coronal magnetic flux tubes. *Astron. Astrophys.*, 406:1043–1059, August 2003. doi: 10.1051/0004-6361:20030692.

A. A. van Ballegooijen, M. Asgari-Targhi, S. R. Cranmer, and E. E. DeLuca. Heating of the Solar Chromosphere and Corona by Alfvén Wave Turbulence. *Astrophys. J.*, 736:3, July 2011. doi: 10.1088/0004-637X/736/1/3.

T. Van Doorsselaere, J. Andries, S. Poedts, and M. Goossens. Damping of Coronal Loop Oscillations: Calculation of Resonantly Damped Kink Oscillations of One-dimensional Nonuniform Loops. *Astrophys. J.*, 606:1223–1232, May 2004. doi: 10.1086/383191.

T. Van Doorsselaere, J. Andries, and S. Poedts. Observational evidence favors a resistive wave heating mechanism for coronal loops over a viscous phenomenon. *Astron. Astrophys.*, 471:311–314, August 2007. doi: 10.1051/0004-6361:20066658.

E. Verwichte, V. M. Nakariakov, L. Ofman, and E. E. Deluca. Characteristics of transverse oscillations in a coronal loop arcade. *Solar Phys.*, 223, September 2004. doi: 10.1007/s11207-004-0807-6.

A. L. Wilmot-Smith, D. I. Pontin, and G. Hornig. Dynamics of braided coronal loops. I. Onset of magnetic reconnection. *Astron. Astrophys.*, 516:A5, June 2010. doi: 10.1051/0004-6361/201014041.

A. L. Wilmot-Smith, D. I. Pontin, A. R. Yeates, and G. Hornig. Heating of braided coronal loops. *Astron. Astrophys.*, 536:A67, December 2011. doi: 10.1051/0004-6361/201117942.

G. L. Withbroe. The temperature structure, mass, and energy flow in the corona and inner solar wind. *Astrophys. J.*, 325:442–467, February 1988. doi: 10.1086/166015.

G. L. Withbroe and R. W. Noyes. Mass and energy flow in the solar chromosphere and corona. *Annual Review of Astron and Astrophys*, 15:363–387, 1977. doi: 10.1146/annurev.aa.15.090177.002051.

L. N. Woolsey and S. R. Cranmer. Time-dependent Turbulent Heating of Open Flux Tubes in the Chromosphere, Corona, and Solar Wind. *Astrophys. J.*, 811:136, October 2015. doi: 10.1088/0004-637X/811/2/136.

A. N. Wright and T. Elsden. The Theoretical Foundation of 3D Alfvén Resonances: Normal Modes. *Astrophys. J.*, 833:230, December 2016. doi: 10.3847/1538-4357/833/2/230.

A. N. Wright and M. J. Thompson. Analytical treatment of Alfvén resonances and singularities in nonuniform magnetoplasmas. *Physics of Plasmas*, 1:691–705, March 1994. doi: 10.1063/1.870815.

C. Xia, R. Keppens, and X. Fang. Coronal rain in magnetic bipolar weak fields. *Astron. Astrophys.*, 603:A42, July 2017. doi: 10.1051/0004-6361/201730660.

Masaaki Yamada, Russell Kulsrud, and Hantao Ji. Magnetic reconnection. *Reviews of Modern Physics*, 82:603–664, January 2010. doi: 10.1103/RevModPhys.82.603.

A. R. Yeates, G. Hornig, and A. L. Wilmot-Smith. Topological Constraints on Magnetic Relaxation. *Phys. Rev. Lett.*, 105:085002, August 2010. doi: 10.1103/PhysRevLett.105.085002.

D. J. Yu, T. Van Doorsselaere, and M. Goossens. Resonant Absorption of Surface Sausage and Surface Kink Modes under Photospheric Conditions. *Astrophys. J.*, 850:44, November 2017. doi: 10.3847/1538-4357/aa9223.

Dae Jung Yu and Tom Van Doorsselaere. A Study on the Excitation and Resonant Absorption of Coronal Loop Kink Oscillations. *Astrophys. J.*, 831:30, November 2016. doi: 10.3847/0004-637X/831/1/30.

Teimuraz V. Zaqarashvili, Ivan Zhelyazkov, and Leon Ofman. Stability of Rotating Magnetized Jets in the Solar Atmosphere. I. Kelvin-Helmholtz Instability. *Astrophys. J.*, 813:123, November 2015. doi: 10.1088/0004-637X/813/2/123.

I. V. Zimovets and V. M. Nakariakov. Excitation of kink oscillations of coronal loops: statistical study. *Astron. Astrophys.*, 577:A4, May 2015. doi: 10.1051/0004-6361/201424960.